Kent Academic Repository

Lennox, Robert Christopher (2015) ***Structure-Property Correlations in doped Bismuth Ferrite Ceramics.*** **Master of Philosophy (MPhil) thesis, University of Kent.**

STRUCTURE-PROPERTY CORRELATIONS IN DOPED BISMUTH FERRITE CERAMICS

by
ROBERT CHRISTOPHER LENNOX

A thesis submitted for the degree of
Master of Philosophy of the University of Kent

September 2015

Department of Physical Science
University of Kent
Canterbury

Abstract

A detailed powder neutron diffraction study coupled with a complementary characterisation of the ferroelectricity and ferromagnetism, concerning two different compositions based on a parent $BiFeO_3$ crystal lattice. The addition of Dy^{3+} into $BiFeO_3$ ceramics shows how the parent polar $R3c$ symmetry destabilises due to strain, linking to a large size variance between the two A-site cations (Dy^{3+} and Bi^{3+}). This results in a loss of symmetry to polar *Cc* followed by a broad competitive phase system between strained *Cc* and non-polar *Pnma* symmetries. Increasingly strain on the lattice is seen until x=0.12 at which point the *Pnma* phase becomes dominant. However, phase co-existence persists until beyond x=0.25. Preliminary magnetisation measurements indicate a developing ferromagnetic character which increases in magnitude with Dy^{3+} content; electrical measurements suggest that whilst initial compositions of $Bi_{0.95}Dy_{0.05}FeO_3$ show signs of polarity, more Dy^{3+} rich materials such as $Bi_{0.70}Dy_{0.30}FeO_3$ shows relaxor like characteristics.

This study also examines the addition of Alkali Metal Niobates to $BiFeO_3$, looking at the $Bi_{1-x}K_xFe_{1-x}Nb_xO_3$ solid solution. Despite much individual attention on both $BiFeO_3$ and $KNbO_3$ a solid solution between the two has received less interest. Reported in this work is a detailed neutron and synchrotron X-ray powder diffraction study which demonstrates a polar $R3c$ → polar $P4mm$ → polar $Amm2$ series of structural phase transitions similar to that exhibited by $PbZrO_3$–$PbTiO_3$. Early electrical measurements show a non-ohmic electrode effects, making it difficult to determine the polar nature of the P4mm phase. Preliminary magnetic data suggests that the G-type anti-ferromagnetic spin cycloid may be retained, but some canting may occur, however the exact nature of the magnetic structure is unconfirmed, and evidence may initially suggest paramagnetism, canted antiferromagnetism or a spin glass like structure. All materials seem to exhibit a similar magnetic transition consistent with the parent lattice.

Acknowledgements

I would like to thank the South East Physics Network (SEPnet) for the provision of a studentship.

Thanks Dr Nikitas Gidopoulos for support in the early stages of the project.

I would also like to acknowledge the University of Maryland's X-ray Crystallography Center and thank the the STFC for facilities access and the Diamond Light Source and the ISIS neutron source for access to I11 (EE9194) and HRPD (RB1220271) beamlines respectively. Special thanks also to Dr Claire Murray, Dr Chui Tang and Dr Aziz Daoud-Aladine for assistance conducting these experiments.

A particular mention has to go to Dr Finlay Morrison all his support, and for access to impedance spectroscopy equipment.

Thanks also need to be extended to Dr Mark Price, Dr Christopher Kavanagh, Jonathan Gardner, Richard Hamlyn, Dr Marc Williams, Laura Vera Stimpson and Daniel Jackson, Dr Marek Jura and Michaela Regan for their contributions to this work.

Special thanks to Dr Paul Strange for all his support during my university career.

The biggest appreciation has to be Dr Donna Arnold. My PhD has been an amazing experience and I thank Donna wholeheartedly, both for tremendous academic support, and for all the wonderful opportunities I have been given.

Finally, I must dedicate this work to my Mum and Dad, Brother Daniel and Sister Emily, Nan and Granddad and the lovely Amy Carr.

Table of Contents

List of Figure Captions

List of Tables

Chapter 1: Introduction

Whilst existing ferroelectric and multiferroic materials fulfil a role in electronic applications, recent safety directives have led to a need for alternative materials. The main cause of this is the toxicity of lead (Pb). This stems from the Directive 2002/95/EC of the European Parliament and of the Council of the 27th January 2003, from the official Journal of the European Union which states that "*Member states shall ensure that, from 1st July 2006, new electrical and electronic equipment put on the market does not contain lead... due to the health and environmental risks associated with the toxicity*"

There is much desire therefore to research some alternative lead-free ferroelectrics for application, namely in this work, doped Bismuth Ferrite ($BiFeO_3$). Particular attention is focused on how local and long range effects on the lattice affect both structure and properties. This introduction will include a brief look at electronic functional materials, including their current uses, and discuss the potential to move towards lead-free materials. The technological importance of these materials lends great importance to their research, and there will be some discussion of different multiferroic compounds currently known and their relative merits, before moving on to look more closely at these existing studies of $BiFeO_3$. $BiFeO_3$ is one of the most commonly studied materials, primarily due to the observation of both room temperature magnetic and electric ordering. However, much contradiction exists as to the exact nature of the phase diagram, the literature giving several different interpretations, and as a result our understanding of the structure and property correlations in this material is lacking. Arguments from the literature will be presented here, particularly those pertinent to the known dopant effects of Dy^{3+} and K^+, Nb^{5+} co-doping $BiFeO_3$-based materials on which this work builds.

In this thesis we present a concise review of dopant driven structural phase transitions at room temperature and variable temperature for several different doped species.

1.1. Functional Properties of Materials

Before discussing the functional properties of materials, it is important to consider symmetry in these crystal systems. In crystallography, symmetry is used to characterize crystals, identify repeating parts of molecules, and simplify both data collection and nearly all calculations. The symmetry of a crystal is given by the unit cell. This is the smallest available arrangement of atoms in which the cell can be translated within the material to give an identical state to the initial state, post transformation.

By convention the unit cell edges are chosen to have the highest symmetry, and to have the smallest cell volume. If other symmetry considerations do not override, then the cell is chosen such that $a \le b \le c$, and α, β, and γ all < 90 ° or all ≥ 90 °.

Crystalline materials are separated into 7 different crystal systems (As shown in Table 1.1). These crystal systems are most easily identified by the constraints on the cell parameters. (1)

Table 1.1: *The 7 Crystal Systems with their crystal constraints*

Crystal System	**Cell Parameters**
Triclinic	$a \neq b \neq c$; $\alpha \neq \beta \neq \gamma$
Monoclinic	$a \neq b \neq c$; $\alpha = \gamma = 90°$, $\beta \ge 90°$
Orthorhombic	$a \neq b \neq c$; $\alpha = \beta = \gamma = 90°$
Tetragonal	$a = b \neq c$; $\alpha = \beta = \gamma = 90°$
Trigonal	$a = b = c$; $\alpha = \beta = \gamma \neq 90°$
Hexagonal	$a = b \neq c$; $\alpha = \beta = 90°$, $\gamma = 120°$
Cubic	$a = b = c$; $\alpha = \beta = \gamma = 90°$

These seven crystal systems each describe how a 3-dimensional lattice may be constructed. Lattices with lattice points only on the corners are called primitive lattices (P).

All other lattices are known as non-primitive. Some of these lattices can have one, two, or three additional lattice points, and are named depending on the location of these points. Lattices with one additional lattice point can be known as an (A-, B-, or C-centred cells), which have an additional lattice point at the centre of the one of the faces of the cell. Body-centred lattices (I) cells have an additional lattice point in the centre of the cell. Face-centred (F) cells have additional lattice points on all faces.

This spread of available lattices along with the different symmetry operations, lead to a total number of 14 Bravais lattices. The various lattice centrings are shown in Figure 1.1.

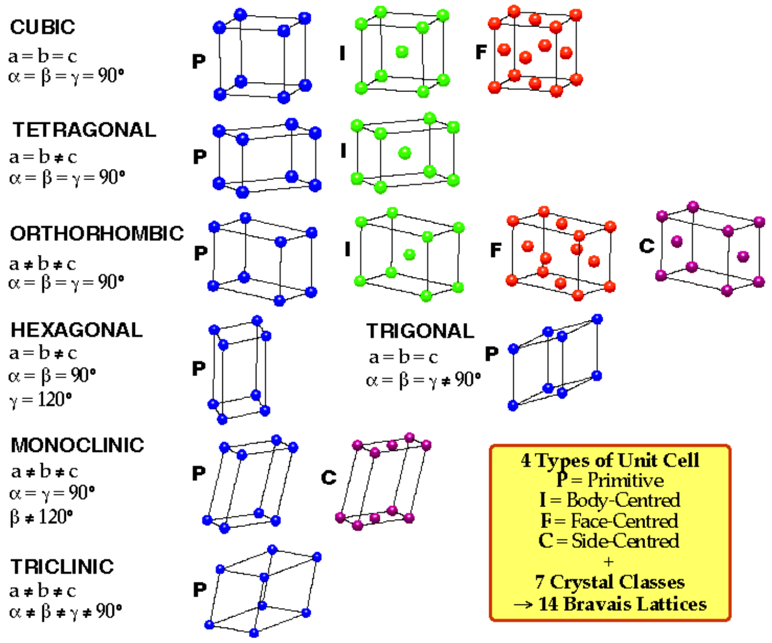

Figure 1.1: *Graphic representations of the 14 available Bravais lattices*(2)

These variations in unit cell arrangement can lead to different materials exhibiting a range of different properties linked to the symmetry of lattice.

Materials that exhibit electrical ordering on an atomic scale can give rise to some degree of functionality, (3) using the known responses when exposed to an electric field, with the exact behaviour being dependent on the type of electronic ordering within the lattice

These dielectric materials can be characterised according to like properties, and these different forms of behaviour fall into the following types:

- Piezoelectric
- Pyroelectric
- Ferroelectric

Much of the technology now employed is heavily dependent on use of their functional electronics, and material which fall into the categories of piezo-, pyro- or ferroelectric are in high demand. (4-6)

Much research currently being carried out is to either enhance the properties of known applicable materials, or find alternative for specific electronic applications by developing new materials with properties tailored to the role.

1.2. Types of Polar Dielectric

Dielectrics are materials that remain electrically insulated even when introduced to high voltages. They should also exhibit low loss, i.e. there should be little energy lost to heat when an alternating field is applied.(7) Figure 1.2 shows the different forms of polar dielectric, and how they relate to one another.

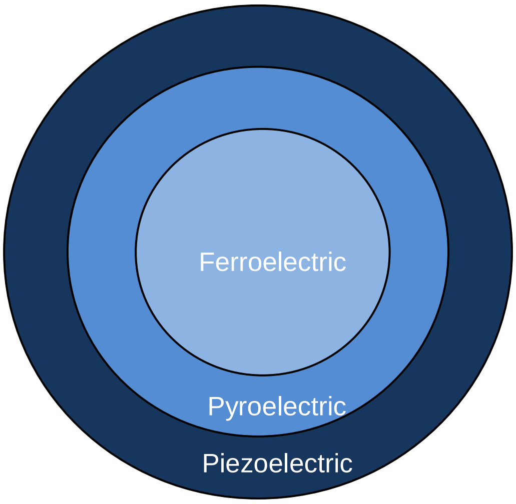

***Figure 1.2**: Venn diagram demonstrating the three classes of polar dielectric.*

1.2.1. Piezoelectrics

A piezoelectric material exhibits a lattice where the central cation does not occupy the exact centre of the lattice (centrosymmetric) as it would in a fully cubic cell, but instead is slightly offset from the centre of the lattice (non-centrosymmetric), this can lead to formation of an electric dipole, as the cation can then switch between the two available symmetric positions. A piezoelectric crystal can become polarised on the application of an external mechanical force. Given that this is a reversible process, the magnitude of the polarisation is directly linked to the force applied and hence the tensile or compressional stress. All non-centrosymmetric materials are classified as piezoelectric. Figure 1.3 how electrical properties depend on symmetry.

Given that there is a direct relationship between stress and polarisation this means that the effect can be approached from two different directions. The use of stress to cause physical change to a sample and hence to the polarisation state is known as the direct piezoelectric effect, whilst the application of an electric field to induce physical strain is known as the converse piezoelectric effect.(1)

One of the first applications of the piezoelectric effect was in the ultrasonic submarine detector developed during the WW1. This was the initial basis for the later development of sonar. This development has encouraged many other applications of piezoelectric devices such as microphones, signal filters and ultrasonic transducers.

The continued development of piezoelectric materials has led to a much more extensive market of products ranging from everyday products to specialised scientific and military devices.

1.2.2. Pyroelectrics

One subgroup of piezoelectrics are those that form permanent dipoles, the modulus of which links to both stress and temperature of the material. As with piezoelectrics, a crystal can be classified as pyroelectric purely by its symmetry, by examining the polarity of the material.

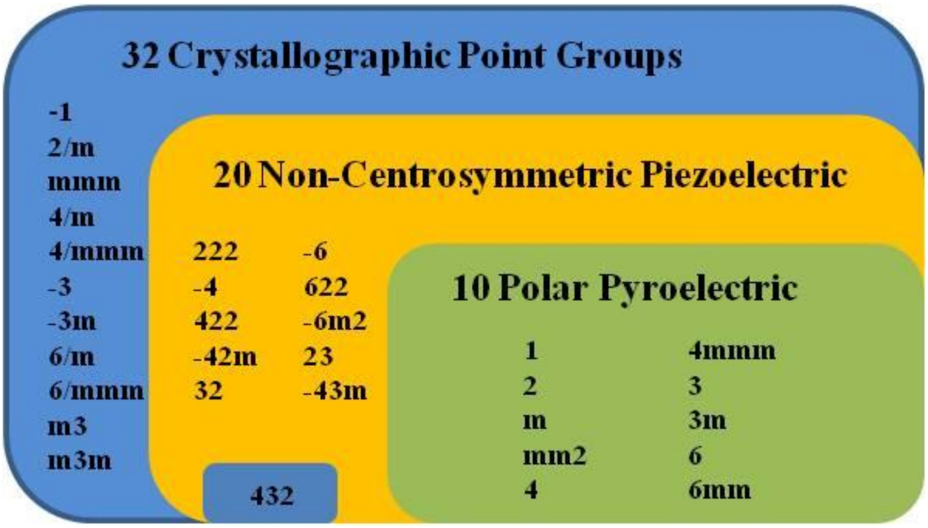

***Figure 1.3**: Relationship between crystallographic point groups and piezo-pyroelectric behavior.*(8)

1.2.3. Ferroelectrics

Ferroelectric materials are a further subgroup of pyroelectrics in the case that the spontaneous (permanent) polarisation can be switched upon the application of a suitable applied electric field, changing the vector orientation of the electrical dipole. Unlike piezoelectric and pyroelectric materials, it is not possible to determine whether a material will exhibit ferroelectric properties by knowledge of the crystal class alone.

As a result of the switching, the electrical polarisation of the material can be examined and plotted within a changing field to yield a hysteresis loop is observed [Figure 1.4].

After the application of an electric field to the material, the individual dipoles align with the field lines causing a polarisation in the direction of the field. Upon removal of the field the polarisation does not disappear [Figure 1.4(a)-(c)], it remains; this is called the remnant polarisation. Only when a field is applied in the opposite direction does the polarisation begin to reduce. Application of a certain strength of field will return the material to give zero net polarisation [Figure 1.4(d)] (the coercive field). If a stronger electric field is applied then the material will be polarised fully in the opposite direction [Figure 1.4(e)].

This is property is important for application, as it can be exploited to create a 1/0 binary state, where each direction of polarisation represent either an on or off state, and the application of an alternating field can be used to switch between them. Only by the observation of this hysteric behaviour can it be determined whether or not a material is ferroelectric.

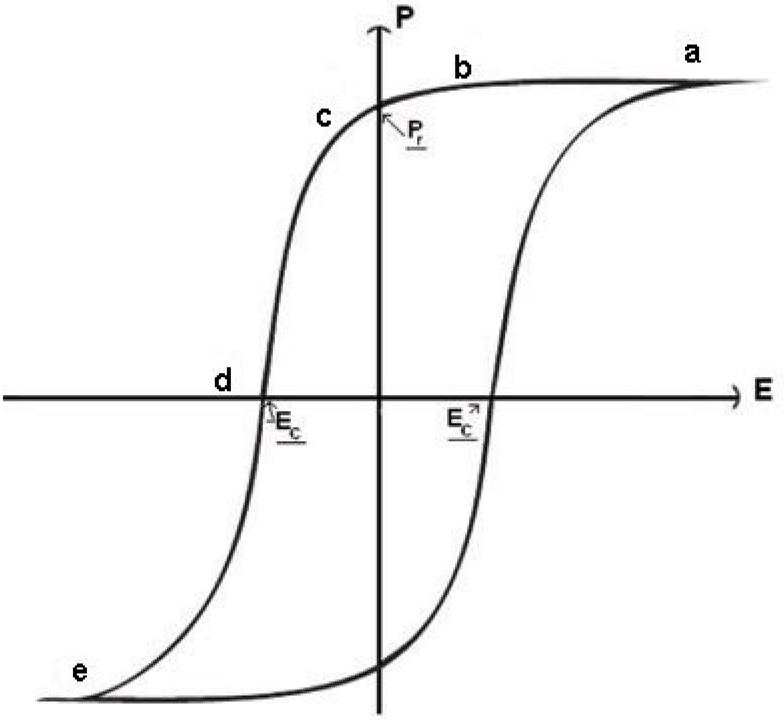

Figure 1.4: *Ferroelectric polarisation shown in a hysteresis loop* (9)

As previously stated, the lattice and the ferroelectric dipole can be coupled, and as such change in one cause a change in the other. There are two ways by which this can occur, leading to two different types of ferroelectric phase transitions, displacive (10) (e.g. $BaTiO_3$) and order-disorder (48,49) (e.g. $Pb(ScNb)O_3$), though a material may also contain elements of both behaviours (10,11). In a displacive ferroelectric, the force from the local electric fields increasing more quickly than it can be corrected by the lattice restoring forces. This leads to change in cation position, and therefore leads to the formation of a permanent dipole. In an order-disorder ferroelectric, the dipole moment of each unit cell points in a random direction (mainly ay high temperature). As temperature decreases, these dipoles order all pointing in the same direction and giving rise to an net polarisation.

One thing all of these materials share is that the properties of interest initially derive from the non-centrosymmetric nature of the material. A change to the external environment then leads to a change in polarisation. If there is any substantial change to this environment, then there can be loss of these properties. This can be linked to distortion in the lattice through temperature or physical strain and therefore loss of symmetry, or as in the order-disorder ferroelectric, random distribution of individual dipoles leading to a loss of net polarisation.

In many cases, this change in sample environment can be due to large variation of temperature can lead to a loss of the spontaneous polarisation, as it falls to zero, the temperature at which this occurs is known as the Curie temperature, T_C, and is often accompanied by a physical phase change to a phase of higher symmetry (centrosymmetric), as this displacement of the ions leads to loss of the dipole moment. This subsequent phase will be paraelectric, such that any remaining dipole moments are either non-existent or randomly orientated to the point that the net dipole moment of the material is zero [Figure 1.5].

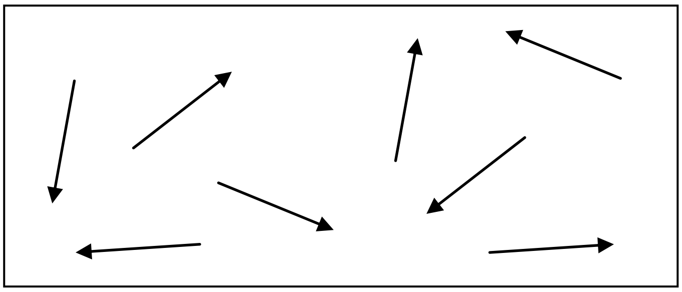

***Figure 1.5**: Schematic representation of paraelectric behaviour in materials* *(12)*

An important ferroelectric material in current technology is Lead Zirconate Titanate (PZT), which is used for memory applications.

1.2.4. Ferroelectric memory

One of the main application of ferroelectrics, and a strong reason to support their continued study is their use in computer memory. Semiconductor memories, particularly Dynamic random access memories (DRAM's) and Static random access memories (SRAM's) currently dominate the market. Semiconductor memory however has the disadvantage that they are volatile, i.e. the stored information is lost when the power fails. Often, more desirable are non-volatile memories are those that maintain a permanent state until they are manually switched to another state.

Ferroelectric random access memories (FRAM's) are non-volatile.

As previously stated, ferroelectric materials spontaneously polarise on cooling below the T_c. The magnitude and direction of this polarisation can be reversed by the application of an electric field. The FRAM can make use of this characteristic to store data in a 1/0 binary system using the two possible unit cell polarisations.

To maximise the application properties of the material used, there are certain conditions required. As the FRAM operates on the basis of changing polarisation, the ferroelectric material should have a large remnant polarisation. This will therefore be one focus when investigating ferroelectric materials.

1.3. Ferromagnetic materials

Similarly to ferroelectricity, which relies on a dipole due to displacement of electric charge, materials can exhibit magnetic dipoles which have the potential to facilitate memory applications.

A material is ferromagnetic only if all of its magnetic dipoles add a positive contribution to the net magnetization (11,13), i.e. they are aligned. If the moments of the dipoles align in an anti-parallel arrangement, giving no net magnetization, they are anti-ferromagnetic [

Figure 1.6]. All of these effects only occur however below a certain critical temperatures, either the Curie temperature (ferromagnetic →

paramagnetic) or the Néels temperature (paramagnetic → anti-ferromagnets).

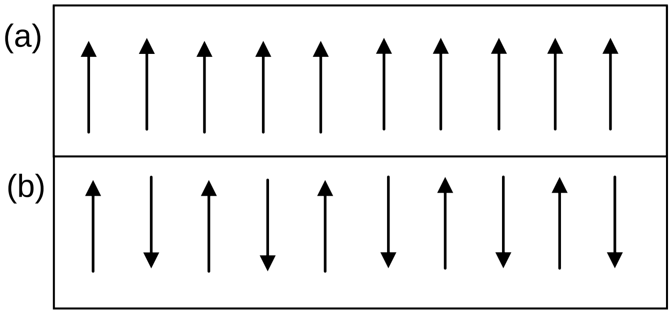

***Figure 1.6**: Schematic representation of spin ordering in (a) Ferromagnetism and (b) Anti-ferromagnetism* (12)

If the spins are aligned, then all ferromagnetic materials should have a strong permanent field. However, a bulk piece of ferromagnetic material is divided into a series of smaller magnetic domains. In the case of an anti-ferromagnetic materials, whilst the spins within each domain may align, the net spins across the materials domains do not, but instead line up such that no net magnetic moment is generated [Figure 1.7(a)], whilst in ferromagnetic materials, the spins align to give a net moment. [Figure 1.7(b)]

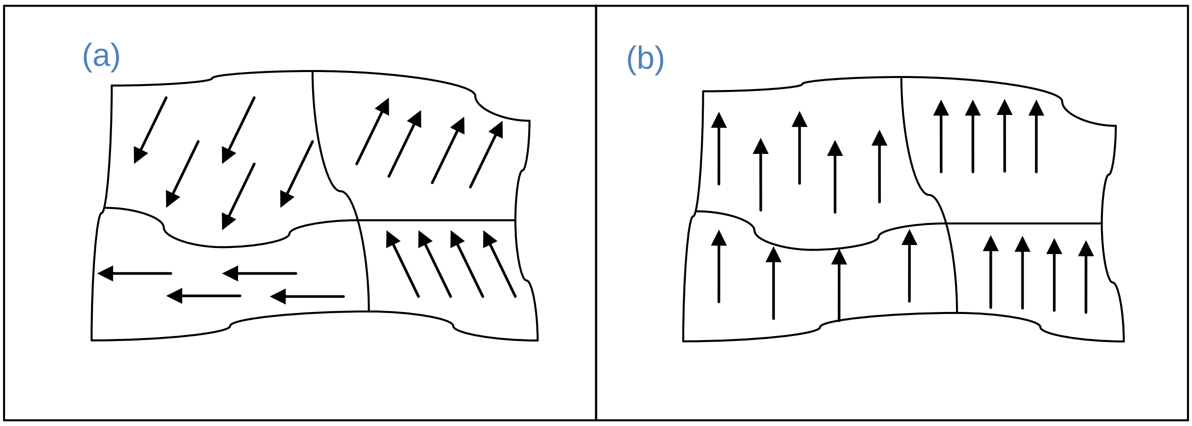

***Figure 1.7:** Schematic representation of domain division in bulk ferromagnetic materials (a) the random domain ordering in the presence of no external field and (b) the alignment of the spins in the presence of a magnetic field.*(12)

This magnetization as a function of the external field behaves in a similar fashion to that observed in ferroelectircity, and is also described by a hysteresis curve [Figure 1.4].

1.4. Multiferroic materials

Multiferroic materials are formally defined as materials that exhibit more than one primary ferroic order parameter simultaneously. (14) The three basic primary ferroic order parameters are ferromagnetism, ferroelectricity and ferroelasticity. [Figure 1.8]

Single phase multiferroics are rare because in most ferroelectrics, the ferroelectricity requires empty *d* orbitals, whilst in transition metals, magnetism often arises from unpaired electrons in the *d* orbital, and thus very few ferroelectrics can also exhibit long range magnetic order. This means that it is rarer still for a material to show both types of order parameter exist or exhibit significant coupling between these orders.

As such many composite materials exist, with each exhibiting more than one ferroic order parameter. Both composite and single phase multiferroic materials are studied extensively; either two successfully integrate of two different materials into a single geometry by e.g. multilayer thin films, or inserting tubes or wires into a bulk material, where each material exhibits different ferroic ordering or to develop a single phase material (often by doping) which give multiple ferroic responses. This allows the final material to exhibit with both ferroic properties.

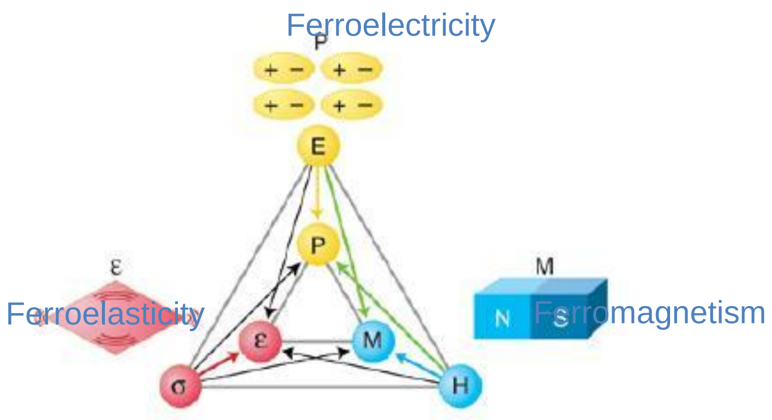

Figure 1.8: *Representation of the interactions between the three types of ferroic order.*(15)

The combination of ferroelectricity and ferromagnetism could be useful for similar applications to the previously mentioned FRAM, with the magnetic and electric dipoles being able to operate as linked binary states.

Natural single phase multiferroics as most common ferroelectrics are driven by hybridisation of empty d orbitals, with occupied p orbitals. This cannot lead to magnetic behaviour as the d orbitals must remain empty, whilst magnetism relies upon these orbitals having unpaired electrons to provide the magnetic dipole moment. There are however some natural multiferroics and using doping to enhance these materials is one available avenue of investigation. Many of these natural multiferroic materials are perovskite ceramics such as $BiFeO_3$.

The ideal scenario in this case is that the onset of ferroelectricity also results in a magnetically ordered state. Although this may lead to the ferroelectric polarisation being weaker, the magnetic coupling will ideally be strong enough to still show strong interaction from both types of ordering upon application of a field.

1.5. Perovskite materials

The basic perovskite cell is shown in Figure 1.10, and consists of anion octahedra (usually oxygen) encompassing a B site cation, with an A cations between each set of four octahedra. The ideal cubic structure is seen in materials such as $SrTiO_3$ [Figure 1.10(a)] at room temperature, although more usually the structure is distorted; either by cation displacement as in $BaTiO_3$ and PZT [Figure 1.10(b)], or by the tilting of the octahedral as in $CaTiO_3$ [Figure 1.10(c)], or by a combination of these effects.

The structure of an ideal perovskite, consists of a cubic $Pm\bar{3}m$ unit cell with an A-site species located at [½,½,½], B-site species at [0,0,0] and oxygen located at [½,0,0] resulting in the B-site species forming the previously mentioned octahedral.

There exists a mathematical model by which the stability of the ideal perovskite can be numerically defined (16). This was based on the system being purely ionic, where each cation would be surrounded by as many anions as could make physical contact, such that the cation-anion bond length would be the sum of their two ionic radii [Figure (1.9)]. This would lead to a cubic cell, and would the following correlation between the cation and anion ionic radii:

$$r_A + r_O = \sqrt{2}(r_B + r_O)$$

$$t = \frac{r_A + r_O}{\sqrt{2}(r_B + r_O)}$$

Where in an ideal perovskite the Goldschmidt tolerance factor would be 1.

However, for actual crystal systems the true cell is somehow distorted from this ideal model, often having octahedral that are tilted away from the perpendicular resulting in structures of more complex symmetry.(17-19)

The tolerance factor can be used to determine the distortion of the lattice. When 0.75 $\leq$ t $\leq$ 0.90, this usually coincides with an orthorhombic symmetry, 0.9 $\leq$ t $\leq$ 0.98 rhombohedral symmetry, and distortions where t>1 gives rise to a tetragonal symmetry.

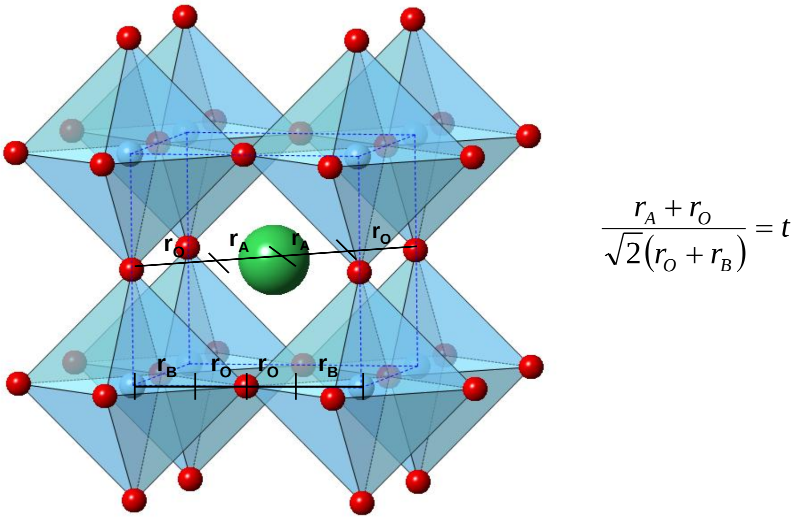

Figure 1.9: *Diagram showing the mathematical reasoning behind the tolerance factor*.(20)

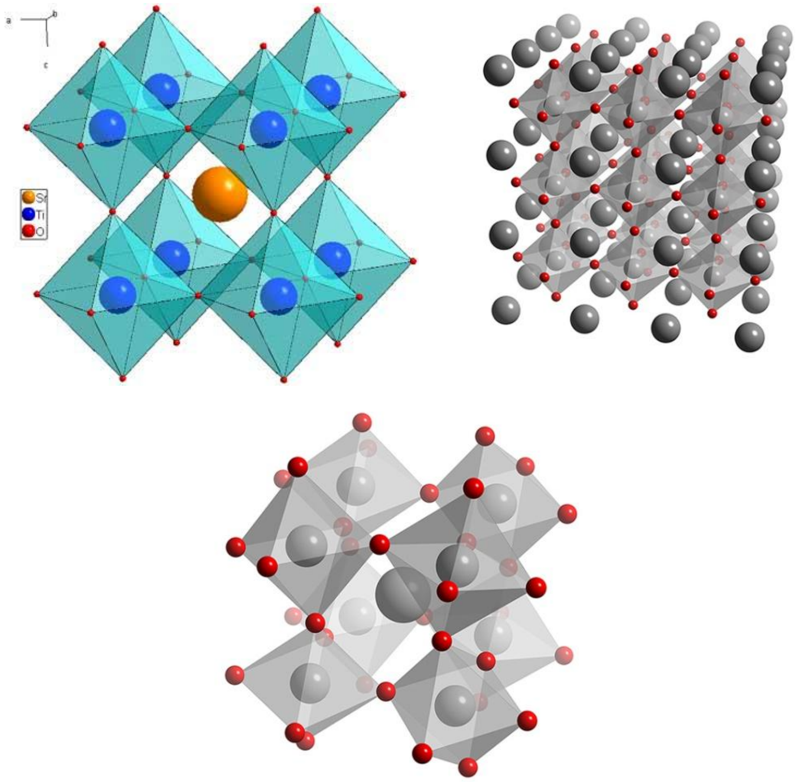

***Figure 1.10**: Schematic representations of the various types of displacement in a perovskite, with (a) the standard SrTiO*$_3$ *Perovskite in Pm3m symmetry* (25)*, (b) BaTiO*$_3$ *in P4/mmm symmetry, which shows A site cation displacement* (21) *and (c) CaTiO*$_3$ *which shows tilted octahedra and I4-mcm symmetry* (24)*.*

One well known perovskite ferroelectric that is being studied as an alternative is $BaTiO_3$ [Figure (1.11)]. The electric properties of $BaTiO_3$ doped with large quantities of magnetic species are already well studied, but the magnetic characteristics are only recently of interest (22,23,25). The known phases of $BaTiO_3$ are Rhombohedral (until -80^{o}C), Orthorhombic (until 5^{o}C), Tetragonal (until 120^{o}C) and Cubic.

Upon cooling past the Curie Temperature of 120^{o}C $BaTiO_3$ exhibits spontaneous polarisation. This is due to the translation of the unit cell from cubic to tetragonal structure. This tetragonal cell is no longer centrosymmetric, with the central Ba^{2+} on sitting slightly off centre, such that an electric dipole is generated.

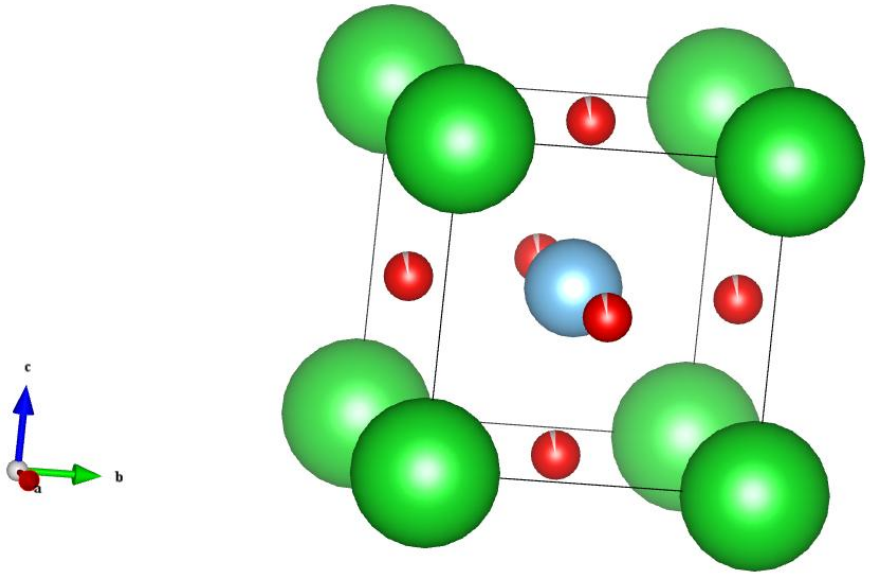

Figure 1.11: *The structure of Barium Titanate drawn using the VESTA suit with the ions represented by the following coloured spheres, red: oxygen ions, blue: titanium ion, green:barium ion*(26)

$BaTiO_3$ doped with 5% Fe has been shown to exhibit room temperature ferromagnetism and ferroelectricity (22), however there is some discussion as to whether or not the crystal undergoes a phase change from tetragonal to hexagonal symmetry, and how this affects the ferroelectric properties of $BaTiO_3$. Also the oxides of Fe all exhibit a degree of ferromagnetic ordering at room temperature, so it is impossible to tell if small amounts of iron oxide impurity phases are responsible for the resultant magnetic ordering.

Along with existing ferroelectrics, the search for an alternate memory material may provide an opportunity to exploit other classes of materials in emerging technologies such as multiferroic materials. Multiferroic materials have been pursued as a candidate for the development of new functional devices to fill this niche, with particular focus on their applications in spintronics and memory materials. This stems from the ability of multiferroic materials to exhibit magneto-electric properties, making potential devices multifunctional.

The temperature range over which a material may exhibit piezoelectricity is dependent its composition and symmetry, which obviously has a significant impact on the practicality of the material being used in devices, particularly the Curie temperature of that material. For many devices wide operating temperature ranges are required in order that the material does not undergo a phase change to a non-piezoelectric symmetry or depolarise due to temperature during its operation. This is particularly critical for materials to be used in computational electronics. This leads to a general requirement of piezoelectric characteristics well in excess of room temperature (i.e. T_C must be significantly larger than 300K).

Another characteristic requirement for the application of piezoelectrics is that the observed effect is great enough to be able to convert supplied electrical power into a useful amount of mechanical power or mechanical to electrical. To be commercially viable the process also needs to be efficient, *i.e.* have small dielectric loss, be stable, reproducible and non-toxic.

Many of the piezoelectric materials of interest are ferroelectric perovskites. The piezoelectric properties in these materials arise due to a Jahn-Teller like distortion of the B-site octahedra resulting in a displacement of the cation with respect to the oxygen anions [Figure 1.12], creating a dipole. This requires that the unit cell distorts from the previous mentioned ideal cubic perovskite structure to maintain stability. The application of an electric field to the material can further promote or reduce off-centring, depending on the direction of the applied field relative to the dipole. This can then result change to the physical structure of the material. Alternatively, physical stress can be exerted on the material in order to distort the lattice. This unit cell distortion can either enhance or reduce the off-centring of the cation, which will result in a change in the polarisation as it will change the magnitude of the polarisation vector.

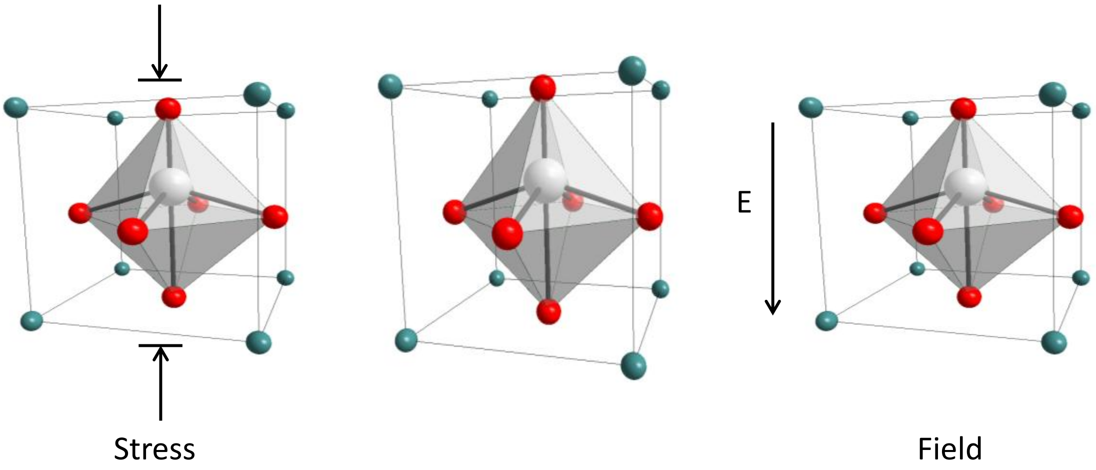

Figure 1.12: *Distortion of a piezoelectric perovskite by an stress (left) and applied electric field (right), causing deformation and changing the polarisation*

These materials worthy of investigation due to their ability to adopt a range of geometries from cubic to rhombohedral(17-19) giving a wide range of stable compositions. As previously stated, many commercial uses require that the materials be doped with other chemical elements in order to tailor specific properties or enhance the temperature or mechanical range under which the material remains operational. As previously noted this change to the crystal structure will also affect any electrical or magnetic domain structures, and hence the net polarisation/magnetisation.

1.6. Structural effects from doping

1.6.1. Doping – size effects

The effect of introducing dopant species of a different size to the perovskite lattice will alter the tolerance factor of the material as it will change the size of the average cation on that site. This has an effect on the stability of phase diagram characteristic to that material. In general, if a smaller A-site cation is added the tolerance factor will decrease and therefore alter T_C depending on if the value moves towards or away from 1. Similarly a smaller B-site species would be expected to increase the tolerance factor and again alter T_C based on the change in value.

The change to lattice constants will therefore depend on the concentration of the dopant added (assuming that the temperature and mechanical strain is unchanged). (97) This obviously still depend upon the assumptions made when discussing Goldschmidt's tolerance factor being close to accurate.

As stated, this change to the lattice parameters will also lead to alteration of the Curie temperature of the material, with smaller lattices exhibiting a lower T_C and vice versa. However, this is not the only characteristic that can influence T_C, and is only prevalent when there is no change to the electronic structure (overall charge) of the new cation compared to the original. It can also be disrupted by vastly different sized cation dopant which may lead to large changes to the lattice strain.

1.6.2. Doping – strain effects

There is some suggestion in the literature, that whilst there is some effect from the average cation size, there is also a contribution from the cation variance on any given site. Variance accounts for the relative size difference between the multiple cations now occupying the site. Some studies (Atlee *et al.* (27)) synthesised several different composition such that the overall average cation radius ,r_A, was constant (1.23Å), but the various materials did not have a consistent Neéls temperature, indicating some affect from the variance, σ^2, on T_N. It was found that changing the variance led to changes in bond angles and lengths, despite cell volume remaining consistent. The overall relationship concluded that decrease in T_N was consistent with increasing variance.

This strain due to change in cation radius can be expressed mathematically using the following relationship; where r_A is the mean ionic radii of the A-site cations:

$$\sigma^2 = \langle r_A{}^2 \rangle - \langle r_A \rangle^2$$

Equation (1.1)

The concept of variance was further developed by Sinclair *et.al.*. (28), where it was shown that for a ferroelectric perovskite material, T_C increases when the size of the doped species is significantly varied from the size of the parent A site cation.

This suggests that in some systems T_C is affected by both average cation size and variance. The effect on T_C due to size and strain is summative; hence decreasing the average r_A will decrease T_C due to the change in size, if this also results in a high σ^2 then T_C will also increase due to the additional strain. Therefore these effects are competing, so depending on the magnitude of their individual affects the final T_C may vary from expectations.(27)

1.6.3. Morphotropic phase boundaries

One commonly used piezoelectric perovskite is Lead Zirconate Titanate (PZT) based compounds. They are popular due to the presence of a morphotropic phase boundary (MPB) which exists in these materials. A morphotropic phase boundary occurs when there is a substantial and rapid change in the structure of a solid solution. At such a phase boundary two or more different structures with different polarisations may co-exist. As each of the different structures will have different polarisations, the application of an electric field can result in alignment along different axis simultaneously, giving rise to enhanced properties. (29,30)

As the usual mechanisms for structural change can be temperature independent it is possible to observe a MPB over a large temperature range by targeting the correct chemical composition. (29,31)

1.6.4. Lead Zirconate Titanate (PZT)

The information industry is currently heavily reliant on the compound $Pb(Zr,Ti)O_3$, known as PZT. The electrical properties found in PZT make it ideal for use in piezoceramic memory. Zavara et al (31) describes PZT as a ferroelectric perovskite material, with a well-defined electrical hysteresis loop. It can also exhibit favourable piezoelectric properties including a high dielectric constant of up to 3850, a typical T_C of >750 K and polarisations >70 μC cm^{-2} (32). This high dielectric constant and remnant polarisation make it an ideal material for use in ferroelectric memory.

Initially rhombohedral, upon reaching T_C (which varies with composition) the compound becomes cubic upon losing its ferroelectric character [Figure 1.13]. (32) As previously discussed, the dielectric properties of PZT can be further improved at a MPB, where the beginnings of the monoclinic deformation can lead to an enhancement of the electrical properties, with a maximum recorded DC in excess of 3000. (33)

Whilst PZT fulfils its role well, there is substantial opportunity for research into alternative materials. As previously stated, Pb is toxic, and this means that there is dire need for a replacement material which with similar or enhanced properties. There are several ferroelectric contenders to replace PZT currently under investigation, with the most promising suggested by Shrout et al (29) to be $BaTiO_3$, $NaBiTiO_3$ and $KNaNbO_3$. Each of these materials is being examined in an attempt to match their electrical properties to that of PZT.

In the case of PZT, the composition $PbZr_{0.46}Ti_{0.54}O_3$ gives an MPB with the material on the boundary of a rhombohedral/tetragonal symmetry [Figure(1.13)]. At this point there are multiple axes of polarisation due to contributions from both phases that may align with an applied field.(30)

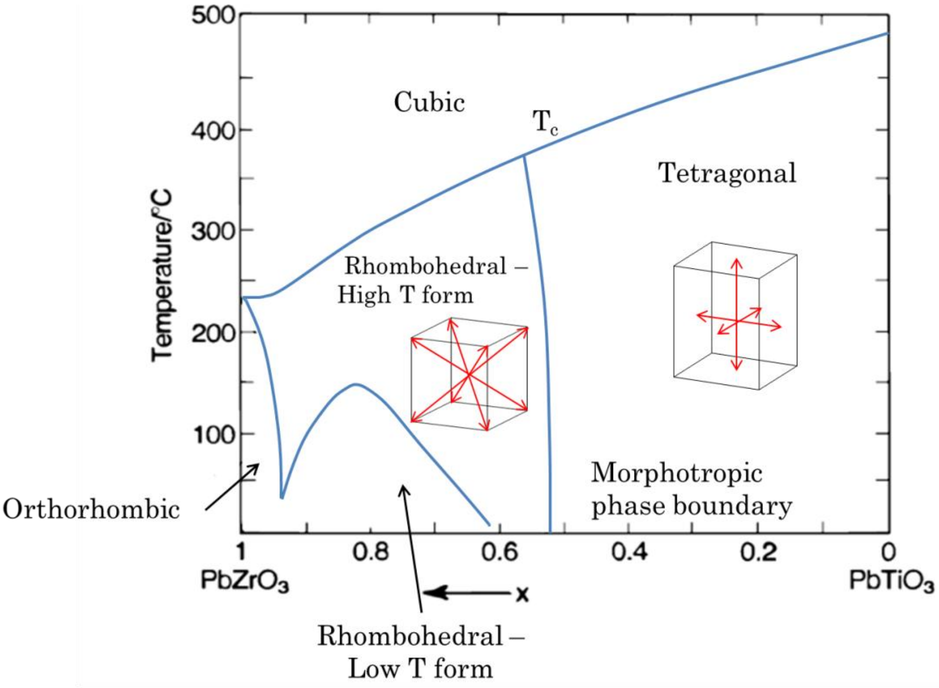

***Figure 1.13**: Phase diagram for PZT* (30)

One such property which can be greatly enhanced at a MPB is the relative permittivity, ε_r, which gives an indication of the amount of electrical energy that can be stored by a material by an applied voltage. These enhancements provided at the MPB can obviously be beneficial for application. As previously stated, one of the requirement for memory application is a high remnant polarisation, which can be found to be enhanced at the MPB. This means that the location of these boundaries allow materials to be optimised for application.

1.7. Bismuth Ferrite ($BiFeO_3$)

$BiFeO_3$ [Figure 1.14] is a good candidate for application, a multiferroic perovskite; it has high magnetic (T_N ~ 643K) and ferroelectric (T_C ~ 1103K) transition temperatures. One preventative issue is that $BiFeO_3$ is difficult to produce in high purity. It is prone to the development of secondary phases, notably $Bi_{25}FeO_{39}$ and $Bi_2Fe_4O_9$ (39). Synthesis above 850^{o}C can also lead to the loss of Bi, which can cause non-stoichiometry due to the volatile nature of Bi.

The existing phase diagram for $BiFeO_3$ is the result of several comprehensive variable temperature structural studies into $BiFeO_3$ using a range of techniques, and consists of three phases before decomposition. Below T_C, it inhabits a rhombohedrally distorted trigonal cell (α phase) with space group *R3c* and approximate lattice parameters of a= 5.6 Å and c= 13.9 Å at room temperature (34-36). Like all perovskites this consists of the centrally offset Bi^{3+} ion, surrounded by octahedra composed of an Fe^{3+} ion caged by O^{2-} ions. The cations displace off their centre of symmetry along the [111]*c* direction with the FeO_6 octahedra rotated around the rhombohedral axis (Glazer notation *a-a-a-*).(31) The Bi^{3+} ions have a larger displacement, as a result of the *d* shell stereoactive lone pair electrons. (105,107,109) The displacement of the Bi^{3+} ion causes a shift in the electron density, which is responsible for both the off-centring of the B site Fe3+ ion within the octahedral oxygen cages, and leads to the generation of electrical dipoles, so the material should crystallise in a non-centrosymmetric space group, and hence be ferroelectric. (35)

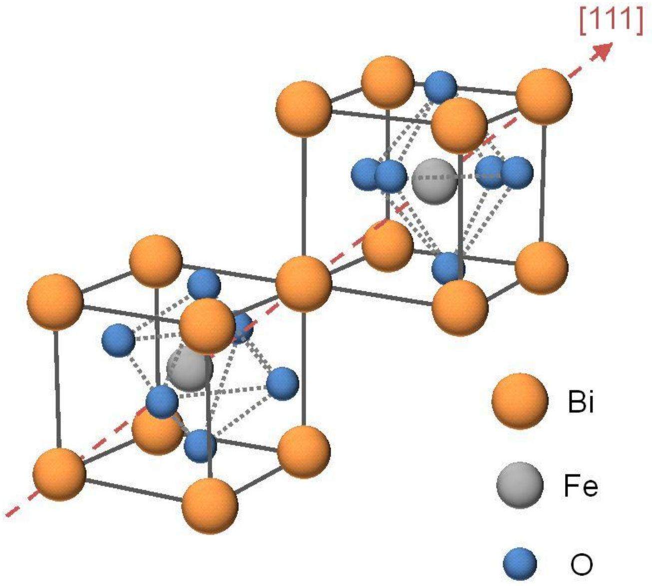

Figure 1.14: *The crystal structure of $BiFeO_3$ taken from Materials Science - Advanced Topics*

The secondary (β) phase of $BiFeO_3$, occurring post T_C between 1103-1198K is orthorhombic, with a √2a, √2a, 2a unit cell relationship and a symmetry of *Pbnm/Pnma*, and can be confirmed by observation of loss of cell volume and convergence of the Fe-O bonds.(34.36 ,39).

The transition from the β phase at 1198K is where some uncertainty generates in the literature. Palai *et al* (36) note that the tertiary (γ) phase seems cubic, whilst a later study by Arnold *et al* (34) instead find that the γ phases in fact a second orthorhombic space group. Unfortunately there has yet to be a final conclusion on the structure of the γ phase as investigation is hampered by the final decomposition of $BiFeO_3$ occurs at 1233K.

$BiFeO_3$ also exhibits anti-ferromagnetism, with a G-type modulated cyclic structure with a periodicity of 620 Å (40,41) [Figure 1.15]. Palewicz (40) reports that shifts in the Fe and O ions with temperature bring about the loss of magnetism at ~643K.

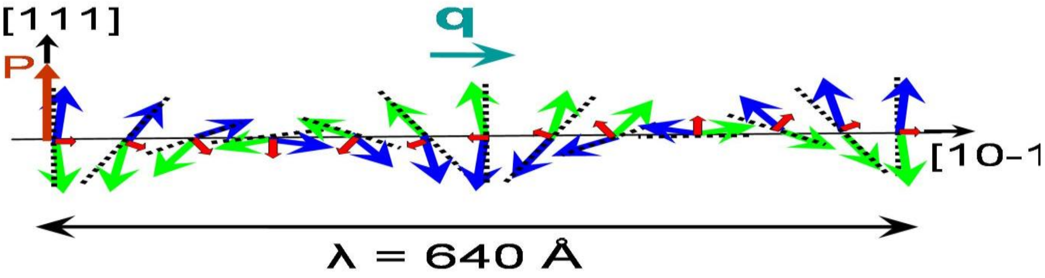

Figure 1.15: *The canted antiferromagnetic spin cycloid found in $BiFeO_3$. The net magnetic moments average to zero over the period of the cycloidal rotation.* (34)

Currently, $BiFeO_3$ is not a commercially feasible material, as the material alone has some limitations:

The high leakage current seen in $BiFeO_3$ has been suggested to arise due to the electric domain structure. However, recent studies has linked the volatile nature of Bi^{3+} during synthesis, leading to the reduction of Fe^{3+} to Fe^{2+}This leads to the subsequent formation of ion vacancies.(42,43). Formation of cation vacancies would allow them to act as electron acceptors, improving the conductance of the material.(44) The formation of A site cation vacancies can also lead to the generation of oxygen vacancies which can result in increased conductivity.(44)

The initial interest in $BiFeO_3$ stemmed from theoretical modelling using density functional theory, predicting large polarisations of up to 100 $\mu C/cm^2$.(45) Experimentally, similar polarisations have not been observed in bulk $BiFeO_3$ ceramics; however there have been observations of comparable values in thin films (46) and single crystals (47). The problem therefore links to the previously mentioned difficulties in synthesis entire single phase bulk materials.

Some studies have suggested that $BiFeO_3$ may show some signs of weak magneto-electric coupling, where a change in of magnetization changes linearly with electric field or vice versa. However the cyclic effect of the combined magnetic spins within $BiFeO_3$ make this kind of linear relationship unsustainable. (48,49) If any magneto-eletric coupling is observed it is due to much weaker ME effects. (50)

These problems have had several different attempted solutions, beginning with attempts to try and improve synthesis quality, to reduce Bi^{3+} loss and prevent the formation of Fe^{2+} ions. However, whilst these techniques may improve the observed remnant polarisation and dielectric loss they do little to effect the observed magnetic structure. The destruction of the spin cycloid is a priority to try and make $BiFeO_3$ commercially viable.

Doping has also been used in attempt to alter the magnetic helix usually found in $BiFeO_3$ in an attempt to induce a more linear ferro/anti-ferromagnetic ordering.

1.7.1. Doping with rare earth materials to give compositions $Bi_{1-x}RE_xFeO_3$

Many of the available studies look at room temperature studies of various compositions of $Bi_{1-x}RE_xFeO_3$ with a view to stabilise some of the previous mentioned weaknesses of pure $BiFeO_3$, in attempt to locate potential morphotropic phase boundaries and thus generate enhanced properties in these materials.

One well studied dopant material is La^{3+} doped into $Bi_{1-x}La_xFeO_3$ materials with low concentrations of $x \leq 0.125$. These studies report that at these low values, the rhombohedral, *R*3*c*, symmetry is maintained. (111,112) When the amount of doped La^{3+} exceeds this value, the reported secondary phases vary between studies. Whilst some studies indicate the retention of the R3c phase to much higher La^{3+} compositions, others predict a more complex set of phase transitions and symmetries.

Several studies report that the subsequent phase is of orthorhombic symmetry, linked to the parent $LaFeO_3$ material and it has been reported that this transition occurs at compositions of $x= 0.150$, 0.155, 0.3, respectively. (113,114)

Karimi *et al.* reported that below $x = 0.20$ the material takes an *R*3*c* symmetry.(51) Above $x = 0.20$ there is significant peak broadening, the material begins to transition to *Pnma* symmetry, however, confirmation of the final *Pnma* phase was not possible due to instrument limitation. However consistent work by Yang *et.al.* shows transition to the *Pnma* phases although there is a wide phase transition, with phase coexistence reported between $0.3 \leq x \leq 0.8$.(52)

More recent studies by Zhang *et al.* again report *Pnma* symmetry, but at a much lower tolerance of $x \leq 0.1$ and that the transformation to orthorhombic *Pnma* symmetry is complete by $x = 0.2$. A similar phase diagram is suggested by several other studies with reports of high La^{3+} content linking to *Pnma* symmetry. (44,53)

Other authors report contrary symmetry formations. Cheng *et.al.* note the formation of orthorhombic, *C*222 symmetry for compositions of $x = 0.2$ with a later transitions at $x=0.3$ *P*4*mm,* with this transition being confirmed in other works also. (54-56) However, these studies lack a logical series of Rietveld refinements, so the explanation for the choices of symmetry is not developed.

Yet more phase diagrams are reported, with Pandit *et.al.* showing a transition from *R*3*c* to triclinic *P*1 for compositions in excess of x = 0.05 in $Bi_{1-x}La_xFeO_3$ materials.(57) This is supported by the reporting of phase transitions from *P*1 → *P*4*mm* → *P*4/*mmm* at x = 0.05, 0.2 and 0.25 (36,58) , although each of these transitions could be intermediary phases, as there is still evidence that for significantly higher La^{3+} compositions the materials again transitions to *Pnma* (parent $LaFeO_3$ phase).(59-61)

One powder neutron diffraction study shows that there may be some issues with synthesis of the materials, and show a change in composition with phase, and link this to the temperature at which the material was synthesised. The R3c phase formed with a composition of x=0.15, whilst the secondary *Imma* phase showed values closer to x=0.45. (60) They noted that each of these phases became more stable at different synthesis temperatures.(61)

More recently there has also been some study into the time dependence of the stability of $Bi_{1-x}La_xFeO_3$ samples. In one study, the composition x = 0.1 was indexed as R3c, whilst the x = 0.20 sample was assigned a *Pbam* symmetry. The x = 0.16 material was also indexed as *R3c* but after one month the sample was re-examined and found to have developed a secondary phase which could be indexed as the *Pbam* phase seen in higher La^{3+} compositions, which is an anti-ferroelectric phase, so development over time has impacted on the electrical properties of the material. (62-64)

Another widely studied material is Nd doped $BiFeO_3$ ceramics and a range of symmetries have been reported. Similarly to other studies, small percentage compositions maintain the parent *R*3*c* symmetry ($0 \leq x \leq 0.1$(65,66) whilst others noted *R*3*c* phase was stable until much higher compositions.

Several phases are again shown, similar to the previous mentioned La^{3+} studies. One reported transition at x=0.2 gives *Pnma* symmetry (67), whilst another reports a rhombohedral to orthorhombic phase transition, at x=0.125 however the study only reports a transition from polar – anti-polar and not the exact symmetry (68), however a transition to *Pbam* or *Pnam* would be consistent with other findings.

One study of $Bi_{1-x}Nd_xFeO_3$ reports the following series of phase transitions R3c→Pbam→Pna21 at compositions of x=0.15 and 0.25 respectively. (69) After x=0.25 the phase is unconfirmed, but the possible space groups are limited to either *Pnam* or *Pna*21. However, the authors note that refinement of the data using the higher symmetry *Pnam* symmetry does not significantly improve the fit statistics indicating that the more complex system is not necessary to describe the structure. Similar results were also reported other works.(61)

Similar to some La^{3+} based studies, an *R3c→Pnma* transition is seen in Gd doped samples although Khomchenko (70) also suggest the possibility of polar $Pn2_1a$ which they claim in their $Bi_{0.9}Gd_{0.1}FeO_3$ material. Khomchenko also shows that the addition of Gd greatly enhances the magnetization as Gd has a high magnetic contribution, but also leads to suppression of the off-centring responsible for the ferroelectricity (as previously noted by Ivanova (47) for $DyMnO_3$). In a later study (71) looking at both Gd and Nd, they suggest that the Pn21a phase is in fact an intermediary phase found between the α (R3c) and β (Pnma) phases which is present in clusters in the mixed phase region.

Kharel *et al* (45) reports that the substitution of transition metal species (notably Mn, Ti) for Fe leads to an increase in magnetic saturation along with lower resistivity and a slight reduction in leakage current. Whilst other studies indicate an alteration to the magnetic ordering, supposing a translation towards linear anti-ferromagnetism. Both of these studies have used large levels of dopant to achieve this effect. Ivanova (47) indicates that the danger of doping in large amounts (in this case Dy and Mn) is that whilst there can be benefit to the magnetism; it comes at the price of loss of the ferroelectricity, as doping the material lowers the transition to the non-polar β phase.

Hu *et al* (72) managed to achieve a reduction of the leakage current by an order of magnitude using Nd doped $BiFeO_3$ materials. There was however some loss of magnetization, although the study suggests that this can be rectified by co-doping with Mn.

Both Lahmar (73) and Yao (74) have examined a range of RE doped $BiFeO_3$ compounds. Lahmar concluded that the addition of La, Gd and Dy leads to slight enhancement of the ferroelectricity and reduction of leakage current, and that doping with Gd and Dy best enhance the magnetism, giving some indication of developing ferromagnetic ordering. Yao also notes that the addition of Dy leads to a substantial improvement to the magnetism and gives a remnant polarisation of $34.5\mu Ccm^{-2}$.

1.7.2. Doping with Dy^{3+} to replace Bi^{3+} compositions $Bi_{1-x}Dy_xFeO_3$

It has been suggested that the introduction of Dy^{3+} into $BiFeO_3$ can result in suppression of the anti-ferromagnetic spin cycloid.(75,76) However, despite many studies there is still little agreement on the structural, electronic and magnetic properties of the lattice after doping. Like previously mentioned RE studies, there is much controversy on determining the stability of the parent R3c phase, with different authors reporting stability until x=0.1(75,77), 0.075(78), 0.08(79,80), 0.15(81) and 0.20(82). The subsequent phase formation is also a matter of some debate, with reported phases including *Pnma*(83-5), $Pn2_1a$(85) and *Pbnm*(79-81).

There are some studies that have begun investigating $Bi_{1-x}Dy_xFeO_3$. Khomchenko (86) for example has found that at low Dy^{3+} content there exists a broad mixed phase region between x=0.10-0.20 which they characterise as mostly orthorhombic with some rhombohedral polar clusters. In addition the authors saw a small amount of the anti-ferroelectric orthorhombic, *Pbam* phase (similar to that found in $PbZrO_3$) in the $x = 0.15$ material. However, insufficient amounts were present to properly quantify and isolation of this phase was not possible.

This is also seen by both Sun (87) and Xu (88) who both report either mixed phase rhombohedral-orthorhombic materials, in the case of Sun *et al.*, a single orthorhombic phase by x=0.20. Lotey *et al* also reports this phase change, noting the contraction in the lattice parameters in the resultant *Pnma* phase (89).

There is however some disagreement in other studies, with several reporting a much higher Dy^{3+} content being required to cause sufficient lattice distortion to result in a deviation from rhombohedral and induction of a phase change. Sati *et al* (90) states that $Bi_{1-x}Dy_xFeO_3$ remains single phase until x=0.12, at which point there is a rapid distortion in the bond lengths of the FeO_6 octahedral cage, forcing the material into non-polar orthorhombic symmetry.

Further still, Li (91) does not report a loss of rhombohedral symmetry until x=0.20, although there is some reduction in T_c with Dy^{3+} content due to lattice distortion. Li also reports an enhancement of the dielectric properties of $BiFeO_3$ with increasing Dy^{3+} content, and an increase in dielectric constant which they attribute to the significant reduction in the leakage current.

There are many other reports of enhancement of the ‘leaky’ dielectric nature of $BiFeO_3$ with Dy^{3+} doping. Reghavan *et al.* (92) notices a reduction of four orders of magnitude in their recorded leakage current compared to that of pure $BiFeO_3$. Koval also reports initial enhancement of the dielectric properties, although their findings state that the ferroelectricity becomes disrupted by higher Dy^{3+} content, as the material transitions to the Pnma phase.(93) This would likely also occur in Li’s (91) work, but they do not progress beyond x-0.20.

Along with the enhancement and following loss of the ferroelectricity, there is also a weak but noticeable ferromagnetic characteristic that strengthens with Dy^{3+} content, which the author concludes to be a result of suppression of the characteristic $BiFeO_3$ spin cycloid. The 2014 study by Xu *et al* (88) also shows weak ferromagnetism from x=0.15 upwards.

At higher Dy^{3+} content, Zhang *et al* (94) report significant improvement to the (initially) weak ferromagnetic character that develops with Dy content. Prashanthi *et al* (95) see a similar enhancement, which is present in both $(BiDy)FeO_3$ and $(BiLaDy)FeO_3$, however they also see total loss of ferroelectricity, starting at high concentrations of Dy (x=0.30).

Another are of interest in the development of multiferroic materials with memory applications are the Alkali metal Niobates, as they can be known to exhibit similarly high polarisations to PZT. THIS alternative class of lead-free compounds known to exhibit piezoelectric characteristics have a perovskite structure $MNbO_3$, where M may be any of the alkali metals or a combination of several species of alkali metal. The most extensively studied of this material class are $KNbO_3$, $NaNbO_3$ and $K_{1/2}Na_{1/2}NbO_3$.

Of these compositions, $K_{1/2}Na_{1/2}NbO_3$ is of particular interest, and has MPB at an orthorhombic-orthorhombic phase transition (where both phases are ferroelectric)(96). This material has a Curie temperature of approximately 420 ˚C(97) and good electrical responses. The limitation of this material is in difficulty of synthesis because the alkali metal cation is volatile and is prone to loss during heating, leaving products that are not of the expected stoichiometry, and possibly the formation of cation and anion vacancies as a result. There is also a need to thoroughly dry the materials before synthesis, as the alkali metal components can be heavily hydroscopic (which could lead to further issues with stoichiometry), a property that can be passed on to the daughter material.(98)

1.7.3. Co-doping with K^+ and Nb^{5+} to give compositions $Bi_{1-x}K_xFe_{1-x}Nb_xO_3$

$KNbO_3$ is another good candidate for application, as a Pb-free ferroelectric material.(58) At room temperature $KNbO_3$ exhibits *Amm*2 symmetry, with the ferroelectricity being driven by off-centring of the Nb^{5+} ions within the NbO_6 octahedra.(99) Nakamura *at al* (100) reports that lattice parameters as a= 5.721 Å, b = 5.695 Å and c = 3.974 Å for the orthorhombic phase and a sharp phase transition from orthorhombic to tetragonal. Rai *et al* (40) reports a similar occurrence,

Kim *et al* have studied the piezoelectric characteristics of $KNbO_3$ around this phase transition, and their data indicates a substantial enhancement of the piezoelectricity around the phase boundary. They also show relaxor like dielectric properties in the tetragonal phase (101).

During synthesis, different synthesis temperatures, Liu *et al* (102) see that sintering in the range 1065-1100K improves the piezoelectric properties, whilst temperatures above 1100K lead to some deterioration. The reason for this investigation of different synthesis strategies is that one of the issues faced with $KNbO_3$ which limits is its current use, is that it is very difficult to synthesise, and is often low density. This is also true of the other commonly used material $(K,Na)NbO_3$ compositions.

The difficulty of synthesis has led to several studies attempting to circumvent this through doping, and Choi *et al* (52) attempted this with Li and Li, Ta doping. Whilst they do notice some ease of synthesis, and even some enhancement of the dielectric properties, the doping of these materials also leads to large reduction in T_C.

Several other studies also note that doping can lead to densification and better synthesis of these materials, and enhancement of properties. One example of this is the study by Du (103) which shows La addition to markedly increase the powder density along with enhancing the dielectric constant. A similar study by Wang *et al* has shown that addition of Ta again enhances the dielectric properties, particularly around the orthorhombic-tetragonal phase boundary although the temperature of this transition and T_C are both reduced (104).

Co-doping with Gd and Fe shows a similar effect on the piezoelectric and T_C, with loss of PE at high $GdFeO_3$ content. The introduction of a magnetic species also leads to weak ferromagnetism, with increasing magnetisation as Fe content increases (105).

One method of stabilising the synthesis of $KNbO_3$ and $(Na,K)NbO_3$ is combination with $BiFeO_3$. Zuo *et al* (97) report that even a small amount of $BiFeO_3$ ($K_{0.99}Bi_{0.01}Nb_{0.99}Fe_{0.01}O_3$) can ease the synthesis, as K^+ can be volatile during the synthesis process. Like other dopants, $BiFeO_3$ is reported to show some enhancement of the electrical properties, and an increase in the remnant polarisation (106).

There is also a change to the magnetic properties of the $KNbO_3$ and $NaNbO_3$, although despite the similarity of the materials there is some contrast in the literature, with Dash *et al* show anti-ferromagnetism charcter in $BiFeO_3$ doped $NaNbO_3$ (106), whilst Huo *et al* report weak ferromagnetism in $BiFeO_3$ doped $KNbO_3$ (107). This combination of $BiFeO_3$ and $KNbO_3$, and the changes that it may make to the magneto-electric properties of $Bi_{1-x}K_xFe_{1-x}Nb_xO_3$ a possible contender for replacement of PZT in electroceramics.

There are a few existing studies, but this solid-solution between $BiFeO_3$ and $KNbO_3$ has so far been somewhat overlooked despite the fact that the combination of these two materials can result in generation of an ideal ionic lattice (by considering Goldschmidt's tolerance factor). In comparison with the PZT phase diagram there is an increase in tolerance factor Zr^{4+} rich end of the phase diagram, and subsequent generation of the AFM character. Similarly, the addition of doping with K^+ and Nb^{5+} to the $BiFeO_3$ lattice would be expected to lead to a similar increase the tolerance factor (towards the K^+ rich end) with the potential for the discovery of a similar MPB to that in the PZT series being located.

One study that did consider this solid solution examined percentage compositions between $0 \leq x \leq 0.70$, reporting that values $x \leq 0.20$ crystallised in R3c symmetry and x=0.30 showed a pseudo-cubic lattice. Values in excess of $x \geq 0.30$ were to be cubic.(108)Initially, Nakashima report weak FE and FM in materials with composition x=0.10, but significant dielectric losses is reported for materials of higher composition.

Another work by Teslenko *et al.* reports in depth examination of the solid solution across a similar range of compositions (x = 0.00, 0.30, 0.50, 0.70 and 1.00).(109) They show that the parent *R3c* phase is stable until x = 0.25 which transitions to an orthorhombic non-polar, *Pbnm* until x=0.55, at which point the structure remains orthorhombic, but becomes polar forming a *P*4*mm* symmetry, finally they predict a transition to tetragonal polar *Amm*2 (parent $KNbO_3$). They report that each of these transitions also show a small region of phase coexistence, which may suggest that the phase boundaries are more broad than those seen in PZT, however the solid solution clearly warrants further investigation into whether it is possible to sharpen these phase transitions and help locate morphotropic phase boundaries within the material, and give a PZT like phase diagram.

1.8. Aims of this work

The aim of this research is to study novel lead-free piezoelectric materials, may result in location of a morphotropic phase boundaries and to be able to confirm the phase diagram for these materials in order to resolve conflicting reports in previous studies.

Initial aims are to synthesise polar perovskite ceramics which have a Curie temperature suitable for application. The properties of these materials, particularly with regards to any structural developments will need to be known for each composition.

This work will consider the doping of both single rare earth cation onto the A site, and the effect of doping cations simultaneously onto the A and B sites.

The selected rare earth cation is Dy^{3+} as it is one of the smaller rare earths, in an attempt to reduce variance, and will not lead to charge imbalance so will not result in the subsequent reduction of the Fe^{3+} B site ion. The K^+, Nb^{5+} dopant pair has been chosen both due to the promise of studies into $KNbO_3$, and because again there will be no overall imbalance in cation charge. In each case the same amount of A-site and B-site dopant species will be added. They were also selected to result in a range of tolerance factors that could lead to the formation of an ideal perovskite material.

In Chapter 3, prepared $Bi_{1-x}Dy_xFeO_3$ ceramics will be investigated between composition values of x=0.06-0.30. The investigation will be into the structure and multiferroic properties of the materials, looking to understand the new phase diagram, with focus on the single phase materials at either end of the synthesised region. Initial findings are presented as a structural study utilising room temperature XRD and SEM and, powder neutron diffraction (PND) data and Raman spectra taken across a broad temperature range. Later characterisation of electromagnetic properties will be carried out using electrical impedance spectroscopy and superconducting quantum interference device (SQUID) magnetometry.

In Chapter 4, prepared $Bi_{1-x}K_xFe_{1-x}Nb_xO_3$ ceramics will be investigated across the entire solid solution. The investigation will be into the structural changes that occur across the composition range, looking to understand the new phase diagram, with focus on the single phase materials at either end of the synthesised region. Initial findings are presented as a structural study utilising room temperature XRD and Synchrotron and Powder Neutron Diffraction (PND) data taken across a broad temperature range. A preliminary examination of the electromagnetic properties will be carried out using electrical impedance spectroscopy and superconducting quantum interference device (SQUID) magnetometry.

Final conclusions of the project will then be presented along with some ideas for future work on this topic in Chapter 5.

References

1. *Basic Solid State Chemistry*, West. A.R, *John Wiley & Sons Ltd*. **1988**
Intensive BCA/BCG School Durham **2011**
2. H Yokota, N Zhang, AE Taylor, PA Thomas, AM Glazer. s.l. : *Phys Rev B*, **2009**, 80.
3. R.E. Newnham, *Acta Cryst. A*, **1998**, 54, 729-737.
4. W.W. Wolny, *J. Eur. Ceram. Soc.*, **2005,** 25, 1971-1976
5. Q.X. Chen, et al., *Ultrasonics*, **1994**, 32, 309-313
6. I. Nudelman and A. Rybyanets, **2009**, *Ultrashape LTD (ULTR-Non-standard)* US: 7709997
7. A.J. Moulson and J.M. Herbert, *Electroceramics*, **1997**, Chapman & Hall.
8. https://explorermaterials.wordpress.com/basic-concepts/piezoelectric-and-ferroelectric-materials/
9. www.doitpoms.ac.uk/tlplib/ferroelectrics/printall.php
10. M. Stachiotti, A. Dobry, R. Migoni and A. Bussmann-Holder , *Phys. Rev. B*, **1993**, 47, 2473–2479
11. *Lecture Notes on Semiconductor Spintronics* T. Dietl, *Institute of Physics,* **2007**
12. *Fundamentals of Solid-State Phase Transitions*, *Ferromagnetism and Ferroelectricity*, Mnyukh Y, **1998**
13. H. Akai, *Phys. Rev. Letters*, **1998**, 81, 3002–3005
14. M*ultiferroics: An Introduction*, R.N.P. Choudry and S.K. Patri, *Indian Institute of Technology*, **2008**
15. http://www.uic.edu/labs/AMReL/NIRT/
16. V.M. Goldschmidt, *Die Naturwissenschaften*, **1926**, 21, 477-487
17. R.E. Cohen, *Nature*, **1992**, 358, 136-138
18. D.M. Lin and K.W. Kwok,*. Curr. Appl. Phys,* **2001**, 10**,** 422-427
19. W.Wong-Ng, J.A. Kaduk, I. Levin, W. Greenwood, J. Dillingham, *Powder Diffr*., **2000**. 15, 227-233
20. J. Jeong and Y.H. Han, *J. Electroceram.*, **2004**, 13, 549-553.

21. http://www.3dchem.com/inorganics/BaTiO3-poly.jpg

22. B. Xu, B. Yin, J. Lin, Y.D. Xia, X.G. Wan, J. Yin, X.J. Bai, J. Du and Z.G. Liu, *Phys. Rev. B*, **2009**, 79, 134109

23. L. B. Luo, Y. G. Zhao, H. F. Tian, J. J. Yang, J. Q. Li, J. J. Ding, B. He, S. Q. Wei, and C. Gao *Phys. Rev. B*, **2009**, 79, 115210

24. http://www.3dchem.com/inorganics/catio3-poly.jpg

25. http://www.princeton.edu/~cavalab/tutorials/public/structures/pics/SrTiO3.jpg

26. K. Momma and F. Izumi**,** VESTA 3 for three-dimensional visualization of crystal, volumetric and morphology data," *J. Appl. Crystallogr.*,**44**, 1272-1276 2011

27. L.M. Rodrıguez-Martınez and J.P. Attfield, *Structural Effects of Cation Size Variance in Magnetoresistive Manganese Oxide Perovskites.* Chem. Mater., 1999. **11**: p. 1504-1509.

28. D.C. Sinclair and J.P. Attfield, *The influence of A-cation disorder on the Curie temperature of ferroelectric* $ATiO_3$ *perovskites.* Chem. Commun., 1999(16): p. 1497-1498.

29. TR Shrout, SJ Zhang. s.l. : *J Electroceram*, **2007**, 19.

30. B. Jaffe, W.R. Cook, and H. Jaffe, *Piezoelectric Ceramics*. **1971,** Academic Press London.

31. G Zavara, JH Fendler, A Trolier-McKinstry. 11, s.l. : *J Appl Phys*, **1997**, 81.

32. P. Baettig, Ch. F. Schelle, R. LeSar, U. V. Waghmare, and N. A. Spaldin., *Chem. Mater.*, **2005**, 17, 1376-1380.

33. R Guo, LE Cross, SE Park, B Noheda, DE Cox, G Shirane. 23, s.l. : *Phys Rev Letts*, **2000**, 84.

34. DC Arnold, KS Knight, G Catalan, SAT Redfern, JF Scott, P Lightfoot, FD Morrison. s.l. : *Adv Funct Mater*, **2010**,. 20.

35. P Fischer, M Polomska, I Sosnowska, M Syzmanski. s.l. : *J Phys C: Solid St Phys*, **1980**, 13.

36. R Palai, RS Katiyar, H SChmid, P Tissot, SJ Clark, J Robertson, SAT Redfern, JF Scott. s.l. : *Phys Rev B*, **2008,** 77.

37. CM Kavanagh, RJ Goff, A Daoud-Aladin, P Lightfoot, FD Morrison. s.l. : *Chem Mater*, **2012**, 24.

38. A.M. Glazer, *Acta. Cryst*. **1972**, B28, 3384

39. DC Arnold, KS Knight, FD Morrison, P Lightfoot. s.l. : *Phys Rev Letts*, **2009**, 102.

40. A Palewicz, R Prezenioslo, AW Hewat. s.l. : *Acta Physica Polonica* A, **2010**, 117.

41. S Zhang, L Wang, Y Chen, D Wang, Y Yao, Y Ma. s.l. : *J Appl Phys*, **2012**, 111.

42. S. R. Das, R. N. P. Choudhary, P. Bhattacharya, R. S. Katiyar, P. Dutta, A. Manivannan and M. S. Seehra, *J. Appl. Phys.,* **2007**, 101, 034104.

43. S. Zhang, L. Wang, Y. Chen, D. Wang, Y. Yao and Y. Ma, *J. Appl. Phys.,* **2012**, 111, 074105.

44. M. Khodabakhsh, C. Sen, H. Kassaf, M. A. Gulun and I. B. Misirlioglu, *J. Alloys Compd.,* **2014**, 604, 117.

45. P Kharel. S Talebi, B Ramachandra, A Dixit, VM Naik, MB Sahana, C Sudakar, R Naik, MSR Rao, G Lawes. s.l. : *J Phys Condens Matter*, **2009**, 21.

46. I Sosnowska, W Schafer, W Kockelmann, KH Andersen, IO Troyanchuk. s.l. : *App Phys A*, **2001**, 74.

47. W Ivanova, W Gagulin, SK Korchagina, YA Shevchuk, VV Bogatko. s.l. : *In Mater*, **2003**, 39.

48. G. Catalan and J. F. Scott, *Adv. Mater.,* **2009,** 21**,** 2463.

49. V. L. Mathe, K. K. Patankar, R. N. Patil and C. D. Lokhande, *J. Magn. Magn. Mater.,* **2004**, 270, 380.

50. P. Uniyal and K. L. Yadav, *J. Alloys Compd.,* **2012**, 511, 149.

51. S. Karimi, I. M. Reaney, Y. Han, J. Pokorny and L. Sterianou, *J. Mater. Sci.,* **2009,** 44, 5102.

52. Choi JH, Kim JS, Hong SB, Chae KW, Cheon CI, *J Korean Phys Soc*, **2012**, 61, 6, 956-60

53. C. M. Kavanagh, R. J. Goff, A. Daoud-Aladine, P. Lightfoot and F. D. Morrison, *Chem. Mater.,* **2012**, 24, 4563.

54. Y.-P. Liu and J.-M. Wu, *Electrochem. Solid-State Lett.,* **2007**, 10, G39.

55. G. Le Bras, D. Colson, A. Forget, N. Genand-Riondet, R. Tourbot and P. Bonville, *Phys. Rev. B.,* **2009**, 80, 13447.

56. G. Le Bras, P. Bonville, D. Colson, A. Forget, N. Genand-Riondet and R. Tourbot, *Physica B,* **2011**, 406, 1492.

57. P. Pandit, S. Satapathy and P. K. Gupta, *Physica B,* **2011**, 406, 2669.

58. T. R. Shrout and S. J. Zhang, *J. Electroceram.*, **2007**, 19, 11345

59. I. O. Troyanchuk, M. V. Bushinsky, A. N. Chobot, O. S. Mantyskaya and N. V. Tereshko, *JEPT Letters,* **2009**, 89, 180.

60. I. O. Troyanchuk, M. V. Bushinsky, D. V. Karpinsky, O. S. Mantyskaya, V. V. Fedotova and O. I. Prokhnenko, *Phys. Status Solidi B.,* **2009**, 246, 1901.

61. I. O. Troyanchuk, D. V. Karpinsky, M. V. Bushinsky, O. S. Mantyskaya, N. V. Tereshko and V. N. Shut, *J. Am. Ceram. Soc.,* 2011, **94**, 4502.

62. D. V. Karpinsky, I. O. Troyanchuk, O. S. Mantyskaya, V. A. Khomchenko and A. L. Kholkin, *Solid State Commun***., 2011,** 151, 186.

63. D. V. Karpinsky, I. O. Troyanchuk, M. Tovar, V. Sikolenko, V. Efimov and A. L. Kholkin, *J. Alloys Compd.,* **2013**, 555, 101.

64. D. V. Karpinsky, I. O. Troyanchuk, O. S. Mantyskaya, A. N. Chobot, V. Sikolenko, V. Efimov and M. Tovar, *Phys. Solid State,* **2014**, 56, 701.

65. A. A. Amirov, I. K. Kamilov, A. B. Batdalov, I. A. Verbenko, O. N. Razumovskaya, L. A. Reznichenko and L. A. Shilkina, *Tech. Phys. Lett.,* **2008**, 34, 760.

66. J. Schiemer, R. L. Withers, M. A. Carpenter, Y. Lin, J. L. Wang, L. Nore, O. Li and W. Hutchison, *J. Phys.: Condens. Mater.,* **2012,** 24, 125901.

67. J. Dzik, H. Bernard, K. Osinska, A. Lisinska-Czekaj and D. Czekaj, *Arch. Metall. Mater.,* **2011**, 56, 119.

68. Y.-J. Wu, X.-K. Chen, J. Zhang and X.-J. Chen, *J. Appl. Phys.,* **2012**, 111, 053927.

69. I. Levin, M. G. Tucker, H. Wu, V. Provenzano, C. L. Dennis, S. Karimi, T. Comyn, T. Stevenson

70. 7VA Khomchenko, JA Paixao, DA Kiselev, AL Khokin. s.l. : *Materials Research Bulletin*, **2010**, 45.

71. VA Khomchenko, VV Shvartsman, P Borisov, W Kleemann, DA Kiselev, IK Bdikin, JM Vieira, AL Khokin. s.l. : *Acta Materialia*, **2009**, 57.

72. Z Hu, M Li, B Yu, M Pei, J Liu, J Wang, X Zhao. s.l. : *J Phys D: Appl Phys*, **2009**, 42.

73. A Lahmar, S Habouti, M Dietze, CH Solterbeck, M Es-Souni. s.l. : *Appl Phys Letts*, **2009**,. 94.

74. Y Yao, W Liu, Y Chan, C Leung, C Mak, B Ploss. s.l. : *J Appl Ceram Technol*, **2011**, 8.

75. P. Uniyal and K. L. Yadav, *J. Phys.: Condens. Matter*, **2009**, 21, 012205

76. J. W. Lin, Y. H. Tang, C. S. Lue and J. G. Lin, *Appl. Phys. Lett.*, **2010,** 96**,** 232507

77. W.-M. Zhu, L. W. Su, Z.-G. Ye and W. Ren, *Appl. Phys. Lett.*, **2009,** 94, 142908

78. I. O. Troyanchuk, D. V. Karpinsky, M. V. Bushinsky, O. S. Mantytskaya, N. V. Tereshko and V. N. Shut, *J. Am. Ceram. Soc.*, **2011,** 94, 4502

79. C. Sun, X. Chen, J. Wang, G. Yuan, J. Yin and Z. Liu, *Solid State Commun.*, **2012,** 152, 1194

80. C. Sun, Y. Wang, Y. Yang, G. Yuan, J. Yin and Z. Liu, *Mater. Lett.*, **2012,** 72**,** 160

81. V. A. Khomchenko, D. V. Karpinsky, A. L. Kholkin, N. A. Sobolev, G. N. Kakazei, J. P. Araujo, I. O. Troyanchuk, B. F. O. Costa and J. A. Paixao, *J. Appl. Phys.*, **2010,** 108, 074109

82. J. Xu, G. Wang, H. Wang, D. Ding and Y. He, *Mater. Lett.*, 2009, **63**, 855

83. S. Zhang, L. Wang, Y. Chen, D. Wang, Y. Yao and Y. Ma, *J. Appl. Phys.*, **2012,** 111**,** 074105

84. S. Zhang, W. Luo, D. Wang and Y. Ma, *Mater. Lett.*, **2009,** 63, 1820

85. V. A. Khomchenko, I. O. Troyanchuk, M. V. Bushinsky, O. S. Mantytskaya, V. Sikolenko and J. A. Paixao, *Mater. Lett.*, **2011,** 65, 1970

86. VA Khomchenko, DV Karpinsky, AL Khokin, NA Sobolev, GN Kakazei, JP Aravjo, D Troyanchuk, BFO Costa, JA Paixao. s.l. : *J Appl Phys*, **2010**, 108.

87. Sun C, Wang Y, Yang Y, Yuan G, Yin J, Liu Z, *Matt Letts*, **2012**, 72, 160-3

88. Xu J, Ye G, Zeng M, *J Alloy Compd*, **2014**, 587, 308-12

89. Lotey GS, Verma NK, *Superlattice Microstr*, **2013**, 53, 184–194

90. Sati PC, Arora M, Chauhan S, Kumar M, Chhoker S*, J Phys Chem Solids*, **2014**, 75, 105-8

91. Li Y, Yu J, Zheng C, Wu Y, Zhao Y, Wang M, Wang Y, *J Mater Sci: Mater Electron*, **2011**, 22, 323-7

92. Raghavan CM, Kim JW, Kim SS, *Ceram Int*, **2014**, 40, 2281-6

93. Koval V, Skorvanek I, Reece M, Mitoseriu L, Yan H, *J Eur Ceram Soc***, 2014**, 34, 641-51

94. S Zhang, W Luo, D Wang, Y Ma. s.l. : *Materials Letts*, **2009**, 63.

95. K Prashanthi, BA Chalke, KC Barick, A Das, L Dhiman, VR Palkar. s.l. : *Solid State Communications*, **2009**, 140.

96. Nakashima Y, Shimura T, Sakamato W, Yugo T, *Ferroelectrics*, **2007**, 356, 180-4

97. Zuo R, Ye C, Fang X, *J Phys Chem Solids*, **2008**, 69, 23-5

98. I Masuda, K Kakimoto, H Oshato, *Journal of Electroceramics,* **13**, 555-9, 2004

99. A.W. Hewat, *J. Phys. C.: Solid State Phys.*, **1973**, 6, 2559

100. Nakamura K, Tokiwa T, Kawamura Y, *J Appl Phys*, **2002**, 91, 11

101. Kim JS, Kim MH, Hussain A, Park TG, Park J, Chung ST, Lee HS, *Ferroelectrics*, **2014**, 458, 111-7

102. Liu XY, Jiang MH, Chen GH, Cheng J, Zhou XJ, *Adv Appl Ceram*, **2010**, 109, 6

103. Du J, Xu Z, Deng B, Chu R, Yi X, Zheng L, Li Y, *Ceram Int*, **2014**, 40, 4319-22

104. Wang CC, Wang J, Sun XH, Liu LN, Zhang J, Zheng J, *Solid State Commun*, **2014**, 179, 29-33

105. Christen HM, Harshavardhan KS, Chisholm MF, Specht JD, Norton BDP, Boatner LA, Pickering IJ, *J Electroceram*, **2000**, 4:2/3, 279-87

106. Dash S, Padhee R, Das PR, J Mater Sci: *Mater Electron*, **2013**, 24, 3315-23

107. Huo SX, Yuan SL, Qiu Y, Ma ZZ, Wang CH, *Matt Letts*, **2012**, 68, 8-10

108. Y. Nakashima, T. Shimura, W. Sakamoto and T. Yogo, *Ferroelectrics*, **2007**, 356, 180

109. P. Y. Teslenko, A. G. Razumnaya, V. O. Ponomarenko, A. G. Rudskaya, A. V. Nazarenko, A. S. Anokhin, M. V. Avramenko, D. I. Leshov, M. F. Kupriyanov and Y. I. Yuzyuk, *Phys. Solid State*, **2014**, 56, 1866

110. M. Fujimoto, S. Jerzak and W. Windsch, *Phys. Rev. B*, **1986**, 34, 1668–1676

111. *Lecture Notes on Semiconductor Spintronics* T. Dietl, *Institute of Physics*, **2007**

112. H.A. Jahn, E. Teller, *Proc. R. Soc. Lond. A*, **1937** 161 220-235

113. *Elementary Scattering Theory*, D. Sivia, *Oxford University Press* **2011**

114. Pribošič I, Darko Makovec D, Drofenik M, *Journal of Materials Research*, **2002**, 17, 12, 2989-2992

115. Shima H, Naganuma H, Okamura S, *Materials Science - Advanced Topics*, InTech, 2013

116. V. A. Khomchenko, J. A. Paixao, D. A. Kiselev and A. L. Kholkin, *Mater. Res. Bull.*, **2010,** 45, 416

117. Rakvski P, Kubrin SP, Dellis JL, Raevskaya SI, Satychev DA, Smotrakov VG, Eremkin VV, Seredkina MA, *Ferroelectrics*, **2008**, 371, 113-8

118. Neumann T, Borstel G, Scharfschwerdt C, Neumann *M, Phys Rev B*, **1992**, 46, 17

119. Rai R, Sharma S, Rani R, Valente MA, Kholkin AL, *Matt Letts*, **2011**, 65, 2703-6

120. Zhen Y, Li J-F, *J Am Ceram Soc*, **2006**, 89, 3669-75

121. Shi J, Grinberg I, Wang X, Rapper AM, *Phys Rev B*, **2014**, 89, 094105

122. Barbar SK, Jangid S, Roy M, Chou FC, *Ceram Int*, **2013**, 39, 5359-63

123. A. Kumar and D. Varshney, *Ceram Int.,* **2012,** 38, 3935.

124. C. Maunders, H.J. Whitfield, D.G. Hay, J. Etheridge, *Acta Cryst. B*, **2007**. 63, 390-395

125. A. R. Denton and N.W. Ashcroft, *Phys. Rev. A*, **1991**. 43

126. L. Egerton and D.M. Dillon, *J. Am. Ceram. Soc.*, **1959**, 42, 438-42.

127. DM. Lin, K.W. Kwok, K.H. Lam and H.L.W. Chan, *J. Phys. D. Appl. Phys.*, **2007**, 40, 3500-3505.

128. J. Bielecki, P. Svedlindh, D. T. Tibebu, S. Cai, S.-G. Eriksson, L. Borjesson and C. S. Knee, *Phys. Rev. B.,* 2012, **86**, 184422.

129. S. K. Pradhan, J. Das, R. R. Rout, V. R. Mohanta, S. K. Das, S. Samantray, D. R. Sahu, J. L. Huang, S. Verma and B. K. Roul, *J. Phys. Chem. Solds,* **2010**, 71, 1557.

130. A. A. Amirov, A. B. Batdalov, S. N. Kallaev, Z. N. Omarov, I. A. Verbenko, O. N. Razumovskaya, L. A. Reznichenko and L. A. Shilkina, *Phys. Solid State,* **2009**, 51, 1189.

131. F. Gonzalez Garcia, C. S. Riccardi and A. S. Simoes, *J. Alloys Compd.,* **2010**, 501, 25.

132. A. S. Simoes, F. Gonzalez Garcia and C. S. Riccardi, *Mater. Chem. Phys.,* **2009**, 116, 305.

133. I. O. Troyanchuk, M. V. Bushinsky, D. V. Karpinskii, O. S. Mantyskaya, V. V. Fedotova and O. I. Prokhnenko, *JEPT Letters,* **2008**, 87, 641.
134. R. I. Smith and I. M. Reaney, *Chem. Mater.,* **2011**, 23, 2166.
135. Y.-P. Jiang, X.-G. Tang, Q.-X. Liu, D.-G. Chen and C.-B. Ma, *J. Mater. Sci.: Mater. Electron.,* **2014**, 25, 495.
136. *An overview of the electronics industry*. Accessed 04/05/2014
137. http://www.businesslink.gov.uk/bdotg/action/detail?type=RESOURCES&itemId=1078165387

Chapter 2: Experimental theory and Methodology

A series of investigative techniques were used over the course of this investigation in order to provide information about the chemical crystalline structure of the material, as well as analysis of the ferroelectric and ferromagnetic characteristics mentioned in Chapter 1. Powder X-ray (both conventional and synchrotron) and Neutron diffraction were used to confirm and investigate the chemical composition and crystallographic phase, along with Raman spectroscopy. Ferroelectric properties were analysed using Impedance spectroscopy, and SQUID magnetometry was used to investigate the ferromagnetism. This Chapter will outline the theory behind the different experimental techniques that were used within this study, how the sample materials were produced, and the conditions under which they were tested.

2.1. Experimental techniques

A wave incident on a crystal lattice can be treated, purely hypothetically, From a theoretical point of view, a crystal lattice upon which a wave is incident can be imagined as a series of semi-transparent mirror planes. This would indicate that when the radiation reaches one of these mirror planes, that some incident radiation is reflected, whilst the rest is transmitted. The position of these theoretical mirror planes are dependent on atom positions on the plane.

So if two beams are reflected by adjacent planes, we can use the supposition of mirror planes to derive a relationship to describe the scattering, this is known as Bragg’s law. Beam 22’ [seen in Figure 2.2] has travelled further than beam 11’, by a distance of xyz. If these two beams are two remain in phase, and therefore constructively interfere, xyz must be a whole number of wavelengths (1).

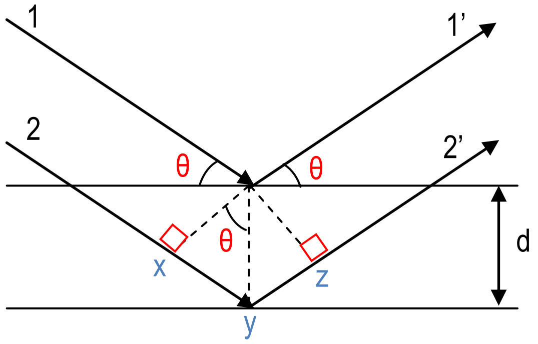

Figure 2.1: *Schematic representation of Bragg Scattering. Beam 1 and 2 are incident on a lattice, and reflected from adjacent lattice planes to give beam 1’ and 2’. The incident angle is θ and the distance between the planes is d.*

This distance xyz is determined by the distance between the miller planes (h,k,l), lattice planes (*d*) and the angle of incidence of the beam θ as shown: (1)

$$xy = yz = dsin(\theta)$$

(Equation 2.1)

$$xyz = 2dsin(\theta)$$

(Equation 2.2)

$$xyz = n\lambda$$

(Equation 2.3)

Combining equations 2.2. and 2.3:

$$2dsin(\theta) = n\lambda$$

(Equation 2.4)

This is Bragg’s Law

Bragg’s Law can then be related to the h,k,l values of the crystal.

Equation 1.4 can be arranged to give:

$$\sin(\theta) = \frac{n\lambda}{2d}$$

(Equation 2.5)

If Bragg’s law is satisfied, then the reflected beams are in phase (as θ is a function of nλ), so will interfere constructively, and give noticeable peaks on the final diffraction pattern.

The reflected beams must be in phase to give an recordable signal, if they are out of phase, even by a fraction, then they will interfere with one another destructively. Ewald develop the best method to observe these reflections is to view them from reciprocal space (4) (Figure 2.2), using the Ewald sphere. The origin O is the point where the incident beam ends, and C is the centre of the sphere which has radius 1/λ. If the observation condition is met then one or more lattice points, such as point P, lie on the surface of the sphere. This will give a measurable angle OCP of 2θ.

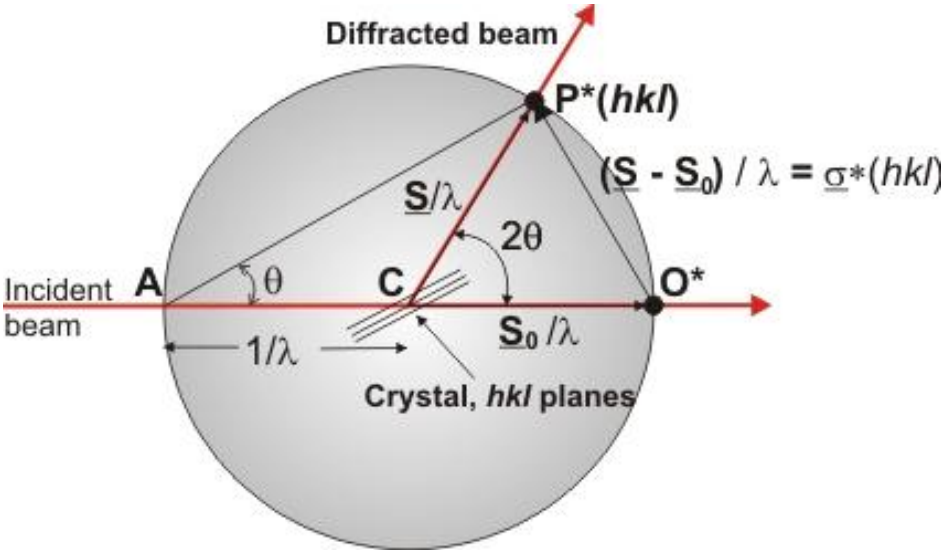

Figure 2.2: *Schematic representation of elastic X-rays scattering in reciprocal space using the Ewald sphere.* (3)

The Intensities of these Bragg reflections (I_{hkl}) depend on several factors, the most notable of which is the atom positions in the unit cell. An indication of the expected intensities can be taken from the structure factor (F_{hkl}) which can be computed mathematically (1):

$$F_{hkl} = \sum_{i} f_i e^{[2\pi i(hx_i + ky_i + lz_i)]}$$

(Equation 2.8)

Where x_i, y_i and z_i are the coordinate positions of the i^{th} atom, f_i is the scattering factor. The calculated structure factor can then be related to the intensity as follow:

$$I_{hkl} = |F_{hkl}|^2$$

(Equation 2.9)

In structure determination, phases can be estimated and an initial description of the unit cell, atomic positions displacements can be deduced from this structure factor. From this initial model, iterative refinement procedures can then be carried out to minimize the difference between calculation and experiment.

As previously stated, each set of lattice planes can give rise to Bragg reflection. However in practice, some Lattice planes do not give observable reflections. This is due to systematic absences within the material, which can be caused by non-primitive space groups, or elements of translational symmetry within the material (screw axis or glide planes), which result in the two incident waves being in antiphase and therefore resulting in destructive interference. (1,4,5).

The simplest interaction is elastic scattering. This type of diffraction can be very simply represented as an elastic collision between the incident beam wave packet and the electrons within the atom, with the beam losing no energy. This interaction causes vibration of the subject electrons, and this vibrating charge becomes analogous to a secondary point source, producing further X-rays which are in phase with the original wave. The intensity of these waves can be defined using Thomson's relation (4):

$$I\ \alpha (1 + cos^2 2\theta)$$

(Equation 2.1)

This is not the only way that X-rays interact with atoms however, there is another mechanism, known as Compton scattering. This is primarily an interaction with the valence electrons of the materials, so is particularly prominent in samples containing lighter elements, making them (hydrogen especially) hard to detect.

Compton scattering is inelastic, with the X-ray imparting a portion of its energy to one of the atoms valence electrons. The X-ray, now having a new energy will no longer have a consistent phase with any X-rays that have scattered elastically, or indeed any others that have scattered inelastically. It is these X-rays that are responsible for a significant part of the recorded background signal (4).

There are two main factors defining the diffraction pattern;

(a) The atoms present in the material.

(b) The size and shape of the unit cell, with the atomic positions within it.

This allows two materials of similar unit cell to still exhibit substantially different powder pattern, due to their chemical composition. The powder pattern shape is defined based on the scattering of incident radiation from the sample, and is dependent on how this radiation interacts with the material.

2.1.1. X-ray Powder diffraction (XRD)

X-rays are part of the electromagnetic spectrum, and are a transverse wave with an electrical and magnetic component, which means they are able to interact with electrons. X-rays have wavelengths (λ) in the range of 0.1-100 Å, which encompasses the range of interatomic bonds, making them useful for the study of crystal structure, as this allows for diffraction.

X-rays are generated using a lab based x-ray vacuum tube with a typically copper or iron target. Electrons are liberated from a tungsten filament by heating and are accelerated towards the copper target using a high potential difference. Multiple inelastic collisions on impact with the target material result in a reduction in the velocity of the accelerated electrons the emission of X-rays.

The metal target therefore accounts for the specific wavelengths of the emitted X-rays, corresponding to the discrete energy levels of the electron orbitals specific to that material. This radiation of known wavelength is used for diffraction experiments, and the primary beam is passed through a monochromator, to ensure that only the desired wavelength X-rays are incident on the sample. In the case of the copper source diffractometers, the radiation has a wavelength of 1.541 Å ($K\alpha_1$) and 1.544 Å ($K\alpha_2$).

These X-rays are then diffracted from the samples and detected. A powder diffractometer has either a proportional detector, scintillation detector or Geiger counter. This detector is then connected to a digital output. The diffractometer scans the sample across a range of 2θ values; generally 10^o-70^o is sufficient, due to a loss of intensity at higher angles.

A proportional detector measures the energy of incident radiation, by producing a detector output that is proportional to the radiation energy; hence the detector's name. A scintillation counter detects and measures both the intensity and the energy of incident radiation. A scintillator generates photons of light in response to ionisation by incident radiation, which reaches a sensitive photomultiplier tube and is transmitted as an electrical signal. These detectors are placed inside the diffractometer along with the X-ray source and the material sample. The sample is usually placed in a small disc container and its surface carefully flattened to avoid preferred orientation.

One configuration is for the disc to then be put on one axis of the diffractometer and tilted by an angle θ while a detector rotates around it on an arm at twice this angle. This configuration is known under the name Bragg–Brentano theta-2 theta.

The configuration used in this investigation for the confirmation of phase purity was a Bruker D8 Advance, which uses a Bragg–Brentano theta-theta (Figure 2.3) set-up in which the sample is stationary while the X-ray tube and the detector are rotated around it. The angle formed between the tube and the detector is 2theta. This prevents the loss of loose powder from tilting, and allows the sample stage to rotate, in order to prevent inaccuracies in peak intensities. This preferred orientation arises when there is a stronger tendency for the crystallites in a powder or a texture to be oriented in one particular direction. This would mean that particular reflections may appear more intense than they actually should be. Rotation of the sample stage prevents this, as it means that radiation is incident from multiple angles rather than just the direction of the preferred orientation.

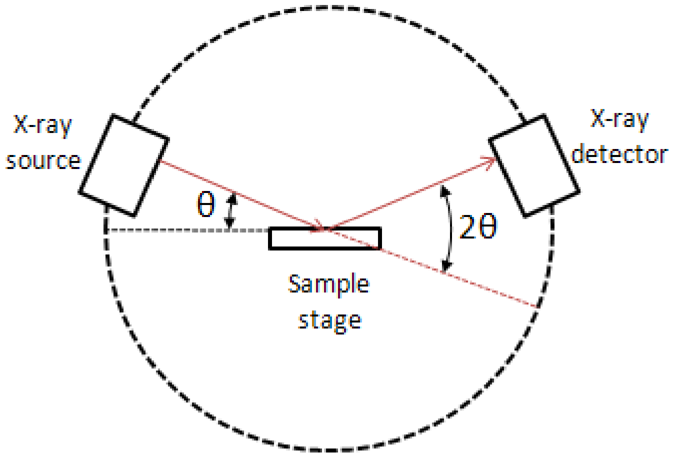

Figure 2.3: *A schematic of a Bragg-Brentano theta-theta configuration in which the sample stage remain fixed whilst the X-ray source and detector are mobile.*

2.1.2. Powder Neutron Diffraction (PND)

Similar diffraction techniques are used not only with X-rays as the incident radiation, but also incident high energy neutrons, as this can yield alternative information about the structure of the material.

Neutrons are scattered by atomic nuclei rather than outer orbital electrons. This means that neutrons are more sensitive to smaller atoms with fewer electrons.

Neutrons diffraction can also give some information about the magnetic structure of the materials, as the spin ½ neutrons can interact with unpaired electrons in the valence band provided those electrons exhibit long-range magnetic order, which will result in coherent scattering of the neutrons. This means that there are two origins of scattering of neutrons - magnetic diffraction and nuclear diffraction. (6,7)

Powder neutron diffraction uses neutrons from a reactor or spallation source.

The instrument used in this investigation was at the ISIS facility, and relied upon a spallation source to generate the beam of neutrons. This involves producing a source of negative hydrogen ions from a plasma. The stream of H^- ions is then accelerated before being passed through a series of intense electric fields (radio frequency range) to focus the particles and bunches them before injecting them into the linear accelerator (Linac). The Linac significantly accelerates the particles in pulses after which they are passed into the synchrotron. Upon entering the synchrotron, the H^- ions are stripped of their electrons using high energy electromagnets and the proton beam is accelerated towards the target (spallation source). This target consists of a metal tungsten plate cooled by water. High-energy neutrons are emitted when the proton beam hits the target, then passed through a series of moderators (different media at variable temperatures), for use in various experiments. (8)

The data collected in this experiment was obtained at the ISIS Neutron facility using the HRPD instrument, which is a high resolution Neutron diffractometer.

The HRPD instrument consists of three detector banks at fixed angles (Figure 2.4). The first is a 'backscattering' bank at 180^{o}, a 90° bank, and a 30° 'low angle' bank. The detectors are at a fixed angles, as the instrument utilises time of flight. (9)

HRPD uses a spallation source, which produces neutrons with a range of different energies and therefore a range of velocities. This means the wavelength is varied rather than the angle of incidence of the beam. The wavelength and consequently the d-spacing are determined from the time of flight.

Given a large range of energies, the detector banks need to cover a large number of d spacings. The backscattering bank at 168° from the incident beam is based on a ZnS scintillator and can collect data from 0.6 – 4.6 Å *d*-spacing. The detectors at 90° also use ZnS scintillators and collect data from 0.9- 6.6 Å *d*-spacing. The low angle bank uses Helium based detector collecting from 2.2 – 16.5 Å. The disadvantage of the 90^o and 30^o banks are that they have much lower resolution. However, the accessibility of higher *d*-spacings in these banks can be useful to detect the presence of predominantly magnetic reflections.

The data from the backscattering bank has been used for Rietveld refinements, although some higher composition samples have been refined in the 90^o bank.

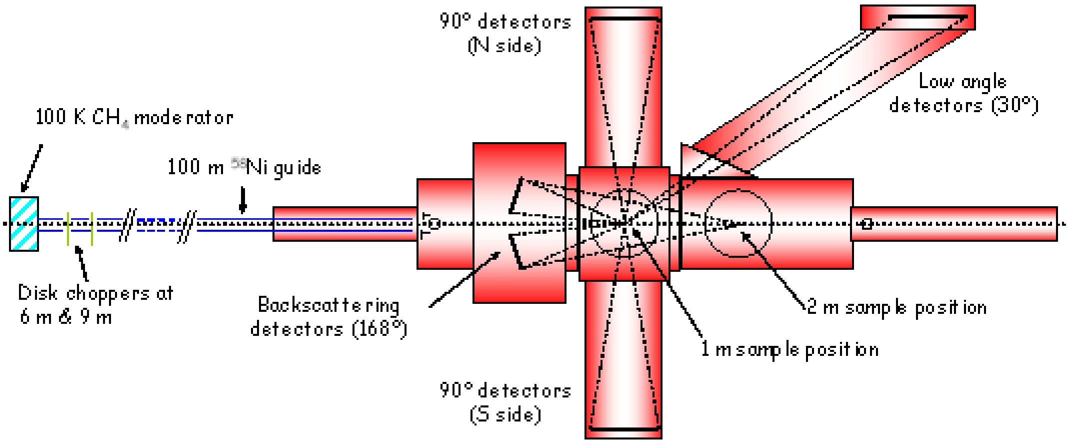

Figure 2.4: *A schematic of HRPD showing the three detector banks: backscattering, 90° and low angle 30°.* (9)

2.1.3. Rietveld Refinement

Powder patterns from PND and XRD experiments were analysed using the Rietveld refinement to structurally categorise each different sample. Refinements were carried out using the general structural analysis system (GSAS) and its associated graphical user interface program (EXPGUI). (10-13)

The Rietveld method is used to refine a calculated line pattern to evaluate potential matches with the experimental pattern. The method aims to minimise the difference between the calculated and experimental patterns by least squares refinement. It does this by making small incremental changes to the model using a series of changeable parameters. The technique was originally developed by Rietveld for nuclear and magnetic structural refinements, but has subsequently been adapted to allow for different peak profiles found in XRD patterns. (14,15)

The power of this method lies in its ability to deal reliably with strongly overlapping reflections, due to the fact that it uses a large number of variable parameters to improve the fit between the two patterns.

These parameters are split into several types, which combine to contribute to the overall refinement.

2.1.3.1. Background Contribution

There are two approaches to dealing with the background in a powder diffraction pattern. It can either be estimated by plotting a series of data points between peaks and subsequently subtracting them, or be modelled by a function containing several refinable parameters. Both have their advantages and disadvantages. (10,11)

For a simple pattern where most peaks are resolved to the baseline, both methods tend to work well and the fit is easily verified. For complex patterns with a high degree of reflection overlap or noisy background, however, the majority of the peaks are not resolved to the baseline, so the estimation of the background is more difficult. This means that if a background subtraction approach is used, the background usually has to be re-estimated and re-subtracted several times during a refinement. (5) However, equally there can be issues with a refinable background, as if the initial polynomial is unable to at least partly describe the experimental data, and a more complex mathematical function also proves insufficient, then it becomes impossible to then force that polynomial to fit the spectra regardless of how many refinement iterations are carried out. (10)

Of course, the ideal solution is to use the two methods simultaneously by estimating a simple function and then using several deviations to best describe the experimental data.

2.1.3.2. Peak-shape and Peak analysis functions

Before the refinement of the actual structural parameters can be started, the initial positions of the observed and calculated peaks must overlap. The parameters used to initially match these parameters are the background, unit-cell parameters and the zero correction all of which allow for data affects from the sample environment.

Once this initial contrast has been made, accurate description of the shapes of the peaks in a powder pattern is needed. If the peaks are poorly described, the refinement will be poor quality. Contributing factors to peak shape can come from both the sample (chemical or structural defects) and the instrument (radiation source, geometry, slit sizes), and they vary as a function of angle (2θ).

The most widely used peak analysis function is a linear combination of Lorentzian and Gaussian (Figure 2.5) mathematical components, known as the pseudo-Voigt approximation, which uses both of these descriptors to model the overall peak shape. (10).

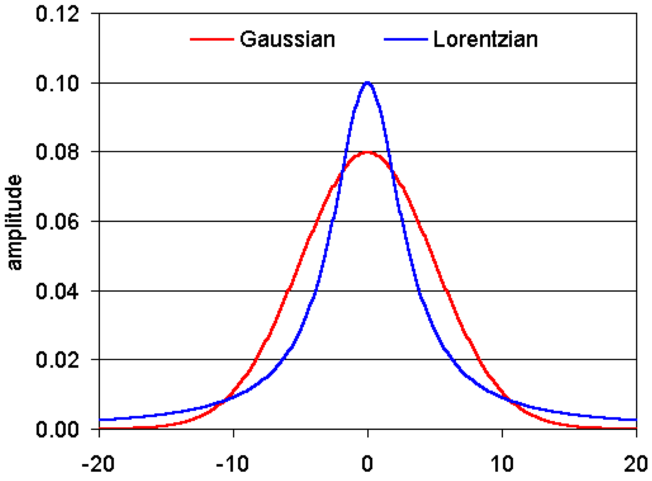

Figure 2.5: *Graphical representation of the Gaussian and Lorentzian peak descriptor functions.*

2.1.3.3. Peak parameters

In the case where only a basic structural model is available, the calculated intensities significantly differ from the experimental equivalent peaks, and this can hinder the initial refinement. In this case, a more accurate fit will come from a structure-free approach (Le Bail), in which the intensities of the reflections are simply adjusted to fit the observed ones to obtain initial values for the profile parameters with no accounting for atom positions. (11)

Le Bail refinement is a good way to valuate a structural model, and give and assessment of whether the model is a good initial fit to experimental data. Basic unit cell parameters can be refined using this method, and the data can then be further refined using Rietveld techniques from the structural model that has been validated.

With a complete structural model and good starting values for the background contribution, the unit-cell parameters and the profile parameters, the process of Rietveld refinement can be initiated.

To monitor the progress of a refinement, the two most useful pieces of information are the profile fit and the nature of the parameters shifts (oscillation, divergence or convergence). The quality of the refinement is best seen in a plot of the experimental and calculated patterns, but can also be followed numerically with a goodness of fit factor or χ^2 value (Equation 2.13). There are also other factors such as the weighted profile that can give an indication of fit quality, which are discussed below.

The structure should be refined to convergence. That is, the maximum standard deviation in the final cycle of refinement should be no more than $\chi^2<10$. All parameters should be refined simultaneously to obtain correct estimated standard deviations.

Although a difference profile plot is probably the best way of following and guiding a Rietveld refinement, the fit of the calculated pattern to the observed data can also be calculated and expressed as a series of numerical coefficients. One such coefficient is the weighted-profile *R* value, R_{wp}, is defined as(15)

$$R_{wp} = \left\{\frac{\sum_i w_i\left(y_i(obs) - y_i(calc)\right)^2}{\sum_i w_i\left(y_i(obs)\right)^2}\right\}^{1/2}$$

(Equation 2.11)

where $y_{i(obs)}$ is the observed intensity, $y_{i(calc)}$ the intensity from the calculated model, and w_i the weight. When the background is refined, $y_{i(obs)}$ and $y_{i(calc)}$ will include the background. Ideally, the final R_{wp} should approach the statistically expected *R* value, R_{exp},

$$R_{exp} = \left\{\frac{(N - P)}{\sum_i^N w_i y_i(obs)^2}\right\}^{1/2}$$

(Equation 2.12)

where *N* is the number of observations and *P* the number of parameters. R_{exp} reflects the quality of the data before refinement, and therefore when compared to R_{wp}, gives an overall view of quality. Thus, the ratio between the two gives a “goodness-of-fit”. This is a good indicator of the overall quality of both the experimental and calculated profiles.

$$\chi^2 = \frac{R_{wp}}{R_{exp}}$$

(Equation 2.13)

The final R_{wp} obtained in a Le Bail is a good indication of the best possible fit of the data that can be obtained, and the R_{wp} in an accurate Rietveld refinement should approach the same value as that from the Le Bail.

In general, the criteria for judging the quality of a Rietveld refinement are:

(i) the fit of the calculated pattern to the observed data

(ii) a sensible set of chemical compositions and position in the structural model.

The first can be judged on the basis of the final plot and the second on inspection of the final atomic parameters.

2.1.4. Impedance Spectroscopy

Ferroelectricity relates to the ability to allow flow of electrical current. Whilst Ohm's law defines this in terms of resistance, the ideal resistor is purely theoretical in materials. Equivalent circuit elements in materials exhibit much more complex behaviour. Like resistance, impedance is a measure of the ability of a circuit to resist the flow of electrical current.

An idealised model of a ceramic is composed of grains of conducting ceramic material that are connected by a grain boundary of different resistance.

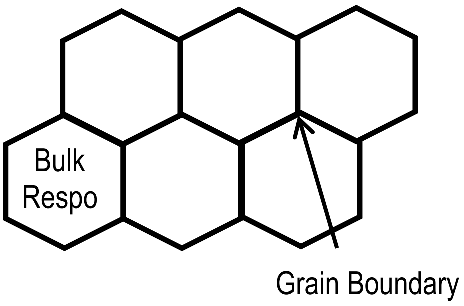

Figure 2.1.4.6: *Idealised ceramic microstructure consisting of bulk ceramic and grain boundary.*

The shortest electrical path through this material will take the current through both the grain and grain boundary regions. Data collected is interpreted as a number of equivalent electrical circuits; a parallel *RC* (Resistor and Capacitor) circuit, with each circuit in series with the others (Figure 2.7). Each *RC* element represents a region of the material *(*bulk or grain boundary), with values of resistance and capacitance varying accordingly. This then shows the shortest electrical path through bulk and grain boundary.

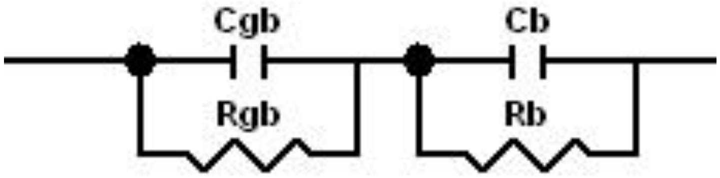

Figure 2.1.4.7: *Model RC circuit showing the grain (bulk) (R_b,C_b) and grain boundary (R_{gb},C_{gb}) resistances and capacitances.*

The resistance of an electroactive region can vary significantly but the capacitive behaviour of each region is likely to be within a similar magnitude for each different region. The magnitude of the capacitor response forms the basis of the electrical response, and provides a value for the bulk capacitance of the sample, containing contributions from the bulk response and grain boundary. (16)

The sample preparation procedure forms a parallel plate capacitor, separated by the thickness of the sample pellet (Figure 2.8). The material is then exposed to an applied field and polarised. The measured capacitance of the capacitor given by ε' which is the relative permittivity of the material (or dielectric constant), ε_0 is the permittivity of free space (8.854×10^{-14} F cm^{-1}), *A* is the top and bottom surface area of the pellet, and *d* is the separation between parallel plates (i.e. the thickness of the pellet). A/d is known as the geometric factor.

$$C = \varepsilon' \varepsilon^0 \frac{A}{d}$$

(Equation 2.14)

For a known pellet size, this measured value can then be used to calculate the dielectric constant of the material.

The actual permittivity of the material (ε) is complex, and contains a real part, the dielectric constant (ε'), which is a measure of the stored energy per cycle of a.c. field and links to the measured capacitance, and an imaginary part, ε'', which relates to the energy dissipation per cycle and is referred to as the dielectric loss.

$$\varepsilon = \varepsilon' + i\varepsilon''$$

(Equation 2.15)

This can also be calculated from impedance measurements, although usually, a normalised loss is plotted (Equation 2.15). This is a measure of the displacement of the material.

$$D = \tan(\delta) = \frac{\varepsilon''}{\varepsilon'}$$

(Equation 2.16)

In order to test the electrical properties of a sample metal contacts or electrodes are required. The electrodes are applied to the pellets. These electrodes are placed on the opposite circular faces of the pellet in order to maximise their surface area.

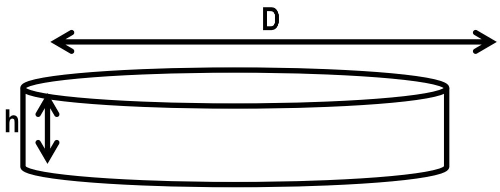

Figure 2.8: *The diameter and thickness of the pellet are measured to aid for calculation of the area and geometric factor, used for later calculations.*

In the measurements performed here, the electrodes are placed by exposing the surfaces of the pellet to sputtered Pt via vapour deposition using an Emitech K550x sputter coater. The side of the pellet is covered with electrical tape to prevent formation of a low resistance electrical pathway between the electrodes. The pellets are placed into a vacuum chamber where the atmosphere is exchanged with argon at low pressure. A metal plasma generated above the sample cools and deposits metal onto the exposed surfaces. Whilst there are alternative methods of applying and electrode, and a range of conductive materials can be used, the above method was selected for this data, due to the availability of equipment, and the high conductivity of Pt.

Once prepared, the pellets were available for dielectric measurements, and were subjected to several techniques. The two methods used in this study were isothermal data acquisition and automated temperature sweep recording.

For the temperature sweeps, the samples were mounted in one of two custom jigs design by Dr F Morrison at St Andrews University, intended for sub-ambient analysis and work at elevated temperatures. A thermocouple is mounted at the end of the jig alongside two platinum wires used to provide electrical contact to the pellet. High temperature (above ambient) measurements were performed in a jig represented in Figure 2.9.

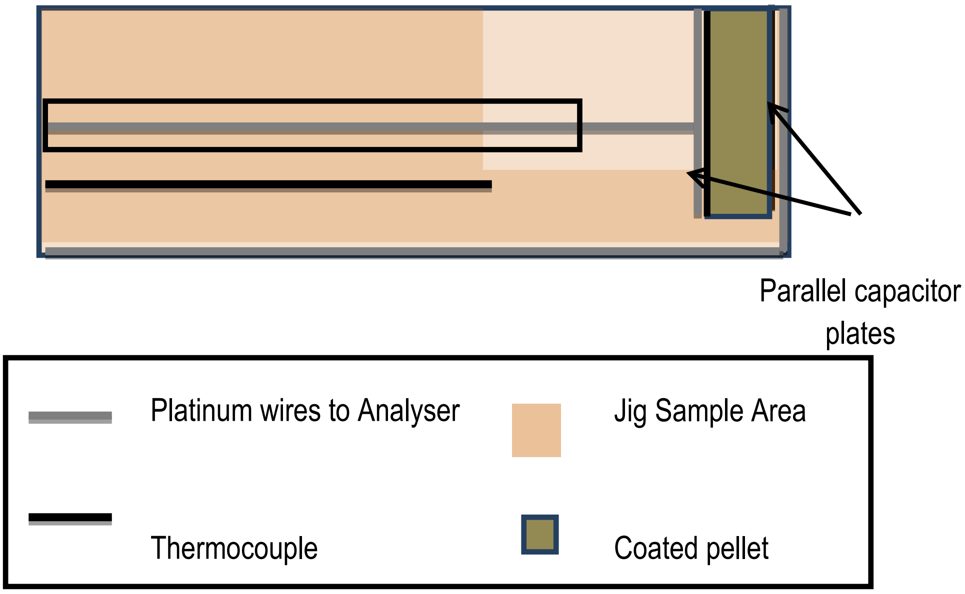

Figure 2.9: *Schematic representation of the sample environment during data collection.*

The sample is mounted in the indicated sample area and the movable wire is adjusted to make contact with the pellet. The platinum wires are connected to the external impedance analyser. Temperature adjustment is made by a Carbolite furnace surrounding the jig.

Low temperature work was performed by a similar vertical system using a Sumitomo HC-2 cryogenics system and mounted within a cold head. Temperature adjustments of the cryogenics system were made by a Scientific Instruments 9700 temperature controller. In both cases, the temperature adjustments and readings were controlled by computer software, written by Dr Kavanagh, and the whole process was automated. This means that the temperature was subject to slight fluctuation in magnitude whilst readings are being taken. Temperature readings from a thermocouple situated next to the sample are automatically recorded every 2 seconds. Frequency readings are taken quickly to avoid significant temperature changes.

In both cases, the total capacitance of the sample response, (bulk response) was recorded. This data was then used to calculate the dielectric constant and loss as a function temperature. The dielectric constant was calculated from the total capacitance (C_p) measurement.

Isothermal readings were taken on the Hewlett Packard 4192A LF impedance analyser. The temperature was again controlled using a Carbolite furnace. However the reading were regulated manually rather than by computer. These readings are isothermal, as there is no significant fluctuation in the temperature while the impedance analyser is taking its readings. The temperature is then changed in steps, and each reading taken records results at a number of frequencies, cycled by the analyser (5 to 10^7Hz).

Data analysis of isothermal readings can be used to determine the magnitudes of bulk and grain boundary responses. These reading can then be used to support the bulk readings from the temperature sweep. Data analysis was performed using ZView version 2.9 produced by Scribner

Associates Inc. This program provides the user with a number of different complex plots to extract data from. The resistance and capacitance of the components can be interpreted from these by simulating the data using the model RC circuit shown above (Figure 2.7).

2.1.4.1. Polarisation field hysteresis measurements

As previously discussed, ferroelectric materials are a polar material in which the electric dipole of which can be re-orientated by the application of an electric field.

Hysteresis data was collected by measuring the polarisation of a sample in an applied electric field. The electric field was cycled through from a large positive field through to a large negative field and back. As the field strength was altered and ultimately switches sign, the orientation of the electric dipoles reverses to realign with the new field direction.

Hysteresis data for many samples was poor, due to large leakage currents resulting in hysteresis loops with a oval shape where an increase in the polarisation is observed between the remnant and saturated polarisations, this is discussed further in Chapters 3 and 4. (17)

2.1.5. Magnetic Field Detection in Materials

The determination of the ferromagnetic character of a material requires the detection of extremely subtle magnetic field, and is often done using a SQUID magnetometer. This device is very sensitive and is based on a pair of superconducting loops.

2.1.5.1. Josephson Devices

Josephson junction standards can yield voltages with accuracies of one part in 10^{10}. Devices based upon the characteristics of a Josephson junction are employed in high speed circuits. Josephson junctions can be designed to switch in times of a few picoseconds and low power dissipation makes them useful in high-density computer circuits. These Josephson devices are extremely sensitive and very useful in constructing extremely sensitive magnetometers and voltmeters.

As seen in Figure 2.10, two superconductors are separated by a thin insulating layer and can experience tunnelling of Cooper pairs of electrons through the junction. The Cooper pairs on each side of the junction can be represented by a wavefunction similar to a free particle wavefunction, given that Cooper pairs act in a boson like state (18,19). In the DC Josephson effect, a current related to the phase difference of the wavefunctions flows in the junction in the absence of voltage.

The wavefunction which describes a Cooper pair of electrons in a superconductor is an exponential like the free particle wavefunction. In fact, all the Cooper pairs in a superconductor can be described by a single wavefunction in the absence of a current because all the pairs have the same phase. If two superconductors are separated by a thin insulating layer, then quantum mechanical tunnelling can occur for the Cooper pairs without breaking up the pairs. Under these conditions, a current will flow through the junction in the absence of an applied voltage (20-23).

In the AC Josephson effect, a Josephson junction will oscillate with a characteristic frequency which is proportional to the voltage across the junction. Therefore, allowing the voltage to be measured as a function of frequency.

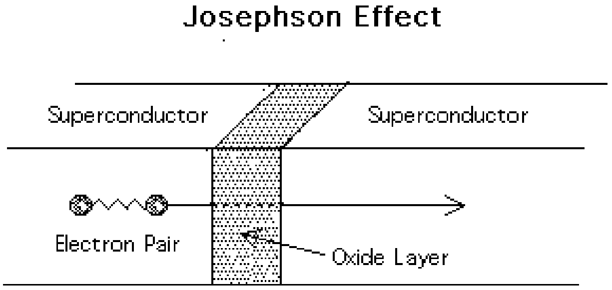

Figure 2.10: *Graphical representation of the effect at a Josephson Junction (20)*

2.1.5.2. Superconducting Quantum Interference Device (SQUID)

One of the discoveries associated with Josephson junctions was that flux is quantized in units;

$$\Phi_o = \frac{2\pi h}{2e} \equiv 2.0678x10^{-15}Tm^2$$

(Equation 2.19)

The superconducting quantum interference device (SQUID) consists of two superconductors separated by thin insulating layers to form two parallel Josephson junctions (Figure 2.11). The device may be configured as a magnetometer to detect incredibly small magnetic fields. The great sensitivity of the SQUID devices is associated with measuring changes in magnetic field associated with one flux quantum, which is a dependent on the magnetic flux, and the size of the loop area being used (Figure 2.11) (24,25).

If a constant biasing current is maintained in the SQUID device, the measured voltage oscillates with the changes in phase at the two junctions, which depends upon the change in the magnetic flux. Counting the oscillations allows you to evaluate the flux change which has occurred (16,17).

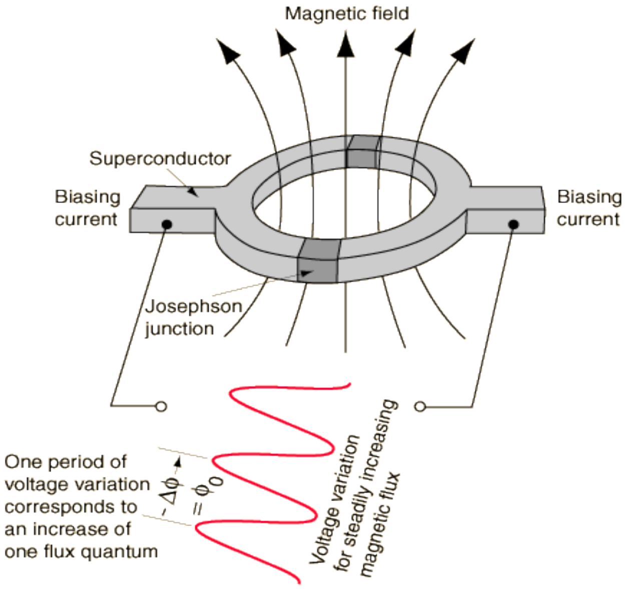

Figure 2.11: *Schematic representation of the SQUID magnetometer* (26)

2.1.6. Raman Analysis

Raman spectroscopy is commonly used in chemistry as a tool of structural analysis, since the vibrational information that can be extracted is specific to the chemical bonds and symmetry of each independent material. This gives another interpretation of the characteristic material structure.

When photons are scattered from an atom, most are scattered elastically (Raleigh scattering [Figure 2.12 (b)]). However, some are scattered via excitation, the result being a frequency discrepancy between the incident photon and the scattered photon (generally a decrease).

For the spontaneous Raman Effect a photon from the incident laser excites the molecule from the ground state to a higher (non-discrete) energy state. When the molecule relaxes it emits another photon, returning to a different energy state. The difference in energy between the original state and this new state leads to a shift in the emitted photon's frequency away from the excitation wavelength.

Raman scattering can be characterised based upon how this frequency alters.

- Stokes: The absorbed photon is emitted with less energy than the incident beam; the atom has gained energy. (Figure 2.12)
- Anti-Stokes: The absorbed photon is emitted with greater energy than the incident beam; the atom has lost energy. (Figure 2.12)

The effect taking place is measured by the subtraction of the energy of the laser from the energy of the scattered photons.

This is a different mechanism to fluorescence in that it is not a resonant effect, and can occur at any incident frequency of radiation. However when taking Raman spectra, fluorescence can be a problem if the frequency of the incident laser falls at one of the specific fluorescent frequencies of the material under study.

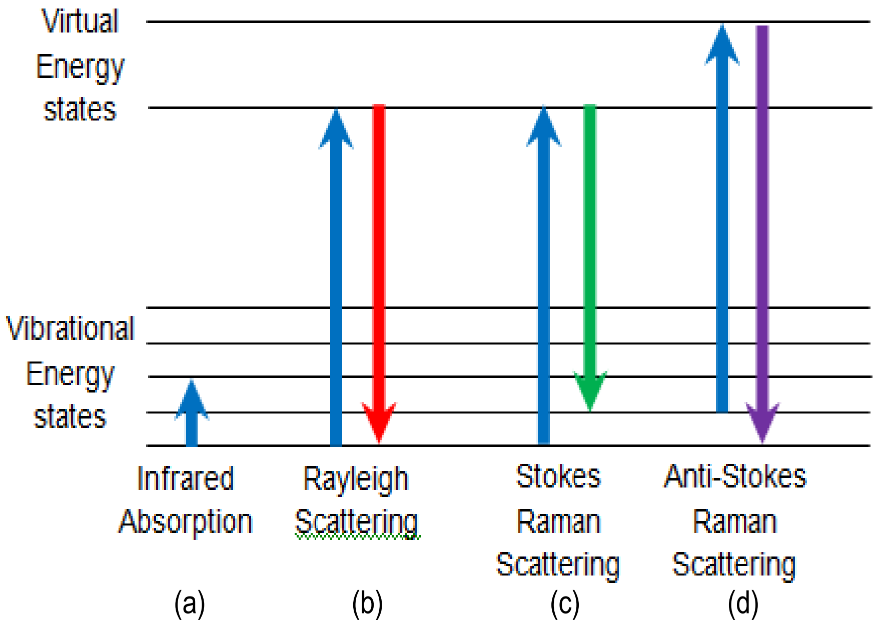

Figure 2.12: *Schematic representation of different scattering mechanisms within Raman spectroscopy.*(4)

In a typical Raman experiment, a sample is illuminated with a laser beam. Light from the illuminated spot is collected with a lens and sent through a monochromator. Wavelengths close to the laser line due to elastic Rayleigh scattering are filtered out while the rest of the collected light is dispersed onto a detector.

Spontaneous Raman scattering is typically very weak, and as a result the main difficulty of Raman spectroscopy is separating the weak inelastically scattered light from the intense Rayleigh scattered laser light. Historically, Raman spectrometers used holographic gratings and multiple dispersion stages to achieve a high degree of laser rejection. In the past, photomultipliers were the detectors of choice for dispersive Raman setups, which resulted in long acquisition times. However, modern instrumentation almost universally employs notch or edge filters for laser rejection as they allow for better quality data over a lower acquisition time.

The Raman Effect requires a change in the molecular polarization potential (i.e. the amount of deformation of the electron cloud) with respect to the vibrational coordinate. This polarisability determines the intensity. The pattern of shifted frequencies is determined by the rotational and vibrational energy states of the sample.

Raman shifts are measured in wavenumbers, which have units of inverse length.

Each chemical bond and symmetry element found in a material has a unique vibrational characterisation; these combined allow the molecule to be identified by Raman spectroscopy. Using spectral data from a Raman device can characterize materials and find their crystallographic orientation. As with molecules, a given solid material has characteristic phonon modes that can be identified. The Raman signal gives information on the population these given phonon modes from comparison between the Stokes and anti-Stokes intensities.

2.2. Experimental Methods

The initial synthesis used (22,23) standard solid state techniques and stoichiometric ratios of Bi_2O_3, Fe2O_3 and the dopant material (Dy_2O_3, K_2CO_3, Nb_2O_5) (Aldrich, 99+ %) (29). The starting materials were dried 1000OC – DY, 600OC KN, NB, ground under acetone with a mortar and pestle and then subjected to the following heating regime; 5 hours at 800°C, with a 6 mol% excess of Bi to prevent volatilisation of bismuth. The resulting powder was leached with 2.5 M HNO_3 under continuous stirring for two hours, washed with ddH_2O and dried for one hour at 400^{o}C to eliminate any small amounts of parasitic phase ($Bi_{24}FeO_{39}$) to yield single phase materials. Phase purity was assessed using a Bruker D8 Advance diffractometer equipped with Cu Ka1 radiation (40 kV and 40 mA, l = 1.54413 Å) over a range of 10^{o}>2θ> 70^{o}.

Room temperature powder neutron diffraction data was collected on HRPD at the ISIS facility, UK. The materials were loaded into 6 mm diameter cylindrical vanadium cans for data retrieval. Room temperature synchrotron diffraction data were collected on the high resolution diffraction beamline (I11) at the Diamond Light Source, UK (l = 0.826943(5) Å and 2θ zeropoint = 0.001533(3)). In order to minimise absorption effects, associated with bismuth, the samples were loaded onto the outside surface of 0.3 mm diameter glass capillary. This was achieved with a thin layer of hand cream and rolling the capillary in the sample to provide an even coat of material. Variable temperature studies of specific composition were also taken on the HRPD instrument between 10K and 973K for some compositions in both $Bi_{1-x}Dy_xFeO_3$ and $Bi_{1-x}K_xFe_{1-x}Nb_xO_3$ materials. All refinements were performed using the General Structure Analysis System (GSAS) suite. (22,23)

Pellets were prepared for Raman spectroscopy and electrical characterisation by pressing the material into 10 mm diameter pellets and sintering them at 850^{o}C for three hours. The pellets were polished to give a near mirror surface for Raman analysis. It was noted that with increasing Dy^{3+} and K^+/Nb^{5+} content it became harder to achieve mirror surfaces on the pellets as strength of the pellets reduced and they were more likely to fracture.

Raman spectra were collected on a Horiba Yvon Jobin LabRAM instrument. Room temperature mapping was performed using a 633 nm laser over an area of approximately 50μm × 50μm. These measurements were performed using ten integrations with a two second acquisition time with ×50 objective and 600 lines per mm grating over a Raman shift range of between 80 cm-1 and 1280 cm-1. Single point high resolution Raman spectroscopy was performed with a 633 nm wavelength laser at 77 K using a Linkam Examina THMS 600 cold stage. Measurements were performed using ten integrations with a one second acquisition time with a ×50 objective and 1800 lines per mm grating.

Dielectric measurements were made on the pre-prepared10 mm pellets, which had been sintered for 3 hours at 850 ^{o}C, using an Agilent 4294A impedance analyser over a frequency range of approximately 100 Hz to 5 MHz and a temperature range of approximately 50 to 340 K using a cryostat and Carbolite furnace (cooling/heating rates of 2 Kmin-1). For dielectric measurements, platinum electrodes were applied to polished pellets using the Emitech K550x sputter coater.

SQUID magnetometry was performed using a Magnetic Property Measurement System (MPMS) XL-7 instrument. A temperature range of 2 K to 300 K was used in both zero field and in an applied field of 1000 Oe. Hysteresis behaviour was investigated at 120 K and 300 K in a variable field of approximately (+/-) 70000 Oe using a step size of 100 Oe between 0 and 1000 Oe, 500 Oe between 1000 Oe and 5000 Oe and 5000 Oe between 5000 Oe and 70000 Oe.

References

1. *Elementary Scattering Theory*, D. Sivia, Oxford University Press (2011)
2. *Lecture Notes on Semiconductor Spintronics,* T. Dietl, *Institute of Physics* (2007)
3. http://www.xtal.iqfr.csic.es/Cristalografia/archivos_05/ewald-en.jpg
4. *Basic solid State Chemistry*, West. A.R, John Wiley & Sons Ltd. (1988)
5. Intensive BCA/BCG School Durham (2011)
6. V. K. Pecharsky and P. Y. Zavalij, *Fundamentals of Powder Diffraction and Structural Characterization of Materials*, Springer US, (2009).
7. J. Cui, Q. Huang and B. H. Toby, *Powder Diffr.* (2006) **21**, 71-79.
8. How ISIS works - in depth, http://www.isis.stfc.ac.uk/about-isis/how-isis-works---in-depth4371.html, Accessed 03/08/2012
9. HRPD User Manual, http://www.isis.stfc.ac.uk/instruments/hrpd/documents/hrpd-manual6735.pdf
10. L. B. McCusker, R. B. Von Dreele, D. E. Cox, D. Louër and P. Scardi, *J. Appl. Cryst.* (1999). **32**, 36-50
11. A. Le Bail, H. Duroy, and J.L. Fourquet, *Materials Research Bulletin* (1988) **23** 447-452
12. H. Rietveld, *J. Appl. Crystallogr.*, 1969, **2**, 65-71.
13. V. K. Pecharsky and P. Y. Zavalij, *Fundamentals of Powder Diffraction and Structural Characterization of Materials*, Springer US, 2009.
14. A. C. Larson and R. B. Von Dreele, Los Alamos National Laboratory 1994.
15. H. Rietveld, *J. Appl. Crystallogr.*, 1969, **2**, 65-71.

16. J. T. S. Irvine, D. C. Sinclair and A. R. West, *Adv. Mater.*, 1990, **2**, 132-138.

17. S. Bose and S.B. Krupanidhi, *Appl. Phys. Lett.*, (2007), **90**

18. E. A. Demler , G. B. Arnold, M. R. Beasley, Phys. Rev. B, (1997), **55**, 15174–15182

19. G.L. Ingold and H.Grabert , U. Eberhardt Phys. Rev. B, (1994), 50, 395–402

20. D. C. Arnold, K. S. Knight, F. D. Morrison, P. Lightfoot, *Phys. Rev. Lett. (*2009), **102**, 027602

21. D. C. Arnold, K. S. Knight, G. Catalan, S. A. T. Redfern, J. F. Scott, P. Lightfoot, F. D.Morrison, *Adv. Funct. Mater. (*2010), **20**, 2116.

22. R.C. Lennox, M.C. Price, W. Jamieson, M. Jura, A. Daoud-Aladine, C.A. Murray, C. Tang, D.C. Arnold, *J. Mater. Chem. C*, **2014**,2, 3345-60

23. R. C. Lennox, D. D. Taylor, L. V. Stimpson, G. B. G. Stenning, M. Jura, M. C. Price, E. E. Rodrigeuz, and D. C. Arnold, *Dalton Trans*, 2015, **44**, 10608-10613

24. *SQUID sensors: fundamentals, fabrication, and applications*, H. Weinstock, NATO Science Series E (1996)

25. E. Keiji, M. Tadashi; G. Takemitsu, K. Yukinori, I. Yuzuru, Y. Makiko, K. Yoshinori, K. Satoru, *Japanese Journal of Applied Physics*, (1999), **38**, 10A, 1102-1105

26. http://hyperphysics.phy-astr.gsu.edu/hbase/solids/squid.html

27. *Multiferroics: An Introduction*, R.N.P. Choudry and S.K. Patri, *Indian Institute of Technology*, (2008)

28. M. Stachiotti, A. Dobry, R. Migoni and A. Bussmann-Holder , *Phys. Rev. B*, (1993), **47**,2473–2479

29. F.D. Morrison, D.C. Sinclair and A.R. West, *J. Appl. Phys*, (1999), **86**, 6355

30. B. H. Toby, *J. Appl. Cryst.(* 2001), **34**, 210

31. N. J. Kidner, N. H. Perry, T. O. Mason and E. J. Garboczi, *J. Am. Ceram. Soc.*, (2008), **91**, 1733-1746

32. L. Brugemann, E.K.E Gerndt, *Nucl Instrum Methods*, (2004), **531**, 292-301

33. N.J. Kidner, N.H. Perry, T.O. Mason, *J. Am. Ceram. Soc.* (2008), **91**, 1733-1746

34. Aviram, S. Goshen, D. Mukamel and S. Shtrikman, *Phys. Rev. B*, (1975), 12, 438–442

35. M. Fujimoto, S. Jerzak and W. Windsch, *Phys. Rev. B*, (1986), **34**, 1668–1676

Chapter 3: Investigation of Dysprosium doped $BiFeO_3$

This study looks at the phase diagram associated with $Bi_{1-x}Dy_xFeO_3$ between values of x = 0.05 and 0.30. Diffraction data presented below shows that the material begins in the *R3c* $BiFeO_3$ parent phase, and as Dy^{3+} composition increases, there follows a large mixed phase region between the parent $BiFeO_3$ (*R3c*) and DyFeO3 (*Pnma*) phase, with the transition spanning the 0.5 > x > 0.30 range, and at x=0.30 the material is only *Pnma* symmetry. There is also some suggestion from data that there may be some secondary phase transitions to both polar *Cc* and a range of Pnma phases, both of which will be discussed when the individual x=0.05 and x=0.30 compositions are studied in more detail later in the text.

3.1. Preliminary Structural Analysis $Bi_{1-x}Dy_xFeO_3$

Diffraction data was collected on the HRPD powder neutron diffractometer at the ISIS Neutron facility, after initial structural confirmation using lab based X-ray diffraction. These data show the evolution of the mixed phase with the increase in Dy^{3+} composition , which can be seen clearly from PND data presented in Figure 3.1, with the emergence of additional *Pnma* symmetry peaks, particularly at 1.95 and 2.35 Å and the loss of a characteristic *R3c* peak at 2.00Å. In $BiFeO_3$ this transition from ferro-paraelectricity, would be expected to occur at a temperature of approximately 1083K (T_C). This is significantly lowered by the addition of Dy^{3+}, causing the mixed phase.

In addition to this alteration to T_C, the increase in Dy^{3+} content results in significant broadening of the peaks, as shown in Figure 1.1. In contrast to the literature, single phase *Pnma* was not found until x=0.30. (1,2,3) Although there is some suggestion that this material may actually inhabit several simultaneous *Pnma* phases. Both the lattice parameters and the cell volume decrease with increasing Dy^{3+} content. This conforms to expectations, as Dy^{3+} has a significantly smaller ionic radius than Bi^{3+} (0.912Å and 1.03Å respectively) [Figure 3.3].(4)

On inspection of the *R3c* refinements, the goodness of fit factors demonstrate that the *R3c* model could be insufficient to describe both the peak intensity and shape seen in the refinement data, and that the addition of Dy^{3+} results in a significant broadening of the peaks. The origin of peak broadening could arise as a result from size and strain effects or as a result of a small secondary phase. Further investigation into this peak broadening will be discussed later.

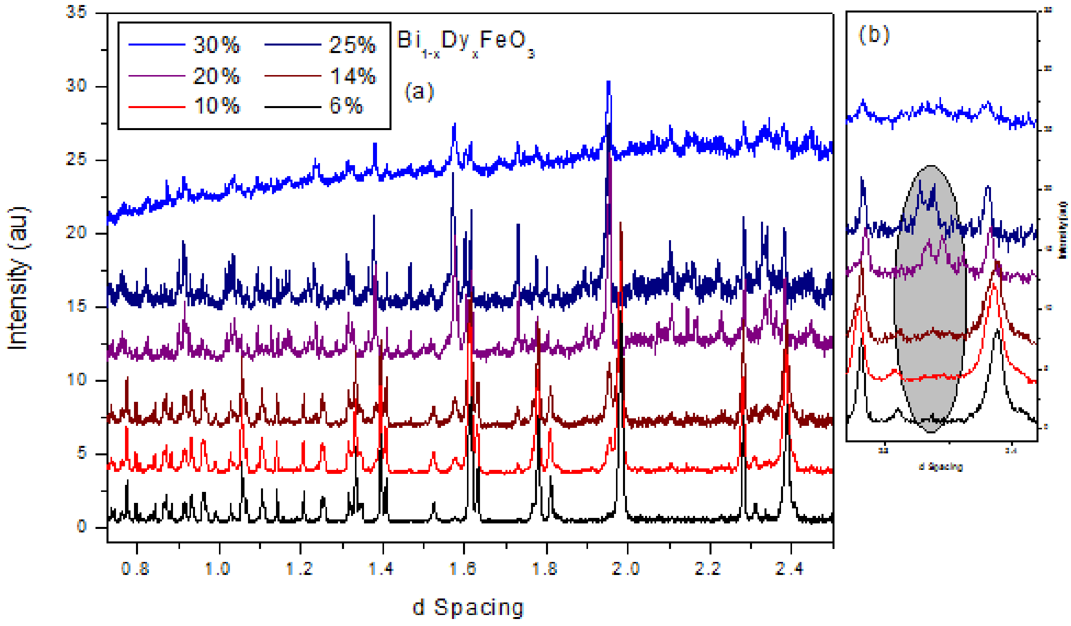

Figure 3.1: *Powder Neutron diffraction data showing a cross section of the development of the two primary phases as a function of* Dy^{3+} *content changed within the material across the studied range of* $Bi_{1-x}Dy_xFeO_3$ *materials. (x=0.05-0.30) This data was obtained from the HRPD high resolution instrument and all reading shown were taken at room temperature. High* Dy^{3+} *compositions (above x=0.20) are shown from the bank 2 detector due to neutron absorption of* Dy^{3+} *distorting the bank 1 reading. The zoomed in (b) shows the development of the Pnma phase across the data range.*

The mixed phase region of this composition also changes the nature by which the structure can be analysed, with a 2 phase Rietveld refinement necessary, allowing for determination of the relative % of both phases. All refinement patterns show the observed results, calculated model that has been fitted and the difference curve [Figure 3.2]. All refinements show atomic positions, bond lengths and angles that agree well with existing data [Table 3.1]. (5)

Unfortunately Dysprosium absorbs neutrons so after around x=0.20, the only useable data come from detector bank 2 (90° bank) of the Neutron data [Figure 3.3 (d)], as bank 1 is swamped by the background. In the mixed phase region, there is significant peak broadening, which could arise from the change in the size of the A site cation, or structural strain due to the size different between the two different A cations(6), it could also lead from (or mask) subtle changes in phase between the suggested *R3c* and *Pnma* phases.

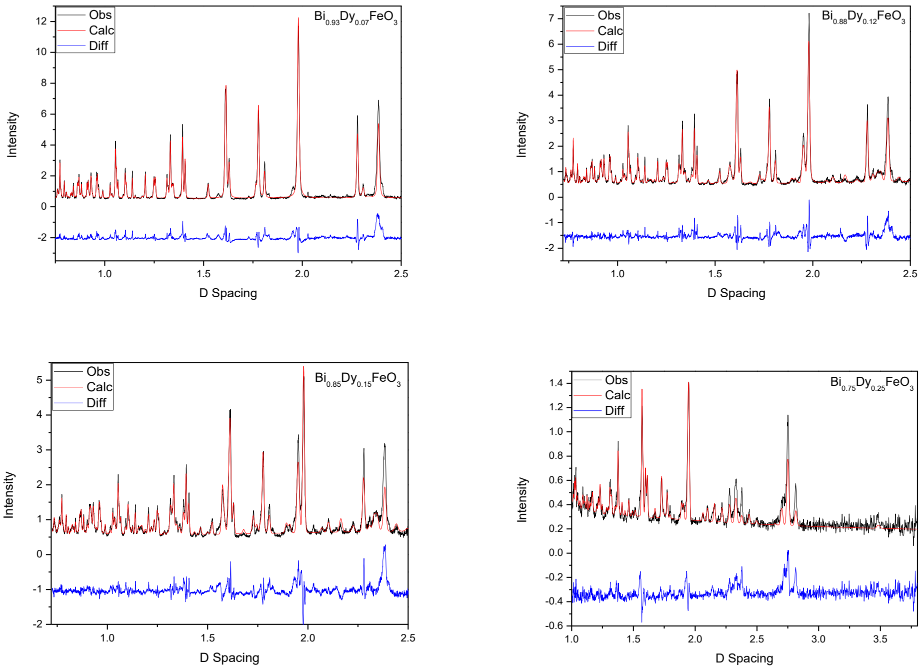

Figure 3.2: *Rietveld refinement profiles between 0.75Å and 2.5Å and 1.0Å and 3.75Å for neutron diffraction data collected for various compositions of* $Bi_{1-x}Dy_xFeO_3$*, showing reasonable fits for both peak shape and intensity. The black line represents experimental data, the red line the fitted model, and the subsequent blue line the difference between the data and the fit.*

The relationship between the phase formations and the Dysprosium content of the sample has been taken from the Rietveld refinement data and is shown in Figure 3.3, giving the percentage composition of the *R3c* and *Pnma* phases. The data shows an almost linear proportionality between x=0.05 and 0.30.

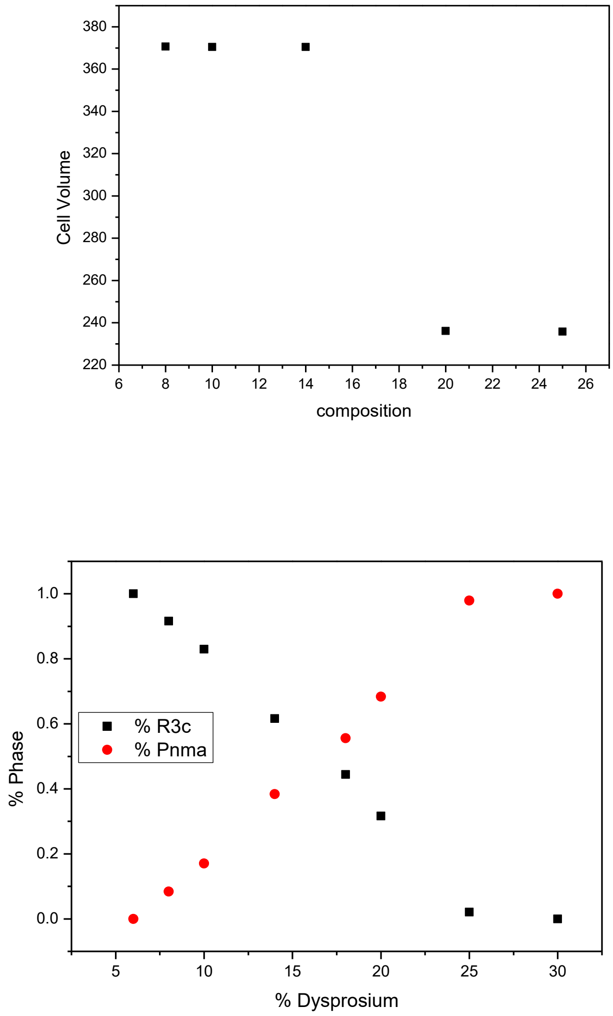

Figure 3.3: *(a) Scatter graph showing the change in cell volume with composition, with the inset showing the change in cell volume across the Pnma phase. Error bars are smaller than symbol size. (b) Plot showing the calculated phase fractions of the R3c and Pnma phases respectively as the composition of* $Bi_{1-x}Dy_xFeO_3$ *varies; these fractions have been taken from Rietveld refinement data. Black squares represent extracted R3c phase fraction and red dots represent the extracted Pnma phase fraction respectively.*

Further inspection of refinements (x=0.08-0.25) indicated that crystal size does not contribute to the broadening observed in these materials, as the Lorenztian LX term consistently refines to zero across the range. Variation of the Lorentzian strain term (LY) indicates a linear increase in LY with increasing Dy^{3+} content, indicating there may be some strain effects. Inspection of the data, and observation of the peak broadening seen, indicated that the strain effects can not be the sole source of the broadening observed with the addition of Dy^{3+}. When considering the peak broadening, it is possible for compositional variations across a sample to lead to multiple sets of lattice parameters.. Leineweber *et al.* reported the use of the Stephen's micro strain broadening to model these types of variations.(7) This did not improve the fit of the peak shape in these materials, and coupled with the low level of Dy^{3+} doping it is unlikely that lattice parameter variations fully explain the peak broadening observed here. Recently symmetry mode analysis of distortions in materials is emerging as an additional methods of identifying structural phase transitions.(8,9).

In this method the structural distortions within perovskites are described by tilts in the oxygen octahedra displacement of either cation. These tilts can be used to characterise the materials symmetry. Individual tilts can be examined and their contribution to the overall distortion recorded. Distortion mode symmetry analysis using ISODISTORT(10,11), and considered potential distortions of the crystal structure, as a method of explaining the peak broadening observed in the refinements. Distortion modes were suggested as Γ3, F, L and T modes, which lead to the conclusion of a loss of the symmetry from rhombohedral to monoclinic or triclinic (Cc or P1 respectively). This will be discussed further in the analysis of $Bi_{0.95}Dy_{0.05}FeO_3$.

Raman spectroscopy was collected out by Dr D. C. Arnold, and used to collect room temperature phase maps over a region of 50x50μm using a 633nm wavelength laser. Compositions *x*=0.05 as with the PND study, showed a single phase by examination of characteristic peaks(12), whilst compositions between shows a clear mix of the $BiFeO_3$ and $LaFeO_3$ (x=0.30) structures. By selecting peaks indicative of each phase it was possible to create a contrast map to show the evolution of the mixed phase region. It is clear from the spectra [Figure 3.4] that the ratio between the *R3c* and *Pnma* phases becomes more favourable towards the *Pnma* as Dy^{3+} content increases, which is consistent with the PND refinement data.

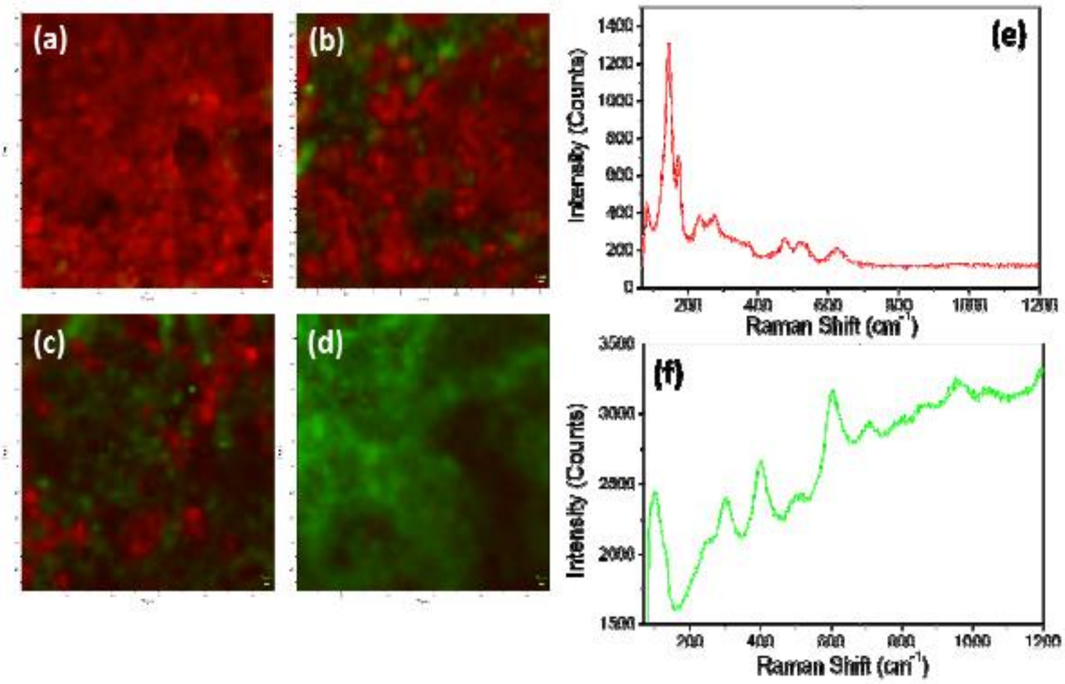

Figure 3.4: *Raman mapping data using a 633nm laser. showing the evolution of the Pnma phase (green) and the loss of the R3c phase (red) with increasing* Dy^{3+} *content in agreement with PND data, both the 5% and 30% APPEAR single phase.*

Having identified the phase region, more in depths studies where focussed on the single phase materials at either side of the mixed phase region at x values of 0.05 and 0.30 respectively.

Variable composition studies (0.05-x-0.25) indicate small amounts of secondary phase at Dy^{3+} contents as low as x=0.05 consistent with the work by Sun *et.al.* and Troyanchuk *et.al*.(13,14) presenting a combined *Cc-Pnma* symmetry with indication that Dy^{3+} continues to dope into the *Cc* phase with the lattice parameters and cell volume continuing to decrease with increasing Dy^{3+} contents. The Lorentzian strain term, LY, continues to increase, before reaching a plateau at approximately x=0.12 then dropping sharply. This would indicate that following x=0.14, the cell volume and lattice parameters indicating that no more dysprosium is doped into the Cc phase, and instead into the Pnma phase.

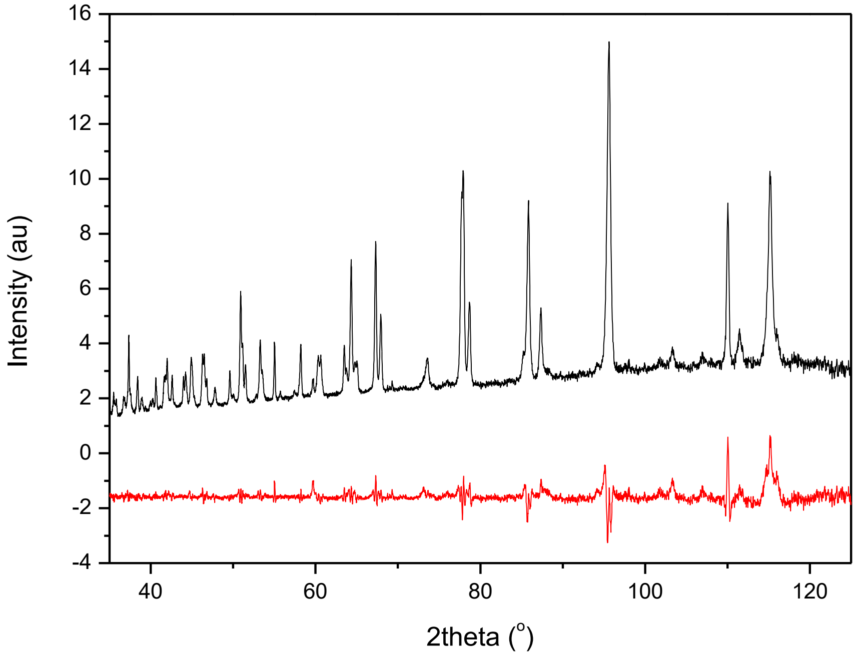

Figure 3.5: *Neutron diffraction data Rietveld refinements of $Bi_{0.95}Dy_{0.05}FeO_3$ using the Cc structural model. The black line represents experimental data, the red line represents the difference between the data and the Cc model.*

This suggests that the most strained material in the monoclinic phase at approximately x=0.14 and as such if a single phase material could be isolated, it may show enhanced properties as it appears to be close to the morphotropic phase boundary. This is consistent with Li *et. al.* whom reported enhanced ferroelectric properties were observed in $Bi_{0.90}Dy_{0.10}FeO_3$ materials.(15)

In addition, as discussed previously the large A-site variance between Bi^{3+} and Dy^{3+}, which was determined to not be the primary contributor to the initial peak broadening, may lead to some structural instability of the *Pnma* phase causing some variance in the lattice parameters in the x=0.18 sample. In contrast with the literature a single *Pnma* phase was not obtained until *x*=0.30.(16-18)

3.2. $Bi_{0.95}Dy_{0.05}FeO_3$

Symmetry mode analysis indicates the possibility of an alternative symmetry to the *R3c* phase either *Cc* or *P1*. In order to investigate the probability of these models to accurately describe our data, Lebail refinements were performed on both the powder neutron data for $Bi_{0.95}Dy_{0.05}FeO_3$. The Lebail method allows for the ‘best fit’ achievable to be realised by disregarding physical atom positions but still optimising peak shape and intensity. Inspection of the data shows that the distortion modes F, L and T can be discounted as they lead to the development of supercell peaks not evident in experimental data. However, the Γ3 modes (which results in either *P*1 or *Cc* symmetries) provides sensible models to describe the data.

Both proposed space groups show a lowering of the goodness of fit parameters and improved modelling of both the peak shape and peak intensities compared to the previous fits of *R*3*c*. Interestingly both *P*1 and *Cc* symmetries have recently been proposed as an alternative phase of the parent $BiFeO_3$ material.(19) However, whilst the *P*1 model proposed by Wang *et.al.*(20) is similar to that which resulted from the structural mode analysis there was no similar *Cc* model to that proposed by Sosnowska *et.al.*(19). In order to further investigate the models determined through symmetry mode analysis, full Rietveld refinements were performed for the diffraction data collected for the $Bi_{0.95}Dy_{0.05}FeO_3$. Refinements of showed instability, with unrealistic values observed for some parameters, excluding this model from further investigation. Refinements performed in the *Cc* model yielded better fits to both peak shape and peak intensity profiles than other tested models, and comparison of the goodness of fit parameters achieved for these refinements suggest a significant enhancement in the quality of the fit. Cc refinement data is shown in Figures 3.8, along with substantial improvement to goodness of fit parameters.

Both *R*3*c* and *Cc* phases has also been reported for related $Na_{0.5}Bi_{0.5}TiO_3$-$BaTiO_3$ materials.(21) The model determined from our symmetry mode analysis is consistent with the models proposed for

$Na_{0.5}Bi_{0.5}TiO_3$.(19,21) The rhombohedral *R*3*c* model can be described as a Glazer tilt notation $a^-a^-a^-$, with the ferroelectric polarisation along the [111] pseudocubic direction ([001] hexagonal direction].(22) The monoclincic distortions calculated show an $a^-a^-c^-$ tilt system with the ferroelectric axis being along the [110] axis.(223) This implies that the addition of Dy^{3+} onto the Bi^{3+} site results in a rotation of the ferroelectric polarisation vector.

For the study into the effect of increasing temperature, only the R3c model was used, as it showed reasonable fit to the low temperature data, and allowed the change in phase to be observed without the initial complication of the composite R3c, Cc phases. The *R3c* α phase that is seen in $BiFeO_3$ is still present in samples of $Bi_{0.95}Dy_{0.05}FeO_3$ at low temperatures, up to beyond room temperature, as demonstrated by Rietveld refinements fitted to the *R3c* model with initial signs of a first order phase transition at ~750K. This transition is signified by both the development of additional peaks (i.e. ~2.7Å) and the loss of intensity on existing structural peaks (i.e. ~2.6, 2.75Å). Despite the phase change not being seen until 750K, the disruption of the lattice parameters can been seen to begin at ~373K, with both the a/b and c values increasing steadily with temperature [Table 3.1, Figure 3.5 (a)]. This change is the lattice parameters will be likely due to thermal expansion of the lattice rather than significant structural effect of the doped Dy^{3+}. The secondary phase which becomes evident is fitted in a 2 phase refinement as being *Pnma* symmetry consistent with previous studies. (16,24)

***Table 3.1**: Table showing the lattice parameters, cell volume, phase fraction, lattice distortion and χ^2 refinement parameter for $Bi_{0.95}Dy_{0.05}FeO_3$ refined in R3c symmetry, the indicated region signals the beginning of the 2 phase refinements between R3c and Pnma.*

$Bi_{0.95}Dy_{0.05}FeO_3$	**Phase**	**Phase fraction *R3c***	**Second phase**	**Lattice parameters**		**c/a**	**Cell Volume**	**χ^2**
Temp(K)				**a**	**c**			
10	*R3c*	1.00000		5.5654	13.8182	2.4829	370.6570	8.9910
30	*R3c*	1.00000		5.5647	13.8161	2.4828	370.5140	20.0200
50	*R3c*	1.00000		5.5649	13.8166	2.4828	370.5700	8.2050
70	*R3c*	1.00000		5.5651	13.8184	2.4831	370.6380	7.5490
90	*R3c*	1.00000		5.5663	13.8221	2.4832	370.7260	7.9560
110	*R3c*	1.00000		5.5659	13.8221	2.4834	370.8290	7.8280
130	*R3c*	1.00000		5.5664	13.8239	2.4835	370.9420	17.0200
150	*R3c*	1.00000		5.5668	13.8259	2.4836	371.0680	12.5500
170	*R3c*	1.00000		5.5676	13.8290	2.4838	371.2350	7.6180
190	*R3c*	1.00000		5.5690	13.8338	2.4841	371.5540	7.4640
210	*R3c*	1.00000		5.5696	13.8361	2.4842	371.7040	5.4040
230	*R3c*	1.00000		5.5697	13.8369	2.4843	371.7500	9.2630
250	*R3c*	1.00000		5.5711	13.8413	2.4845	372.0380	3.8910
270	*R3c*	1.00000		5.5713	13.8418	2.4845	372.0820	7.9130
373	*R3c*	1.00000		5.5770	13.8604	2.4853	373.4980	6.6820
473	*R3c*	1.00000		5.5825	13.8785	2.4861	374.5620	2.7730
573	*R3c*	1.00000		5.5891	13.8983	2.4867	375.9920	3.7690
673	*R3c*	1.00000		5.5961	13.9187	2.4872	377.4920	2.5720
773	*R3c*	0.94268	*Pnma*	5.6031	13.9346	2.4869	377.6580	7.8580
778	*R3c*	0.90180	*Pnma*	5.6036	13.9353	2.4869	377.9450	3.1440
793	*R3c*	0.89425	*Pnma*	5.6045	13.9384	2.4870	378.2150	3.6690
803	*R3c*	0.83853	*Pnma*	5.6052	13.9394	2.4869	378.4150	3.7910
813	*R3c*	0.82568	*Pnma*	5.6059	13.9407	2.4868	379.7480	2.4720
823	*R3c*	0.76511	*Pnma*	5.6068	13.9431	2.4868	379.7510	3.2000
833	*R3c*	0.68125	*Pnma*	5.6077	13.9442	2.4866	379.7520	3.7930
843	*R3c*	0.66886	*Pnma*	5.6083	13.9451	2.4865	379.7520	3.3330
853	*R3c*	0.59014	*Pnma*	5.6092	13.9465	2.4864	380.0100	2.7180
863	*R3c*	0.52786	*Pnma*	5.6102	13.9480	2.4862	380.1850	3.5020
873	*R3c*	0.53914	*Pnma*	5.6109	13.9497	2.4862	380.3210	3.0870
903	*R3c*	0.44700	*Pnma*	5.6135	13.9569	2.4863	380.8760	3.8240
923	*R3c*	0.39751	*Pnma*	5.6147	13.9620	2.4867	381.1460	3.1780
973	*R3c*	0.2403	*Pnma*	5.6186	13.9813	2.4884	381.2600	4.5250

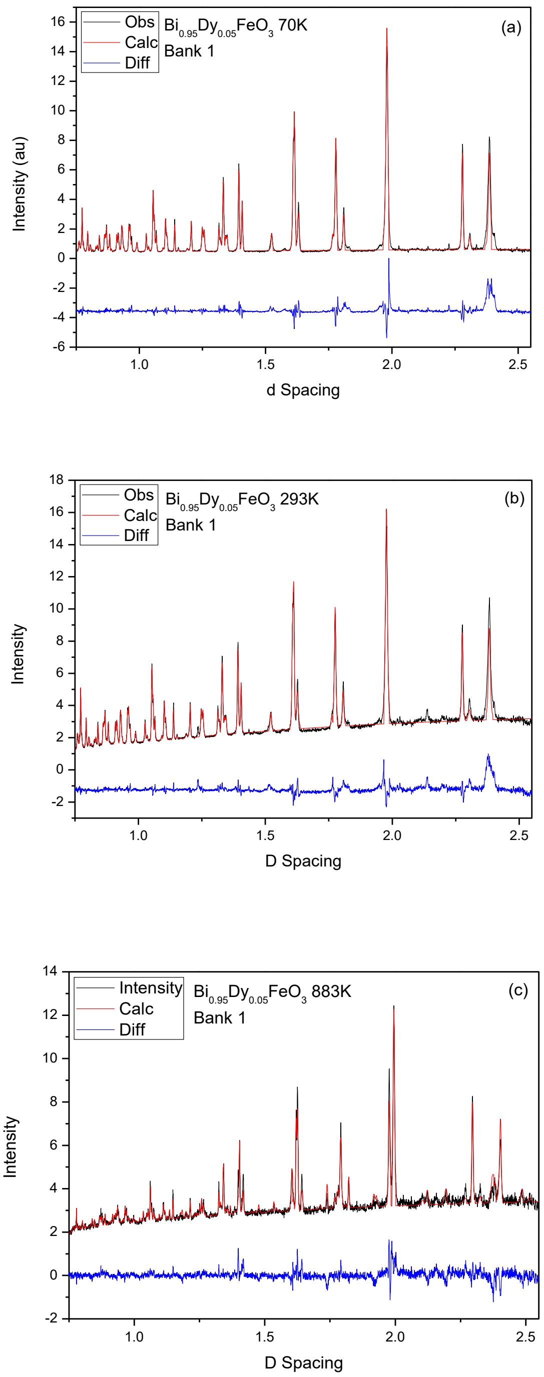

Figure 3.6: *Rietveld refinement profiles between 0.75Å and 2.6Å for neutron diffraction data collected for* $Bi_{0.95}Dy_{0.05}FeO_3$*, showing reasonable fits for both peak shape and intensity. The black line represents experimental data, the red line the fitted model, and the subsequent blue line the difference between the data and the fit. This data shows a single phase The R3c phase at 70K. Refinements that are given show a preview of the changes across the temperature range. All other refinements can be found in Appendix 6.1.*

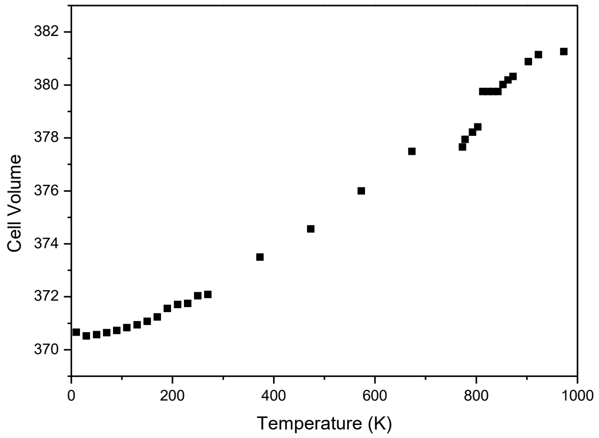

Figure 3.7: *Plot to show the change in cell volume with temperature for* $Bi_{0.95}Dy_{0.05}FeO_3$*, showing the expected expansion of the lattice as temperature increases. Error bars are smaller than symbol size.*

As the amount of Dy^{3+} increases, there is some broadening of the peak, which leads to an increase of noise in the difference curves, primarily due to the introduction of the potential *Cc* phase previously discussed. There is also some change to the peak height in Bragg peaks at higher d spacings, which may be linked to magnetic contributions. However the peaks do not disappear entirely, suggesting that there is no complete loss of the G-type magnetic spin cycloid.

The transition itself is also extremely broad, with both phases being present across a large temperature range, the final transition not culminating within the limits of experimental data. The progress of the phase transition can be mapped using the relative amounts of each existent phase, which has been calculated and extracted from Rietveld refinement data and displayed in Figure 3.8 (b), There is some disparity in the lattice parameters (c) at higher temperature, which agrees with the percentage composition plotted in Figure 3.8 (b) as this is around the phase transition, so the lattice structure will be changing. Alternatively this could be due to temperature strain on the lattice as the material approaches the decomposition temperature of the parent $BiFeO_3$. This range for the phase transition to Pnma is consistent with previous studies. (4)

This broad transition likely links to the inhomogenous nature of the samples, and the still unclear phase formations within the crystals. This could be further developed in the future with a more in depth structural study, incorporating different methods of sample preparation to help reduces absorption effects, along with symmetry mode analysis and local environmental analysis techniques. The possibility of utilising these techniques will be discussed further in section 3.4.

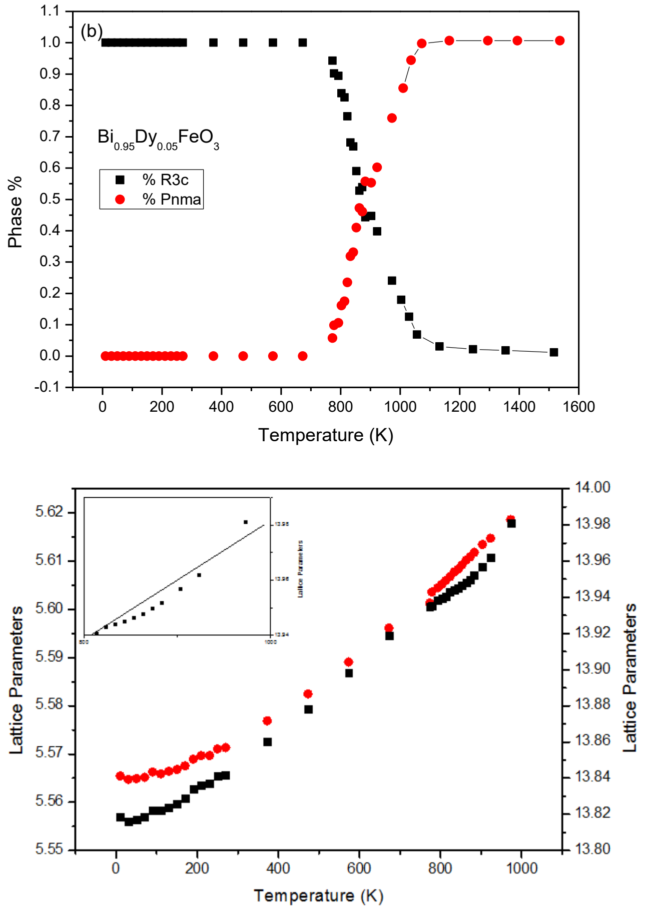

Figure 3.8: *Data extracted from Rietveld refinements to show (a) the change in lattice parameters with temperature, with the inset showing possible strain effects on the lattice shown in the distortion of the c parameter and (b) the relative compositions of R3c and Pnma across the broad temperature range of the transition. Error bars shown are smaller than the symbols size.*

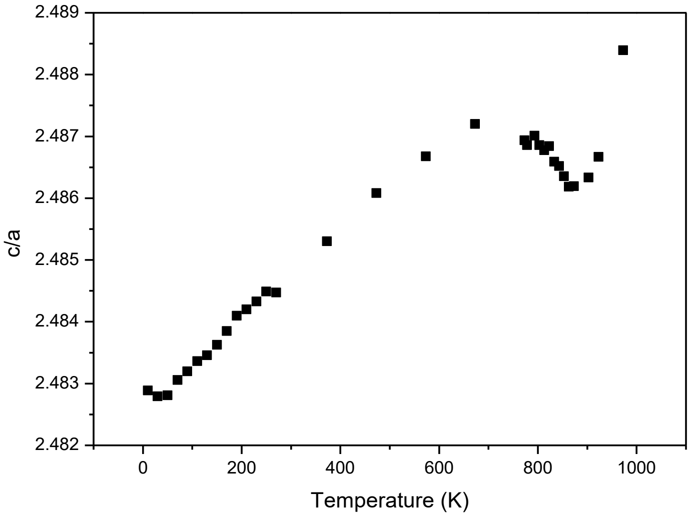

Figure 3.9: *Data extracted from Rietveld refinements to show variation in the lattice distortion (c/a)*

The change in the FeO_6 octahedra is shown by distortion of the Fe_O bonds, enhanced by the aforementioned variance between the two A site ions, which signifies loss of the ferroelectricity was previously noted can be confirmed as the two Fe_O bonds converge in conjunction with the loss of the R3c phase. [Figure 3.10] This centring of the B site ions, likely leads to a shift of electron density within the octahedral cages and the change in length of the Fe_O bonds. As can be seen from Figure 3.9, the loss of Fe3+ displacement happens very rapidly from approximately 800K onwards, but bond lengths fail to fully converge before the limits of the data.

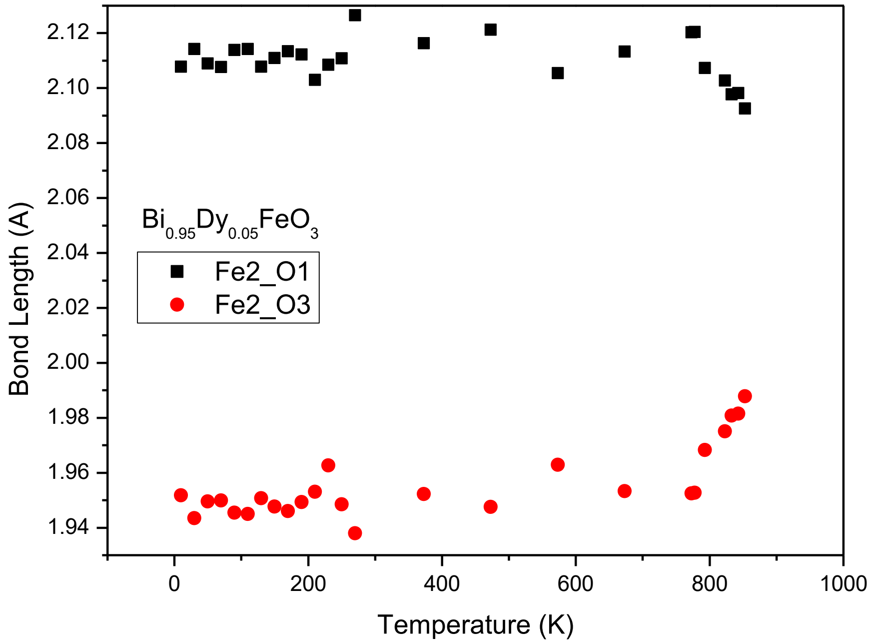

Figure 3.10: *Further data extracted from Rietveld refinements to show the distortion of the bonds between the Fe and the O1 and O3 oxygen site in the* FeO_6 *octahedra of the R3c cell.*

High resolution Raman data was also obtained at 77k, some peak broadening due to Dy^{3+} content can be seen compared to previous studies of $BiFeO_3$, including Hinkla et.al. [Figure 3.11]. There is also a change in the octahedral tilt mode between the two studies suggesting that there is a contribution from developing strain on the FeO_6 octahedra, which is to be expected given the phase change that occur as Dy^{3+} content is increased further. There is also a developing shoulder evident at approximately $100cm^{-1}$ that could also be linked these to changes in the octahedral tilt system.

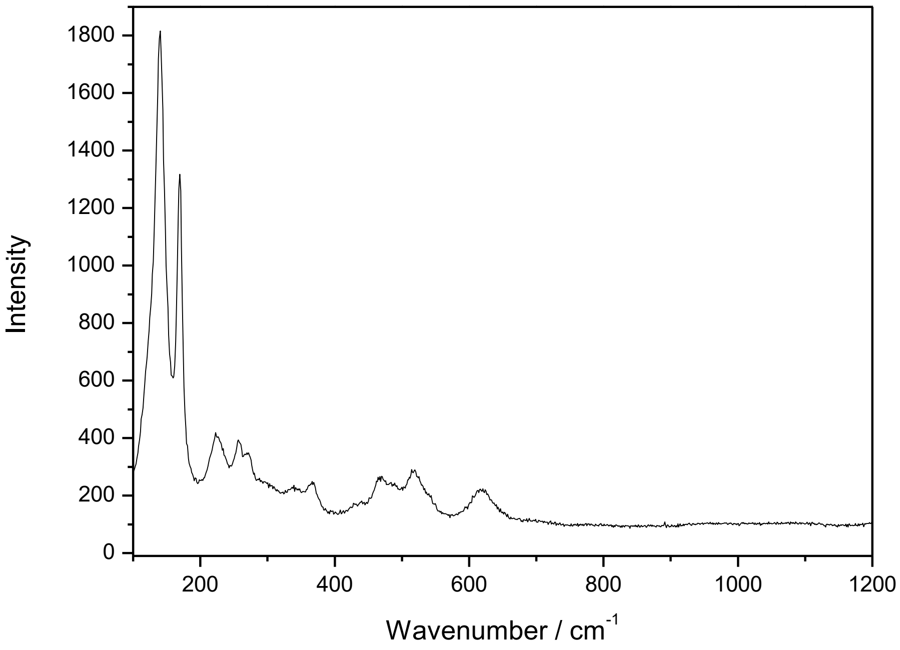

Figure 3.11: *Single point Raman spectra taken using a 633nm laser at 307K for* $Bi_{0.95}Dy_{0.05}FeO_3$.(35)

Electrical measurements for $Bi_{0.95}Dy_{0.05}FeO_3$ (shown in Figure 3.12) showed the gradual loss of ferroelectricity with increasing Dy^{3+}, along with an anomaly seen at 600-675K, which by comparison with the parent $BiFeO_3$ could be linked to the anti-ferromagnetic to paramagnetic transition. (22,26)

Several attempts were made to collect variable frequency data to investigate the predicted ferroelectric to paraelectric phase transition. All of this data showed the expected increase in permittivity that would be consistent with previous dielectric data for rare-earth ferrites. (9) The most prominent feature seen in this data [Figure 3.12] is the large peak at approx 600K, which masks any other features in the high temperature range. Using this data and the geometric factor of the pelleted material, the dielectric constant of the material was calculated across the temperature range, using the calculations outlined in Chapter 2.

Following calculations of the dielectric constant and comparison with existing studies (27,28) showed the peak not to represent the expected electrical transition, but a relaxor like characteristic given by non-ohmic electrode effects due to the ‘leaky’ dielectric In character typical to BiFeO3 (4,27,28)

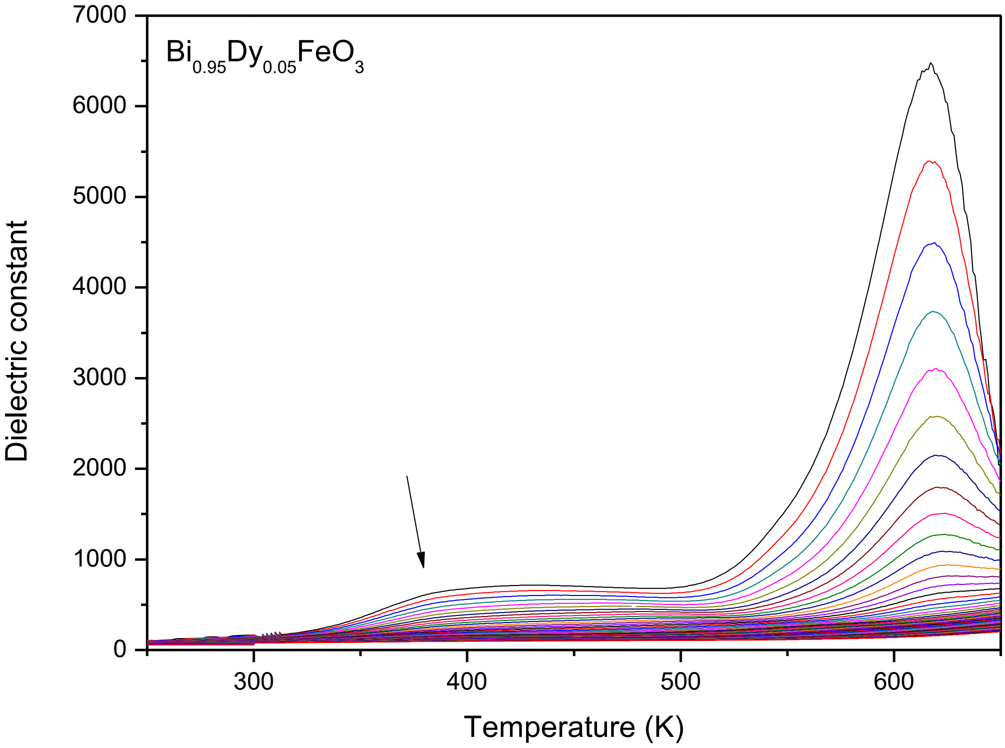

Figure 3.12: *Dielectric data collected for* $Bi_{0.95}Dy_{0.05}FeO_3$ *each colour represent the frequency at which the reading was taken between 100Hz AND 10MHz. The data shows an anomaly at ~675K consistent with a magnetic phase transition (marked with an arrow), and shows a high permittivity relaxor like electrode effect.*

This leaky nature also prevented the acquisition of polarisation field data, making it difficult to determine if the sample was polar or non-polar. However, as discussed in the structural study, the transition from the R3c phase to the Pnma phase would imply that there has been a ferroelectric to paraelectric transition coincident with and so potentially masked by the non-ohmic electrode effect.

Despite the lack of electrical evidence as to the polar nature of the material, the structural data already presented indicates that there is a transition from *R3c* to *Pnma.* This transition is consistent with the loss of the Fe^{3+} displacement within the octahedral cages of oxygen in $Bi_{1-x}Dy_xFeO_3$ as the Fe_O bond lengths begin displace. The driving mechanism of the ferroelectricity is the offset of the Fe^{3+} ions within the oxygen cage octahedra. The ferroelectric dipole will be reduced and eventually removed, as these bonds converge together, as the driving force of this is the off centring of the Bi, with the ferroelectricity caused by its stereoactive lone pair. As the octahedra reorient due to the loss of Fe^{3+} displacement, and become more regular, so too does the central Bi^{3+} ion, leading to a non-polar cell.

Similarly to $BiFeO_3$, the sample of $Bi_{0.95}Dy_{0.05}FeO_3$ shows a loss of anti-ferromagnetism at approximately 633K, suggesting a similar Néels temperature although the T_N indicated is slightly higher than the parent $BiFeO_3$, however these findings are consistent with other studies into RE doped materials. (29) This has been confirmed by an anomaly in the dielectric data, and can also be seen in Figure 3.13, which shows the loss of the magnetic Bragg peaks associated with the spin cycloid as the temperature was increase, until almost complete loss of intensity at 673K.

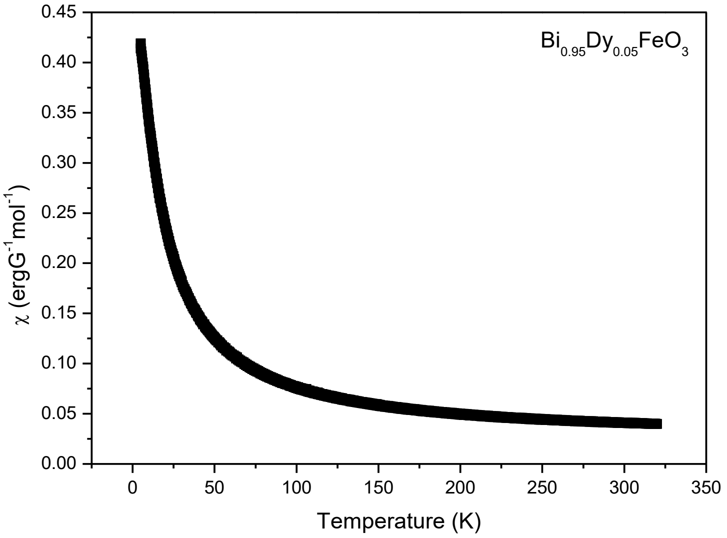

Figure

Figure 3.13: *SQUID data for $Bi_{0.95}Dy_{0.05}FeO_3$ showing ZFC/FC data*

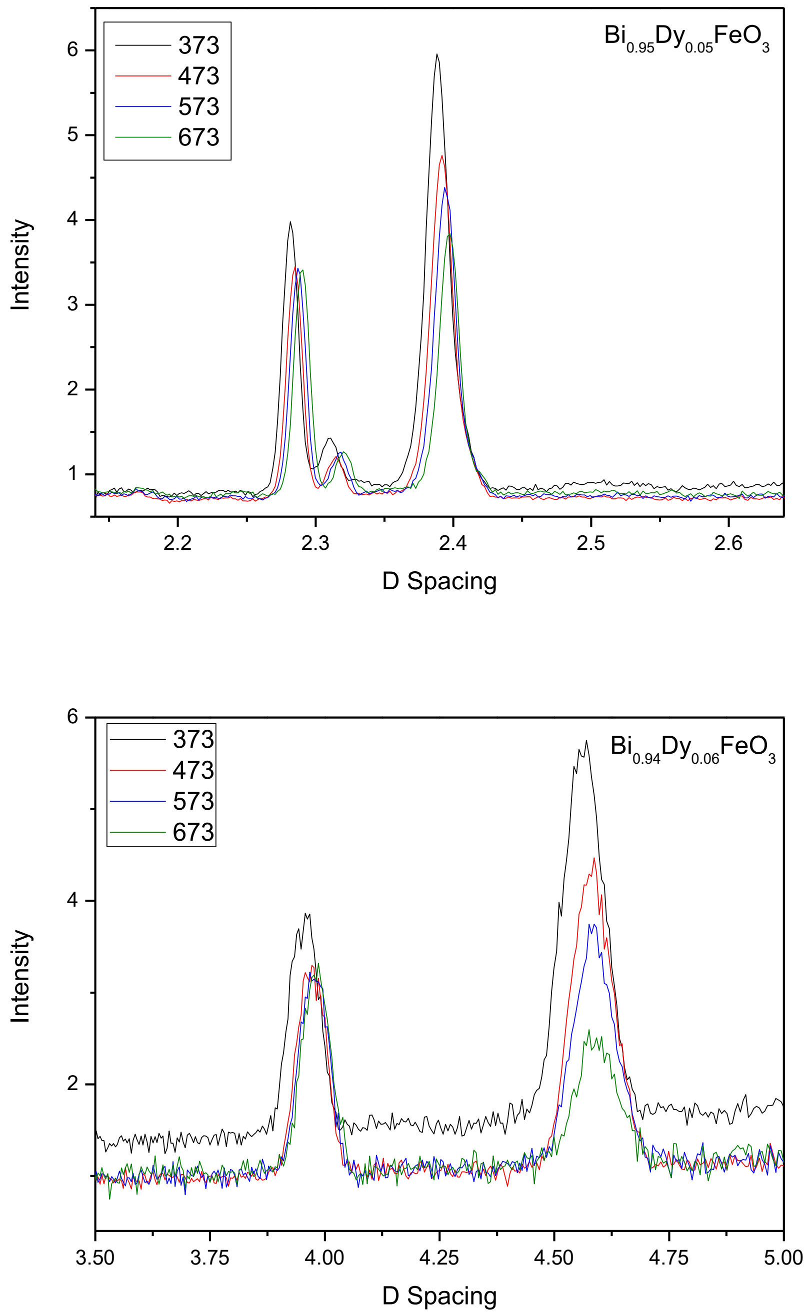

Figure 3.14: *Zoomed in PND data for $Bi_{0.95}Dy_{0.05}FeO_3$ shows the loss of the Magnetic Bragg peaks at 2.4Å and 4.6Å as temperature increase. This indicates the anti-ferromagnetic to paramagnetic phase transition.*

Below this transition, magnetic field dependence data was collected for $Bi_{0.95}Dy_{0.05}FeO_3$ at room temperature, and showed evidence of weak ferromagnetism. Suggestions in the literature that influenced this study has been that the substitution of Dy^{3+} for Bi^{3+} can lead to modification of the parent G-type cycloid to give canted magnetic spins, that may lead to a small but measurable magnetic moment, as suggested by the weak ferromagnetic moment found in the SQUID response. (3,17,30,31)

The remnant magnetisation was determined to be 0.039 emu/g and 0.035 emu/g for 120K and 300K respectively, values comparable to existing wok (16,17,30) Zero field cooled (ZFC)/Field cooled (FC) measurements taken between 5 and 300K showed a clear Curie tail, with no evidence of variation between the ZFC and FC data. This confirms that anti-ferromagnetism is retained.

Further investigation into the magnetic structure of this weak ferromagnetic character can come from considering the magnetic Bragg reflection seen in $BiFeO_3$. Comparison between $BiFeO_3$ and $Bi_{0.95}Dy_{0.05}FeO_3$ shows peaks of similar position and intensity, which would imply that the characteristic G-type spin cycloid is preserved.

One mechanism that could lead to the formation of a weak ferromagnetic moment within the structure is the formation of a small amount of parasitic Fe_2O_3 phase during synthesis; however PND structural data offers no evidence of any impurity phases.

Studies into $CaMnO_3$ perovskites also show the formation of ferromagnetic clusters which yield a small remnant magnetisation. This is a possibility, and the ferromagnetism seen in the $Bi_{0.95}Dy_{0.05}FeO_3$ sample could be caused by the product of canted anti-ferromagnetic or ferromagnetic polar nano-regions within the crystal structure.(32) This would account for the SQUID response whilst retaining the long range cycloid. If this was the case, it would suggest regions of cation concentration, leading to Dy^{3+} rich regions and Bi^{3+} regions. The problem is that due to materials in use, it is not possible to accurately determine whether the canted regions are a product of the Dy^{3+} rich or the Bi^{3+} rich domains. This is because in all of the structural data, there is some degree of absorption, leading to peak broadening not due to the structure of the material, and inability to identify more subtle magnetic Bragg peaks. Future work could produce a more detailed study with use of either a more specialised beamline (such as WISH at the ISIS facility), or through minimisation of Dy^{3+} absorption by using less absorbing isotopes of Dy^{3+}.

3.3. $Bi_{0.70}Dy_{0.30}FeO_3$

As previously stated, lattice strain increases to a plateau at approximately x=0.14 before dropping sharply. This is consistent with the *Cc* phase losing tolerance for further addition of Dy^{3+}. Simultaneously, the cell volume and lattice parameters indicate very little further change, suggesting that no more Dy^{3+} is incident onto the lattice.

However close inspection of both the powder neutron diffraction data indicates severe anisotropic tails on some structural peaks. The inclusion of an *R3c* or *Cc* phase, which would indicate that the change in symmetries was incomplete did not improve refinement quality, or explain this broadening. The most accurate model arises by considering two different *Pnma* phases with slightly different lattice parameters, indicating that the previously suggested phase segregation of the Dy^{3+} and Bi^{3+} cations continues. However due to the mentioned absorption effects with , it was not possible to accurately determine the distribution of Dy^{3+} and Bi^{3+} cations in these phases through examination of the fractional occupancies. This phase segregation could be due to the formation of cation clusters, which support the suggestion of polar nanoregions (discussed below).

In addition the large size variance between Bi^{3+} and Dy^{3+} causes some structural instability, and this appears to cause some phase segregation within the *Pnma* phases, possibly leading to several Pnma phases alongside some remanants of the *R3c*/*Cc* phases, which would likely exhibit varying lattice constants. In contrast with the literature a single *Pnma* phase was not obtained until x=0.30.(3,5,9,17,22)

Analysis of the PND data, taken between 10 and 773K for $Bi_{0.70}Dy_{0.30}FeO_3$, initially indicated that the material is now single phase

Pnma. The material appeared to remain single phase across the temperature range, with no additional phase development at high temperature, as can be seen from the range of refinements presented in Figure 3.15 (a)-(c), although there is some addition to the background and extensive peak broadening due to Dy^{3+} absorption when compared to the $Bi_{0.95}Dy_{0.05}FeO_3$ sample.

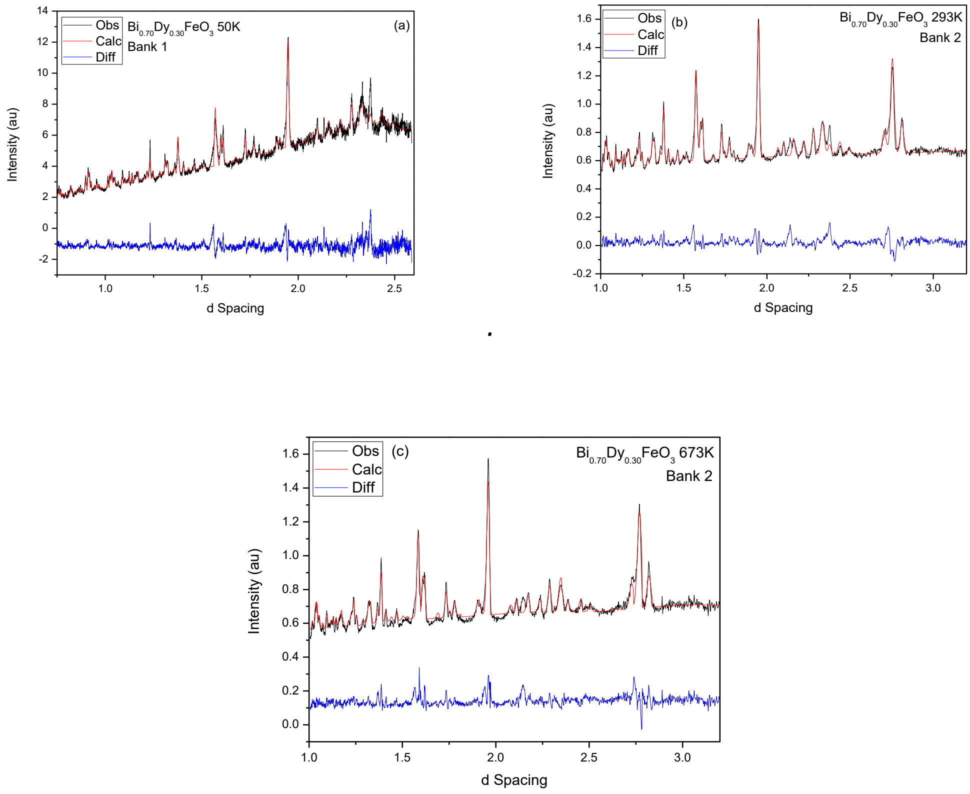

Figure 3.15: *Neutron diffraction data Rietveld refinements of $Bi_{0.70}Dy_{0.30}FeO_3$ using the Pnma structural model (a) between 0.5 and 2.6Å at 50K for Bank 1 (b) 1.0 and 3.75Å at room temperature for Bank 2 (c) 1.0 and 3.75Å at 673K for Bank 2. The refinements show no change in phase across the temperature range. The black line represents experimental data, the red line the fitted model, and the blue line the difference between the experimental and calculated profiles.*

Figure 3.16 and Table 3.2 show a steady but proportional increase in the lattice parameters with temperature, as would be expected under such a heating regime. The Fe_O bond lengths also lengthen, but indicate no further distortion of the FeO_6 octahedral cage, subsequently implying no polarisation vector, consistent with a paraelectric material.

Whilst the *Pnma* shows reasonable goodness of fit, the most accurate model arises by considering two different *Pnma* phases with slightly different lattice parameters showing a phase variance due to the distribution of the Dy^{3+} and Bi^{3+} cations. Due to absorption effects, it was not possible to accurately investigate the fractional occupancies and thus determine the exact distribution of the cations.

This may suggest that, in fact, a mixture of non-polar *Pnma* and the equivalent polar *Pn*21*a* symmetries is perhaps more appropriate, but it was not possible to differentiate between these two space groups from these data. One reason for this could be due to the “Invar effect” as studied by Kiyama et.al, who suggest that there if some invariance in the positions of the two A site cations occurs, then this can lead to their equivalent positions being offset, and can lead to the strain and subsequent distortion of the lattice.(33) This can also lead to variation in the tilt system across the lattice along the axis of the invariance. It is interesting to note for later discussion that if magnetisation also occurs along this axis, then there may be development of the magnetic dipole in polar regions rather than across the material.(9,33)

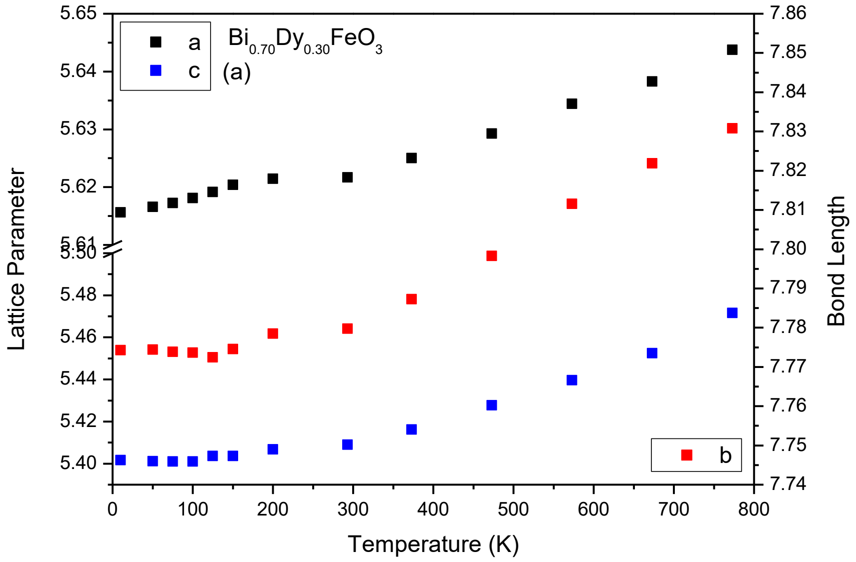

Figure 3.16: *Data extracted from Rietveld refinements to show the change in lattice parameters(extracted from the Rietveld refinement data) with temperature*

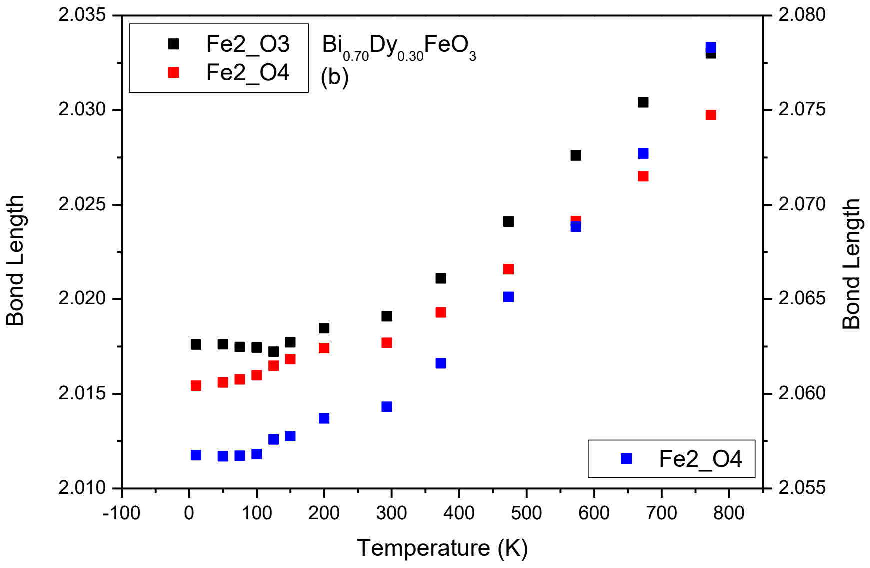

Figure 3.17: *Data extracted from Rietveld refinements to show the change in length of the Fe2-O3 and Fe2-O4 bond lengths of the Pnma phase (also extracted from the Rietveld refinements).*

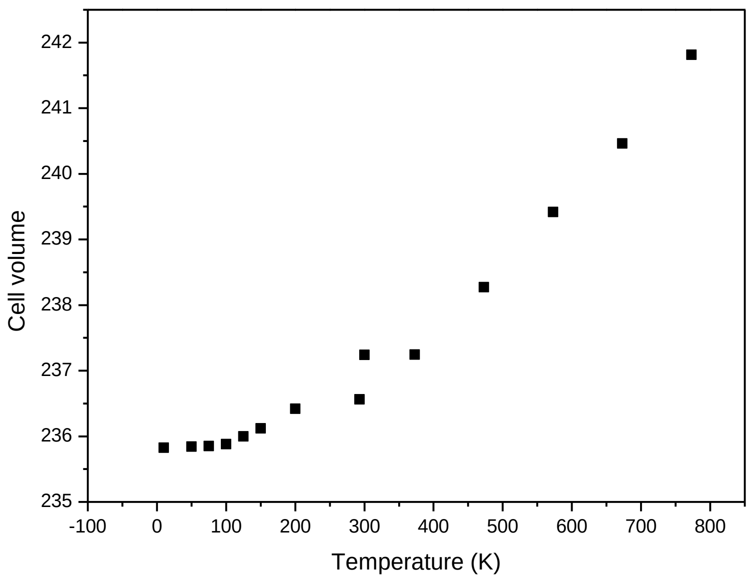

Figure 3.18: *Plot to show the change in cell volume with temperature for* $Bi_{0.70}Dy_{0.30}FeO_3$*, showing the expected expansion of the lattice as temperature increases.*

Table 3.2: *Table showing the lattice parameters, cell volume and* χ^2 *refinement parameter for* $Bi_{0.70}Dy_{0.30}FeO_3$ *refined in R3c symmetry.*

$Bi_{0.70}Dy_{0.30}FeO_3$	Phase	Lattice parameters			c/a	Cell Volume	X^2
Temp (K)		**a**	**b**	**c**			
10	*Pnma*	5.6156	7.7743	5.4017	0.96191	235.825	6.71
50	*Pnma*	5.6166	7.7744	5.4011	0.961632	235.843	4.729
75	*Pnma*	5.6173	7.7738	5.401	0.961494	235.847	4.473
100	*Pnma*	5.6181	7.7737	5.401	0.961357	235.878	4.204
125	*Pnma*	5.6191	7.7725	5.4036	0.961649	235.999	4.259
150	*Pnma*	5.6204	7.7745	5.4037	0.961444	236.119	3.621
200	*Pnma*	5.6215	7.7785	5.4067	0.96179	236.415	3.982
293	*Pnma*	5.6258	7.7858	5.4163	0.962761	237.084	3.476
300	*Pnma*	5.6217	7.7797	5.409	0.962164	237.237	9.01
473	*Pnma*	5.625	7.7872	5.4162	0.96288	237.239	7.085
573	*Pnma*	5.6293	7.7983	5.4277	0.964187	239.887	6.377
673	*Pnma*	5.6344	7.8116	5.4396	0.965427	240.226	5.731
773	*Pnma*	5.6437	7.8308	5.4716	0.969506	241.373	9.098

The Raman spectra collected for $Bi_{0.70}Dy_{0.30}FeO_3$ contains very broad peaks, consistent with other studies into $Bi_{1-x}RE_xFeO_3$ materials which occupy the *Pnma* symmetry similar to observations by Bielecki *et al.* for Tb^{3+} and Sm^{3+} doped $BiFeO_3$ ceramics.(34) [Figure 3.19].

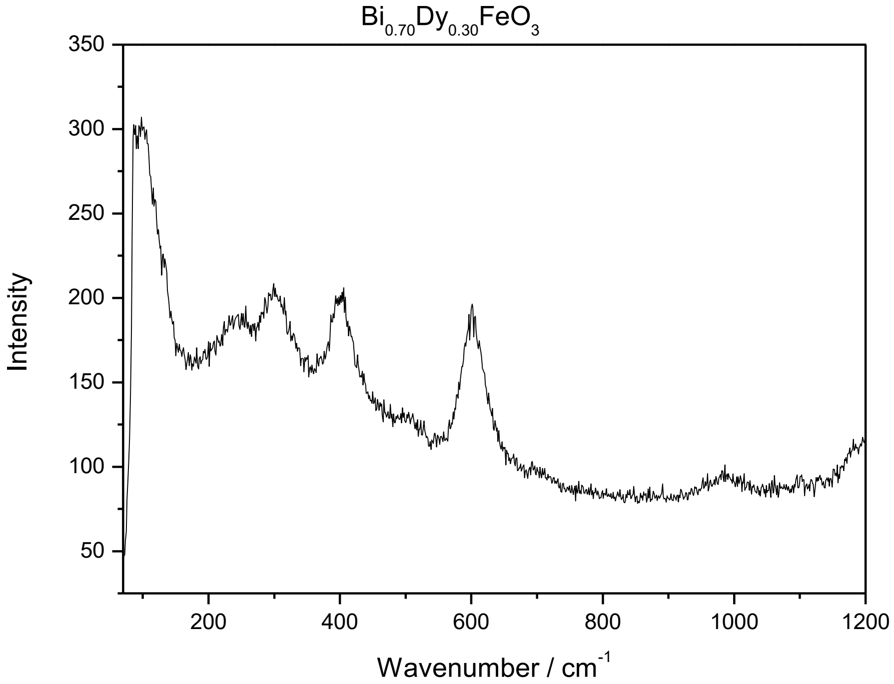

Figure 3.19: *Single point Raman data taken using a 633nm laser at 77K for* $Bi_{0.70}Dy_{0.30}FeO_3$*. Data is consistent with the structure of other rare earth orthoferrites.* *(12)*

Low temperature electrical data collected for $Bi_{0.70}Dy_{0.30}FeO_3$ indicates some frequency dependence at ~100K, which may warrant further investigation, and could be linked to the formation of the polar nano-region as this behaviour can be seen in other studies of Rare Earth doped orthoferrites.(28,35)

Electrical data again displays an anomaly between 675-700K, and as is consistent with previous data this could link to the transition from anti-ferromagnetic to paramagnetic nature.

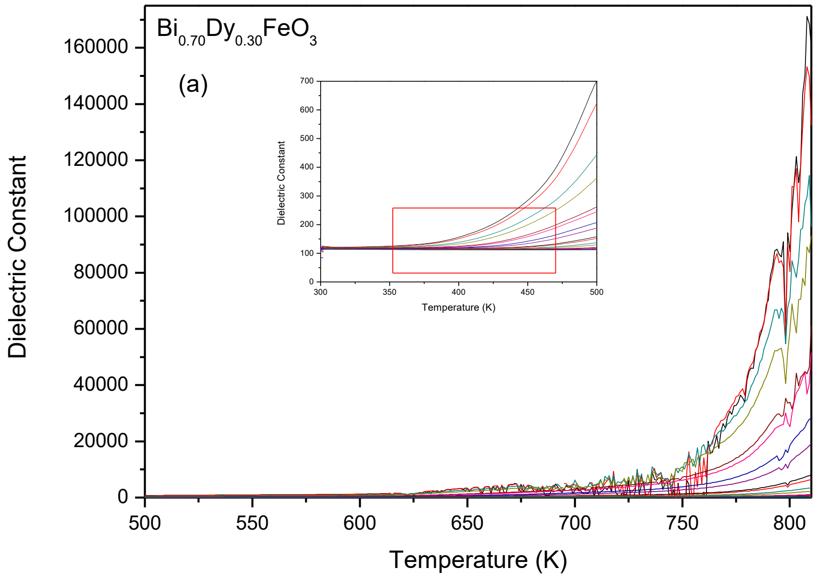

Figure 3.20: *Graph of dielectric data still suggests that the anti-ferromagnetic to paramagnetic phase transition occurs at ~675K, despite the change in Dy^{3+} content.*

Magnetisation data, collected by SQUID, shows a more enhanced ferromagnetic moment then that discussed for $Bi_{0.95}Dy_{0.05}FeO_3$. Remnant magnetisations of 0.548emu/g and 0.367emu/g were recorded for 120 and 300K, although the hysteresis loops did not fully saturate within the range of voltages applied. This suggests the possibility of discrete regions of Dy^{3+} and Bi^{3+} cations, which have become more pronounced with the increase in Dy^{3+} content, but that there is no long range order within the material, as this would lead to saturation of the hysteresis loop.

Another suggestion to evidence the presence of weak ferromagnetism can be seen in Figure 3.21 (b),(c) which show that detection of magnetic Bragg peaks within the material, followed by their loss above 673K, which is consistent with the suggested value of the Néels temperature. This structural data also shows that there was no indication of a parasitic Fe_2O_3 phase in the structural data, and the presence of an impurity seems highly unlikely.

However, the chance of a parasitic phase cannot be completely ruled out due to the high background contribution in the PND resultant from the large Dy^{3+} content causing absorption. As stated previously, this magnetisation could be due to the Invar effect, which would imply that the development of the magnetic dipole is due to polar regions within the material rather than long range ordering across the material.(9,33)

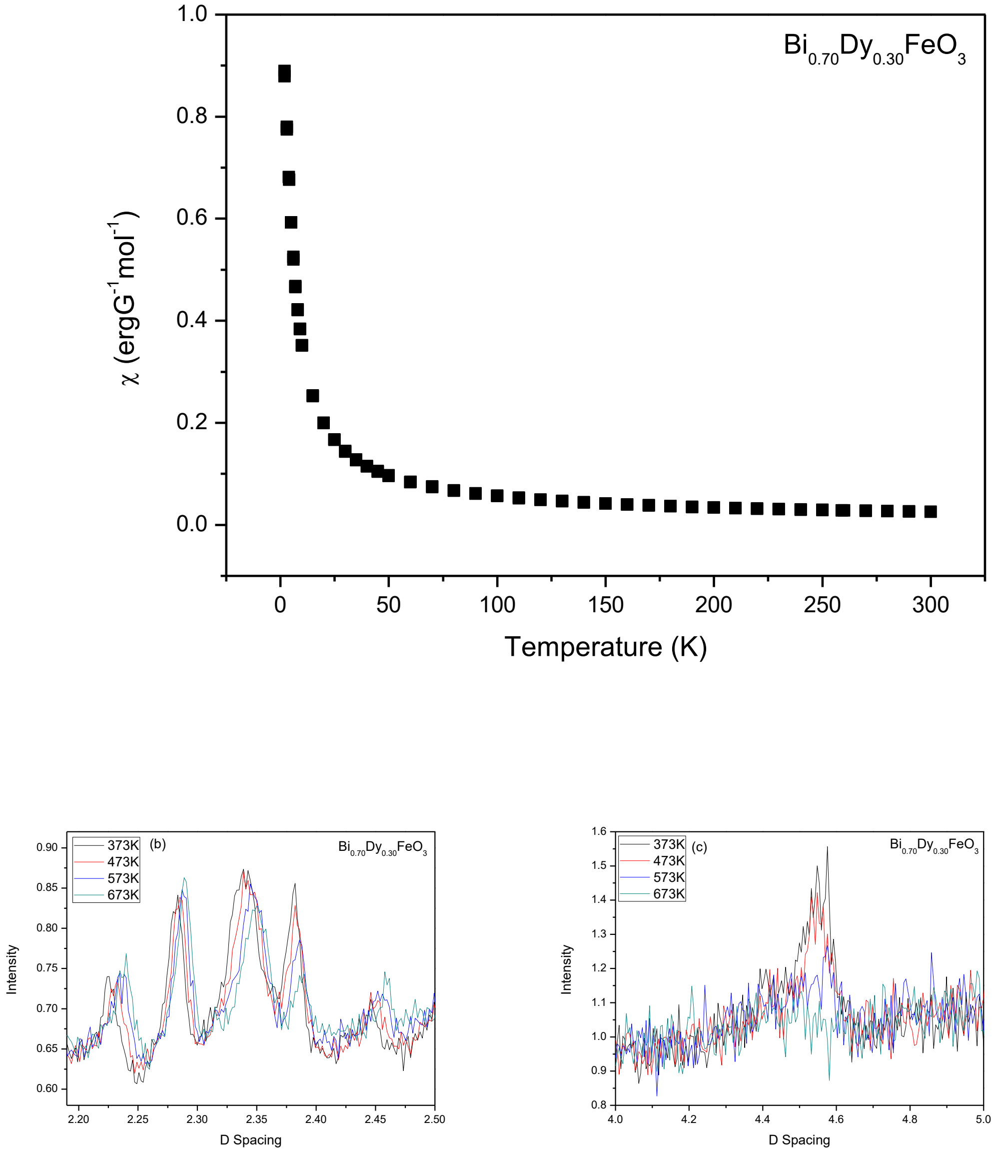

Figure 3.21: *SQUID data for $Bi_{0.70}Dy_{0.30}FeO_3$ showing (a) ZFC/FC data. and zoomed in PND (b), (c) still suggest that the anti-ferromagnetic to paramagnetic phase transition occurs at ~675K, despite the change in Dy^{3+} content*

3.4. Conclusions

In summary, this chapter reports the changing structure of $Bi_{1-x}Dy_xFeO_3$ as Dy^{3+} content increases. There is an observed, composition driven phase transition from polar *R3c* to polar Cc to non-polar *Pnma* with a broad phase coexistence between $0.05 < x < 0.30$, which has proved difficult to fit to either model accurately. The work done so far has lead to the proposal of the phase diagram outlined in Figure 3.22.

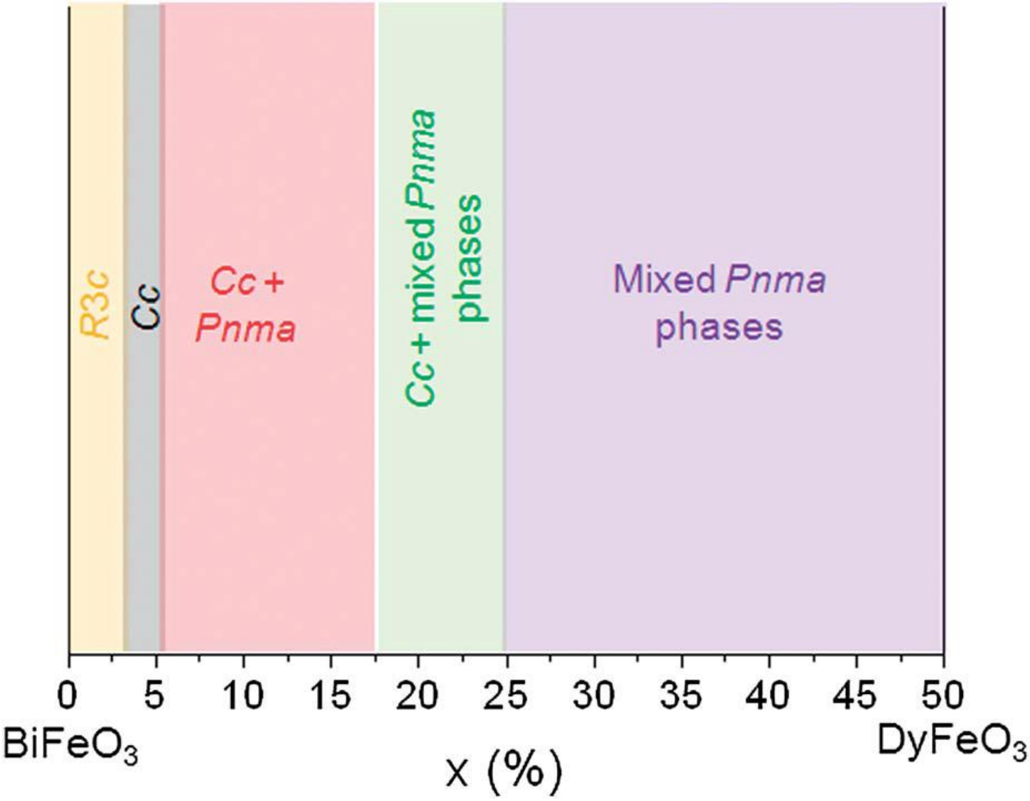

Figure 3.22: *Proposed phase diagram for $Bi_{1-x}Dy_xFeO_3$ based on collection of all of the structural data.*

The increase in background and high concentration of Dy^{3+} absorption made some of the high temperature refinements to also become problematic, and further study could try to circumvent this by use of alternative, less absorbing isotopes of Dy^{3+} in future compositions. Another way to eliminate the issue of Dy^{3+} absorption would be to repeat the variable temperature study, but using synchrotron radiation. This would however also present some issues from absorption, as Bi^{3+} absorbs synchrotron radiation.

However it would be possible to tune the wavelength of the incident radiation away from the Bi^{3+} absorption edge.

Since this work, symmetry mode analysis has suggested that there may also be another phase transition previous to the change to *Pnma*, and it has been reported that at x=0.03 there is a transition to polar Cc. (35) As stated above, further diffractions study could try and reduce absorption and allow better resolution of the structural peaks, giving a clearer idea of the phase.

Dielectric constant measurements for $Bi_{0.95}Dy_{0.05}FeO_3$ were unreliable due to non-ohmic electrode effects, whilst $Bi_{0.70}Dy_{0.30}FeO_3$ showed possible low temperature relaxor like behaviour. The ohmic effects seen for $Bi_{0.95}Dy_{0.05}FeO_3$ could be overcome by improving the density of the pellets used for the impedance analysis or possible the use of a different electrode material and mechanism other than platinum sputtering.

Lack of accurate dielectric data makes it difficult to determine polar Cc phase, and whilst structural data confirms *Pnma*, use of PDF or EXAFS to more thoroughly probe the local environment of the sample could provide a more detailed view of the structure. This would also help determine if there was a domain structure within the material. This could be backed up by the use of atomic force microscopy or piezo force microscopy, which would also allow the imaging of any existing ferroelectric domains within materials of a low Dy^{3+} content. (Such as $Bi_{0.95}Dy_{0.05}FeO_3$).

Confirmation of the local area environment would help establish whether the weak ferromagnetic observed was caused by the likely formation of small magnetic clusters within the material, and would determine which cation was responsible for these magnetically rich areas, although it is likely due to the presence of Fe^{3+}.

Magnetic data for $Bi_{0.95}Dy_{0.05}FeO_3$ suggests that the G-type anti-ferromagnetic spin cycloid is retained alongside the weak ferromagnetism. In the $Bi_{0.70}Dy_{0.30}FeO_3$ sample, there is some suppression of the spin cycloid. Both materials exhibit a magnetic transition between 657-700K, which is consistent with the parent $BiFeO_3$ (633K) and indicates only a slight change in Néels temperature.

The magnetic study could be enhanced by the collection of further data on a more specialised beamline (such as WISH), however some steps would need to be taken to minimise Dy^{3+} absorption. Again, this could be done through the use of less absorbing isotopes of Dy^{3+}.

This study shows that despite needing a number of techniques to begin understanding the complex structures within $Bi_{1-x}Dy_xFeO_3$, it yield some interesting properties that warrant further consideration and study. The initial results shown indicate that the composite $Bi_{1-x}Dy_xFeO_3$ material has some interesting properties. As well as the previously mentioned use of a variable temperature study using synchrotron radiation, there is much potential that could be gained from further investigation into the crystal environment. An investigation using surface second harmonic generation (SHG) would be able to conclusively determine when the initial R3c/Cc phase becomes non-centrosymmetric (therefore losing polarity). Similarly, Mossballer Spectroscopy or EXAFS techniques could be used to probe the local environment of the Fe^{3+} within the octahedra and give a clearer indication of the mechanism that is responsible for the loss of ferroelectricity. Additionally specific studies into the magnetic characteristics using instruments such as the WISH beamline at the ISIS Neutron facility would allow a more thorough insight into the magnetic character of the material.

References

1. S. Zhang. Y. Yao, Y. Chen, D. Wang, X. Zhang, S. Awaji. K. Watanabe and Y. Ma, *J. Magn. Magn. Mater.* **2012**, 324, 2205-2210
2. V.A. Khomchenko, I.O. Troyanchuk, M.V. Bushinsky, O.S. Mantytskaya, V.Sikolenko and J.A. Paixão, *Mater. Lett*, **2011** , 65, 1970-1972
3. J. Xu, G. Wang, H. Wang, D. Ding, Y. He, *Materials Letters,* **200**9, 63, 855, 074105.
4. D.C. Arnold, K.S. Knight, F.D. Morrison and P. Lightfoot, *Phys. Rev. Lett*ers, **2009**, 102, 027602
5. A J Jacobson, B E F Fender, J*. Phys. C: Solid State Phys*. **1975**, 8 844
6. R.D. Shannon, *Acta Cryst*, **1976**, A32, 751
7. S. Zhang, W. Luo, D. Wang, T. Ma, *Mater Lett*, **2009**, 62, 1820
8. Leineweber and E.J. Mittemeijer, *J. Appl. Crystallogr.,* **2004**, 37, 123.
9. C.M. Kavanagh, R.J. Goff, A.Z. Daoud-Aladine, P. Lightfoot and F.D. Morrison, Chem. Mater. **2012**, 24, 199-208
10. A.J. Tuxworth, E.E. McCabe, D.G. Free, S.J. Clark and J.S.O. Evans, *Inorg Chem*, **2013**, 52, 2078
11. B.J. Campbell, H.T. Stokes, D.E. Tranner and D.M. Hatch, *J. Apll. Crystallogr*, **2006**, 39, 607
12. J. Hlinka, J. Pokorny, S. Karimi, I.M. Reaney, *Phys Rev B*, **2011**, 83, 020101
13. I.O. Troyanchuk, D.V. Karpinsky, M.V. Bushinsky, O.S. Mantytskaya, N.V. Tereshko, N.V. Shut, *J. Am.Ceram. Soc.* **2011**, 95, 4502
14. C. Sun, X. Cheng, J. Wang, G. Yuan, J. Yin, Z. Liu, *Solid State Commun,* **2012**, 152, 1194
15. Y. Li, J. Yu, J. Li, C. Zheng, Y. Wu, Y. Zhao, M. Wang and Y. Wang, J. Mater. Sci. **2011**, 22, 323-327
16. S. Zhang, L. Wang, Y. Chen, D. Wang, Y. Yao, Y. Ma *J. Appl. Phys.* **2012** 111, 074105

17. V.A. Khomchenko, D. V. Karpinsky, A. L. Kholkin, N. A. Sobolev, G. N. Kakazei, J. P.

18. B.N. Rao and R. Ranjan, *Phys. Rev. B: Codens. Matter Mater. Phys.,* **2012**, 86, 134103

19. S. ISOTROPY Software, http://www.iso.byu.edu

20. Sosnowska, R. Prezenioslo, A. Palewicz, D. Wardecki and A. Fitch, *J. Phys. Soc. Jpn*, **2012**, 81, 044604

21. H. Wang, C. Yang, J. Yu, M. Wu, J. Su, K. Li, J. Zhang, G. Li, T. Jin, T. Kamiyama, F. Liao, J. Lin and Y. Wu, *Inorg. Chem.* **2013**, 52, 2388

22. G. Catalan, J. F. Scott, *Adv. Mater.* **2009**, *21*, 2463.

23. R. Garg, B. Narayana, A. Senyshyn, P.S.R. Krishna and R. Ranjan, *Phys. Rev. B: Condens. Matter Mater. Phys.,* **2013**, 88, 014103

24. J.W. Kim, C.M. Raghavan, H.J. Kim, Y.J. Kim, K.W. Jang, S.S. Kim *J. Korean Phys. Soc.* **2012**, 61, 6, 903-907

25. D.C. Arnold, K.S. Knight, G. Catalan, S.A.T. Redfern, J.F. Scott, P. Lightfoot and F.D. Morrison, Adv. Funct. Mat., **2010**, 20, 2116-2123

26. R. Palai, R. S. Katiyar, H. Schmid, P. Tissot, S. J. Clark, J. Robertson, S. A. T. Redfern, J. F. Scott, *Phys. Rev. B.*, **2008**, *77*, 014110.

27. M. Li, A. Feteira, D. C. Sinclair, *J. Appl. Phys.* **2009**, *105*, 114109.

28. M. Li, D.C. Sinclair, A.R. West, *J Appl Phys*, **2011**, 109, 084106

29. V.A. Khomchenko, I.O. Troyanchuk, M.V. Bushinsky, O.S. Mantatyskata, V. Sikolenko, J.A. Paixao, *Material Letters*, **2011**, 65, 1970

30. P. Uniyal, K. L. Yadav, *J. Phys.: Condens. Matter.*, **2009**, *21*, 012205

31. S. Zhang, W. Luo, D. Wang, Y. Ma, *Materials Letters* **2009**, *63*, 1820.

32. P. Thompson, D.E. Cox, J.B. Hastiongs, *J Appl Cryst*, **1994**, 27, 892

33. J. Xu, G. Wang, H. Wang, D. Ding and Y. He, *Mater. Lett.,* **2009**, 63, 855

34. W.M. Zhu, L.W. Su, Z.G. Ye, W. Ren, *Appl Phys Lett*, **2009**, 94, 142908

35. R.C. Lennox, M.C. Price, W. Jamieson, M. Jura, A. Daoud-Aladine, C.A. Murray, C. Tang, D.C. Arnold, *J. Mater. Chem. C*, **2014**,2, 3345-60

36. S.K. Barber, S. Jangid, M. Roy, F.C. Chou, *Ceramics International*, **2013**, 39, 5359

37. J. Hlinka, J. Porkorny, S. Karimi, I.M. Reaney, *Phys Rev B*, **2011**, 020101

38. C. Sun, Y. Wang, Y. Yang, G. Yuan, J. Yin, Z. Liu *Mat. Lett.* **2012** 72, 160-163

39. J. Wang, J.B. Neaton, H. Zheng, V. Nagarajan, S.B. Ogale, B. Liu, D. Viehland, V. Vaithyanathan, D.G. Schlom, U.V. Waghmare, N.A. Spaldin, K.M. Rabe, M. Wuttig and R.Ramesh *Science*, **2003**, 229, 1719-1722

40. M. Mostovoy *arXiv:cond-mat/0510692v1*

41. V.V. Ivanova, V.V. Gagulin, S.K. Korchagina, Yu.A. Shevchuk and V.V. Bogatko, Inorg. Mater. **2003**, 39, 7, 745-748

42. V.A. Khomchenko, J.A. Paixão, D.A. Kiselev and A.L. Kholkin, Mater. Res. Bull. **2010**, 45, 416-419

43. O.E. González-Vázquez, J.C. Wojdel, O. Diéguez and J. Íniguez, Phys. Rev. B. **2012**, 85, 064119

44. J. Wei, R. Haumont, R. Jarrier, P. Berhtet and B. Dkhil, App. Phys. Lett. **2010**, 96, 102509

45. F.Z. Qian, J.S. Jiang, S.Z. Guo, D.M. Jiang and W.G. Zhang, J. Appl. Phys. **2009**, 106, 084312

46. Levin, M.G. Tucker, H. Wu, V.Provenzano, C.L. Dennis, S. Karimi, T. Comyn, T. Stevenson, R.I. Smith, I. M. Reaney, *Chem Mater*, **2011**, 23, 2166

47. J. Bielecki, P. Svedlindh, D.T. Tibebu, S. Cai, S.G. Eriksson, L. Borjesson, C.S. Knee, *Phys Rev B*, **2012**, 86, 184422

48. Y. Wang, Y. Su, X. Wang, W. Su, X. Lui, *J Appl Phys*, **2010**, 108, 063928

49. B. Rajeswaran, D. Sanyal, M. Chakrabarti, Y. Sundarayya, A. Sundaresan, C.N.R. Rao, *Europhys Lett*, **2013**, 101 , 17001

50. J. Bielecki, P. Svendlich, D.T. Tibebu, S. Cai, S.G. Eriksson, L. Börjesson, C.S. Knee, *Phys Rev B*, **2012**, 86, 184422

51. T. Kiyama, K. Yoshimura, K. Kosuge, Y. Ikeda, Y. Bando. *Phys Rev B Condens Matter.*, **1996**, 54, 756-759.

Chapter 4: Investigation of Bismuth Ferrite and Potassium Niobate co-doped materials.

As previously described, the solid-solution between $BiFeO_3$ and $KNbO_3$ [Figure 4.1] has so far been somewhat overlooked despite the fact that the combination of these two materials can result in generation of an ideal ionic lattice (by considering Goldschmidt’s tolerance factor). Similar to PZT, the addition of doping with K^+ and Nb^{5+} to the $BiFeO_3$ lattice leading to an increase the tolerance factor (towards the K^+ rich end) with the potential for the discovery of a similar MPB with enhanced multiferroic properties being located. Existing studies have already reported weak FE and FM in materials with composition where x is low. (1)

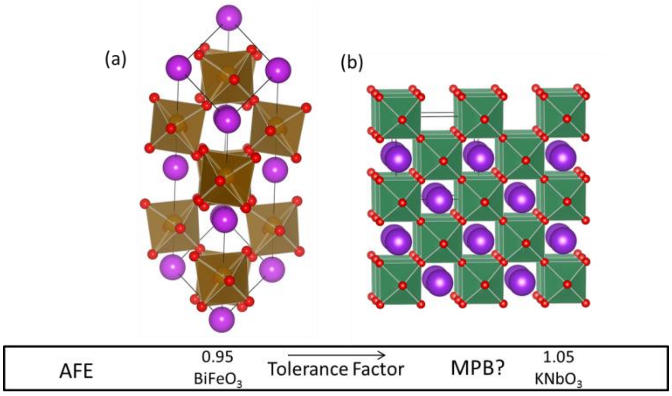

Figure 4.1: *Schematic representations of (a) $BiFeO_3$ in the R3c space group, where the brown squares represent the FeO_6 octahedra, the purple spheres represent the Bi3+ A site cation, and the and the red spheres represent Oxygen ions. (b) KNbO3 in the Amm2 setting, with the green squares representing NbO6 octahedra, the purple sphere again representing the A site cation (K+) and the red spheres denoting oxygen ions. The box below shows the trend of the tolerance factor and the potential location of morphotropic phase boundaries within the solid solution.*

This study examines the compound $Bi_{1-x}K_xFe_{1-x}Nb_xO_3$ across the entire range of the solid solution, from x=0.00 ($BiFeO_3$) to x=1.00 ($KNbO_3$). The full evolution of the phase diagram is shown in Figure 4.3, represented using synchrotron radiation at the I11 instrument (Diamond Light Source UK) and powder neutron diffraction data collected at the HRPD instrument of the ISIS Neutron facility. There is no x=0.30 sample shown in Figure 4.3, as there was an issue with the sample composition found in initial X-ray data. The sample appeared to have a much lower $KNbO_3$ content than expected, due to loss of K= ions in the sintering process, similar to the phenomena reported by Masude et.al. (2) who see a massive loss of potassium in synthesis. This is consistent with refinement data (Table 4.1), which generally reports lower K+ content than expected.

4.1. Preliminary Structural Analysis $Bi_{1-x}K_xFe_{1-x}Nb_xO_3$

$Bi_{1-x}K_xFe_{1-x}Nb_xO_3$ materials were prepared across the whole range of the solid solution with increments of x=0.10. Powder X-ray diffraction data was used to confirm that materials appear to contain no impurity phases [Figure 4.2]. Materials below x=0.10 show a good fit to the rhombohedral *R3c* phase characteristic to the parent $BiFeO_3$, with samples in excess of x = 0.10 showing a tendency towards more pseudo-cubic phases, whilst materials at the other end of the solution in excess of x=0.90 characterise as orthorhombic *Amm2*, which is consistent with other studies of $KNbO_3$.(3.4,5)

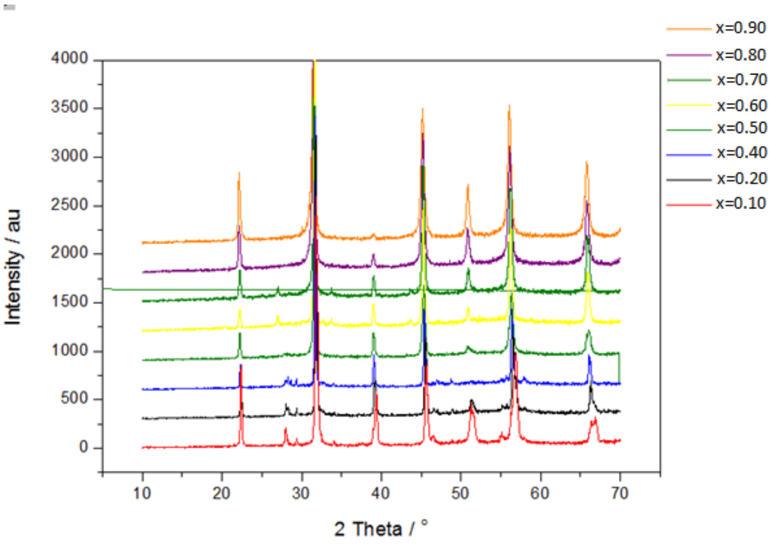

Figure 4.2: *Room temperature X-ray diffraction data showing a cross section of the development of the phases as $KNbO_3$ content changed within the material across the studied range of $Bi_{1-x}K_xFe_{1-x}Nb_xO_3$ materials. (x=0.00-1.00)*

Once purity was confirmed, powder neutron diffraction and synchrotron diffraction were carried out to allow further explanation of the structural progression across the solution. Initial synchrotron analysis shows a shift in peak position due to increasing lattice parameters [Figure 4.2]. This is consistent with expectations, as K^+ is significantly larger than Bi^{3+}, (1.51 and 1.17 Å respectively), there is very little contribution from the B site cations, as they are similar in size (Fe^{3+}, 0.645 Å and Nb^{5+} 0.640 Å).(6)

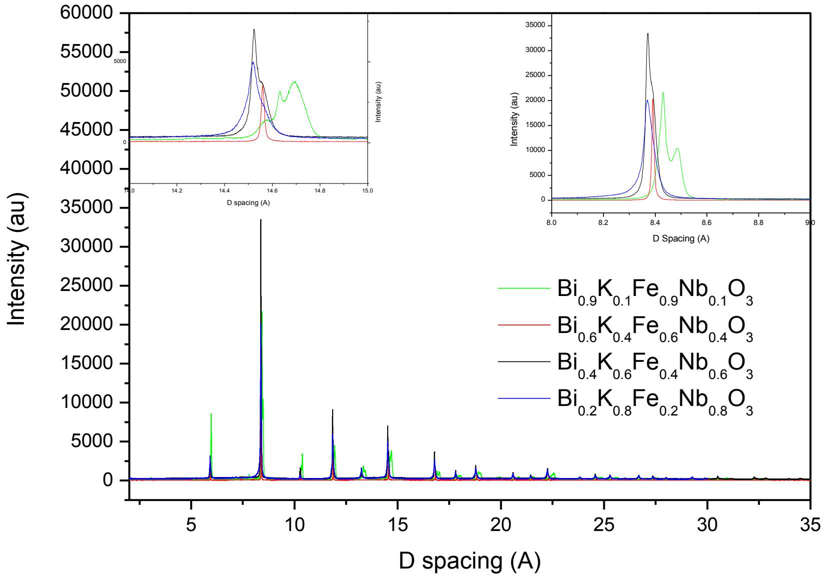

Figure 4.3: *Synchrotron diffraction patterns collected for* $Bi_{1-x}K_xFe_{1-x}Nb_xO_3$ *materials with x = 0.1, 0.4, 0.6 and 0.8 with the insets showing the shift in peak position and thus lattice parameters with increasing values of x. (note, not all data show for ease of comparison)*

Table 4.1: *Synchrotron data showing refinement data for all fit carried out across the solid solution.*

$Bi_{1-x}K_xFe_{1-x}Nb_xO_3$	x	0.1	0.2	0.4	0.5	0.6	0.7	0.8
Phase		R3c	R3c	P4mm	P4mm	P4mm	P4mm	P4mm
Lattice parameters	a	5.600	5.883	4.000	4.004	4.010	4.006	4.009
	b	5.600	5.883	4.000	4.004	4.010	4.006	4.009
	c	13.840	13.761	3.998	3.997	3.995	4.010	4.001
Tetragonality (c/a)		2.471	2.339	0.999	0.998	0.996	1.001	0.998
M-O	1	2.079	2.071	1.863	2.235	1.917	2.234	2.236
	2	2.007	2.012	2.135	2.262	2.022	2.276	2.264
	3			2.004	2.019	2.019	2.018	2.021
Cell Volume		376.02	375.89	63.98	64.08	64.24	64.350	64.301
R(A cation)		1.379	1.408	1.466	1.495	1.524	1.553	1.582
R(Bcation)		0.645	0.644	0.643	0.643	0.642	0.642	0.641
Tolerance factor		0.961	0.971	0.992	1.002	1.013	1.023	1.033

Current synchrotron refinement data strongly suggest that some of these $Bi_{1-x}K_xFe_{1-x}Nb_xO_3$ materials are inhomogeneous and potentially composed of multiple phases with multiple lattice parameters. Despite this, initial refinements allow an estimation of the predominant phase as composition changes between $0.10 \leq x \leq 0.90$, along with an indication of where the phase transitions between these primary phases occur. Between $0.10 \leq x \leq 0.30$ materials have a primarily *R*3*c* composition (parent $BiFeO_3$ phase), with some developing *P4mm* symmetry. There is then a region of single phase *P*4*mm* between $x = 0.40$ and 0.50. Above $x = 0.50$ a mixture of phases with *P*4*mm* and *Amm*2 symmetries is observed (as the material approaches the parent $KNbO_3$ phase).(7)

Data extracted from Rietveld refinement and presented in Figure 4.4, shows that both cell volume and lattice parameters both decrease across the solid solution, with the a and c parameters converging to similar values as *x* increases, showing a tendency towards cubic symmetry. The M-O bonds for the B site cation also initially converge for compositions from $0.2 > x > 0.5$, suggesting a loss of any displacement of the B site ion. There is then some divergence in the bond lengths as *x* increases, and transitions to the *Amm2* phase, which is to be expected as this would lead to the formation of electric dipoles within the lattice, and *Amm2* is a polar phase.

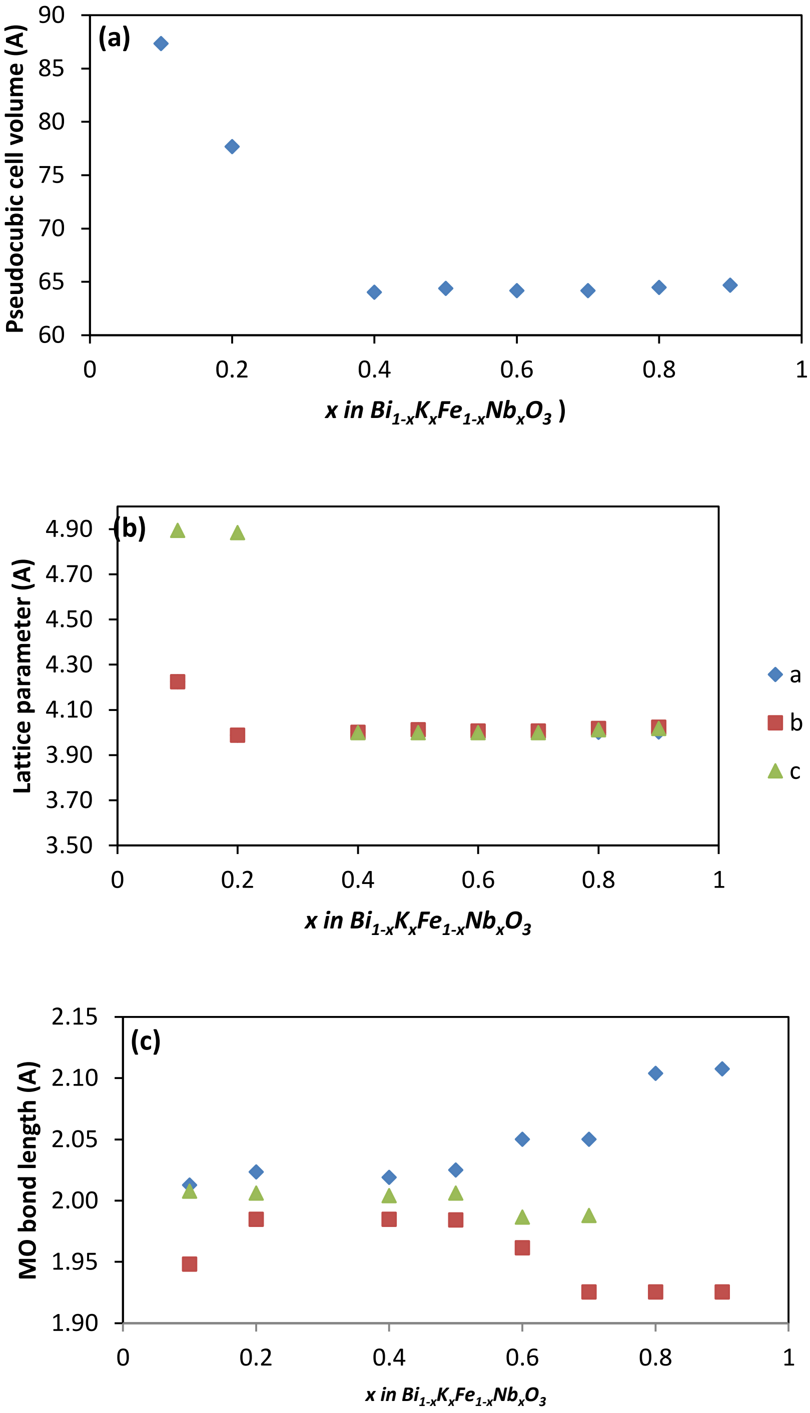

Figure 4.4: *(a) Pseudo-cubic cell volume, (b) pseudo-cubic lattice parameters and (c) Fe/Nb-O bond length (d) Tetragonality (a/c parameters) as a function of x in* $Bi_{1-x}K_xFe_{1-x}Nb_xO_3$ *materials.*

Data from the ISIS Neutron facility collected on the HRPD instrument gives a much stronger correlation to the suggested phase diagram, and shows a clear progression from $BiFeO_3$ like *R*3*c* to *P*4*mm* ending with a $KNbO_3$ like *Amm*2 phase, each phase being consistent with the primary phase in the previously discussed synchrotron data.

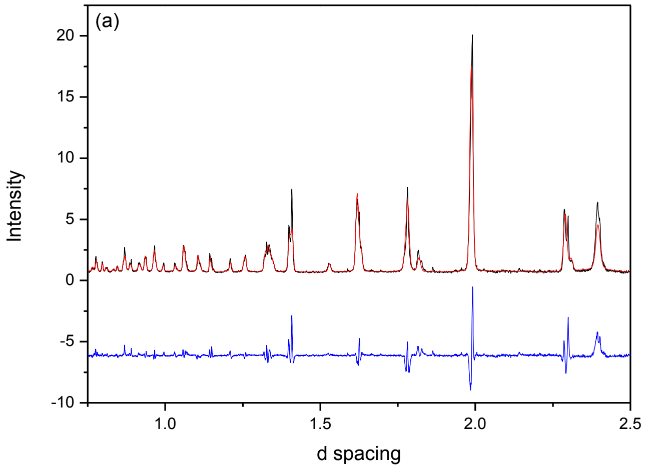

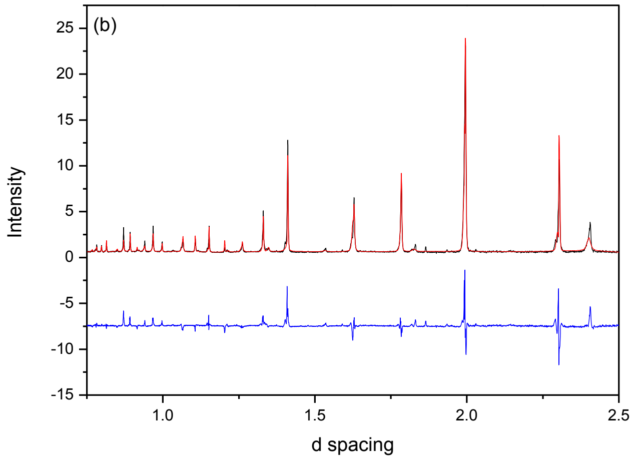

Figure 4.5: *Powder Neutron diffraction data showing a cross section of the development of the R3c phase as* $KNbO_3$ *content changed within the material across the studied range of* $Bi_{1-x}K_xFe_{1-x}Nb_xO_3$ *materials. (x=0.10-0.20) This data was obtained from the HRPD high resolution instrument and all reading shown were taken at room temperature. The black line indicated the experimental data, whilst the red line indicates the difference between the experimental data, and calculated structural model x= (a) 0.10 (b) 0.20*

Table 4.2: *Powder Neutron Diffraction data showing refinement data for all fit carried out using R3c symmetry.*

Bi1-xKxFe1-xNbxO3	x	0.1	0.2
Phase		R3c	R3c
Lattice parameters	a	5.974500	5.639550
	b	5.974500	5.639550
	c	13.84000	13.76100
Tetragonality (a/c)		0.431636	0.408247
M-O	1	2.112750	2.023540
	2	1.948170	1.984850
Cell Volume		375.573	380.488
R(A cation)		1.379	1.408
R(Bcation)		0.645	0.644
Tolerance factor		0.96114	0.971407

Tolerance factor (t) gives a good indication of the stability of the lattice, and indicate how distorted a perovskite material has become. If t=1.0, then then material will have a cubic lattice and show no polarity. As t decreases to below 1, the material becomes less cubic, and is likely to show distorted ferroelectricity, whilst values of t in excess of 1 will likely show displacive ferroelectric characteristics (see Chapter 1, 1.1.3.).(6) Calculation of the tolerance factors shows that across the $Bi_{1-x}K_xFe_{1-x}Nb_xO_3$ solid solution, there is an increase in stability initially as $KNbO_3$ is doped onto the lattice the initial tolerance factor calculated for $BiFeO_3$ is 0.961, which tends towards a more stable structure, with the most stable structure predicted to be at a composition of x=0.50 (with a value of 1.002) before again moving away to a less stable structure with a maximum tolerance factor at the other end of the solid solution when x=1.0 ($KNbO_3$ with a value of 1.043). This shows some similarity to the work carried out by Nakashima et.al (8), although they report that rather than a pseudo-cubic tetragonal system, the addition of $KNbO_3$ drives the lattice cubic between x=0.30-0.70. Data reported in Figure 4.4 shows however, that the a/c ratio never reaches unity, and begins to tend away from cubic at values of x beyond 0.5. This would suggest that the material remains tetragonal throughout this region.

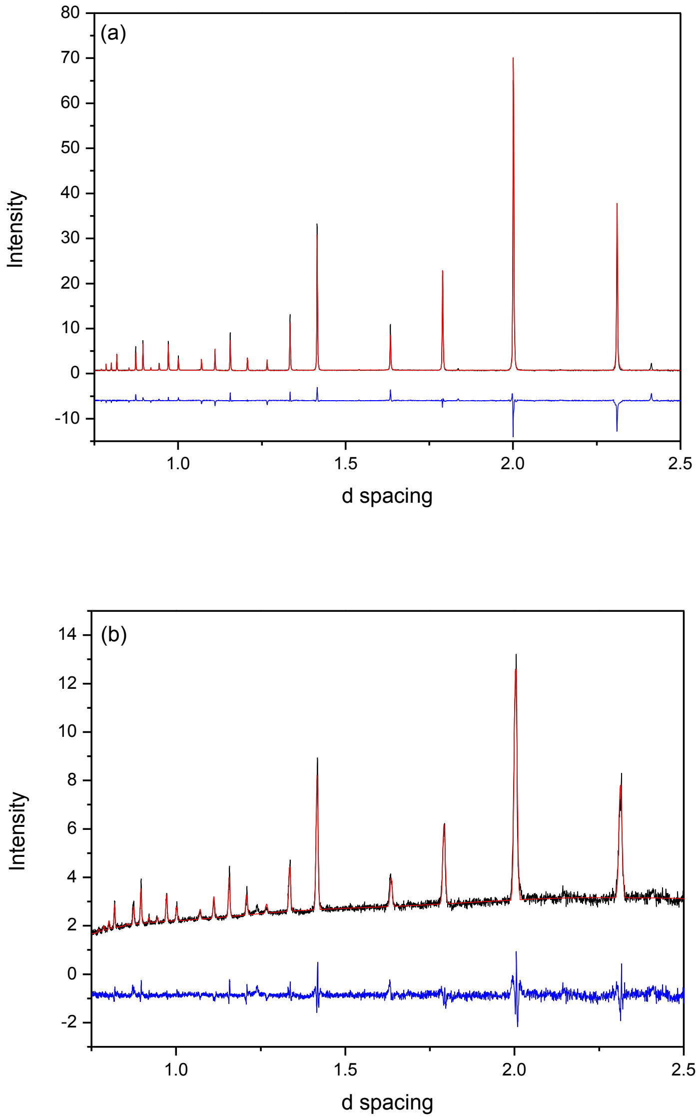

Figure 4.6.1: *Powder Neutron diffraction data showing the development of the P4mm phase as* $KNbO_3$ *content changed within the material across the studied range of* $Bi_{1-x}K_xFe_{1-x}Nb_xO_3$ *materials. (x=0.30-0.70) This data was obtained from the HRPD high resolution instrument and all reading shown were taken at room temperature. The black line indicated the experimental data, whilst the red line indicates the difference between the experimental data, and calculated structural model x= (a) 0.40 (b) 0.50*

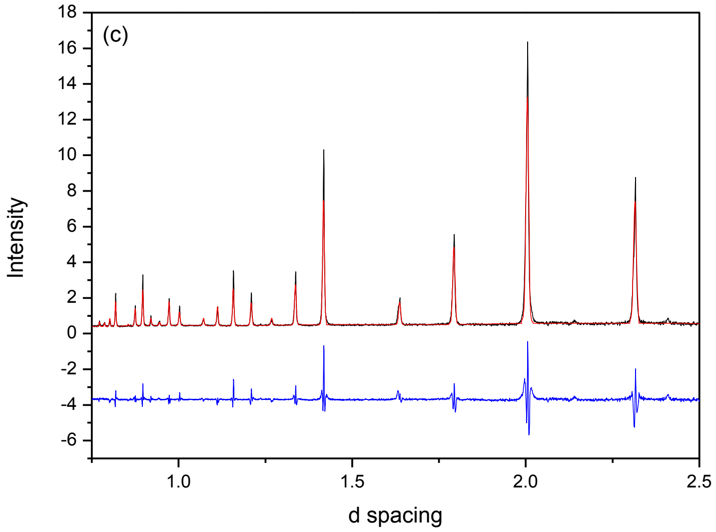

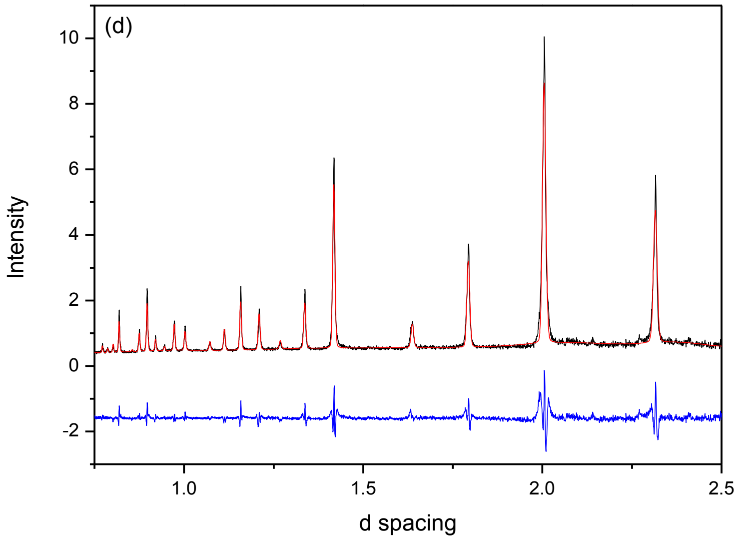

Figure 4.6.2: *Powder Neutron diffraction data showing the development of the P4mm phase as* $KNbO_3$ *content changed within the material across the studied range of* $Bi_{1-x}K_xFe_{1-x}Nb_xO_3$ *materials. (x=0.30-0.70) This data was obtained from the HRPD high resolution instrument and all reading shown were taken at room temperature. The black line indicated the experimental data, whilst the red line indicates the difference between the experimental data, and calculated structural model (c) 0.60 (d) 0.70*

Table 4.3: *Powder Neutron Diffraction data showing refinement data for all fit carried out using P4mm symmetry.*

Bi1-xKxFe1-xNbxO3	x	0.4	0.5	0.6	0.7
Phase		P4mm	P4mm	P4mm	P4mm
Lattice parameters	a	4.000880	4.011634	4.005660	4.005733
	b	4.000880	4.011634	4.005660	4.005733
	c	3.999300	4.009461	4.011795	4.014028
Tetragonality (a/c)		1.000395	1.000542	0.998471	0.997933
M-O	1	2.109140	2.025130	2.050090	2.060070
	2	1.890160	1.984330	1.961710	1.925470
	3	2.007870	2.006210	2.004230	2.006370
Cell Volume		64.017	64.204	64.371	64.409
R(A cation)		1.466	1.495	1.524	1.553
R(Bcation)		0.643	0.643	0.642	0.642
Tolerance factor		0.991957	1.002239	1.012527	1.02282

More $KNbO_3$ rich compositions [Figure 4.5] show a poorer fit to the P4mm model, with the x=0.95 sample and pure $KNbO_3$ both show intensities and positions consistent with the standard diffraction data for the *Amm2* phase.(9) Tolerance factor calculations [Table 4.3] agree that the material is tending towards the $KNbO_3$ Amm2 phase, and away from the pseudo-cubic tetragonal P4mm phase.

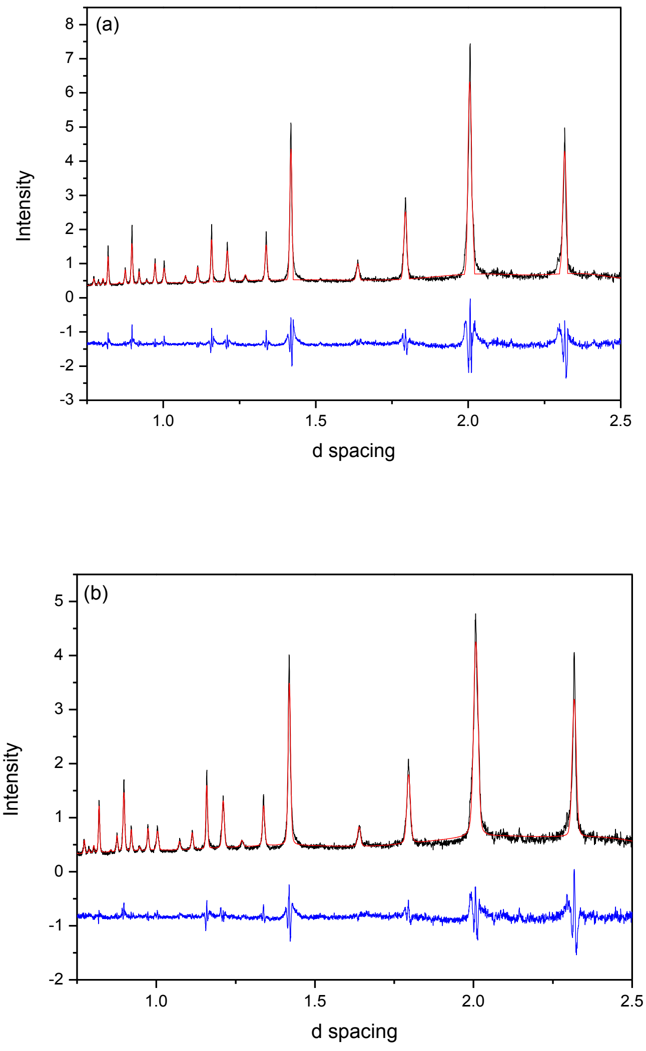

Figure 4.6.3: *Powder Neutron diffraction data showing a cross section of the development of the P4mm and Amm2 phases as $KNbO_3$ content changed within the material across the studied range of $Bi_{1-x}K_xFe_{1-x}Nb_xO_3$ materials. (x=0.80-1.00) This data was obtained from the HRPD high resolution instrument and all readings shown were taken at room temperature. The black line indicated the experimental data, whilst the red line indicates the difference between the experimental data, and calculated structural model x= (a) 0.80 (b) 0.90*

Table 4.4: *Powder Neutron Diffraction data showing refinement data for all fit carried out using Amm2 symmetry.*

Bi1-xKxFe1-xNbxO3	X	0.8	0.9
Phase		Amm2	Amm2
Lattice parameters	a	4.000484	4.002002
	b	5.680642	5.690044
	c	5.674353	5.681470
Tetragonality (a/c)		0.705011	0.704396
M-O	1	2.003920	2.007600
	2	2.029660	2.036860
	3	1.986750	1.988020
Cell Volume		128.951	129.376
R(A cation)		1.582	1.611
R(Bcation)		0.641	0.641
Tolerance factor		1.033117	1.04342

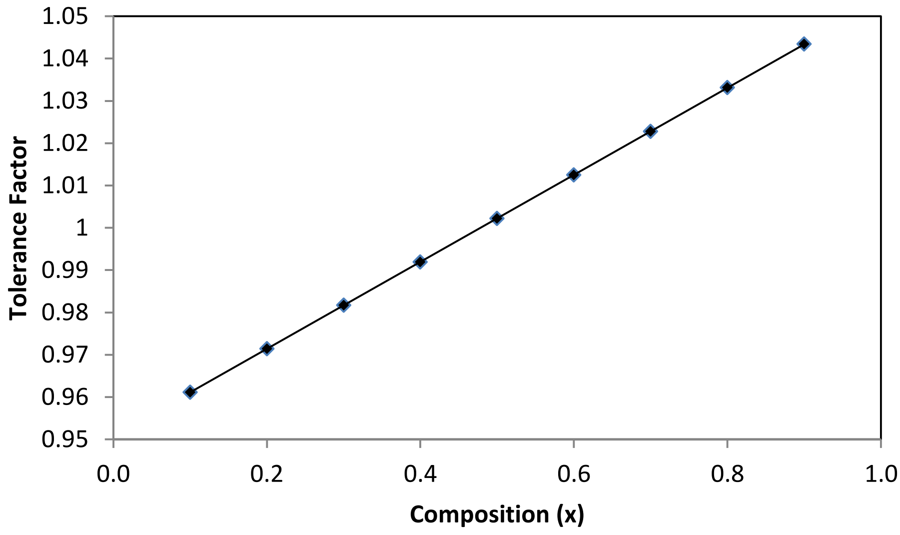

Figure 4.7: *Graph showing the development of the tolerance factors as a function of x in* $Bi_{1-x}K_xFe_{1-x}Nb_xO_3$ *materials.*

At room temperature the crystal structure of $BiFeO_3$ can be described with the Bi^{3+} ions occupying cubo-octahedral positions within the compound, whilst the Fe^{3+} ions sit in octahedral coordinates surrounded by oxygen anions. The cations displace off their centre of symmetry along the [111] c direction with the FeO_6 octahedra rotated around the rhombohedral axis

(Glazer notation $a^-a^-a^-$), the pseudo-cubic axis are $a/b_{rho}=2\sqrt{2}a_{cub}$ $c_{rho}=2a_{cub}$.(11)

The space group *P4mm* has a very different axial tilt, (in Glazer notation as $a^0b^+c^0$) (12) whose symmetry can be described by an order parameter (0, 0, *a*) with any displacement of the atoms being along the [001] direction, with a pseudo-cubic relationship of $a_{tet} = a_{cub}$, $c_{tet} = a_{cub}$.(13,14). Finally, the parent $KNbO_3$ (*Amm*2) phase shows a tilt system described by $a^-b^0c^+$ (15), and the lattice parameters can be related through a $a_{orth} = a_{cub}$, $b_{orth}/c_{orth} = \sqrt{2}a_{cub}$ the tilt system can be described by an order parameter (*a*, *a*, 0) with the atomic displacements lying along the [011] direction. (13,14) As previously stated, Figure 4.3 (b) indicates that the pseudo-cubic lattice parameters begin to decrease, until the a/b and c parameters reach approximately the same value (~4. 00Å) at approximately x=0.40. This would indicate that the lattice shape is tending more towards the cubic, which the expected trend seen in the calculated tolerance factors shown in Figure 4.7, which would initially indicate a tendency towards t=1 (ideal cubic).

The change to the lattice parameters across the solid solution can be seen in Figure 4.3 (b), and show an interesting relationship. In the *R3c* and *P*4*mm* phases, the lattice parameters show a steep linear increase until dopant values of $x = 0.7$, consistent with the effect of addition of a much larger radius cation. The material then begins to transition into *Amm2*, with the a parameter then continuing to increase whilst there is a slight drop in the size of the b/c parameters, with the two values becoming more consistent as x increases.

The complex behaviour exhibited by the lattice parameters in Figure 4.3 (b) arises from the increased tilting of the octahedral coupled with the rotation of the atomic displacements.

Figure 4.3 (b) shows a much more simple trend, indicating that cell volume increases as the proportion of K^+ and Nb^{5+} increases, which follow the predicted pattern indicated by the much larger size of the K+ ion. A clear change in gradient is obvious around x = 0.7 as the material transition to *Amm2*.

As x increases, so does the tetragonality. The *P*4*mm* phase with shows an almost cubic set of lattice parameters (*x* = 0.2) in comparison with the larger difference between *a* and *c* observed for later compositions such as *x* = 0.7. If we consider the bond lengths, *P*4*mm* shows a slight cation displacement in the a/c direction, whilst it is roughly central in the a/b axis. Below *x* = 0.4 there is only a small difference in the bond lengths, representing a very small displacement of the metal cation. This is reinforced by Figure(4.2)(c) , which demonstrates that as *x* further increases, as does this displacement, leading to two distinct Fe-O bonds develop (one long and one short), as the values separate, indicating an increase in displacement of the metal cation within the octahedral cage. Given that between $0.2 \leq x \leq 0.4$ the material is in a pseudo-cubic *P4mm* symmetry, this cation displacement could indicate the existence of an intermediate symmetry that may prompt further investigative work, as it would be expect for a non-polar cubic cell that the B site cation sat centrally within the octahedra. One such work by Teslenko *et al*. suggests that the transition from *R*3*c* to *P*4*mm* symmetry exhibits an intermediary *Pbnm* phase (16,17) however, neither the refined peaks or small unindexed peaks give any indication of *Pbnm* symmetries in these refinements.

In some refinements, high thermal parameters are observed, particularly for the Bi^{3+}/K^+ crystallographic A-site, which can be linked to the inhomogeneous nature of our samples as seen in the synchrotron diffraction data.

Furthermore, close inspection of the refinement data demonstrates some evidence of un-indexed peaks which are attributable to small amounts of secondary phases in some compositions at lower values of x. These peaks may however be very low intensity magnetic Bragg peaks at low values of x (further discussed later).

Using the synchrotron and PND data, the propose phase diagram similar to that observed for the $PbZrO_3$ – $PbTiO_3$ solid solution (18) as shown in Figure 4.8 below. There are region of some phase coexistence between each distinct phase, linked to the inhomogeneous nature of the prepared samples. This inhomogeneity could be eliminated, leading to better defined and sharper phase transitions through optimisation of the synthesis methodology. More recent studies suggest that significantly longer synthesis times are needed to improve the homogeneity of the doped $BiFeO_3$ samples, a similar method was reported for Nd^{3+} doped $BiFeO_3$ in a study by Levin et.al.[9]

Another recent study by Dolgos involved the doping of another rhombohedral perovskite, $Bi(Fe_{2/8}Mg_{3/8}Ti_{3/8})O_3$, with $BaTiO_3$. This work showed a loss of rhombohedral distortion resulting in a phase transition to pseudo-cubic $R3m$ symmetry.(11) This is driven by the larger Ba^{2+} cation substituting for the smaller Bi^{3+} cation on the perovskite A-site (denying the displacing nature of the Bi^{3+} lone pair) suppressing the tilting of the MO_6 octahedra. Dolgos *et al*.'s work could suggest similar effects in study, since K^+ has a much larger ionic radius than Bi^{3+} which could lead to an intermediate phase of $R3m$ symmetry, however investigation into refining the material in an $R3m$ symmetry showed no better fit.

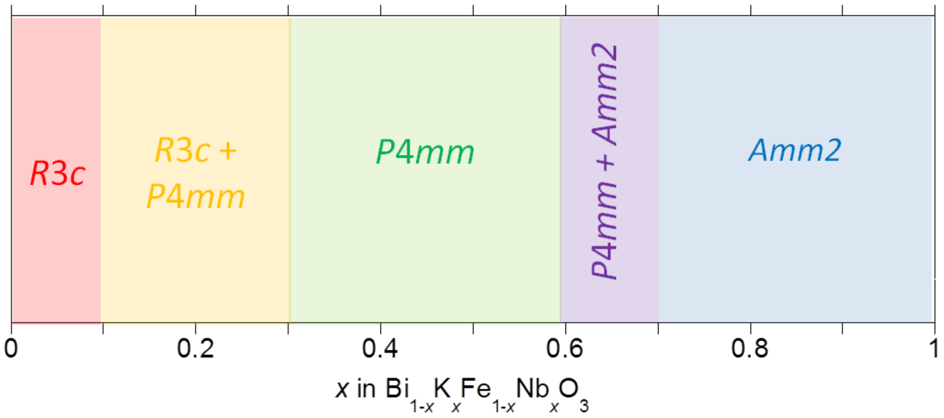

Figure 4.7.1: *Proposed phase diagram for $Bi_{1-x}K_xFe_{1-x}Nb_xO_3$ materials based on powder diffraction studies.*

The effect of temperature on lattice distortion was also investigated, using the $Bi_{0.5}K_{0.5}Fe_{0.5}Nb_{0.5}O_3$ composition, as initially this was thought to be the most promising sample in terms of exhibiting long range ordering similar to that seen in double perovskites. As previously stated, the material exhibits a *P4mm* symmetry, which appears to be consistent across the temperature range, although there are some developing distortions at both high a low temperature as the lattice becomes strained and begins to tend towards the *R3c* and *Amm2* phases known to be exhibited either side of the *P4mm* phase (Figure 4.7.1) This material should tend towards cubic at high temperatures, although no such tendency is seen in this data, so the transition likely occurs in excess of 673K. Similarly, the expectation of the phase diagram would indicate that there should be some presentation of the *R3c* phase at lower temperatures, although this is not seen in the data.

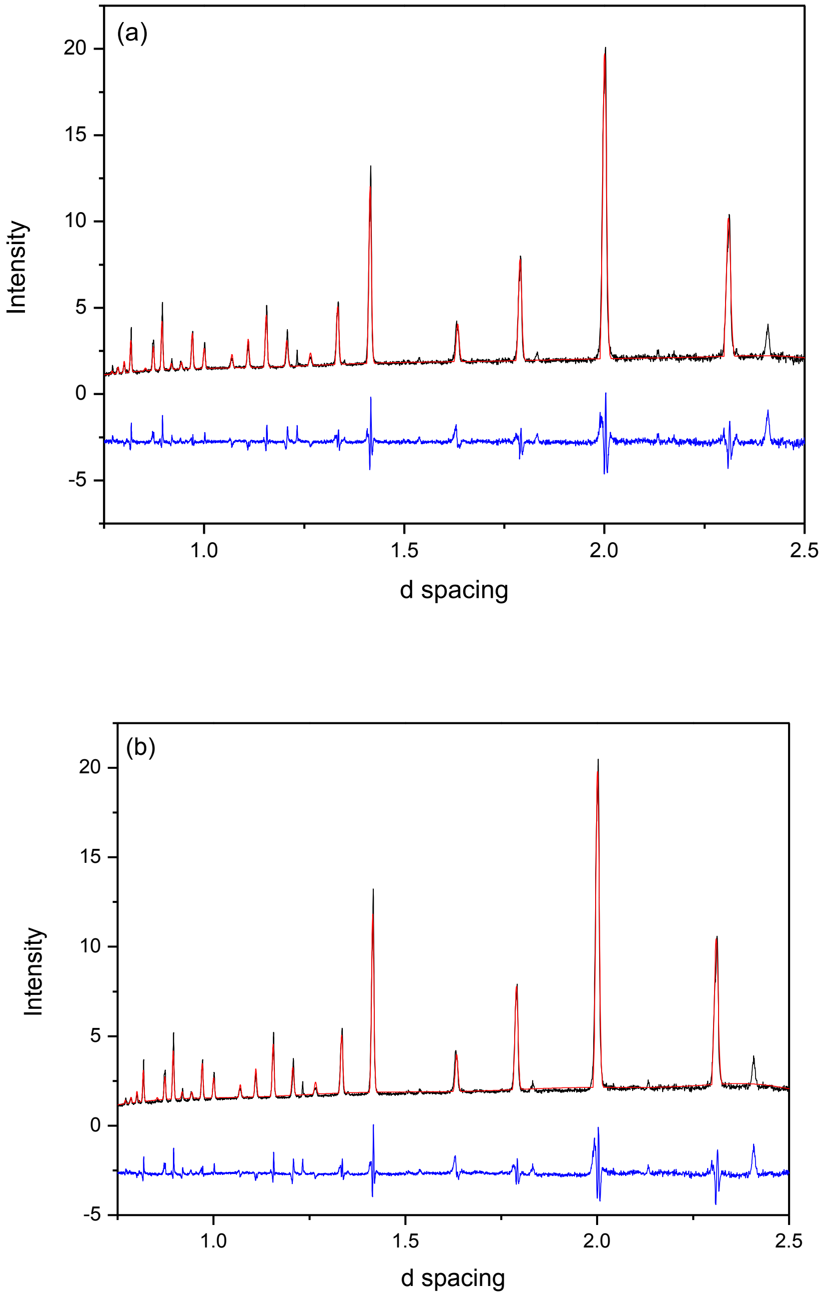

Figure 4.8.1: *Powder Neutron diffraction data showing a cross section of the development of the P4mm phases as temperature changed for the composition of* $Bi_{0.5}K_{0.5}Fe_{0.5}Nb_{0.5}O_3$*. This data was obtained from the HRPD high resolution instrument at a range of temperatures The black line indicated the experimental data, whilst the red line indicates the calculated refinement data, and the blue line the difference between the experimental data, and calculated structural model for (a)9K (b) 100K*

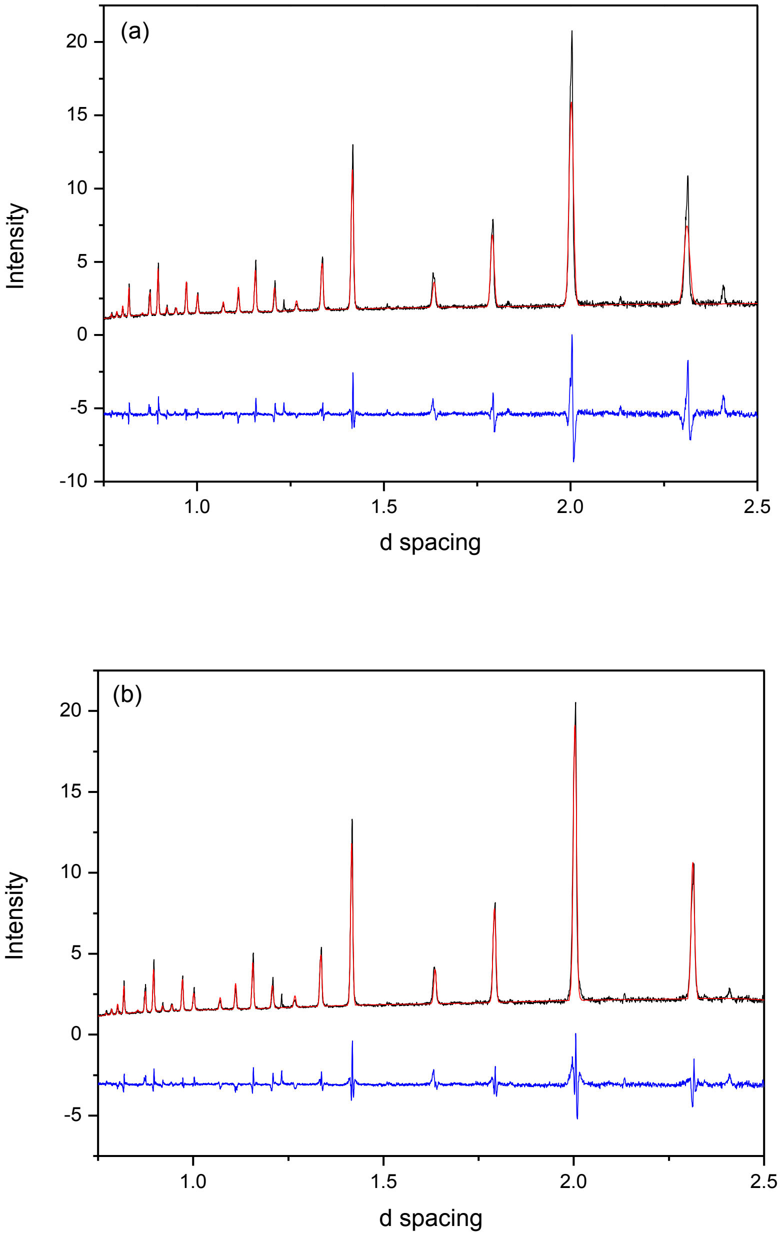

Figure 4.8.2: *Powder Neutron diffraction data showing a cross section of the development of the P4mm phases as temperature changed for the composition of* $Bi_{0.5}K_{0.5}Fe_{0.5}Nb_{0.5}O_3$*. This data was obtained from the HRPD high resolution instrument at a range of temperatures The black line indicated the experimental data, whilst the red line indicates the calculated refinement data, and the blue line the difference between the experimental data, and calculated structural model for (a)200K (b) 300K*

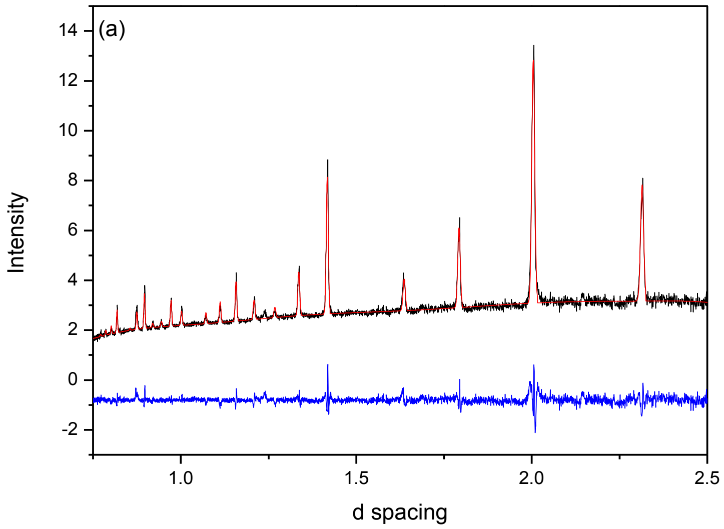

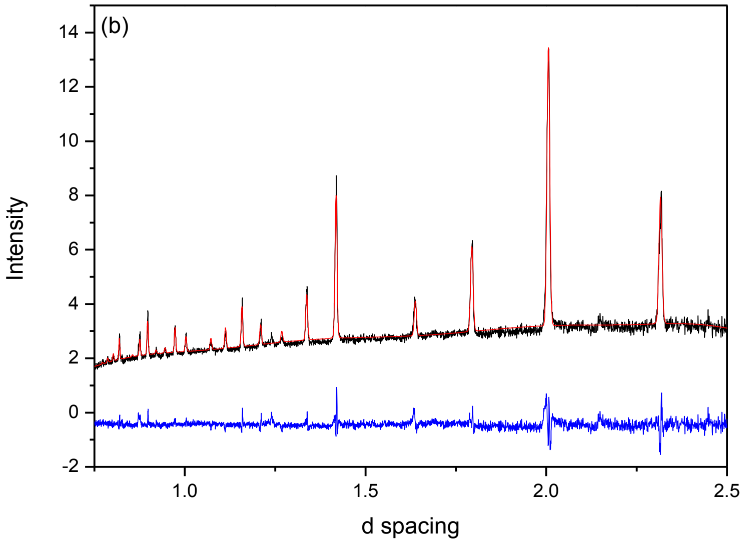

Figure 4.8.3: *Powder Neutron diffraction data showing a cross section of the development of the P4mm phases as temperature changed for the composition of* $Bi_{0.5}K_{0.5}Fe_{0.5}Nb_{0.5}O_3$*. This data was obtained from the HRPD high resolution instrument at a range of temperatures The black line indicated the experimental data, whilst the red line indicates the calculated refinement data, and the blue line the difference between the experimental data, and calculated structural model for (a)373K (b) 473K*

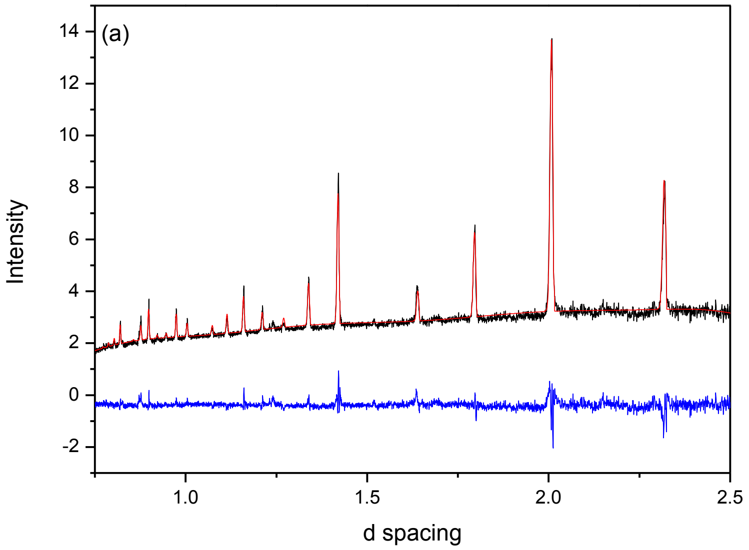

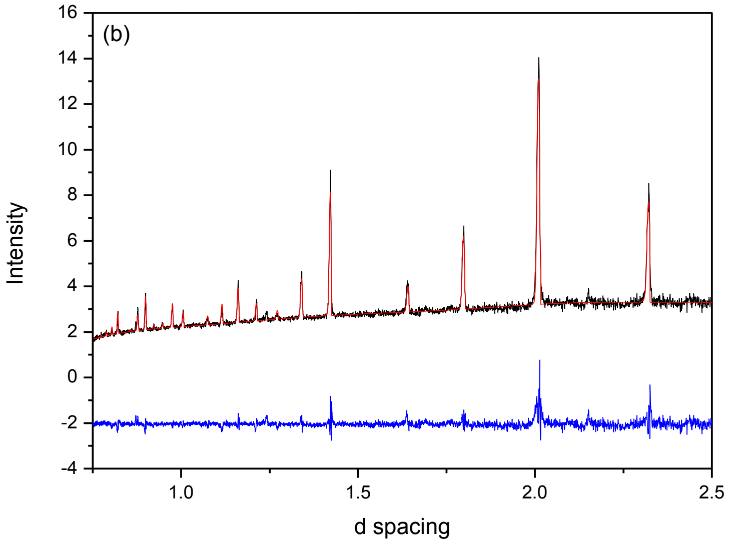

Figure 4.8.4: *Powder Neutron diffraction data showing a cross section of the development of the P4mm phases as temperature changed for the composition of* $Bi_{0.5}K_{0.5}Fe_{0.5}Nb_{0.5}O_3$*. This data was obtained from the HRPD high resolution instrument at a range of temperatures The black line indicated the experimental data, whilst the red line indicates the calculated refinement data, and the blue line the difference between the experimental data, and calculated structural model for (a)573K (b) 673K*

Table 4.5.1: *Powder Neutron Diffraction data showing refinement data for all fit carried out using P4mm symmetry for variable temperature data taken for* $Bi_{0.5}K_{0.5}Fe_{0.5}Nb_{0.5}O_3$.

Bi1-xKxFe1-xNbxO3	x	9K	100K	200K	300K
Phase		P4mm	P4mm	P4mm	P4mm
Lattice parameters	a	3.997969	3.998410	4.000679	4.002080
	b	3.997686	3.998410	4.000679	4.002080
	c	4.002969	4.003540	4.008178	4.009267
Tetragonality (a/c)		0.998751	0.998719	0.998129	0.998207
M-O	1	2.125100	2.125400	2.006310	2.128450
	2	1.877880	1.878140	1.881870	1.880820
	3	2.000380	2.000740	2.001880	2.002580
Cell Volume		63.973	64.006	64.153	64.215
Atom Positions		0.0000	0.0000	0.0000	0.0000
	A	0.0000	0.0000	0.0000	0.0000
		0.0000	0.0000	0.0000	0.0000
		0.5000	0.5000	0.5000	0.5000
	B	0.5000	0.5000	0.5000	0.5000
		0.4820	0.4820	0.4820	0.4820
		0.5000	0.5000	0.5000	0.5000
	O	0.5000	0.5000	0.5000	0.5000
		-0.0489	-0.0489	-0.0186	-0.0489
		0.5000	0.5000	0.5000	0.5000
	O	0.0000	0.0000	0.0000	0.0000
		0.5016	0.5016	0.5016	0.5000
Occupancy	Bi	0.478	0.478	0.4978	0.478
	K	0.522	0.522	0.522	0.522
	Fe	0.497	0.497	0.497	0.497
	Nb	0.503	0.503	0.503	0.503
Chi^2		11.310	13.540	4.983	8.525
Fitted	wRp	0.0750	0.0819	0.0663	0.0649
	Rp	0.0550	0.0657	0.0518	0.0472
Background	wRp	0.1250	0.1239	0.1129	0.1141
	Rp	0.0997	0.0970	0.0884	0.0881

Table 4.5.2: *Powder Neutron Diffraction data showing refinement data for all fit carried out using P4mm symmetry for variable temperature data taken for* $Bi_{0.5}K_{0.5}Fe_{0.5}Nb_{0.5}O_3$.

Bi1-xKxFe1-xNbxO3	x	373K	473K	573K	673K
Phase		P4mm	P4mm	P4mm	P4mm
Lattice parameters	a	4.004974	4.001930	4.012934	4.016202
	b	4.004974	4.001930	4.012934	4.016202
	c	4.011472	4.006326	4.016050	4.023144
Tetragonality (a/c)		0.998380	0.998903	0.999224	0.998274
M-O	1	2.129610	2.126880	2.132040	2.135810
	2	1.881860	1.879450	1.884010	1.887340
	3	2.004030	2.007500	2.008010	2.009650
Cell Volume		64.343	64.484	64.673	64.893
Atom Positions		0.0000	0.0000	0.0000	0.0000
	A	0.0000	0.0000	0.0000	0.0000
		0.0000	0.0000	0.0000	0.0000
		0.5000	0.5000	0.5000	0.5000
	B	0.5000	0.5000	0.5000	0.5000
		0.4820	0.4820	0.4820	0.4820
		0.5000	0.5000	0.5000	0.5000
	O	0.5000	0.5000	0.5000	0.5000
		-0.0482	-0.0489	-0.0482	-0.0489
		0.5000	0.5000	0.2000	0.5000
	O	0.0000	0.0000	0.0000	0.0000
		0.5016	0.5016	0.5016	0.5016
Occupancy	Bi	0.478	0.478	0.478	0.478
	K	0.522	0.522	0.522	0.522
	Fe	0.497	0.497	0.497	0.497
	Nb	0.503	0.503	0.503	0.503
Chi^2		2.221	2.888	2.824	2.404
Fitted	wRp	0.0392	0.0432	0.0462	0.0392
	Rp	0.0340	0.0382	0.0379	0.0334
Background	wRp	0.0753	0.0757	0.0750	0.0784
	Rp	0.0577	0.0603	0.0597	0.0637

4.2. Magneto-electric properties of $Bi_{1-x}K_xFe_{1-x}Nb_xO_3$

Preliminary electrical data (shown in Figure 4.9) across the $Bi_{1-x}K_xFe_{1-x}Nb_xO_3$ solid solution, shows a gradual loss of ferroelectricity across the solid solution as x increases, along with an anomaly seen at 700-760K in low x compositions, which is consistent with the anti-ferromagnetic to paramagnetic phase transition seen in the parent $BiFeO_3$ this anomaly is masked in materials with a higher $KNbO_3$ content due to non-ohmic effects linking to pellet structure.(19) Although the location of this feature is at a higher temperature than the $BiFeO_3$ (633K), increase of dopant content appears to lower the temperature at which this transition occurs. [Figure 4.9]

Electrical measurements for $Bi_{1-x}Dy_xFeO_3$, also indicated a similar anomaly at around 670K, which we have shown to correspond with a transition to paramagnetic behaviour.

The x=0.10 data also shows a feature at around 550K, but the subsequent non-ohmic effect makes it difficult to identify the significance, however it could be linked to the loss of ferroelectricity, with the subsequent change in dielectric constant being linked only to the electrodes.

Several attempts were made to collect variable frequency data to investigate the predicted ferroelectric to paraelectric phase transition. All of this data showed the expected increase in permittivity that would be consistent with previous dielectric data for rare-earth ferrites, however the ‘leaky’ nature of the material a relaxor like characteristic was seen given by non-ohmic electrode effects. (20-22) This is due to the presence of $BiFeO_3$, and the effect appear to lessen as $KNbO_3$ content is increased, however the ductile nature of the material made the pellets too soft to withstand transport and coating in order to take dielectric measurements.

In future studies, more thorough dielectric measurements may be obtained by using a binder in the pellet preparation in order to increase their density and obtain usable dielectric data at higher values of $KNbO_3$. This would be beneficial as low density pellets are more subject to large contributions from surface resistivity rather than contributions from the pellet volume, leading to non-ohmic responses such as those seen below.

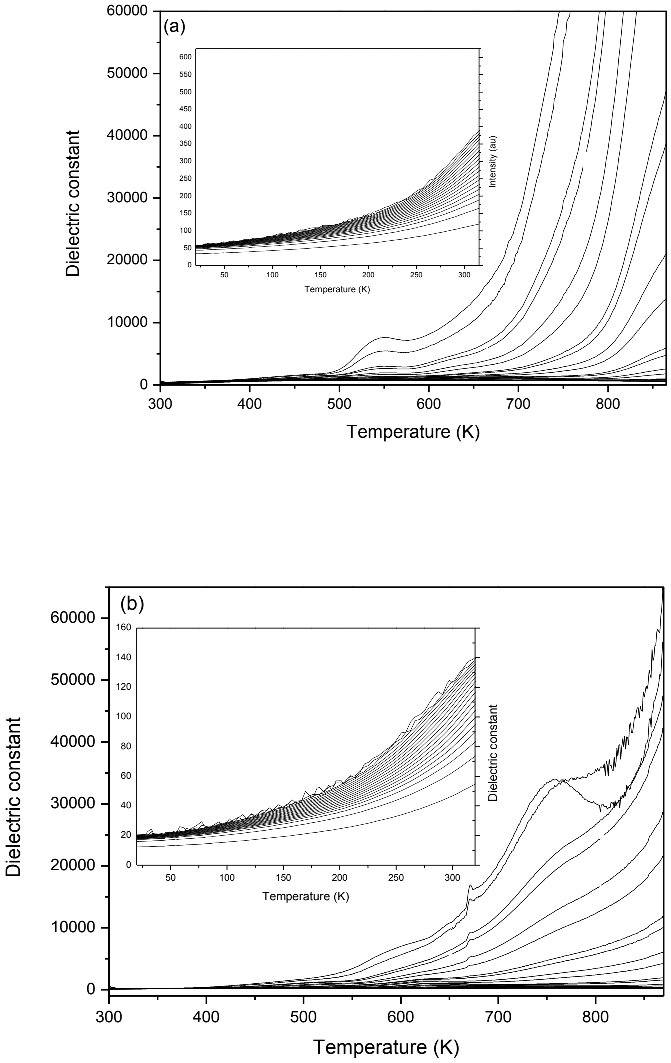

Figure 4.9.1: *Dielectric data collected for* $Bi_{1-x}K_xFe_{1-x}Nb_xO_3$*. With each line representing a different frequency (in the range 100Hz-1MHz) at which the data was recorded. Data is shown for compositions of x= (a) 0.10 (b) 0.40*

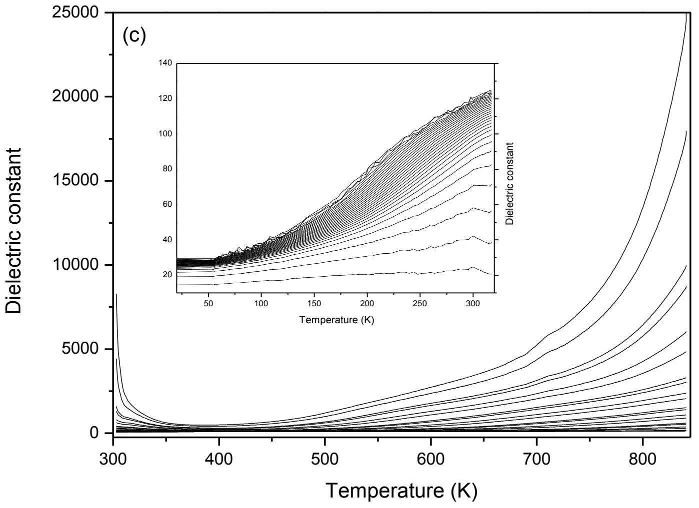

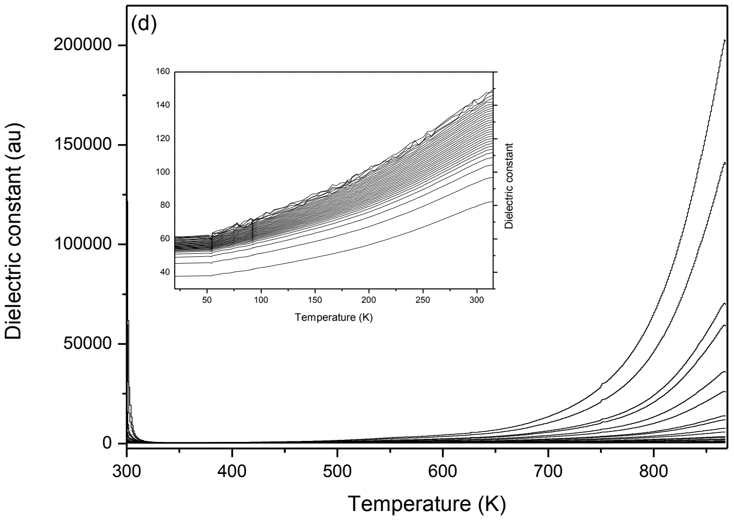

Figure 4.9.2: *Dielectric data collected for* $Bi_{1-X}K_XFe_{1-x}Nb_XO_3$*.With each line representing a different frequency (in the range 100Hz-1MHz)at which the data was recorded. Data is shown for compositions of x= (c) 0.50 (d) 0.80*

This leaky nature, along with the lack of stable pellets made it difficult to collect polarisation field data and as such there is no way of confirming when/if the material loses electrical polarisation. This means that although the material should be ferroelectric across the solid solution, there is no way to confirm this. Whether or not the material is ferroelectric could be masked by the non-ohmic electrode effect.

The driving mechanism of the ferroelectricity in $BiFeO_3$ is the offset of the stereoactive lone pair Bi^{3+} ion, which is caused by ferroelectric effect, along with a shift in electron density, which is responsible for the off-centring of the Fe^{3+} ion within the octahedral cage, and the lattice tilt system. These data indicate that the ferroelectric dipole will be reduced and eventually removed, which can be seen from Figure 4.3 which shows convergence of the Fe^{3+} bond lengths, indicating a lessening effect on the Fe^{3+} as Bi^{3+} is removed from the lattice. This centring shift in the Fe ion, is likely driven by the variance between the sizes of the parent Bi^{3+} and the doped K^{+} cations, as despite it's much larger size, K^{+} lacks the characteristic lone pair responsible for the Fe^{3+} displacement. The loss of the Bi^{3+} lone pair is therefore likely responsible for loss of ferroelectricity.

In $KNbO_3$, the driving mechanism is the spontaneous onset of a dielectric moment caused by the initial random offset of one of the B site cations. The electromagnetic field generated then surpassed the restoring force, and leads to the generation of a permanent moment within the material.

This should indicate that either end of the solid solution (*R3c* x=0.00-0.20 and *Amm2* x=0.80-1.00) should exhibit ferroelectricity. Whilst there is some indication in the literature that *P4mm* can be polar, the lattice parameters suggest that $Bi_{1-x}K_xFe_{1-x}Nb_xO_3$ is pseudo-cubic, so it is unlikely to have any dielectric character, in addition, the Fe/Nb-O bond lengths are comparable, which would indicate a centralised cation within the octahedra.

Magnetic field dependence data was collected for $Bi_{1-x}K_xFe_{1-x}Nb_xO_3$ (Figure 4.10) showed some loss of magnetisation as x increases with materials with values in excess of *x*=0.5 showed curves consistent with paramagnetic behaviour. Materials a composition with values lower than *x*=0.3 demonstrate a non Curie-Weiss like behaviour across the entire temperature range (2 K – 300 K). Instead, we observed a broad peak that straddles up to room temperature in addition to a deviation between the ZFC-FC data at approximately 50 K which may be indicative of a spin glass transition. A slight deviation from linearity is also observed in magnetisation-field curves at 25 K in these materials, particularly in the x=0.10 sample.

These observations may be suggestive of the initial addition of Nb^{5+} leading to canting of the G-type magnetic cycloid by disrupting the short range order within the cycloid. This may be the cause of the weak ferromagnetic moment measured in the SQUID response for low values of x, however this effect is lost by the further addition of Nb^{5+}.(23,24-26) An alternative mechanism is that compositions which still contain large amounts of Fe^{3+} could contain heavily Fe^{3+} rich regions, which would be consistent with the previously noted inhomogeneous nature of the samples.

In addition, contrary to other RE doped materials the magnetization measurements suggest that increasing *x* leads to a lowering of the AFM transition, whilst many studies show that the introduction of RE species leads to an increase in T_N (Chapter 3). (23,26,27)

From *x* = 0.4 there is no evidence for any hysteresis and a similar glass-like transition is observed. Higher values of x also show some remnant polarisation as Nb^{5+} content is much higher, likely leading to the formation of magnetic domains within the material. Again this could be due to formation of areas containing a high density the remaining Fe^{3+} ions, leading to ordered regions within the materials. A small deviation was seen between ZFC and FC data at approximately 15 K, lower than the previous noticed deviation in lower compositions. Curie-Weiss fits to the paramagnetic region (between 200 and 300 K) but calculations give a negative Weiss constants, θ, suggestive of either spin glass or canted antiferromagnetic (AFM) behaviour. One way to further determine the nature if this magnetisation would be to examine the local structure using probing techniques such as EXAFS to identify any local domain structures and determine which of the by which mechanism the Fe^{3+} ions are responsible for the measurable magnetisation.

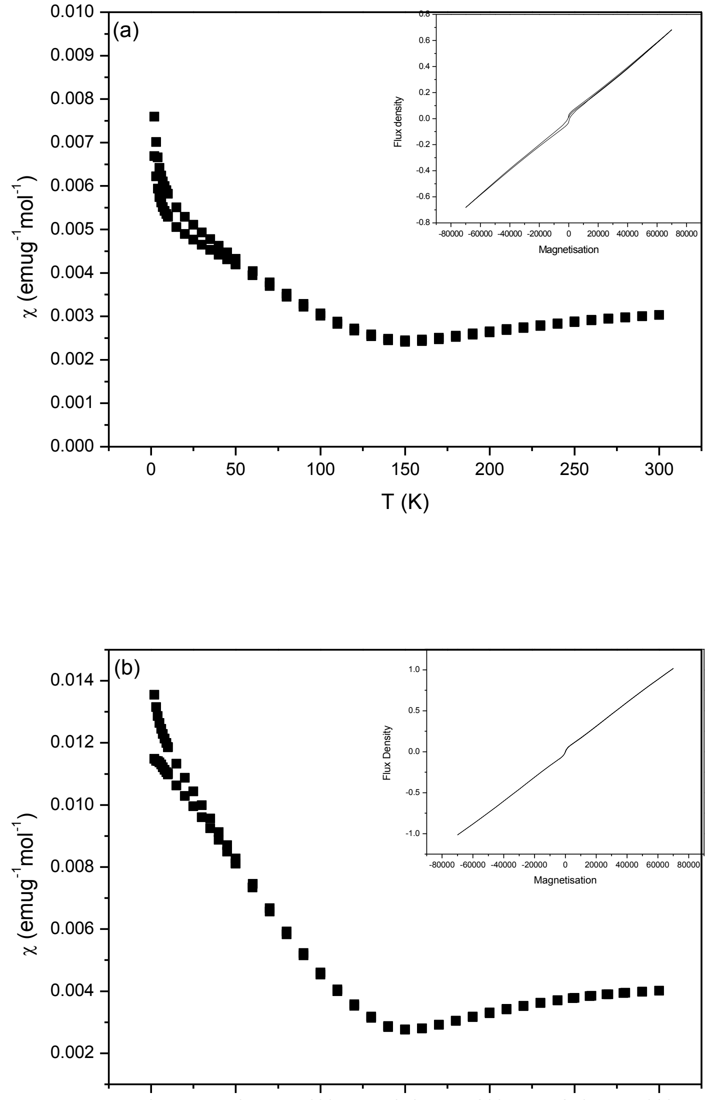

Figure 4.10.1: *SQUID data for $Bi_{1-x}K_xFe_{1-x}Nb_xO_3$ showing ZFC/FC data and hysteresis loops (inset). Larger hysteresis loops are shown in Appendix 6.2 Data is shown for compositions x= (a) 0.10 (b) 0.20*

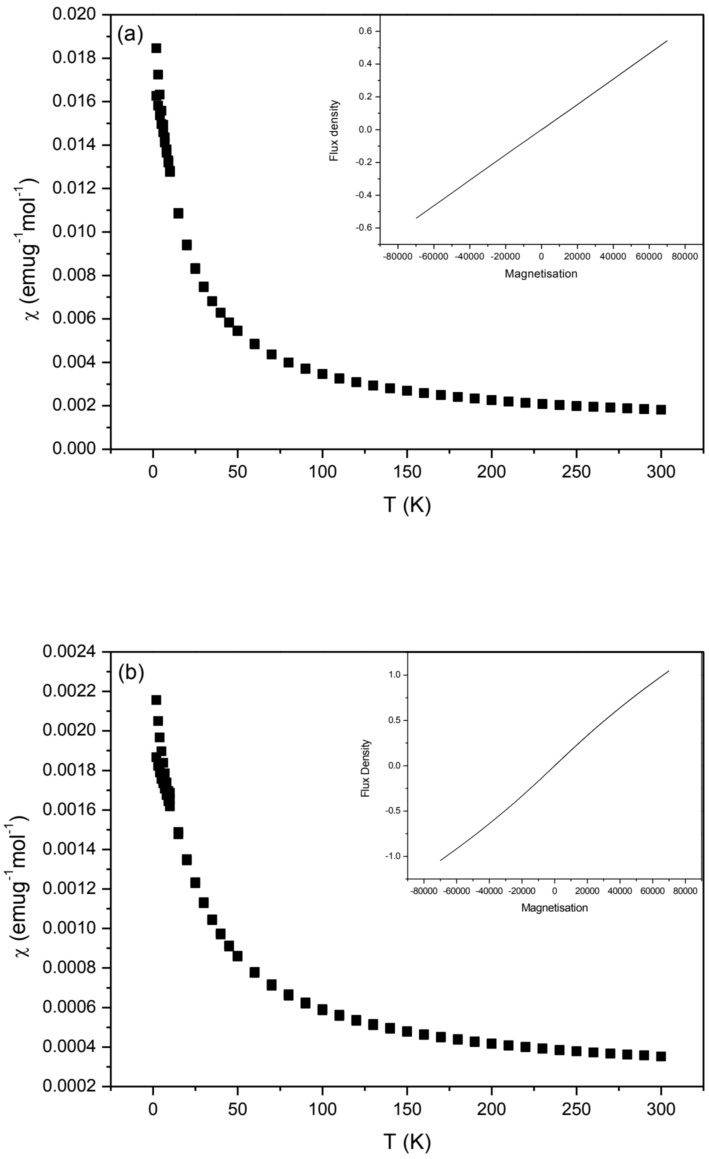

Figure 4.10.2: *SQUID data for $Bi_{1-x}K_xFe_{1-x}Nb_xO_3$ showing ZFC/FC data and hysteresis loops (inset). Larger hysteresis loops are shown in Appendix 6.2 Data is shown for compositions x= (a) 0.40 (b) 0.50*

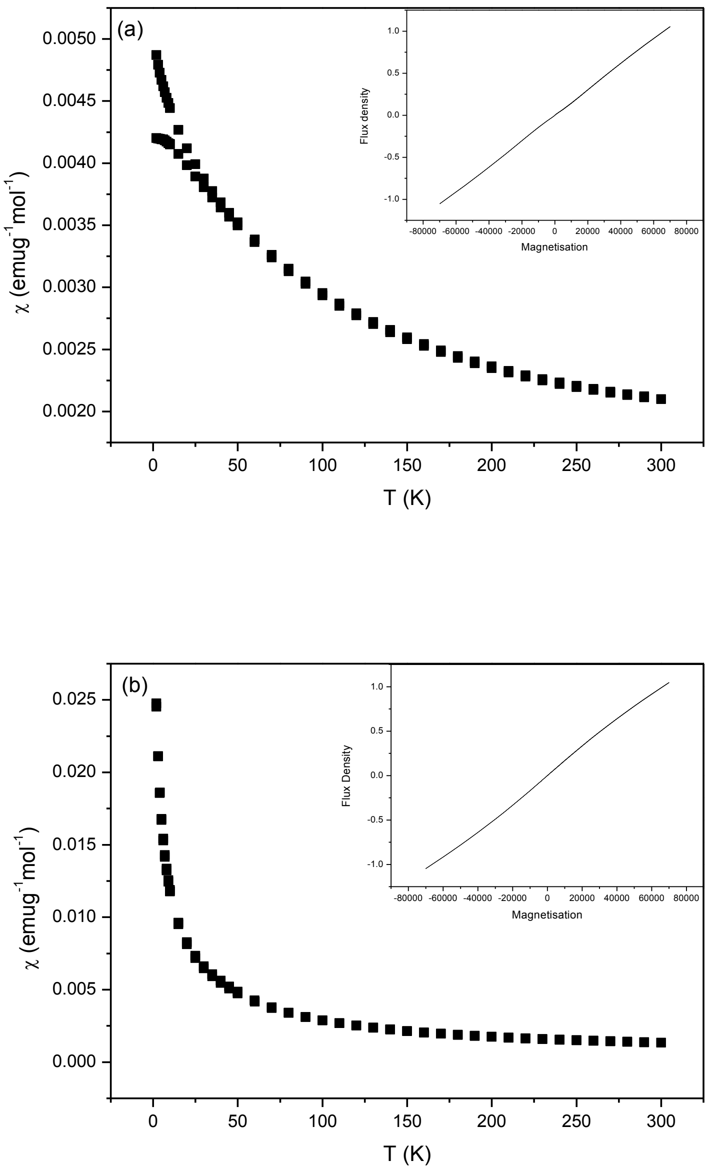

Figure 4.10.3: *SQUID data for* $Bi_{1-x}K_xFe_{1-x}Nb_xO_3$ *showing ZFC/FC data and hysteresis loops (inset). Larger hysteresis loops are shown in Appendix 6.2 Data is shown for compositions x= (a) 0.60 (b) 0.70*

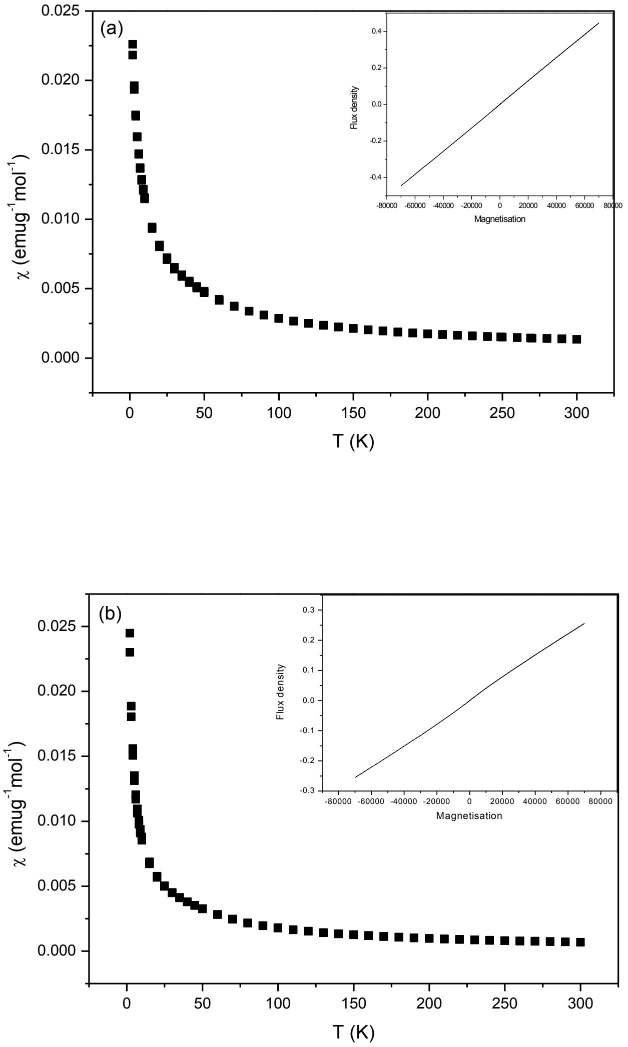

Figure 4.10.4: *SQUID data for $Bi_{1-x}K_xFe_{1-x}Nb_xO_3$ showing ZFC/FC data and hysteresis loops (inset). Larger hysteresis loops are shown in Appendix 6.2 Data is shown for compositions x= (a) 0.80 (b) 0.90*

The remnant magnetisation values for low *x* show comparable magnetisations to existing work (23,24) Zero field cooled (ZFC)/Field cooled (FC) measurements show a clear Curie tail, with very little variation between the ZFC and FC data. This indicates that anti-ferromagnetism is could have been retained. Another possibility for the exhibition of weak ferromagnetism could be the formation of small parasitic Fe_2O_3 phase during synthesis; however synchrotron and PND structural data offers no evidence of any impurity phases, although this could be masked by the secondary phases due to the inhomogenous nature of the sample.

A mechanism that could give rise to this effect, as discussed in Chapter 3, would be an argument for the formation of ferromagnetic Fe^{3+} rich clusters which maintain some remnant magnetisation, and disrupt any ordering within the Nb^{5+} domains. The formation of the polar nano-regions within the crystal structure could account for the SQUID response whilst supporting the idea that the long range spin cycloid has been retained.(2) If this was the case, it would suggest regions of cation concentration; which could be confirmed in future work, by investigation into the local environment of the B site cations, techniques that may accomplish this are discussed below. Currently it is not clear if these data exhibit paramagnetism or antiferromagnetism or spin glass transition, if this behaviour are linked with Fe^{3+} rich and Fe^{3+} deficient areas arising due to sample inhomogeneities.

4.3. Conclusions

This chapter reports the changing structure of $Bi_{1-x}K_xFe_xNb_{1-x}O_3$ as x content increases. The solid solution uses powder neutron and synchrotron diffraction to provide an overview of the structural evolution. In contrast with some previous work, the data shows a phase diagram (Figure 4.8) which indicates a transition from *R3c* to *P4mm* to *Amm*2 between x=0.00-1.00. Materials below *x*=0.2 adopt a $BiFeO_3$ like rhombohedral *R3c* phase whilst compositions above *x*=0.8 adopt Am orthorhombic *Amm*2 symmetry ($KNbO_3$ like). Between x=0.4-0.7 materials with a tetragonal *P4mm* symmetry are seen, with some pseudo-cubic characteristics. There may also be some suggestion of an intermediate phase between the *R3c* and *P4mm* phases which is masked by inhomogeneity.

Dielectric constant measurements for $Bi_{1-x}Dy_xFe_{1-x}Nb_xO_3$ were unreliable due to non-ohmic electrode effects and the leaky nature of the material. The ohmic effects and lack of data for higher values of x, could be overcome by improving the density of the pellets used for the impedance analysis, this could be overcome by improving the quality of the pellets using a silicate binder.

Lack of accurate dielectric data makes it difficult to determine the polar nature of the P4mm phase, so it is difficult to know if the material is ferroelectric, but further investigation would warrant the use of PDF or EXAFS to more thoroughly probe the local environment of the sample could provide a more detailed view of the structure. This would also help determine if there was any domain structure within the material, for both the electrical and magnetic considerations.

SQUID data suggests that the G-type anti-ferromagnetic spin cycloid may be retained, but become canted, alongside some weak ferromagnetism initially, with no remnant polarisation within the *P4mm* phase, however the exact nature of the magnetic structure is unknown, and may result in paramagnetism, canted antiferromagnetism or a spin glass like structure. All materials seem to exhibit a magnetic transition between 700-750K, which is consistent with the parent $BiFeO_3$ and indicates no major change in Néels temperature.. However there could be some evidence for additional magnetic phase transitions between paramagnetism and anti-ferromagentism which occur at lower temperature, but are masked by the non-ohmic effect seen in the dielelectric data, and further study using higher density pellets (through the use of silicate binders) or magnetic studies using PND to identify characteristic Bragg peaks could extend this work and allow further refinement of the magnetism. This could be coupled with local structural studies with existing magnetic data, to give an indication of the domain structure of the *P4mm* phase and the environment of the Fe^{3+} ion.

This study shows that there are several complex formations within the solid solution, and that the development of the ferroelectric and ferromagnetic properties within these $Bi_{1-x}K_xFe_{1-x}Nb_xO_3$ along with the $PbZrO_3$-$PbTiO_3$ like phase transitions could yield some interesting properties with further investigation, and location of the proposed MPB could generate enhance properties and improve functionality of this material.

References

1. Z. Zhang, CJ. Howard, KS. Knight, GR. Lumpkin, *Acta Crystallogr B*, **2005**, 62, 60-67
2. I Masuda, K Kakimoto, H Oshato, *Journal of Electroceramics,* 13, 555-9, **2004**
3. E. Magome, Y. Kuroiwa, H. Yoshimura, C. Moriyoshi, K. Yamashita, I. Fujii, K. Nakashima,N. Kumada and S. Wada, *Jpn J. App. Phys.*, **2012,** 51, 09LE05
4. X. Chao, Z. Yang, Z. Li and Y. Li, *J. Alloys. Cpds.*, **2012**, 518, 1
5. Ma and X. M. Chen, *J. Appl. Phys.*, **2009,** 105, 054107
6. V. M. Goldschmidt, *Naturwissenschaften*, **1926,** 14, 477
7. T Yamamoto, *Jpn J Appl Phys,* **1996,** 35, 5104
8. Y Nakashima, T Shimura, W Sakamoto, T Yogo, *Ferroelectrics*, **2007,** 356, 1890-184
9. S. Zhang, L. Wang, Y. Chen, D. Wang, Y. Yao, Y. Ma *J. Appl. Phys.* **2012** 111, 074105
10. R. C. Lennox, M. C. Price, W. Jamieson, M. Jura, A. Daoud-Aladine, C. Murray, C. Tang, and D. C. Arnold, *J. Mater. Chem. C*, **2014** 2, 3345
11. M. Dolgos, U. Adem, X. Wan, Z. Xu, A. J. Bell, T. P. Comyn, T. Stevenson, J. Bennett, J. B. Claridge and M. J. Rosseinsky, *Chem. Sci.*, **2012,** 3**,** 1426
12. S. Zhang, W. Luo, D. Wang, Y. Ma, *Materials Letters* **2009**, *63*, 1820.
13. T. R. Shrout and S. J. Zhang, *J. Electroceram.*, **2007**, 19, 11345
14. C. J. Howard and H. T. Stokes, *Acta. Cryst.*, **2005**, A61, 93
15. DW. Baker, PA. Thomas, N. Zhang, AM. Glazer *Acta Crystallogr B*. **2009** 65, 22-8.

16. P. Y. Teslenko, A. G. Razumnaya, V. O. Ponomarenko, A. G. Rudskaya, A. V. Nazarenko, A. S. Anokhin, M. V. Avramenko, D. I. Leshov, M. F. Kupriyanov and Y. I. Yuzyuk, *Phys. Solid State*, **2014**, 56, 1866

17. P. Y. Teslenko, Y. V. Kabirov, O. N. Razumovskaya and L. A. Reznichenko, *Bulletin of the Russian Academy of Sciences, Physics*, **2011,** 75, 1133

18. A. M. Glazer, Acta. Crystallogr. A., **1972**, 28, 3384

19. G. Catalan, J. F. Scott, *Adv. Mater.* **2009**, *21*, 2463.

20. D.C. Arnold, K.S. Knight, F.D. Morrison and P. Lightfoot, *Phys. Rev. Letters*, **2009**, 102, 027602

21. M. Li, A. Feteira, D. C. Sinclair, *J. Appl. Phys.* **2009**, *105*, 114109.

22. M. Li, D.C. Sinclair, A.R. West, *J Appl Phys*, **2011**, 109, 084106

23. P. Uniyal, K. L. Yadav, *J. Phys.: Condens. Matter.*, **2009**, *21*, 012205

24. V. A. Khomchenko, D. V. Karpinsky, A. L. Kholkin, N. A. Sobolev, G. N. Kakazei*, J. Appl. Phys*. **2010,** 108, 074109

25. J. Xu, G. Wang, H. Wang, D. Ding, Y. He, *Materials Letters* **2009**, *63*, 855, 074105.

26. P. Thompson, D.E. Cox, J.B. Hastiongs, *J Appl Cryst*, **1994**, 27, 892

27. J. Hlinka, J. Porkorny, S. Karimi and I. M. Reaney, *Phys. Rev. B.: Condens. Matter. Phys.*, 2011, **83**, 020101

28. D. C. Arnold, *IEEE Transactions on Ultrasonics, Ferroelectrics and Frequency Control*, 2015, **62**, 62

29. G. Catalan and J. F. Scott, *Adv. Mater.*, 2009, **21**, 2463

30. R. D. Shannon, *Acta. Crystallogr. A.*, 1976, **32**, 751

31. B. H. Toby, *J. Appl. Crystallogr.*, 2001, **34**, 210

32. Y. Nakashima, T. Shimura, W. Sakamoto and T. Yogo, *Ferroelectrics*, 2007, **356**, 180

33. A. W. Hewat, *J. Phys. C.: Solid State Phys.*, 1973, **6**, 2559

34. V.A. Khomchenko, J.A. Paixão, D.A. Kiselev and A.L. Kholkin, *Mater. Res. Bull.* **2010**, 45, 416-419

35. C.M. Kavanagh, R.J. Goff, A.Z. Daoud-Aladine, P. Lightfoot and F.D. Morrison, *Chem. Mater*. **2012**, 24, 199-208

36. A J Jacobson, B E F Fender, *J. Phys. C: Solid State Phys.* 1975, 8 844

37. V.A. Khomchenko, I.O. Troyanchuk, M.V. Bushinsky, O.S. Mantatyskata, V. Sikolenko, J.A. Paixao, *Material Letters*, **2011**, 65, 1970

38. R. C. Lennox, D. D. Taylor, L. V. Stimpson, G. B. G. Stenning, M. Jura, M. C. Price, E. E. Rodrigeuz, and D. C. Arnold, *Dalton Trans*, 2015, **44**, 10608-10613

Chapter 5: Conclusions

5.1. Conclusions on the composition $Bi_{1-x}Dy_xFeO_3$

The structural and characteristic examination of $Bi_{1-x}Dy_xFeO_3$ undertaken in this thesis has shown some interesting results linking to the changing structure as Dy^{3+} content varies. There is an observed, phase transition early in the phase diagram between the polar *R3c* phase and the polar Cc phase. The material then transitions to a composite of *Cc* and non-polar *Pnma* with a broad phase coexistence between $0.05 < x < 0.30$, which has proved difficult to fit to either model accurately. Higher Dy^{3+} compositions show loss of polar phases, and instead a coexistence of several Pnma phases at x=0.30. The work done so far has led to the proposal of the phase diagram below.

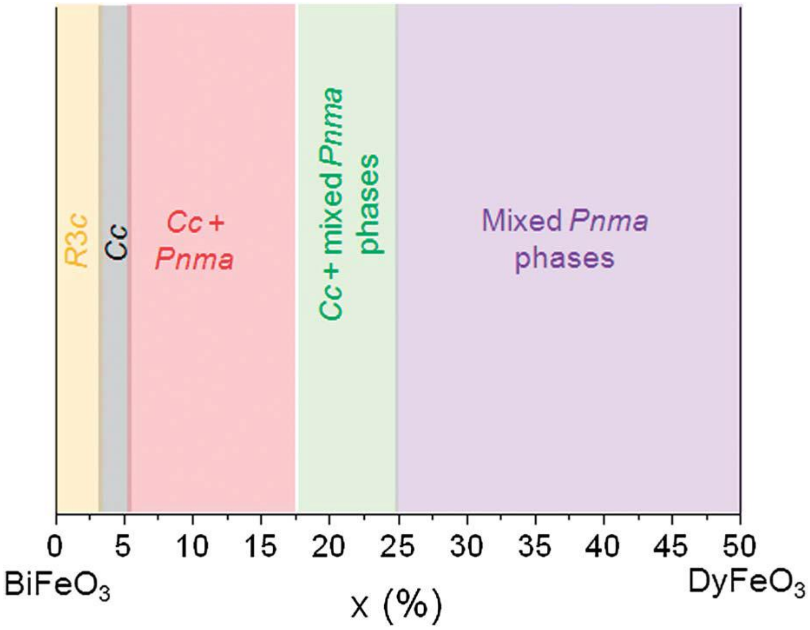

Figure 5.1: *Proposed phase diagram for $Bi_{1-x}Dy_xFeO_3$ based on collection of all of the structural data.*

As previously discussed, the main contributor to the poor quality of the high composition refinements is due to absorption of the incident neutron radiation by Dy^{3+}. One suggested alternative is the use of less absorbing isotopes of Dy^{3+} in future compositions. It is also possible that the use of synchrotron radiation under a variable temperature regime could lead to higher quality results, however similar issues may be encountered as Bi3+ absorbs synchrotron radiation. In order to minimise this effect, it would be prudent to filter the detected radiation to neglect those wavelengths that may be vulnerable to absorption, and tune the data away from the absorption edge.

Furthermore, some interesting work in symmetry mode analysis has suggested that there may also be another phase transition before the material transitions to *Pnma*. This is a change to polar *Cc,* which may have been masked in this work by the absorption effect seen from the A site cation (as stated above).(1) This could further be confirmed through use of local structural probing techniques such as PDF or EXAFS to allow a more detailed view of the crystal structure. This would also help determine if there was a ferroic domain structure within the material.

Lack of accurate dielectric data makes it difficult to determine if the polar *Cc* phase transition occurs, whilst structural data confirms *Pnma*.

This means that there is also scope for further electrical studies of these contributions, as measurements presented here were subject to non-ohmic electrode effects when Dy^{3+} content was low. These effects could be overcome in future studies by improving the density of the pellets used for the impedance analysis use of an alternative electrode material to try and prevent current leakage. Further impedance studies could also be enhanced by the use of atomic force microscopy or piezo force microscopy, which would also allow the imaging of any existing ferroelectric domains within materials of a low Dy^{3+} content.

Additional techniques of interest could be surface second harmonic generation (SHG) which would allow conclusively determination of when the initial R3c/Cc phase becomes non-centrosymmetric (therefore losing polarity). Alternatively, Mossballer Spectroscopy could be used to examine the environment of the Fe^{3+} and Bi^{3+} ions within the Oxygen octahedral cage and give a clearer indication of the mechanism that is responsible for the loss of ferroelectricity.

Further use for EXAFS or PDF data would be that confirmation of the local environment would help establish whether the weak ferromagnetic observed was caused by the beginnings of long range ordering, or the more likely formation of small magnetic clusters within the material, and would determine which cation was responsible for these magnetically rich areas, although it is likely due to the Fe^{3+} ions.

Data suggests that the G-type anti-ferromagnetic spin cycloid is retained alongside the weak ferromagnetism in $Bi_{0.95}Dy_{0.05}FeO_3$, with some suppression of the spin cycloid as Dy^{3+} content increases. The Néels temperature for these material range between 657-700K, which is consistent with the parent $BiFeO_3$ and indicates no significant change. (633K for $BiFeO_3$)

The existing magnetic study could be enhanced by the collection of further data on a more specialised beamline (such as WISH), however some steps would need to be taken to minimise Dy^{3+} absorption. Again, this could be done through the use of less absorbing isotopes of Dy^{3+}. This would allow the observation of magnetic Bragg peaks, and refinement of the magnetic structure.

5.2. Conclusions on the composition $Bi_{1-x}K_xFe_{1-x}Nb_xO_3$

The $Bi_{1-x}K_xFe_xNb_{1-x}O_3$ solid solution was subjected to powder neutron and synchrotron diffraction in order to provide an overview of this previous little known structural evolution. The phase diagram presented [Figure 6.2] varies from previous reports (2), and indicates transitions from *R3c* to *P4mm* to *Amm*2 between x=0.00-1.00.

Materials with composition close to the parent $BiFeO_3$ (below *x*=0.2) adopt a rhombohedral *R3c* phase whilst compositions close to $KNbO_3$ (above *x*=0.8) adopt a similar orthorhombic *Amm*2 symmetry. The mid-range compositions (x=0.4-0.7) exhibit a tetragonal *P4mm* symmetry, with some indication of pseudo-cubic characteristics. There may also be some suggestion of an intermediate phase between the *R3c* and *P4mm* phases which is masked by inhomogeneity of the samples. This inhomogeneity likely arises from the sample preparation techniques used, and further diffraction studies could provide conclusions as to the full phase diagram.

Dielectric constant measurements for $Bi_{1-x}Dy_xFe_{1-x}Nb_xO_3$ showed similar non-ohmic electrode effects, which was due to the leaky nature of the material, and resulted from the low density of the pellets, owing to the softness of the $KNbO_3$. Improving the density of the pellets could be accomplished by use of a silicate binder.

Further investigation could again would warrant the use of PDF or EXAFS to as another method of determining if there was any domain structure within the material, for both the electrical and magnetic considerations, and helping to confirm whether each phase was polar or non-polar.

SQUID data suggests that the G-type anti-ferromagnetic spin cycloid is retained, but canted. This is seen alongside a weak but measurable ferromagnetism initially, with no remnant polarisation within the *P4mm* phase. However the exact nature of the magnetic structure is not yet known, and as such the material may be paramagnetic, canted anti-ferromagnetism or a spin glass like structure. All materials seem to exhibit a magnetic transition between 700-750K, which is reasonably consistent with the parent $BiFeO_3$. However there may be additional magnetic phase transitions related to the para/anti-ferromagentism suggested above, which occur at lower temperature, but are masked by the non-ohmic effect seen in the dielelectric data.

One way to circumvent this would be to pair local structural studies with existing magnetic data, this would not give indication of the structure of the *P4mm* phase, but also allow discovery of the mechanism by which the Fe^{3+} is responsible for this small measurable magnetisation in the high and low x regions of the solid solution.

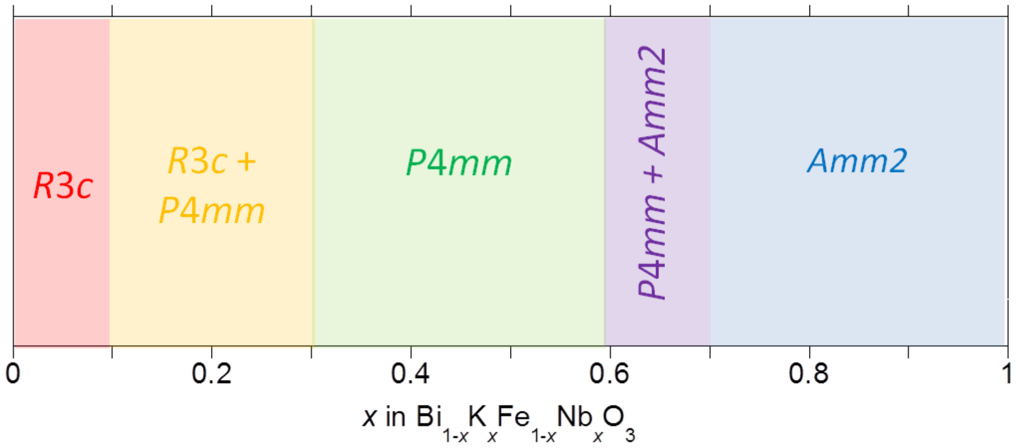

Figure 5.2: *Proposed phase diagram for* $Bi_{1-x}K_xFe_{1-x}Nb_xO_3$ *materials based on powder diffraction studies.*

This study shows that despite needing a number of techniques to begin understanding the complex structures within both $Bi_{1-x}Dy_xFeO_3$ and $Bi_{1-x}K_xFe_{1-x}Nb_xO_3$, both materials exhibit some exciting properties that warrant further consideration and study. The initial results shown indicate that the composite $Bi_{1-x}Dy_xFeO_3$ material has some interesting structural properties and that there is much potential that could be gained from further investigation into the crystal environment. Further studies into the magnetic characteristics using Magnetic interferometry and diffraction instruments such as the WISH beamline could give greater insight into the magnetic character of these materials. Likewise, $Bi_{1-x}K_xFe_{1-x}Nb_xO_3$ shows a range of complex formations throughout the solid solution, and that the further examination of the development of the ferroelectric and ferromagnetic properties within these compositions could yield exciting results, as they are comparable to some $PbZrO_3$-$PbTiO_3$ like phase transitions. Further investigation into these materials may be the first step along the road to replace PZT.

References

1. R.C. Lennox, M.C. Price, W. Jamieson, M. Jura, A. Daoud-Aladine, C.A. Murray, C. Tang, D.C. Arnold, J. Mater. Chem. C, **2014**,2, 3345-60
2. DW. Baker, PA. Thomas, N. Zhang, AM. Glazer Acta Crystallogr B. 2009 65, 22-8.

Appendix 6.1: Investigation of Dysprosium doped $BiFeO_3$

Rietveld refinements were performed for the powder neutron diffraction data for all $Bi_{1-x}Dy_xFeO_3$ ($0 \geq x \geq 0.30$) materials using the General Structure Analysis System (GSAS) suite of programs. Initial refinements were performed for the powder neutron diffraction data collected for the x = 0, 0.02 and 0.05 materials using the *R3c* and *Pnma* model, with approximately 37 variables including 12 background coefficient's fitted using a shifted Chebyschev function and peak shape fitted using a Pseudo-Voigt function for time-of-flight data. An absorption coefficient was also refined in order to model absorption effects resulting from the high neutron absorption observed for dysprosium. Refinement parameters are given in Tables 6.1 and 6.2 with the refinement profiles in Figures 6.1-6.

Data for the $Bi_{0.95}Dy_{0.05}FeO_3$ was recorded on the HRPD instrument across a temperature range of 10-973K.

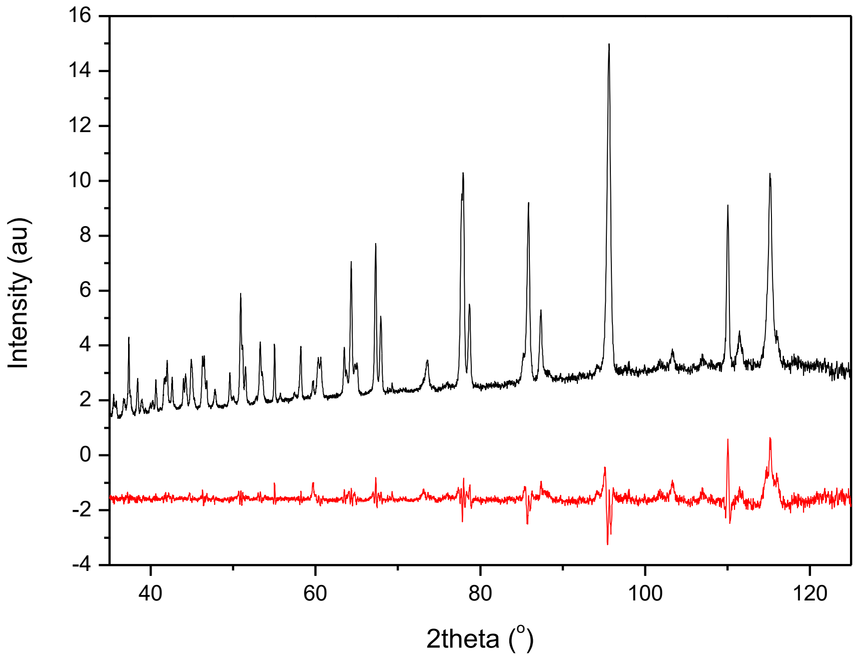

Figure 6.1: *Neutron diffraction data Rietveld refinements of $Bi_{0.95}Dy_{0.05}FeO_3$ using the Cc structural model. The black line represents experimental data, the red line represents the difference between the data and the Cc model.*

Table 6.1*: Table showing the lattice parameters and χ^2, wRp and Rp refinement parameters, along with the phase %, any secondary phases, M-O bond lengths and angles for the B site Fe^{3+} ion, cell volume and atomic positions and thermal information for $Bi_{0.95}Dy_{0.05}FeO_3$ refined in the Cc symmetry. All of this data was extracted from the GSAS refinement suite.*

$Bi_{0.95}Dy_{0.05}FeO_3$		
Phase		*Cc*
Lattice parameters	**a**	11.976836
	b	5.002755
	c	5.009128
c/a		0.418234666
M-O Bond Length	**1**	2.11673(3)
	2	1.94737(2)
M-O Bond Angle	**1**	79.696(1)
	2	164.645(0)
Cell Volume		267.119
Atom Positions	**A (x,y,z)**	0.723620(2)
		0.252260(3)
		-0.076425(2)
	Uiso	0.00032
	B(x,y,z)	-0.028446(11)
		0.276432(8)
		0.612058(12)
	Uiso	0.00032
	O1 (x,y,z)	0.480110(6)
		0.457330(4)
		0.860410(7)
	Uiso	0.00032
	O2 (x,y,z)	0.211490(3)
		0.3111290(2)
		0.860410(5)
	Uiso	0.00032
	O3 (x,y,z)	0.918820(11)
		0.481370(16)
		0.860410(17)
	Uiso	0.00032
Occupancy	**Bi**	0.95
	Dy	0.05
Chi^2		5.961
Fitted	**wRp**	0.0488
	Rp	0.0476

***Table 6.2.1**: Table showing the lattice parameters and χ^2, wRp and Rp refinement parameters, along with the phase %, any secondary phases, M-O bond lengths and angles for the B site Fe^{3+} ion, cell volume and atomic positions and thermal information for $Bi_{0.95}Dy_{0.05}FeO_3$. All of this data was extracted from the GSAS refinement suite.*

$Bi_{0.95}Dy_{0.05}FeO_3$	**Temp**	**10**	**30**	**50**	**70**
Phase		*R3c*	*R3c*	*R3c*	*R3c*
Phase fraction *R3c*		1.00000	1.00000	1.00000	1.00000
Secondary phase					
Lattice parameters	**a**	5.5654	5.5647	5.5649	5.5651
	c	13.8182	13.8161	13.8166	13.8184
c/a		2.4829	2.4828	2.4828	2.4831
M-O Bond Length	**1**	1.95178(3)	1.9434(4)	1.9510.(2)	1.9499(18)
	2	2.10777(4)	2.1142(3)	2.1068(4)	2.1077(19)
M-O Bond Angle	**1**	79.949(7)	80.275(8)	80.170(7)	80.19(8)
	2	164.9610(10)	165.3490(11)	165.2700(11)	165.29(11)
Cell Volume		370.6570	370.5140	370.5700	370.6380
Atom Positions	**A (0,0,0)**	0.000(0)	0.000(0)	0.000(0)	0.000(0)
	Uiso	0.00006	0.0128	0.0069	0.00268
	B (0,0,z)	0.221532(0)	0.2208990(0)	0.22132(11)	0.22102(11)
	Uiso	0.00007	0.00659	0.01000	0.00401
	O (x,y,z)	0.441472(12) 0.18501(3) 0.95258(9)	0.4401700(13) 0.016371(0) 0.952044(1)	0.44111(32) 0.01790(4) 0.95270(17)	0.44116(31) 0.01760(4) 0.95237(17)
	Uiso	0.00144	0.01225	0.0086	0.00386
χ ^2		8.9910	20.0200	8.2050	7.5490
Fitted	**wRp**	0.0525	0.0785	0.0491	0.0483
	Rp	0.0465	0.0701	0.0688	0.0491

***Table 6.2.2**: Table showing the lattice parameters and χ^2, wRp and Rp refinement parameters, along with the phase %, any secondary phases, M-O bond lengths and angles for the B site Fe^{3+} ion, cell volume and atomic positions and thermal information for $Bi_{0.95}Dy_{0.05}FeO_3$. All of this data was extracted from the GSAS refinement suite.*

$Bi_{0.95}Dy_{0.05}FeO_3$	**Temp**	**90**	**110**	**130**	**150**
Phase		*R3c*	*R3c*	*R3c*	*R3c*
Phase fraction *R3c*		1.00000	1.00000	1.00000	1.00000
Secondary phase					
Lattice parameters	**a**	5.5663	5.5659	5.5664	5.5668
	c	13.8221	13.8221	13.8239	13.8259
c/a		2.4832	2.4834	2.4835	2.4836
M-O Bond Length	**1**	1.9453(19)	1.9472(19)	1.9539(18)	1.9513(18)
	2	2.1132(20)	2.1109(19)	2.1029(19)	2.1056(18)
M-O Bond Angle	**1**	80.23(9)	80.21(8)	80.14(8)	80.17(8)
	2	165.30(12)	165.31(12)	165.31(11)	165.34(11)
Cell Volume		370.7260	370.8290	370.9420	371.0680
Atom Positions	**A (0,0,0)**	0.000(0)	0.000(0)	0.000(0)	0.000(0)
	Uiso	0.00049	0.00588	0.00749	0.0802
	B (0,0,z)	0.22106(11)	0.22096(11)	0.22156(11)	0.22156(11)
	Uiso	0.00024	0.00489	0.01000	0.01000
	O (x,y,z)	0.44041(33) 0.01670(4) 0.95222(17)	0.44093(32) 0.01710(4) 0.95222(17)	0.44241(30) 0.01840(4) 0.95314(16)	0.44225(29) 0.01780(4) 0.95309(16)
	Uiso	0.00104	0.00596	0.00839	0.00844
Χ^2		7.9560	7.8280	17.0200	12.5500
Fitted	**wRp**	0.0493	0.0491	0.0721	0.0620
	Rp	0.0455	0.0456	0.0581	0.0514

***Table 6.2.3**: Table showing the lattice parameters and χ^2, wRp and Rp refinement parameters, along with the phase %, any secondary phases, M-O bond lengths and angles for the B site Fe^{3+} ion, cell volume and atomic positions and thermal information for $Bi_{0.95}Dy_{0.05}FeO_3$. All of this data was extracted from the GSAS refinement suite.*

$Bi_{0.95}Dy_{0.05}FeO_3$	**Temp**	**170**	**190**	**210**	**230**
Phase		*R3c*	*R3c*	*R3c*	*R3c*
Phase fraction *R3c*		1.00000	1.00000	1.00000	1.00000
Secondary phase					
Lattice parameters	**a**	5.5676	5.5690	5.5696	5.5697
	c	13.8290	13.8338	13.8361	13.8369
c/a		2.4838	2.4841	2.4842	2.4843
M-O Bond Length	**1**	1.9471(20)	1.94936(2)	1.95307(2)	1.9512(24)
	2	2.1119(20)	2.11221(2)	2.10302(3)	2.1100(25)
M-O Bond Angle	**1**	80.26(9)	79.994(1)	80.380(1)	79.940(11)
	2	165.39(12)	165.043(0)	165.690(0)	165.011(15)
Cell Volume		371.2350	371.5540	371.7040	371.7500
Atom Positions	**A (0,0,0)**	0.000(0)	0.000(0)	0.000(0)	0.000(0)
	Uiso	0.00599	0.00452	0.00263	0.00385
	B (0,0,z)	0.22104(12)	0.2212870(0)	0.2211400(0)	0.1858840(0)
	Uiso	0.00027	0.00044	0.00302	0.00126
	O (x,y,z)	0.44091(34) 0.01680(4) 0.95236(18)	0.4414700(11) 0.017746(3) 0.952291(2)	0.4428350(0) 00174830(0) 0.9531100(0)	0.4423(4) 0.0182(5) 0.91695(20)
	Uiso	0.00416	0.00346	0.00347	0.00308
χ ^2		7.6180	7.4640	5.4040	9.2630
Fitted	**wRp**	0.0482	0.0480	0.0405	0.0531
	Rp	0.0451	0.0450	0.0392	0.0443

***Table 6.2.4**: Table showing the lattice parameters and χ^2, wRp and Rp refinement parameters, along with the phase %, any secondary phases, M-O bond lengths and angles for the B site Fe^{3+} ion, cell volume and atomic positions and thermal information for $Bi_{0.95}Dy_{0.05}FeO_3$. All of this data was extracted from the GSAS refinement suite.*

$Bi_{0.95}Dy_{0.05}FeO_3$	Temp	250	270	373	473
Phase		*R3c*	*R3c*	*R3c*	*R3c*
Phase fraction *R3c*		1.00000	1.00000	1.00000	1.00000
Secondary phase					
Lattice parameters	a	5.5711	5.5713	5.5770	5.5825
	c	13.8413	13.8418	13.8604	13.8785
c/a		2.4845	2.4845	2.4853	2.4861
M-O Bond Length	1	1.9485(20)	1.93801(2)	1.9579(25)	1.94761(2)
	2	2.1108(21)	2.12645(3)	2.1093(26)	2.12128(3)
M-O Bond Angle	1	80.52(9)	80.195(1)	79.62(10)	80.375(1)
	2	165.79(12)	165.206(0)	164.66(14)	165.604(0)
Cell Volume		372.0380	372.0820	373.4980	374.5620
Atom Positions	A (0,0,0)	0.000(0)	0.000(0)	0.000(0)	0.000(0)
	Uiso	0.00445	0.00685	0.00622	0.0143
	B (0,0,z)	0.22138(12)	0.221841(0)	0.2219970(0)	0.2219190(0)
	Uiso	0.00534	0.00708	0.00456	0.01091
	O (x,y,z)	0.44099(34) 0.0162(4) 0.95320(18)	0.439356(0) 0.015163(0) 0.9524790(0)	0.4439(4) 0.0196(5) 0.95287(19)	0.4409150(0) 0.156550(0) 0.9533140(0)
	Uiso	0.00489	0.01106	0.00746	0.01919
Χ ^2		3.8910	7.9130	6.6820	2.7730
Fitted	wRp	0.0466	0.0563	0.0462	0.0415
	Rp	0.0481	0.0551	0.0434	0.0413

***Table 6.2.5**: Table showing the lattice parameters and χ^2, wRp and Rp refinement parameters, along with the phase %, any secondary phases, M-O bond lengths and angles for the B site Fe^{3+} ion, cell volume and atomic positions and thermal information for $Bi_{0.95}Dy_{0.05}FeO_3$. All of this data was extracted from the GSAS refinement suite.*

$Bi_{0.95}Dy_{0.05}FeO_3$	**Temp**	**573**	**673**	**773**	**778**
Phase		*R3c*	*R3c*	*R3c*	*R3c*
Phase fraction *R3c*		1.00000	1.00000	0.94268	0.90180
Secondary phase				*Pnma*	*Pnma*
Lattice parameters	**a**	5.5891	5.5961	5.6031	5.6036
	c	13.8983	13.9187	13.9346	13.9353
c/a		2.4867	2.4872	2.4869	2.4869
M-O Bond Length	**1**	1.96287(3)	1.95327(3)	1.95252(4)	1.95266(4)
	2	2.10537(4)	2.11322(3)	2.12026(5)	2.12039(5)
M-O Bond Angle	**1**	79.619(2)	80.435(1)	80.234(2)	80.235(2)
	2	164.873(0)	165.996(0)	165.686(0)	165.687(0)
Cell Volume		375.9920	377.4920	377.6580	377.9450
Atom Positions	**A (0,0,0)**	0.000(0)	0.000(0)	0.000(0)	0.000(0)
	Uiso	0.03059	0.01832	0.0128	0.128
	B (0,0,z)	0.2198330(0)	0.221316(0)	0.2218(0)	0.2218(0)
	Uiso	0.02027	0.00887	0.00659	0.00659
	O (x,y,z)	0.4476160(0) 0.199340(0) 0.9511580(0)	0.44672(0) 0.0160300(0) 0.9534700(0)	0.44672(0) 0.01603(0) 0.95347(0)	0.44672(0) 0.01603(0) 0.95347(0)
	Uiso	0.02467	0.02162	0.01225	0.01225
Χ ^2		3.7690	2.5720	7.8580	3.1440
Fitted	**wRp**	0.0482	0.0396	0.0375	0.0438
	Rp	0.0412	0.0383	0.0340	0.0404

***Table 6.2.6**: Table showing the lattice parameters and χ^2, wRp and Rp refinement parameters, along with the phase %, any secondary phases, M-O bond lengths and angles for the B site Fe^{3+} ion, cell volume and atomic positions and thermal information for $Bi_{0.95}Dy_{0.05}FeO_3$. All of this data was extracted from the GSAS refinement suite.*

$Bi_{0.95}Dy_{0.05}FeO_3$	**Temp**	**793**	**803**	**813**	**823**
Phase		*R3c*	*R3c*	*R3c*	*R3c*
Phase fraction *R3c*		0.89425	0.83853	0.82568	0.76511
Secondary phase		*Pnma*	*Pnma*	*Pnma*	*Pnma*
Lattice parameters	**a**	5.6045	5.6052	5.6059	5.6068
	c	13.9384	13.9394	13.9407	13.9431
c/a		2.4870	2.4869	2.4868	2.4868
M-O Bond Length	**1**	1.96827(3)	1.95324(5)	1.95348(4)	1.97511(3)
	2	2.10734(3)	2.12102(5)	2.12126(4)	2.10279(3)
M-O Bond Angle	**1**	80.316(1)	80.235(2)	80.237(2)	80.140(1)
	2	165.844(0)	165.686(0)	165.687(0)	165.639(0)
Cell Volume		378.2150	378.4150	379.7480	379.7510
Atom Positions	**A (0,0,0)**	0.000(0)	0.000(0)	0.000(0)	0.000(0)
	Uiso	0.01745	0.0128	0.0128	0.01133
	B (0,0,z)	0.222387(0)	0.2218(0)	0.2218(0)	0.2223610(0)
	Uiso	0.00919	0.00659	0.00659	0.00644
	O (x,y,z)	0.4465190(0) 0.018192(0) 0.9548110(0)	0.44672(0) 0.01603(0) 0.95347(0)	0.44672(0) 0.01603(0) 0.95347(0)	0.4473360(0) 0.01962(0) 0.9548090(0)
	Uiso	0.02264	0.01225	0.01225	0.01826
Χ ^2		3.6690	3.7910	2.4720	3.2000
Fitted	**wRp**	0.0470	0.0441	0.0386	0.0438
	Rp	0.0440	0.0416	0.0372	0.0423

Table 6.2.7: *Table showing the lattice parameters and* χ^2*, wRp and Rp refinement parameters, along with the phase %, any secondary phases, M-O bond lengths and angles for the B site* Fe^{3+} *ion, cell volume and atomic positions and thermal information for* $Bi_{0.95}Dy_{0.05}FeO_3$*. All of this data was extracted from the GSAS refinement suite.*

$Bi_{0.95}Dy_{0.05}FeO_3$	**Temp**	**833**	**843**	**853**	**863**
Phase		*R3c*	*R3c*	*R3c*	*R3c*
Phase fraction *R3c*		0.68125	0.66886	0.59014	0.52786
Secondary phase		*Pnma*	*Pnma*	*Pnma*	*Pnma*
Lattice parameters	**a**	5.6077	5.6083	5.6092	5.6102
	c	13.9442	13.9451	13.9465	13.9480
c/a		2.4866	2.4865	2.4864	2.4862
M-O Bond Length	**1**	1.98079(3)	1.98155(6)	1.98783(3)	1.95486(2)
	2	2.09774(3)	2.09814(7)	2.09256(4)	2.12264(3)
M-O Bond Angle	**1**	80.409(1)	80.153(3)	80.224(2)	80.247(1)
	2	166.001(0)	165.664(0)	165.781(0)	165.688(0)
Cell Volume		379.7520	379.7520	380.0100	380.1850
Atom Positions	**A (0,0,0)**	0.000(0)	0.000(0)	0.000(0)	0.000(0)
	Uiso	0.00263	0.00263	0.0128	0.0128
	B (0,0,z)	0.222213(0)	0.222569(0)	0.221934(0)	0.2218(0)
	Uiso	0.00191	0.00193	0.00659	0.00659
	O (x,y,z)	0.4465800(0) 0.019777(0) 0.9552580(0)	0.447288(0) 0.205270(0) 0.9552710(0)	0.44736(0) 0.0213040(0) 0.955004(0)	0.44672(0) 0.01603(0) 0.95347(0)
	Uiso	0.01108	0.01189	0.01225	0.01225
Χ ^2		3.7930	3.3330	2.7180	3.5020
Fitted	**wRp**	0.0478	0.0447	0.0404	0.0458
	Rp	0.0430	0.0427	0.0385	0.0448

***Table 6.2.8**: Table showing the lattice parameters and χ^2, wRp and Rp refinement parameters, along with the phase %, any secondary phases, M-O bond lengths and angles for the B site Fe^{3+} ion, cell volume and atomic positions and thermal information for $Bi_{0.95}Dy_{0.05}FeO_3$. All of this data was extracted from the GSAS refinement suite.*

$Bi_{0.95}Dy_{0.05}FeO_3$	**Temp**	**873**	**903**	**923**	**973**
Phase		*R3c*	*R3c*	*R3c*	*R3c*
Phase fraction *R3c*		0.53914	0.44700	0.39751	0.2403
Secondary phase		*Pnma*	*Pnma*	*Pnma*	*Pnma*
Lattice parameters	**a**	5.6109	5.6135	5.6147	5.6186
	c	13.9497	13.9569	13.9620	13.9813
c/a		2.4862	2.4863	2.4867	2.4884
M-O Bond Length	**1**	1.95510(3)	1.95603(4)	1.95645(7)	1.95617(13)
	2	2.12291(4)	2.12394(5)	2.12449(9)	2.12433(15)
M-O Bond Angle	**1**	80.247(2)	80.244(2)	80.236(4)	80.224(7)
	2	165.688(0)	165.688(0)	165.687(0)	165.685(1)
Cell Volume		380.3210	380.8760	381.1460	381.2600
Atom Positions	**A (0,0,0)**	0.000(0)	0.000(0)	0.000(0)	0.000(0)
	Uiso	0.0128	0.0128	0.0128	0.0176
	B (0,0,z)	0.2218(0)	0.2218	0.2218(0)	0.2218
	Uiso	0.00659	0.00659	0.00659	0.0103
	O (x,y,z)	0.44672(0) 0.01603(0) 0.95347(0)	0.44672 0.01603 0.95347	0.44672(0) 0.01603(0) 0.95347(0)	0.4467 0.0160 0.9535
	Uiso	0.01225	0.01225	0.01225	0.0170
Χ ^2		3.0870	3.8240	3.1780	4.5250
Fitted	**wRp**	0.0425	0.0479	0.0502	0.0600
	Rp	0.0398	0.0448	0.0480	0.0539

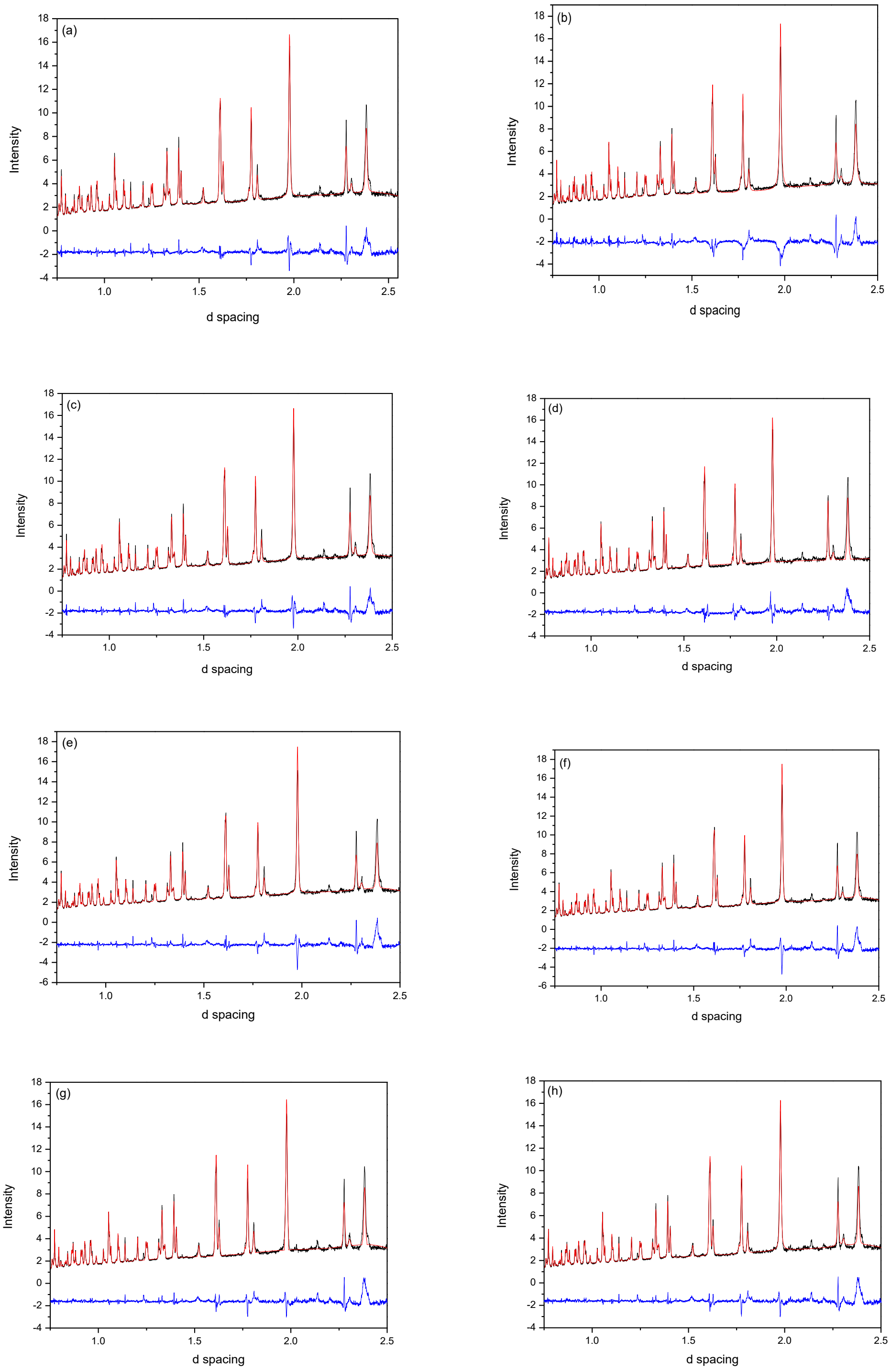

Figure 6.2: Rietveld refinement profiles between 0.75Å and 2.5Å for neutron diffraction data collected for of $Bi_{0.95}Dy_{0.05}FeO_3$, showing reasonable fits for both peak shape and intensity. The black line represents experimental data, the red line the fitted model, and the subsequent blue line the difference between the data and the fit. This refinement uses the R3c symmetry, and was recorded on the HRPD instrument at (a)10K (b)30K (c)50K (d) 70K (e) 90K (f) 100K (g) 130K (h) 150K

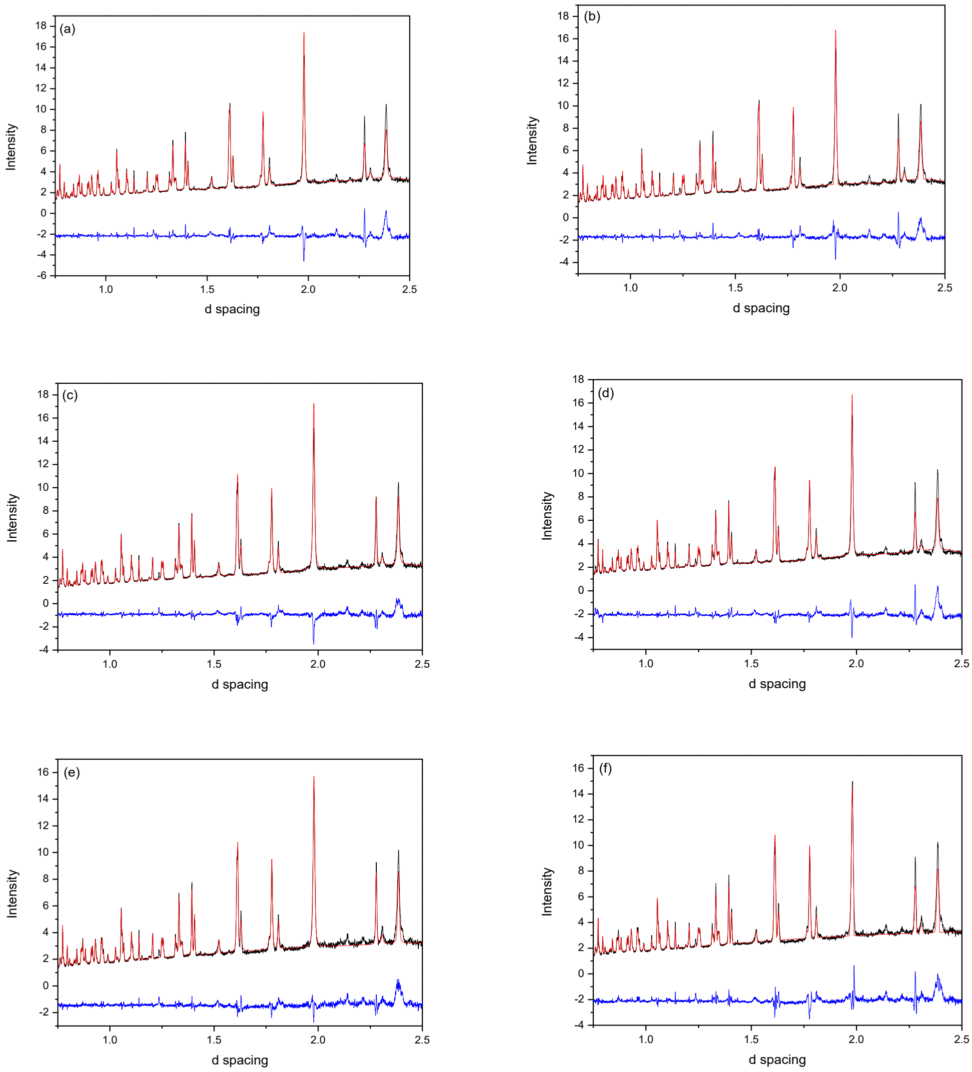

Figure 6.3: *Rietveld refinement profiles between 0.75Å and 2.5Å for neutron diffraction data collected for of* $Bi_{0.95}Dy_{0.05}FeO_3$*, showing reasonable fits for both peak shape and intensity. The black line represents experimental data, the red line the fitted model, and the subsequent blue line the difference between the data and the fit. This refinement uses the R3c symmetry, and was recorded on the HRPD instrument at (a) 170K (b) 190K (c) 210K (d) 230K (e) 250K (f)270K*

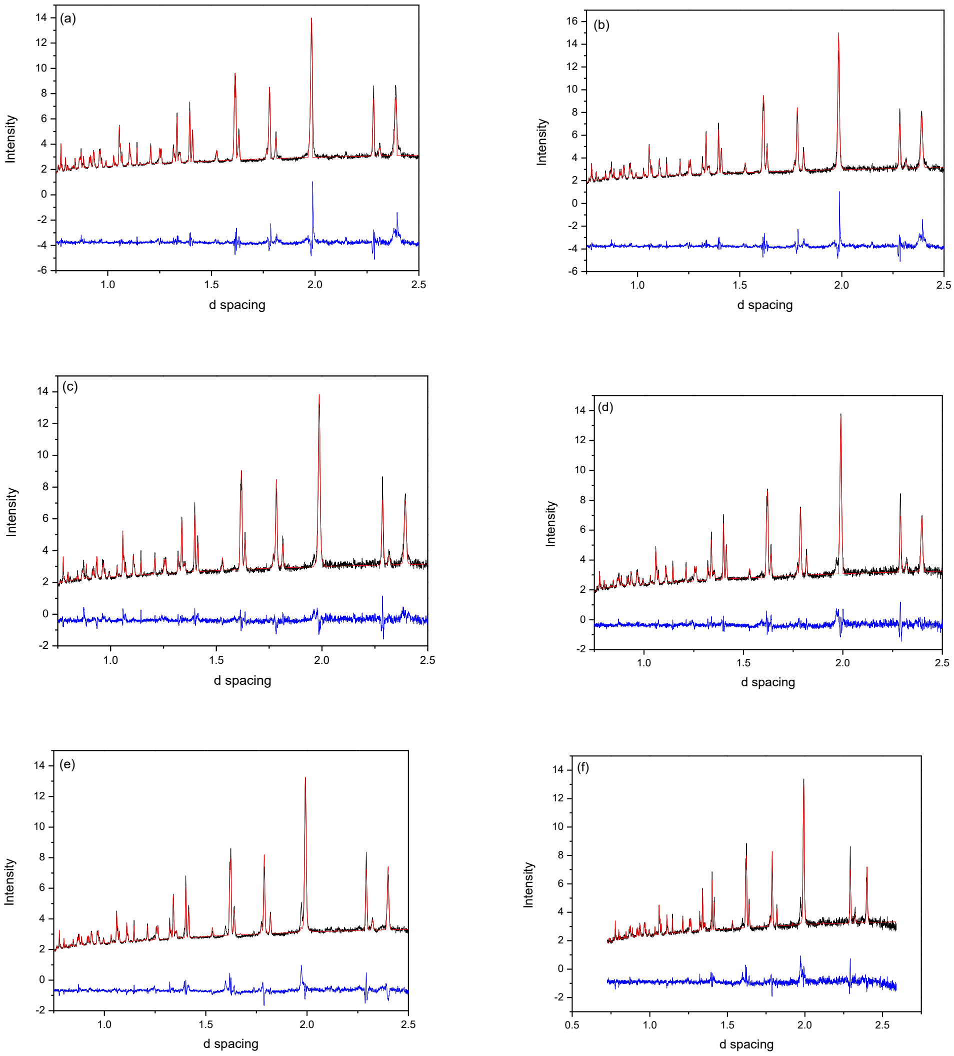

Figure 6.4: *Rietveld refinement profiles between 0.75Å and 2.5Å for neutron diffraction data collected for of* $Bi_{0.95}Dy_{0.05}FeO_3$*, showing reasonable fits for both peak shape and intensity. The black line represents experimental data, the red line the fitted model, and the subsequent blue line the difference between the data and the fit. This refinement uses the R3c symmetry, and was recorded on the HRPD instrument at (a) 373K (b)473K (c) 573K (d) 673K (e) 773K (f) 778K*

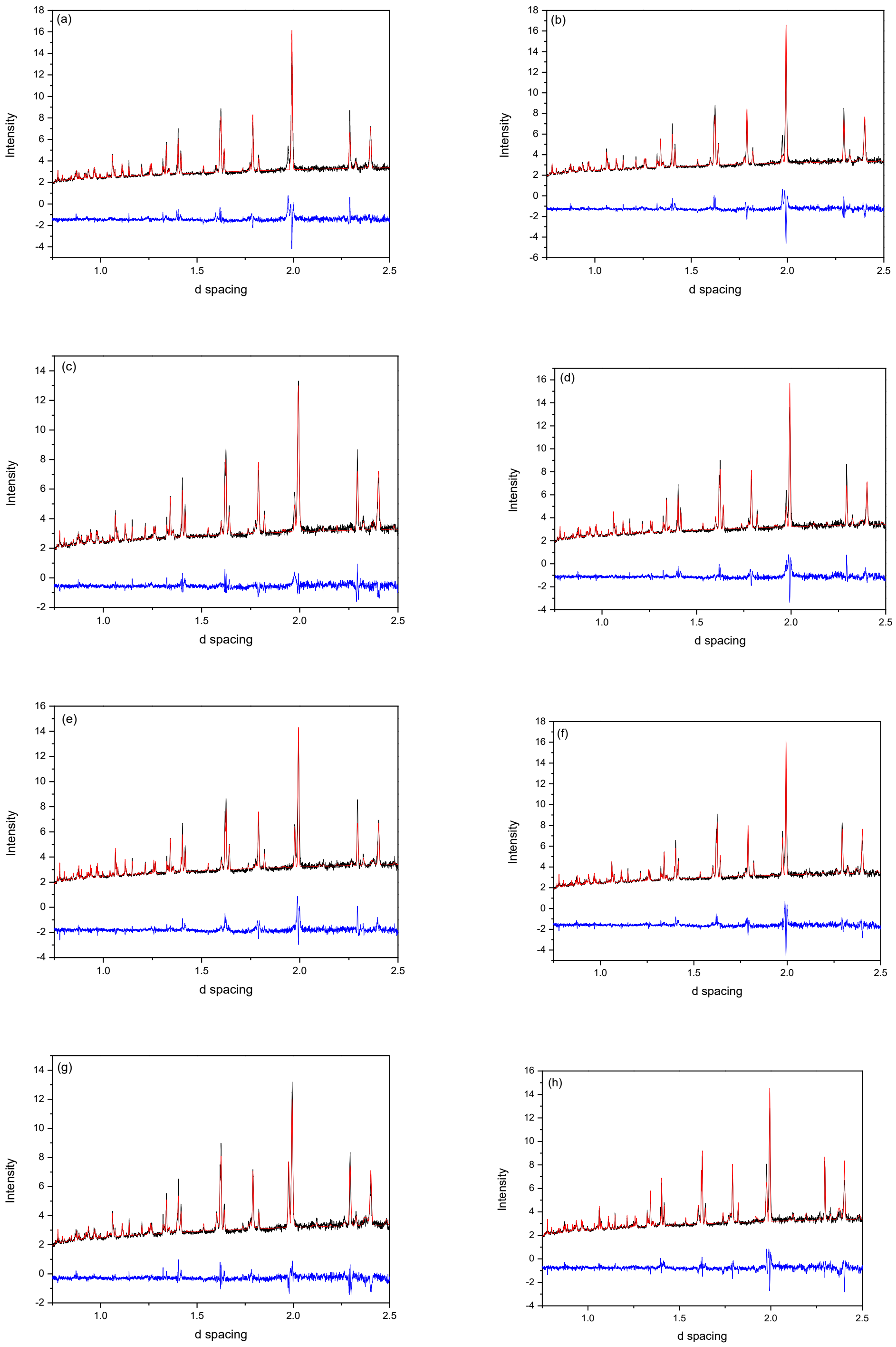

Figure 6.5: *Rietveld refinement profiles between 0.75Å and 2.5Å for neutron diffraction data collected for of* $Bi_{0.95}Dy_{0.05}FeO_3$*, showing reasonable fits for both peak shape and intensity. The black line represents experimental data, the red line the fitted model, and the subsequent blue line the difference between the data and the fit. This refinement uses the R3c and Pnma symmetries, and was recorded on the HRPD instrument at (a) 793K (b) 803K (c) 813K (d) 823K (e) 833K (f) 843K (g) 853K (h)863K*

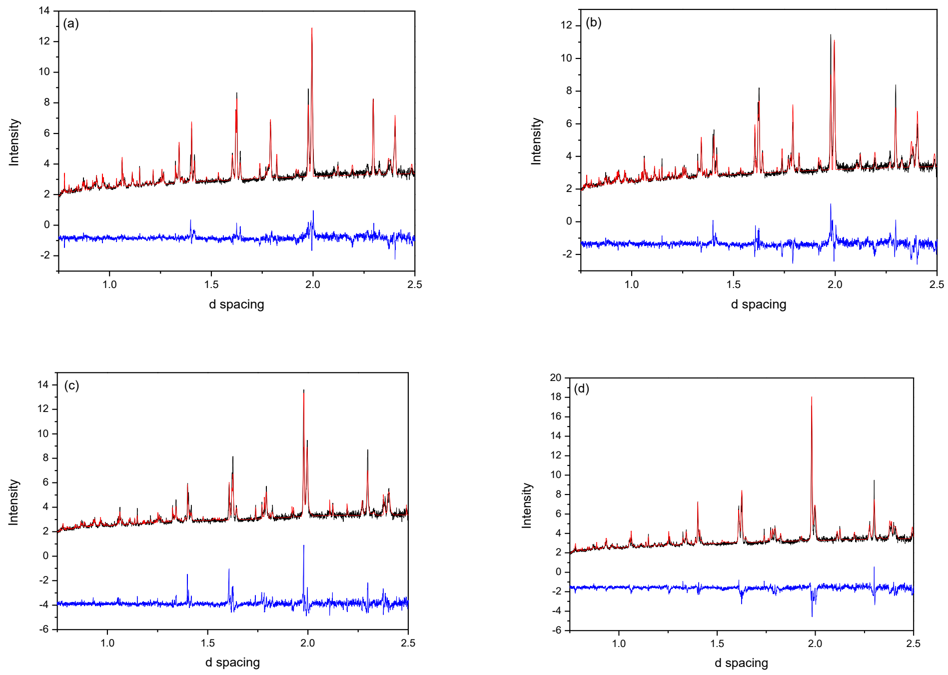

Figure 6.6: *Rietveld refinement profiles between 0.75Å and 2.5Å for neutron diffraction data collected for of* $Bi_{0.95}Dy_{0.05}FeO_{3,}$ *showing reasonable fits for both peak shape and intensity. The black line represents experimental data, the red line the fitted model, and the subsequent blue line the difference between the data and the fit. This refinement uses the R3c and Pnma symmetries, and was recorded on the HRPD instrument at (a) 873K (b) 893K (c) 903K (d) 923K (e) 973K*

***Table 6.3.1**: Table showing the lattice parameters and χ^2, wRp and Rp refinement parameters, along with the phase %, any secondary phases, M-O bond lengths and angles for the B site Fe^{3+} ion, cell volume and atomic positions and thermal information for room temperature refinements of $Bi_{1-x}Dy_xFeO_3$ compositions between x=0.08-0.25, partially refined in the R3c phase. All of this data was extracted from the GSAS refinement suite.*

$Bi_{1-x}Dy_xFeO_3$	x	8	10	14	20	25
Phase		*R3c*	*R3c*	*R3c*	*R3c*	*R3c*
Phase fraction *R3c*		0.91616	0.83613	0.61638	0.11739	0.0182
Lattice parameters	a	5.5709	5.5672	5.5711	5.5211	5.3924
	c	13.8416	13.8301	13.8440	13.5031	13.2723
a/c		2.484600972	2.484238277	2.48498529	2.445702902	2.461310162
M-O Bond Length	1	1.93549(2)	1.93954(3)	1.92810(3)	1.91700(4)	1.90200(11)
	2	2.13042(3)	2.10563(4)	2.13849(4)	2.07400(5)	2.05200(12)
M-O Bond Angle	1	164.675(0)	165.692(0)	165.135(0)	167.770(25)	168.210(25)
Atom Positions	A (0,0,0)	0.000000(0)	0.000000(0)	0.000000(0)	0.000000(0)	0.000000(0)
	Uiso	0.0128	0.0128	0.0128	0.0128	0.0128
	B (0,0,x)	0.2221880(0)	0.2221800(0)	0.2215640(0)	0.2218000(0)	0.2218000(0)
	Uiso	0.00297	0.00659	0.00659	0.00659	0.00659
		0.4400200(0)	0.4467200(0)	0.437650(0)	0.4467200(0)	0.4467200(0)
	O (x,x,x)	0.0157290(0)	0.0160300(0)	0.133920(0)	0.0160300(0)	0.0160300(0)
		0.9521340(0)	0.9534700(0)	0.9516660(0)	0.9534700(0)	0.9534700(0)
	Uiso	0.00721	0.01225	0.0250	0.0250	0.0250
Occupancy	Bi	0.92	0.90	0.86	0.80	0.75
	Dy	0.08	0.10	0.14	0.20	0.25
χ ^2		20.66	16.95	13.82	3.06	3.98
Fitted	wRp	0.1083	0.0968	0.0954	0.0702	0.1091
	Rp	0.1084	0.1101	0.0973	0.0652	0.1035

***Table 6.3.2**: Table showing the lattice parameters and χ^2, wRp and Rp refinement parameters, along with the phase %, any secondary phases, M-O bond lengths and angles for the B site Fe^{3+} ion, cell volume and atomic positions and thermal information for room temperature refinements of $Bi_{1-x}Dy_xFeO_3$ compositions between x=0.08-0.25, partially refined in the Pnma phase. All of this data was extracted from the GSAS refinement suite.*

$Bi_{1-x}Dy_xFeO_3$	**x**	**8**	**10**	**14**	**20**	**25**
Phase		*Pnma*	*Pnma*	*Pnma*	*Pnma*	*Pnma*
Phase fraction *Pnma*		0.08384	0.16387	0.38362	0.8826	0.9818
Lattice parameters	**a**	5.6310	5.6224	5.6200	5.6299	5.6272
	b	7.7936	7.8066	7.8106	7.7942	7.7604
	c	5.4233	5.4215	5.4174	5.4217	5.4015
c/a		0.963119032	0.964260916	0.963952249	0.963016915	0.959897803
M-O Bond Length	**1**	2.06461(3)	2.06260(9)	2.04939(35)	2.04798(4)	2.04192(32)
	2	2.04556(4)	2.04560(5)	2.04506(31)	2.04564(6)	2.0413(24)
	3	2.04821(3)	2.04770(4)	2.04606(28)	2.04778(5)	2.04509(26)
Atom Positions		0.0666500(0)	0.0666500(0)	0.0666500(0)	0.0666500(0)	0.0537820(0)
	A (x,y,z)	0.2500000(0)	0.2500000(0)	0.2500000(0)	0.2500000(0)	0.2500000(0)
		-0.01725(0)	-0.01725(0)	-0.01725(0)	-0.01725(0)	-0.010047(0)
	Uiso	0.01000	0.01000	0.00074	0.01000	0.0079
	B (0,0,z)	0.5000000(0)	0.5000000(0)	0.5000000(0)	0.5000000(0)	0.500000(0)
	Uiso	0.01000	0.01000	0.0070	0.01000	0.0038
		0.4626000(0)	0.4626000(0)	0.4626000(0)	0.4626000(0)	0.4741700(0)
	O1 (x,y,z)	0.2500000(0)	0.2500000(0)	0.2500000(0)	0.2500000(0)	0.2500000(0)
		0.1081000(0)	0.1081000(0)	0.1081000(0)	0.1081000(0)	0.0959440(0)
	Uiso	0.01000	1.01000	0.00615	0.01000	0.0113
		-0.3033000(0)	-0.3033000(0)	-0.3033000(0)	-0.3033000(0)	-0.3029420(0)
	O2 (x,y,z)	-0.0557000(0)	-0.0557000(0)	-0.0557000(0)	-0.0557000(0)	-0.0491640(0)
		0.3075000(0)	0.3075000(0)	0.3075000(0)	0.3075000(0)	0.3109410(0)
	Uiso	0.01000	0.01000	0.01047	0.01000	0.0100
Occupancy	**Bi**	0.92	0.90	0.86	0.80	0.75
	Dy	0.08	0.10	0.14	0.20	0.25
χ ^2		20.66	16.95	13.82	3.06	3.98
Fitted	**wRp**	0.1083	0.0968	0.0954	0.0702	0.1091
	Rp	0.1084	0.1101	0.0973	0.0652	0.1035

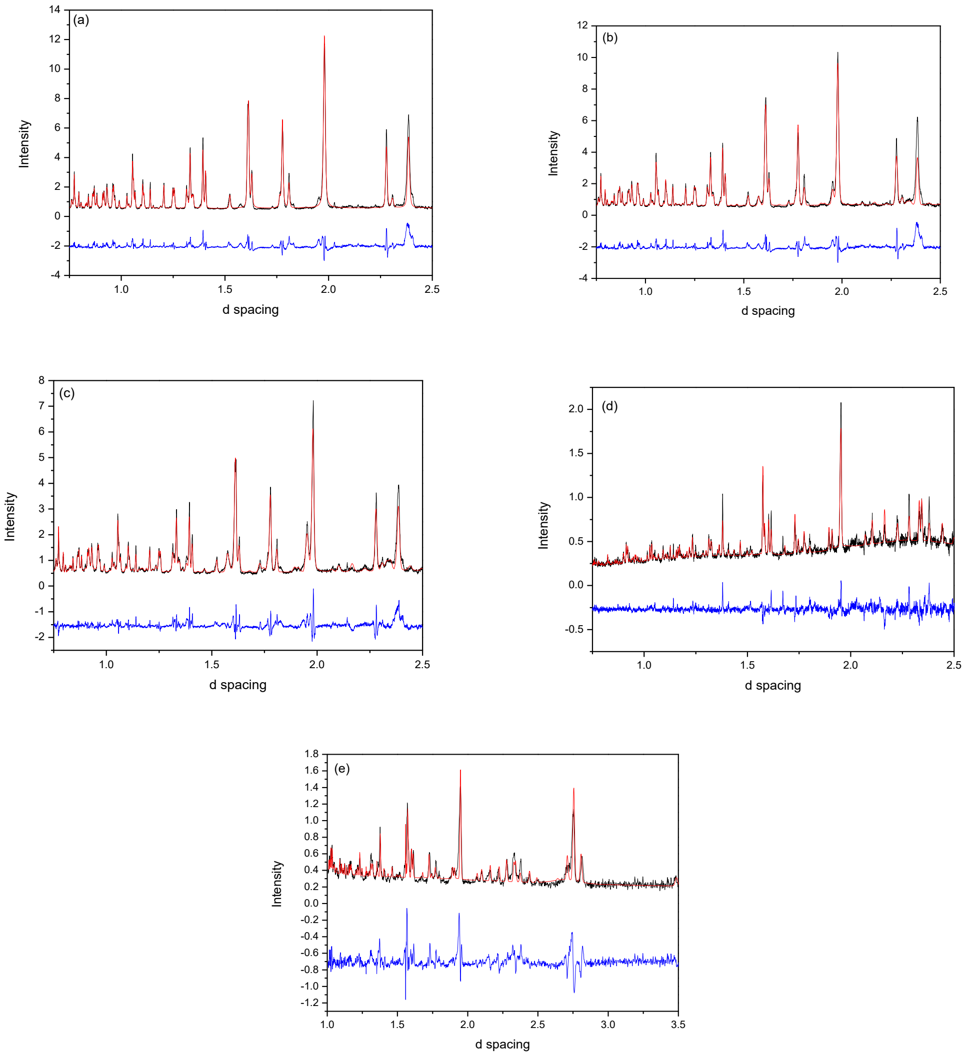

Figure 6.7: *Rietveld refinement profiles between 0.75Å and 2.5Å for neutron diffraction data collected for of* Bi$_{1-x}$Dy$_x$FeO$_3$, *showing reasonable fits for both peak shape and intensity. The black line represents experimental data, the red line the fitted model, and the subsequent blue line the difference between the data and the fit. This refinement uses the R3c and Pnma symmetries, and was recorded on the HRPD instrument at room temperature for compositions of x= (a) 0.08 (b) 0.10 (c) 0.14 (d) 0.20 (e) 0.25 (which is shown from 1.0 -3.5 Å*

Data for the $Bi_{0.70}Dy_{0.30}FeO_3$ was recorded on the HRPD instrument across a temperature range of 10-773K.

***Table 6.4.1**: Table showing the lattice parameters and χ^2, wRp and Rp refinement parameters, along with the phase %, any secondary phases, M-O bond lengths and angles for the B site Fe^{3+} ion, cell volume and atomic positions and thermal information for $Bi_{0.70}Dy_{0.30}FeO_3$ refined in the Pnma symmetry. All of this data was extracted from the GSAS refinement suite.*

$Bi_{0.70}Dy_{0.30}FeO_3$	Temp	10	50	75	100
Phase		*Pnma*	*Pnma*	*Pnma*	*Pnma*
	Secondary phase	*Pnma*	*Pnma*	*Pnma*	*Pnma*
Lattice parameters	a	5.6156	5.6166	5.6173	5.6181
	b	7.7743	7.7744	7.7738	7.7737
	c	5.4017	5.4011	5.401	5.401
c/a		0.96190968	0.961631592	0.961493956	0.961357042
M-O	1	2.01760(12)	2.01762(12)	2.01747(12)	2.01744(13)
	2	2.01542(10)	2.01561(11)	2.01577(10)	2.01598(10)
	3	2.05675(10)	2.05670(10)	2.05673(10)	2.05682(10)
Cell Volume		235.825	235.843	235.847	235.878
Atom Positions	A (x,y,z)	0.0513400(0) 0.2500000(0) -0.01109(0)	0.0513400(0) 0.2500000(0) -0.01109(0)	0.0513400(0) 0.2500000(0) -0.01109(0)	0.0513400(0) 0.2500000(0) -0.01109(0)
	Uiso	0.01332	0.01332	0.01332	0.01332
	B (0,0,z)	0.5000000(0)	0.5000000(0)	0.5000000(0)	0.5000000(0)
	Uiso	0.00507	0.00507	0.00507	0.00507
	O (x,y,z)	0.4743200(0) 0.2500000(0) 0.0966300(0)	0.4743200(0) 0.2500000(0) 0.0966300(0)	0.4743200(0) 0.2500000(0) 0.0966300(0)	0.4743200(0) 0.2500000(0) 0.0966300(0)
	Uiso	0.00742	0.00742	0.00742	0.00742
	O (x,x,x)	-0.3031300(0)	-0.3031300(0)	-0.3031300(0)	-0.3031300(0)
		-0.0491400(0)	-0.0491400(0)	-0.0491400(0)	-0.0491400(0)
		0.3131900(0)	0.3131900(0)	0.3131900(0)	0.3131900(0)
	Uiso	0.01586	0.01586	0.01586	0.01586
χ ^2		6.71	4.729	4.473	4.204
Fitted	wRp	0.0462	0.0474	0.0461	0.0446
	Rp	0.0382	0.041	0.0393	0.0387

***Table 6.4.2**: Table showing the lattice parameters and χ^2, wRp and Rp refinement parameters, along with the phase %, any secondary phases, M-O bond lengths and angles for the B site Fe^{3+} ion, cell volume and atomic positions and thermal information for $Bi_{0.70}Dy_{0.30}FeO_3$ refined in the Pnma symmetry. All of this data was extracted from the GSAS refinement suite.*

$Bi_{0.70}Dy_{0.30}FeO_3$	**Temp**	**125**	**150**	**200**	**293**
Phase		*Pnma*	*Pnma*	*Pnma*	*Pnma*
	Secondary phase	*Pnma*	*Pnma*	*Pnma*	*Pnma*
Lattice parameters	**a**	5.6191	5.6204	5.6215	5.6258
	b	7.7725	7.7745	7.7785	7.7858
	c	5.4036	5.4037	5.4067	5.4163
c/a		0.961648663	0.961444025	0.961789558	0.962760852
M-O	**1**	2.01722(12)	2.01772(10)	2.01874(11)	2.02039(13)
	2	2.01648(10)	2.01683(6)	2.01742(9)	2.01916(13)
	3	2.05759(8)	2.05777(7)	2.05870(8)	2.06105(11)
Cell Volume		235.999	236.119	236.415	237.084
Atom Positions	**A (x,y,z)**	0.0513400(0) 0.2500000(0) -0.01109(0)	0.0513400(0) 0.2500000(0) -0.01109(0)	0.0513400(0) 0.2500000(0) -0.01109(0)	0.0513400(0) 0.2500000(0) -0.01109(0)
	Uiso	0.01332	0.01332	0.01332	0.01332
	B (0,0,z)	0.5000000(0)	0.5000000(0)	0.5000000(0)	0.5000000(0)
	Uiso	0.00507	0.00507	0.00507	0.00507
	O (x,y,z)	0.4743200(0) 0.2500000(0) 0.0966300(0)	0.4743200(0) 0.2500000(0) 0.0966300(0)	0.4743200(0) 0.2500000(0) 0.0966300(0)	0.4743200(0) 0.2500000(0) 0.0966300(0)
	Uiso	0.00742	0.00742	0.00742	0.00742
	O (x,x,x)	-0.3031300(0)	-0.3031300(0)	-0.3031300(0)	-0.3031300(0)
		-0.0491400(0)	-0.0491400(0)	-0.0491400(0)	-0.0491400(0)
		0.3131900(0)	0.3131900(0)	0.3131900(0)	0.3131900(0)
	Uiso	0.01586	0.01586	0.01586	0.01586
χ ^2		4.259	3.621	3.982	3.476
Fitted	**wRp**	0.045	0.0413	0.0434	0.0405
	Rp	0.0375	0.0368	0.0386	0.0373

***Table 6.4.3**: Table showing the lattice parameters and χ^2, wRp and Rp refinement parameters, along with the phase %, any secondary phases, M-O bond lengths and angles for the B site Fe^{3+} ion, cell volume and atomic positions and thermal information for $Bi_{0.70}Dy_{0.30}FeO_3$ refined in the Pnma symmetry. All of this data was extracted from the GSAS refinement suite.*

$Bi_{0.70}Dy_{0.30}FeO_3$	Temp	300	473	573
Phase		*Pnma*	*Pnma*	*Pnma*
	Secondary phase	*Pnma*	*Pnma*	*Pnma*
Lattice parameters	a	5.6217	5.625	5.6293
	b	7.7797	7.7872	7.7983
	c	5.409	5.4162	5.4277
c/a		0.96216447	0.96288	0.964187377
M-O	1	2.02075(10)	2.02038(19)	2.02810(4)
	2	2.01948(8)	2.01967(11)	2.02649(25)
	3	2.06168(7)	2.06188(13)	2.07233(28)
Cell Volume		237.237	237.239	239.887
Atom Positions	A (x,y,z)	0.051340(0) 0.250000(0) -0.01109(0)	0.051340(0) 0.250000(0) -0.01109(0)	0.0513400(0) 0.250000(0) -0.01109(0)
	Uiso	0.01332	0.01332	0.01332
	B (0,0,z)	0.5000000(0)	0.5000000(0)	0.500000(0)
	Uiso	0.00507	0.00507	0.00507
	O (x,y,z)	0.474320(0) 0.250000(0) 0.096630(0)	0.474320(0) 0.250000(0) 0.096630(0)	0.474320(0) 0.250000(0) 0.096630(0)
	Uiso	0.00742	0.00742	0.00742
	O (x,x,x)	-0.303130(0)	-0.303130(0)	-0.303130(0)
		-0.049140(0)	-0.049140(0)	-0.049140(0)
		0.313190(0)	0.313190(0)	0.313190(0)
	Uiso	0.01586	0.01586	0.01586
χ ^2		9.01	7.085	6.377
Fitted	wRp	0.0376	0.0373	0.0354
	Rp	0.0299	0.0297	0.0282

Table 6.4.4: *Table showing the lattice parameters and* χ^2*, wRp and Rp refinement parameters, along with the phase %, any secondary phases, M-O bond lengths and angles for the B site* Fe^{3+} *ion, cell volume and atomic positions and thermal information for* $Bi_{0.70}Dy_{0.30}FeO_3$ *refined in the Pnma symmetry. All of this data was extracted from the GSAS refinement suite.*

$Bi_{0.70}Dy_{0.30}FeO_3$	Temp	673	773
Phase		*Pnma*	*Pnma*
	Secondary phase	*Pnma*	*Pnma*
Lattice parameters	a	5.6344	5.6437
	b	7.8116	7.8308
	c	5.4396	5.4716
c/a		0.965426665	0.969505821
M-O	1	2.03009(35)	2.03323(33)
	2	2.02594(28)	2.02865(22)
	3	2.07139(26)	2.07529(24)
Cell Volume		240.226	241.373
Atom Positions		0.051340(0)	0.0513400(0)
	A (x,y,z)	0.250000(0)	0.2500000(0)
		-0.01109(0)	-0.01109(0)
	Uiso	0.01332	1.01332
	B (0,0,z)	0.5000000(0)	0.500000(0)
	Uiso	0.00507	1.00507
		0.474320(0)	0.474320(0)
	O (x,y,z)	0.250000(0)	0.250000(0)
		0.096630(0)	0.096630(0)
	Uiso	0.00742	1.00742
		-0.303130(0)	-0.303130(0)
	O (x,x,x)	-0.049140(0)	-0.049140(0)
		0.313190(0)	0.313190(0)
	Uiso	0.01586	1.01586
χ ^2		5.731	9.098
Fitted	wRp	0.0336	0.0377
	Rp	0.0275	0.0252

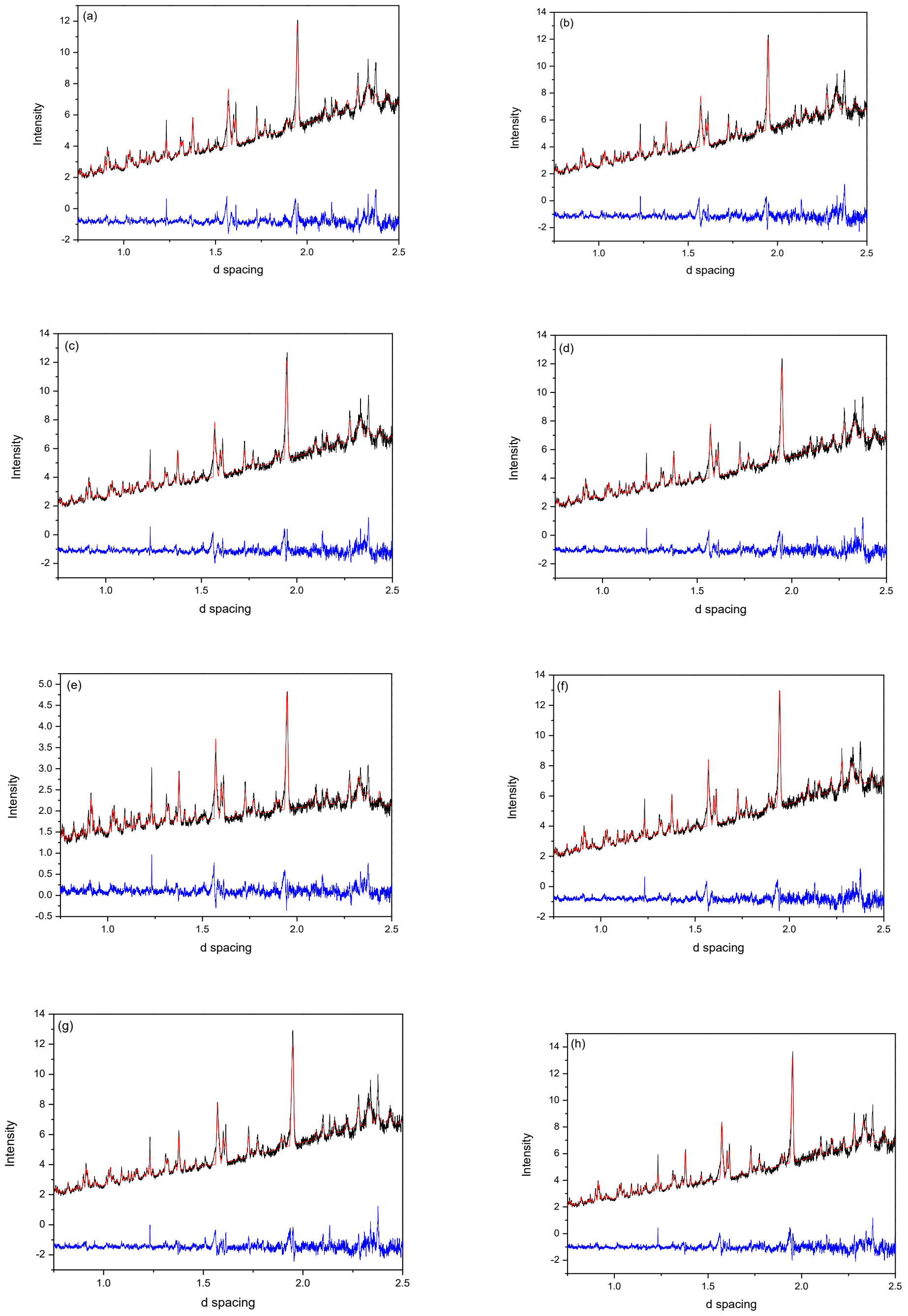

Figure 6.8: *Rietveld refinement profiles between 0.75Å and 2.5Å for neutron diffraction data collected for of* $Bi_{0.70}Dy_{0.030}FeO_{3,}$ *showing reasonable fits for both peak shape and intensity. The black line represents experimental data, the red line the fitted model, and the subsequent blue line the difference between the data and the fit. This refinement uses the Pnma symmetry, and was recorded on the HRPD instrument using a cryostat to regulate temperatures of (a)10K (b) 50K (c) 75 (d) 100K (e) 125K (f) 150K (g) 200K (h) 300K*

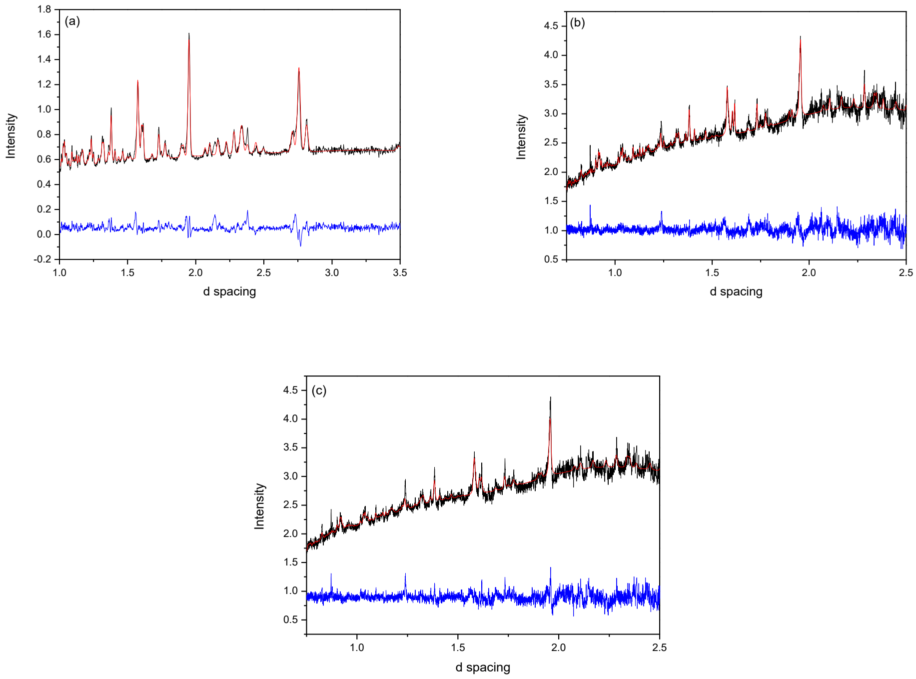

Figure 6.9: *Rietveld refinement profiles between 1.0Å and 3.5Å for neutron diffraction data collected for of* $Bi_{0.70}Dy_{0.030}FeO_{3,}$ *showing reasonable fits for both peak shape and intensity. The black line represents experimental data, the red line the fitted model, and the subsequent blue line the difference between the data and the fit. As can be seen, the Bank 1 data gradually degrade in quality as peak broadening occurs, due to Dysprosium absorption, this resulted in the inability to refine higher temperature data in Bank 1. This refinement uses the Pnma symmetry, and was recorded on the HRPD instrument using a furnace to regulate temperatures of (a)373K (b) 473K (c) 573*

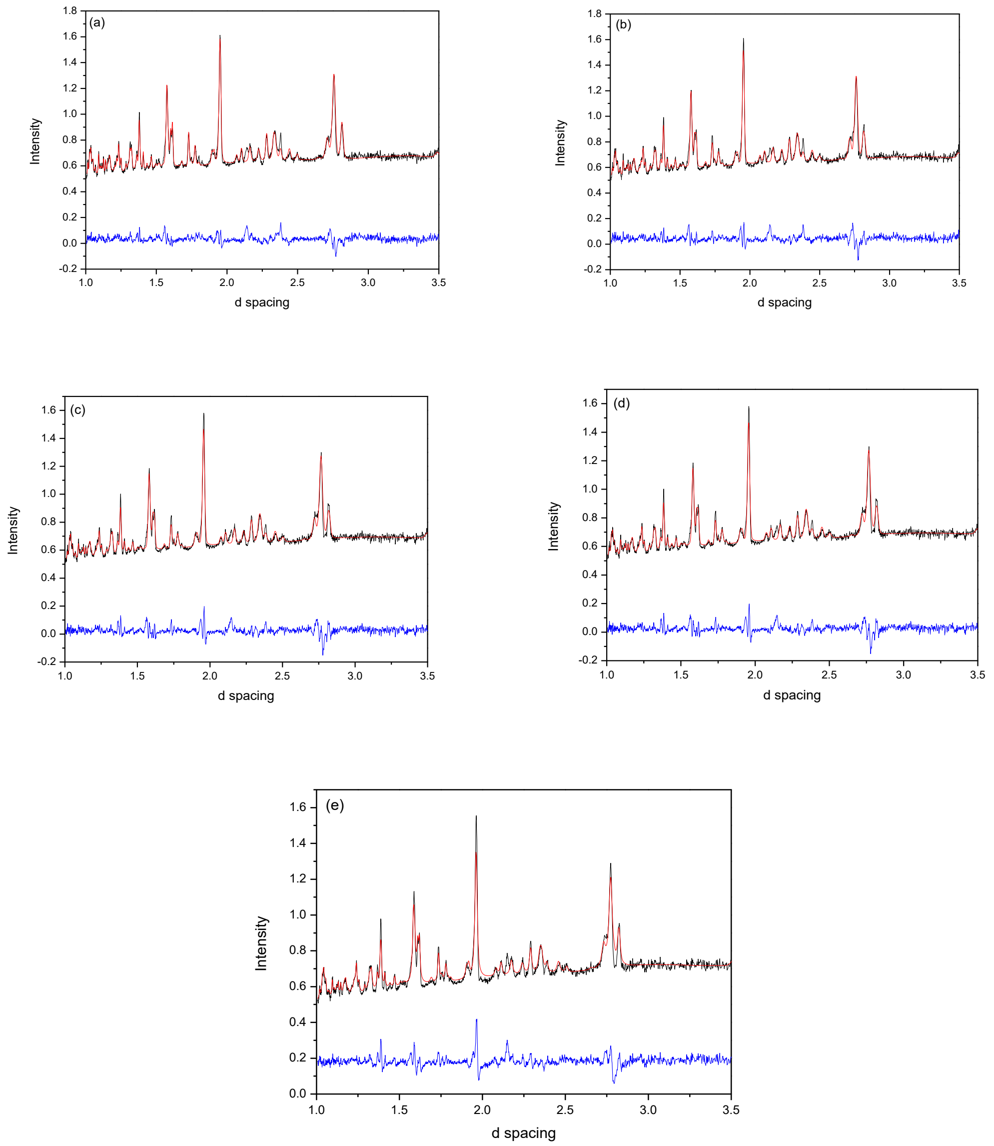

Figure 6.10: *Rietveld refinement profiles between 1.0Å and 3.5Å for neutron diffraction data collected for of* $Bi_{0.70}Dy_{0.030}FeO_3$*, showing reasonable fits for both peak shape and intensity. The black line represents experimental data, the red line the fitted model, and the subsequent blue line the difference between the data and the fit. These refinements show the Bank 2 data, as the quality of Bank 1 was poor due to absorption effects. This refinement uses the Pnma symmetry, and was recorded on the HRPD instrument using a furnace to regulate temperatures of (a)373K (b) 473K (c) 573 (d) 673K (e) 773K*

Dielectric measurements were made on the pre-prepared10 mm pellets, which had been sintered for 3 hours at 850 ^{o}C, using an Agilent 4294A impedance analyser over a frequency range of approximately 100 Hz to 5 MHz and a temperature range of approximately 50 to 340 K using a cryostat and Carbolite furnace (cooling/heating rates of 2 Kmin-1). For dielectric measurements, platinum electrodes were applied to polished pellets using the Emitech K550x sputter coater.

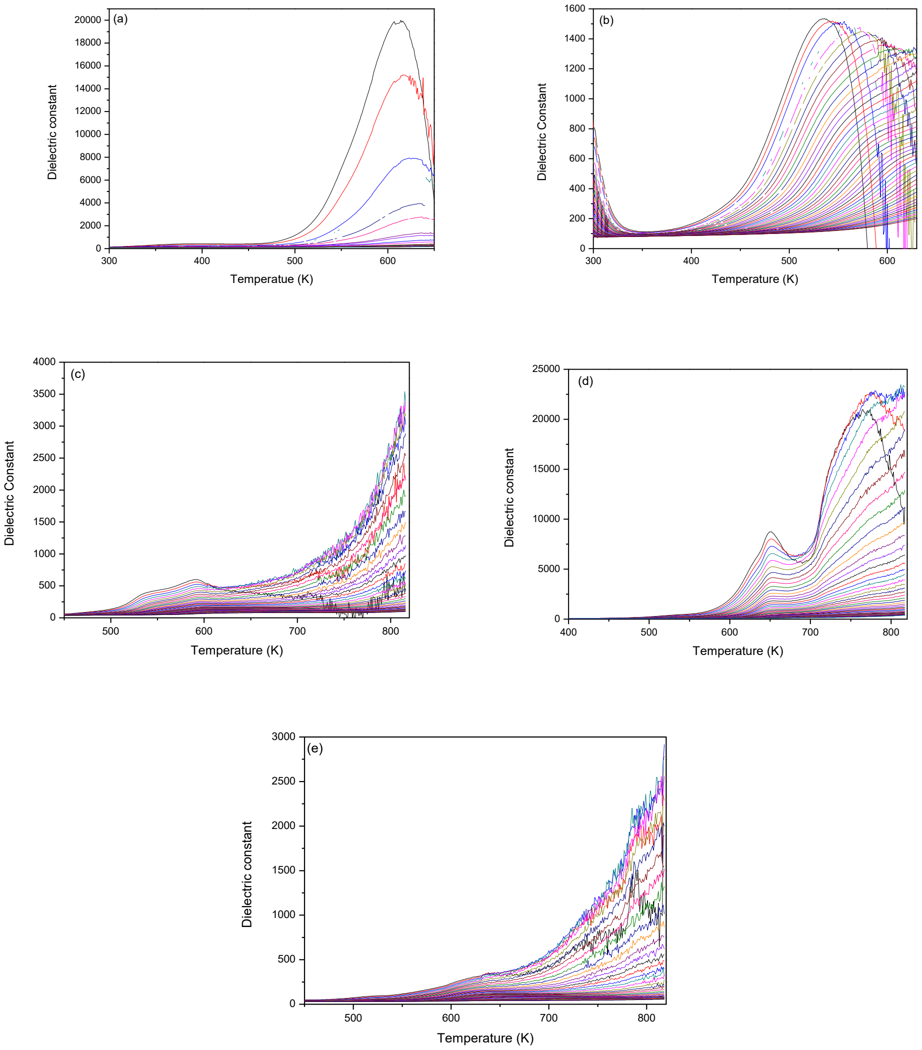

Figure 6.11: *Dielectric constant data collected for* $Bi_{1-x}Dy_xFeO_3$ *each colour represent the frequency at which the reading was taken between 100Hz and 10MHz. The data shows an anomaly between 600-700K, which links to the anti-ferromagnetic/paramagnetic phase transition, and a high permittivity relaxor like electrode effect. Data is shown for compositions of x= (a) 0.08 (b) 0.10 (c) 0.14 (d) 0.20 (e) 0.25*

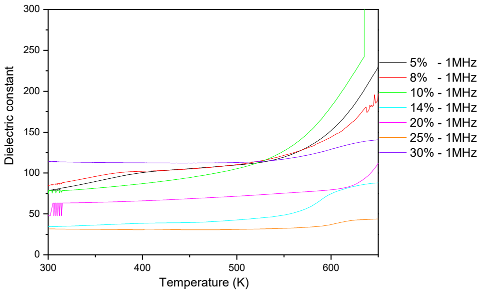

Figure 6.12: *Dielectric data collected for* $Bi_{1-x}Dy_xFeO_3$ *showing the 1MHz plots across the range of compositions from x=0.60-0.30. The data shows an anomaly between 600-700K, which links to the anti-ferromagnetic/paramagnetic phase transition, and a high permittivity relaxor like electrode effect.*

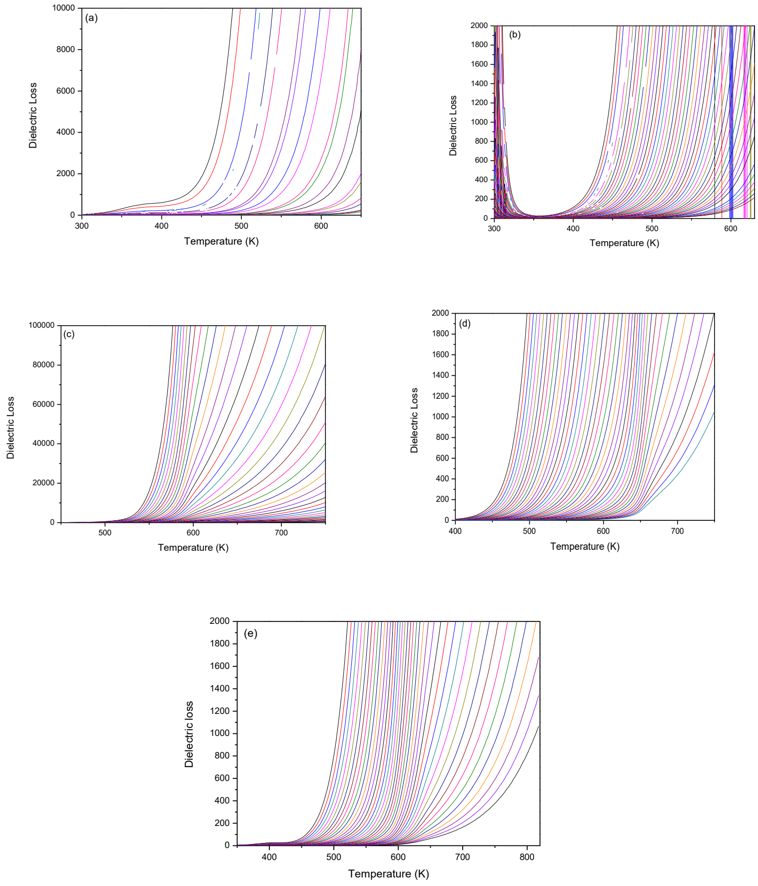

Figure 6.13: *Dielectric data showing the calculated dielectric loss data collected for* $Bi_{1-x}Dy_xFeO_3$ *each colour represent the frequency at which the reading was taken between 100Hz and 10MHz. The data shows shows a high permittivity relaxor like electrode effect. Data is shown for compositions of x= (a) 0.05 (b) 0.08 (c) 0.10 (d) 0.14 (e) 0.20 (f) 0.25*

SQUID magnetometry was performed using a Magnetic Property Measurement System (MPMS) XL-7 instrument. A temperature range of 2 K to 300 K was used in both zero field and in an applied field of 1000 Oe. Hysteresis behaviour was investigated at 120 K and 300 K in a variable field of approximately (+/-) 70000 Oe using a step size of 100 Oe between 0 and 1000 Oe, 500 Oe between 1000 Oe and 5000 Oe and 5000 Oe between 5000 Oe and 70000 Oe.

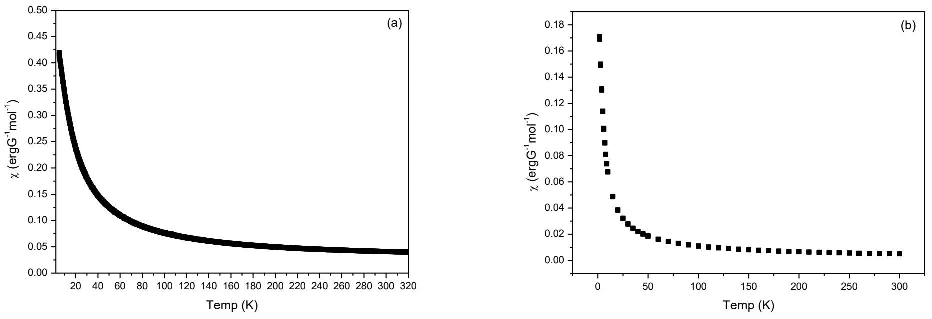

Figure 6.14: *SQUID data showing ZFC/FC data for (a)* $Bi_{0.95}Dy_{0.05}FeO_3$ *(b)* $Bi_{0.70}Dy_{0.30}FeO_3$

Appendix 6.2: Investigation of Bismuth Ferrite and Potassium Niobate co-doped materials.

***Table 6.5.1**: Table showing the lattice parameters and χ^2, wRp and Rp refinement parameters, along with the phase %, any secondary phases, M-O bond lengths and angles for the B site Fe^{3+} ion, cell volume and atomic positions and thermal information for PND data $Bi_{1-x}K_xFe_{1-x}Nb_xO_3$ refined in the R3c symmetry. All of this data was extracted from the GSAS refinement suite.*

$Bi_{1-x}K_xFe_{1-x}Nb_xO_3$	x	0.1	0.2
Phase		R3c	R3c
Lattice parameters	a	5.974500	5.639550
	b	5.974500	5.639550
	c	13.841510	13.814060
Tetragonality (c/a)		2.316765	2.449497
M-O	1	2.112750	2.023540
	2	1.948170	1.984850
Cell Volume		375.573	380.488
Atom Positions		0.0000	0.0000
	A	0.0000	0.0000
		0.0000	0.0000
		0.0197	0.0153
		0.0000	0.0000
	B	0.0000	0.0000
		0.2218	0.2105
		0.0042	0.0034
		0.4467	0.4902
	O	0.0160	0.0227
		0.9535	0.9516
		0.0187	0.0123
Occupancy	Bi	0.823	0.7813
	K	0.177	0.2187
	Fe	0.8601	0.7794
	Nb	0.1399	0.2206
χ ^2		21.600	25.860
Fitted	wRp	0.1334	0.1703
	Rp	0.1197	0.1419
Background	wRp	0.1948	0.2553
	Rp	0.1644	0.2155
R(A cation)		1.379	1.408
R(Bcation)		0.645	0.644
Tolerance factor		0.961139518	0.971406968

***Table 6.5.2**: Table showing the lattice parameters and χ^2, wRp and Rp refinement parameters, along with the phase %, any secondary phases, M-O bond lengths and angles for the B site Fe^{3+} ion, cell volume and atomic positions and thermal information for PND data $Bi_{1-x}K_xFe_{1-x}Nb_xO_3$ refined in the P4mm symmetry. All of this data was extracted from the GSAS refinement suite.*

$Bi_{1-x}K_xFe_{1-x}Nb_xO_3$	x	0.4	0.5	0.6	0.7
Phase		P4mm	P4mm	P4mm	P4mm
Lattice parameters	a	4.000880	4.011634	4.005660	4.005733
	b	4.000880	4.011634	4.005660	4.005733
	c	3.999300	4.009461	4.011795	4.014028
Tetragonality (c/a)		0.999605	0.999458	1.001532	1.002071
M-O	1	2.109140	2.025130	2.050090	2.088560
	2	1.890160	1.984330	1.961710	1.925470
	3	2.007870	2.006210	2.004230	2.006370
Cell Volume		64.017	64.204	64.371	64.409
Atom Positions		0.0000	0.0000	0.0000	0.0000
	A	0.0000	0.0000	0.0000	0.0000
		0.0000	0.0000	0.0000	0.0000
		0.0871	0.0706	0.0624	0.0659
		0.5000	0.5000	0.5000	0.5000
	B	0.5000	0.5000	0.5000	0.5000
		0.4670	0.4609	0.4873	0.4820
		0.0046	0.0054	0.0141	0.0091
		0.5000	0.5000	0.5000	0.5000
	O	0.5000	0.5000	0.5000	0.5000
		-0.0603	-0.0441	-0.0238	-0.0881
		0.0100	0.0290	0.0273	0.0290
		0.5000	0.5000	0.5000	0.5000
	O	0.0000	0.0000	0.0000	0.0000
		0.5102	0.497602	0.46854	0.511519
		0.00777	0.01029	0.01287	0.00923
Occupancy	Bi	0.7379	0.4607	0.3571	0.2284
	K	0.2621	0.5393	0.6429	0.7716
	Fe	0.5835	0.4801	0.4418	0.2988
	Nb	0.4165	0.5199	0.5582	0.712
χ ^2		18.630	6.484	9.363	11.850
Fitted	wRp	0.1301	0.1008	0.1194	0.1339
	Rp	0.1142	0.0847	0.1005	0.1096
Background	wRp	0.1979	0.1397	0.1769	0.2019
	Rp	0.1979	0.1145	0.1538	0.1698
R(A cation)		1.466	1.495	1.524	1.553
R(Bcation)		0.643	0.643	0.642	0.642
Tolerance factor		0.991957	1.002239	1.012527	1.02282

***Table 6.5.3**: Table showing the lattice parameters and χ^2, wRp and Rp refinement parameters, along with the phase %, any secondary phases, M-O bond lengths and angles for the B site Fe^{3+} ion, cell volume and atomic positions and thermal information for PND data $Bi_{1-x}K_xFe_{1-x}Nb_xO_3$ refined in the Amm2 symmetry. All of this data was extracted from the GSAS refinement suite.*

$Bi_{1-x}K_xFe_{1-x}Nb_xO_3$	x	0.8	0.9
Phase		Amm2	Amm2
Lattice parameters	a	4.000484	4.002002
	b	5.680642	5.690044
	c	5.674353	5.681470
Tetragonality (c/a)		1.418417	1.419657
M-O	1	2.003920	2.007600
	2	2.029660	2.036860
	3	1.986750	1.988020
Cell Volume		128.951	129.376
Atom Positions		0.0000	0.0000
	A	0.0000	0.0000
		0.0229	0.0138
		0.0265	0.0037
		0.5000	0.5000
	B	0.0000	0.0000
		0.5412	0.5479
		0.0139	0.0038
		0.0000	0.0000
	O	0.0000	0.0000
		0.5198	0.5193
		0.0134	0.0051
		0.5000	0.5000
	O	0.2452	0.2413
		0.280992	0.283125
		0.00689	0.00431
Occupancy	Bi	0.1166	0.043
	K	0.8834	0.957
	Fe	0.142	0.0409
	Nb	0.858	0.9591
Χ ^2		6.802	4.076
Fitted	wRp	0.1054	0.0861
	Rp	0.0978	0.0807
Background	wRp	0.1422	0.1098
	Rp	0.1400	0.1076
R(A cation)		1.582	1.611
R(Bcation)		0.641	0.641
Tolerance factor		1.033117	1.04342

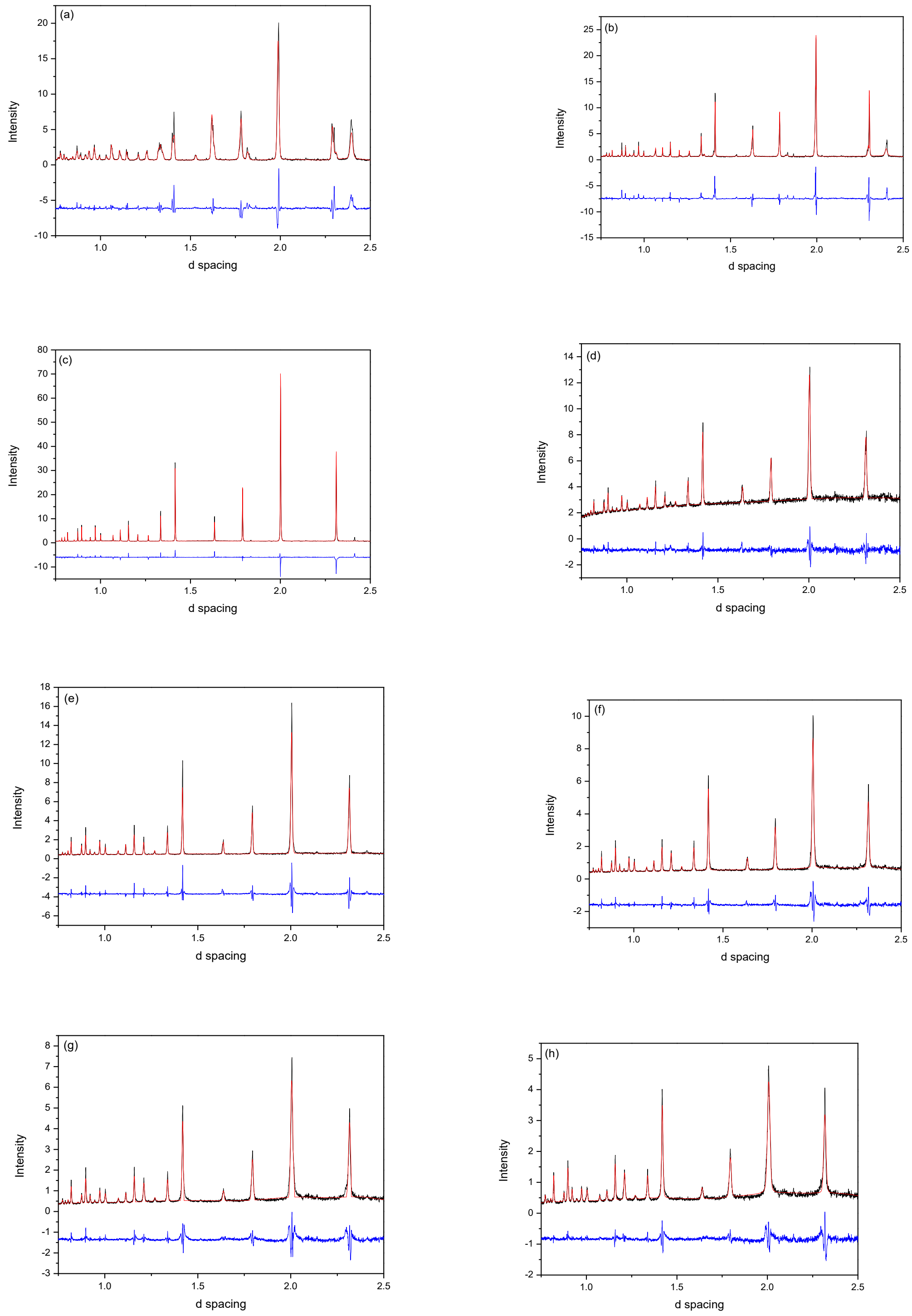

Figure 6.15: *Rietveld refinement profiles between 0.75Å and 2.5Å for neutron diffraction data collected for of $Bi_{1-x}K_xFe_{1-x}Nb_xO_3$, showing reasonable fits for both peak shape and intensity. The black line represents experimental data, the red line the fitted model, and the subsequent blue line the difference between the data and the fit. This refinement uses the P4mm symmetry, and was recorded on the HRPD instrument at for values of x= (a) 0.10 (b) 0.20 (c) 0.40 (d) 0.50 (e) 0.60 (f) 0.70 (g) 0.80 (h) 0.90*

***Table 6.6.1**: Table showing the lattice parameters and χ^2, wRp and Rp refinement parameters, along with the phase %, any secondary phases, M-O bond lengths and angles for the B site Fe^{3+} ion, cell volume and atomic positions and thermal information for PND data $Bi_{0.5}K_{0.5}Fe_{0.5}Nb_{0.5}O_3$ refined in the P4mm symmetry for a range of temperatures. All of this data was extracted from the GSAS refinement suite.*

$Bi_{1-x}K_xFe_{1-x}Nb_xO_3$	Temp(K)	9.0	15.0	20.0	25.0
Phase		P4mm	P4mm	P4mm	P4mm
Secondary Phase					
Lattice parameters	a	3.997680	4.001477	3.995952	3.997602
	b	3.997680	4.001477	3.995952	3.997602
	c	4.002981	4.006681	4.006057	4.001900
Tetragonality (c/a)		1.001326	1.001301	1.002529	1.001075
M-O	1	2.125100	2.005560	2.126740	2.065000
	2	1.877880	2.001120	1.879320	1.937000
	3	2.000380	2.002280	1.995200	2.003400
Cell Volume		63.973	64.154	63.967	63.954
Atom Positions	A (0,0,0)	0.0000 0.0000 0.0000	0.0000 0.0000 0.0000	0.0000 0.0000 0.0000	0.0000 0.0000 0.0000
	Uiso	0.0752	0.0805	0.0741	0.0951
	B (x,x,x)	0.5000 0.5000 0.4820	0.5000 0.5000 0.4820	0.5000 0.5000 0.4820	0.5000 0.5000 0.4671
	Uiso	0.0127	0.0112	0.0106	0.0239
	O (x,x,x)	0.5000 0.5000 -0.0489	0.5000 0.5000 -0.0186	0.5000 0.5000 -0.0482	0.5000 0.5000 -0.0489
	Uiso	0.0321	0.0428	0.0405	0.0337
	O (x,x,x)	0.5000 0.0000 0.5016	0.5000 0.0000 0.5016	0.5000 0.0000 0.5016	0.5000 0.0000 0.5010
	Uiso	0.0094	0.0113	0.0031	0.0290
Occupancy	Bi	0.478	0.498	0.478	0.478
	K	0.522	0.502	0.497	0.497
	Fe	0.497	0.497	0.522	0.522
	Nb	0.503	0.503	0.503	0.503
χ ^2		11.310	4.840	7.530	8.477
Fitted	wRp	0.0750	0.0654	0.0805	0.0865
	Rp	0.0555	0.0504	0.0633	0.0639
Background	wRp	0.1250	0.1131	0.1340	0.1511
	Rp	0.0997	0.0876	0.1098	0.1148
R(A cation)		1.495	1.495	1.495	1.495
R(Bcation)		0.643	0.643	0.643	0.643
Tolerance factor		1.002239	1.002239	1.002239	1.002239

Table 6.6.2: *Table showing the lattice parameters and* χ^2*, wRp and Rp refinement parameters, along with the phase %, any secondary phases, M-O bond lengths and angles for the B site* Fe^{3+} *ion, cell volume and atomic positions and thermal information for PND data* $Bi_{0.5}K_{0.5}Fe_{0.5}Nb_{0.5}O_3$ *refined in the P4mm symmetry for a range of temperatures. All of this data was extracted from the GSAS refinement suite.*

$Bi_{1-x}K_xFe_{1-x}Nb_xO_3$	Temp(K)	30.0	50.0	100.0	150.0
Phase		P4mm	P4mm	P4mm	P4mm
Secondary Phase					
Lattice parameters	a	3.997502	3.997366	3.998410	3.999641
	b	3.997502	3.997366	3.998410	3.999641
	c	4.003536	4.004219	4.003540	4.003456
Tetragonality (c/a)		1.001509	1.001714	1.001283	1.000954
M-O	1	2.251000	2.125760	2.125400	2.125350
	2	1.878140	1.878460	1.878140	1.878100
	3	2.000290	2.000220	2.000740	2.001360
Cell Volume		63.977	63.983	64.006	64.044
Atom Positions	A (0,0,0)	0.0000 0.0000 0.0000	0.0000 0.0000 0.0000	0.0000 0.0000 0.0000	0.0000 0.0000 0.0000
	Uiso	0.0744	0.0764	0.0763	0.0800
	B (x,x,x)	0.5000 0.5000 0.4820	0.5000 0.5000 0.4820	0.5000 0.5000 0.4820	0.5000 0.5000 0.4820
	Uiso	0.0105	0.0123	0.0133	0.0139
	O (x,x,x)	0.5000 0.5000 -0.0489	0.5000 0.5000 -0.0489	0.5000 0.5000 -0.0489	0.5000 0.5000 -0.0489
	Uiso	0.0265	0.0396	0.0342	0.0344
	O (x,x,x)	0.5000 0.0000 0.5000	0.5000 0.0000 0.5016	0.5000 0.0000 0.5016	0.5000 0.0000 0.5016
	Uiso	0.0100	0.0059	0.0094	0.0100
Occupancy	Bi	0.478	0.478	0.478	0.478
	K	0.522	0.522	0.522	0.522
	Fe	0.497	0.497	0.497	0.497
	Nb	0.503	0.503	0.503	0.503
χ ^2		6.299	6.593	13.540	7.749
Fitted	wRp	0.0749	0.0766	0.0819	0.0830
	Rp	0.0580	0.0595	0.0657	0.0680
Background	wRp	0.1256	0.1267	0.1239	0.1219
	Rp	0.0999	0.1012	0.0970	0.0978
R(A cation)		1.495	1.495	1.495	1.495
R(Bcation)		0.643	0.643	0.643	0.643
Tolerance factor		1.002239	1.002239	1.002239	1.002239

***Table 6.6.3**: Table showing the lattice parameters and* χ^2*, wRp and Rp refinement parameters, along with the phase %, any secondary phases, M-O bond lengths and angles for the B site* Fe^{3+} *ion, cell volume and atomic positions and thermal information for PND data* $Bi_{0.5}K_{0.5}Fe_{0.5}Nb_{0.5}O_3$ *refined in the P4mm symmetry for a range of temperatures. All of this data was extracted from the GSAS refinement suite.*

$Bi_{1-x}K_xFe_{1-x}Nb_xO_3$	**Temp(K)**	200.0	250.0	300 Furnace	323.0
Phase		P4mm	P4mm	P4mm	P4mm
Secondary Phase					
Lattice parameters	**a**	4.001858	4.001477	4.002341	4.003908
	b	4.001858	4.001477	4.002341	4.003908
	c	4.002466	4.006681	4.009512	4.008849
Tetragonality (c/a)		1.000152	1.001301	1.0017917	1.001234
M-O	**1**	2.124800	2.005560	2.128570	2.128220
	2	1.877600	2.001120	1.880940	1.880630
	3	2.002470	2.002280	2.002710	2.003490
Cell Volume		64.099	64.154	64.227	64.267
Atom Positions	**A (0,0,0)**	0.0000 0.0000 0.0000	0.0000 0.0000 0.0000	0.0000 0.0000 0.0000	0.0000 0.0000 0.0000
	Uiso	0.0827	0.0805	0.0804	0.0803
	B (x,x,x)	0.5000 0.5000 0.4820	0.5000 0.5000 0.4820	0.5000 0.5000 0.4820	0.5000 0.5000 0.4820
	Uiso	0.0170	0.0112	0.0144	0.0179
	O (x,x,x)	0.5000 0.5000 -0.0489	0.5000 0.5000 -0.0186	0.5000 0.5000 -0.0489	0.5000 0.5000 -0.0489
	Uiso	0.0440	0.0428	0.0452	0.0557
	O (x,x,x)	0.5000 0.0000 0.5016	0.5000 0.0000 0.5016	0.5000 0.0000 0.5016	0.5000 0.0000 0.5016
	Uiso	0.0100	0.0113	0.0082	0.0054
Occupancy	**Bi**	0.478	0.478	0.478	0.478
	K	0.522	0.522	0.522	0.522
	Fe	0.497	0.497	0.497	0.497
	Nb	0.503	0.503	0.503	0.503
χ ^2		7.554	4.840	2.497	3.091
Fitted	**wRp**	0.0818	0.0654	0.0400	0.0446
	Rp	0.0664	0.0504	0.0342	0.0384
Background	**wRp**	0.1454	0.1131	0.0797	0.0828
	Rp	0.1322	0.0876	0.0604	0.0648
R(A cation)		1.495	1.495	1.495	1.495
R(Bcation)		0.643	0.643	0.643	0.643
Tolerance factor		1.002239	1.002239	1.002239	1.002239

Table 6.6.4: *Table showing the lattice parameters and χ^2, wRp and Rp refinement parameters, along with the phase %, any secondary phases, M-O bond lengths and angles for the B site Fe^{3+} ion, cell volume and atomic positions and thermal information for PND data $Bi_{0.5}K_{0.5}Fe_{0.5}Nb_{0.5}O_3$ refined in the P4mm symmetry for a range of temperatures. All of this data was extracted from the GSAS refinement suite.*

$Bi_{1-x}K_xFe_{1-x}Nb_xO_3$	**Temp(K)**	373.0	423.0	448.0	473.0
Phase		P4mm	P4mm	P4mm	P4mm
Secondary Phase					
Lattice parameters	**a**	4.004974	4.006922	4.008042	4.011930
	b	4.004974	4.006922	4.008042	4.011930
	c	4.011472	4.012254	4.012662	4.006326
Tetragonality (c/a)		1.001622	1.001331	1.001153	0.998603
M-O	**1**	2.129610	2.130030	2.130240	2.126880
	2	1.881860	1.882230	1.882420	1.879450
	3	2.004030	2.005000	2.005560	2.007500
Cell Volume		64.343	64.418	64.461	64.484
Atom Positions	**A (0,0,0)**	0.0000 0.0000 0.0000	0.0000 0.0000 0.0000	0.0000 0.0000 0.0000	0.0000 0.0000 0.0000
	Uiso	0.0745	0.0816	0.0825	0.0752
	B (x,x,x)	0.5000 0.5000 0.4820	0.5000 0.5000 0.4820	0.5000 0.5000 0.4820	0.5000 0.5000 0.4820
	Uiso	0.0132	0.0180	0.0176	0.0153
	O (x,x,x)	0.5000 0.5000 -0.0489	0.5000 0.5000 0.0489	0.5000 0.5000 -0.0489	0.5000 0.5000 -0.0489
	Uiso	0.0456	0.0532	0.0599	0.0449
	O (x,x,x)	0.5000 0.0000 0.5016	0.5000 0.0000 0.5016	0.5000 0.0000 0.5016	0.5000 0.0000 0.5016
	Uiso	0.0107	0.0100	0.0100	0.0147
Occupancy	**Bi**	0.478	0.478	0.478	0.478
	K	0.522	0.522	0.522	0.522
	Fe	0.497	0.497	0.497	0.497
	Nb	0.503	0.503	0.503	0.503
χ ^2		2.220	2.945	4.143	2.888
Fitted	**wRp**	0.0392	0.0436	0.0328	0.0432
	Rp	0.0340	0.0386	0.0258	0.0382
Background	**wRp**	0.0753	0.0783	0.0741	0.0757
	Rp	0.0577	0.0618	0.0544	0.0603
R(A cation)		1.495	1.495	1.495	1.495
R(Bcation)		0.643	0.643	0.643	0.643
Tolerance factor		1.002239	1.002239	1.002239	1.002239

Table 6.6.5: *Table showing the lattice parameters and* χ^2*, wRp and Rp refinement parameters, along with the phase %, any secondary phases, M-O bond lengths and angles for the B site* Fe^{3+} *ion, cell volume and atomic positions and thermal information for PND data* $Bi_{0.5}K_{0.5}Fe_{0.5}Nb_{0.5}O_3$ *refined in the P4mm symmetry for a range of temperatures. All of this data was extracted from the GSAS refinement suite.*

$Bi_{1-x}K_xFe_{1-x}Nb_xO_3$	Temp(K)	498.0	523.0	548.0	573.0
Phase		P4mm	P4mm	P4mm	P4mm
Secondary Phase					
Lattice parameters	a	4.010857	4.010560	4.011896	4.012934
	b	4.010857	4.010560	4.011896	4.012934
	c	4.011445	4.014710	4.014561	4.016050
Tetragonality (c/a)		1.0001466	1.00103477	1.00066427	1.000776489
M-O	1	2.0888	2.13133	2.1313	2.13204
	2	1.8826	1.88338	1.88331	1.88401
	3	2.00898	2.00682	2.00749	2.00801
Cell Volume		64.532	64.575	64.616	64.673
Atom Positions	A (0,0,0)	0.0000	0.0000	0.0000	0.0000
		0.0000	0.0000	0.0000	0.0000
		0.0000	0.0000	0.0000	0.0000
	Uiso	0.0752	0.0752	0.0752	0.0752
	B (x,x,x)	0.5000	0.5000	0.5000	0.5000
		0.5000	0.5000	0.5000	0.5000
		0.4820	0.4820	0.4820	0.4820
	Uiso	0.0153	0.0153	0.0153	0.0153
	O (x,x,x)	0.5000	0.5000	0.5000	0.5000
		0.5000	0.5000	0.5000	0.5000
		-0.0489	-0.0489	-0.0489	-0.0489
	Uiso	0.0449	0.0449	0.0449	0.0449
	O (x,x,x)	0.5000	0.5000	0.5000	0.5000
		0.0000	0.0000	0.0000	0.0000
		0.5016	0.5016	0.5016	0.5016
	Uiso	0.0147	0.0147	0.0147	0.0147
Occupancy	Bi	0.478	0.478	0.478	0.478
	K	0.522	0.522	0.522	0.522
	Fe	0.497	0.497	0.497	0.497
	Nb	0.503	0.503	0.503	0.503
χ ^2		2.623	3.172	2.712	2.824
Fitted	wRp	0.0411	0.0338	0.0418	0.0426
	Rp	0.0363	0.0227	0.0373	0.0379
Background	wRp	0.0723	0.0701	0.0760	0.0750
	Rp	0.0579	0.0537	0.0611	0.0597
R(A cation)		1.495	1.495	1.495	1.495
R(Bcation)		0.643	0.643	0.643	0.643
Tolerance factor		1.002239	1.002239	1.002239	1.002239

Table 6.6.6: *Table showing the lattice parameters and* χ^2*, wRp and Rp refinement parameters, along with the phase %, any secondary phases, M-O bond lengths and angles for the B site* Fe^{3+} *ion, cell volume and atomic positions and thermal information for PND data* $Bi_{0.5}K_{0.5}Fe_{0.5}Nb_{0.5}O_3$ *refined in the P4mm symmetry for a range of temperatures. All of this data was extracted from the GSAS refinement suite.*

$Bi_{1-x}K_xFe_{1-x}Nb_xO_3$	**Temp(K)**	598.0	623.0	673.0	773.0	873.0
Phase		P4mm	P4mm	P4mm	P4mm	P4mm
Secondary Phase					Amm2	Amm3
Lattice parameters	**a**	4.013026	4.016848	4.016203	4.026052	4.026218
	b	4.013026	4.016848	4.016203	4.026052	4.026218
	c	4.018052	4.012973	4.013142	4.016190	4.017634
Tetragonality (c/a)		1.001252421	0.99903531	0.99923784	0.99755045	0.997867974
M-O	**1**	2.13310(17)	2.13041(18)	2.13581(12)	2.16225(13)	2.16430(19)
	2	1.88495(15)	1.88257(16)	1.88734(11)	1.88072(12)	1.88320(17)
	3	2.00806(18)	2.00996(8)	2.00965(6)	2.02074(27)	2.02329(32)
Cell Volume		64.708	64.750	64.893	65.050	65.128
Atom Positions	**A (0,0,0)**	0.0000 0.0000 0.0000	0.0000 0.0000 0.0000	0.0000 0.0000 0.0000	0.0000 0.0000 0.0000	0.0000 0.0000 0.0000
	Uiso	0.0752	0.0752	0.0752	0.0752	0.0752
	B (x,x,x)	0.5000 0.5000 0.4820	0.5000 0.5000 0.4820	0.5000 0.5000 0.4820	0.5000 0.5000 0.4820	0.5000 0.5000 0.4820
	Uiso	0.0153	0.0153	0.0153	0.0153	0.0153
	O (x,x,x)	0.5000 0.5000 -0.0489	0.5000 0.5000 -0.0489	0.5000 0.5000 -0.0489	0.5000 0.5000 -0.0489	0.5000 0.5000 -0.0489
	Uiso	0.0449	0.0449	0.0449	0.0449	0.0449
	O (x,x,x)	0.5000 0.0000 0.5016	0.5000 0.0000 0.5016	0.5000 0.0000 0.5016	0.5000 0.0000 0.5016	0.5000 0.0000 0.5016
	Uiso	0.0147	0.0147	0.0147	0.0147	0.0147
Occupancy	**Bi**	0.478	0.478	0.478	0.478	0.478
	K	0.522	0.522	0.522	0.522	0.522
	Fe	0.497	0.497	0.497	0.497	0.497
	Nb	0.503	0.503	0.503	0.503	0.503
χ ^2		2.133	2.122	2.404	7.447	5.626
Fitted	**wRp**	0.0371	0.0368	0.0392	0.0689	0.0600
	Rp	0.0329	0.0325	0.0334	0.0445	0.0434
Background	**wRp**	0.0738	0.0723	0.0784	0.1914	0.1792
	Rp	0.0594	0.0570	0.0637	0.1286	0.1293
R(A cation)		1.495	1.495	1.495	1.495	1.495
R(Bcation)		0.643	0.643	0.643	0.643	0.643
Tolerance factor		1.002239	1.002239	1.002239	1.002239	1.002239

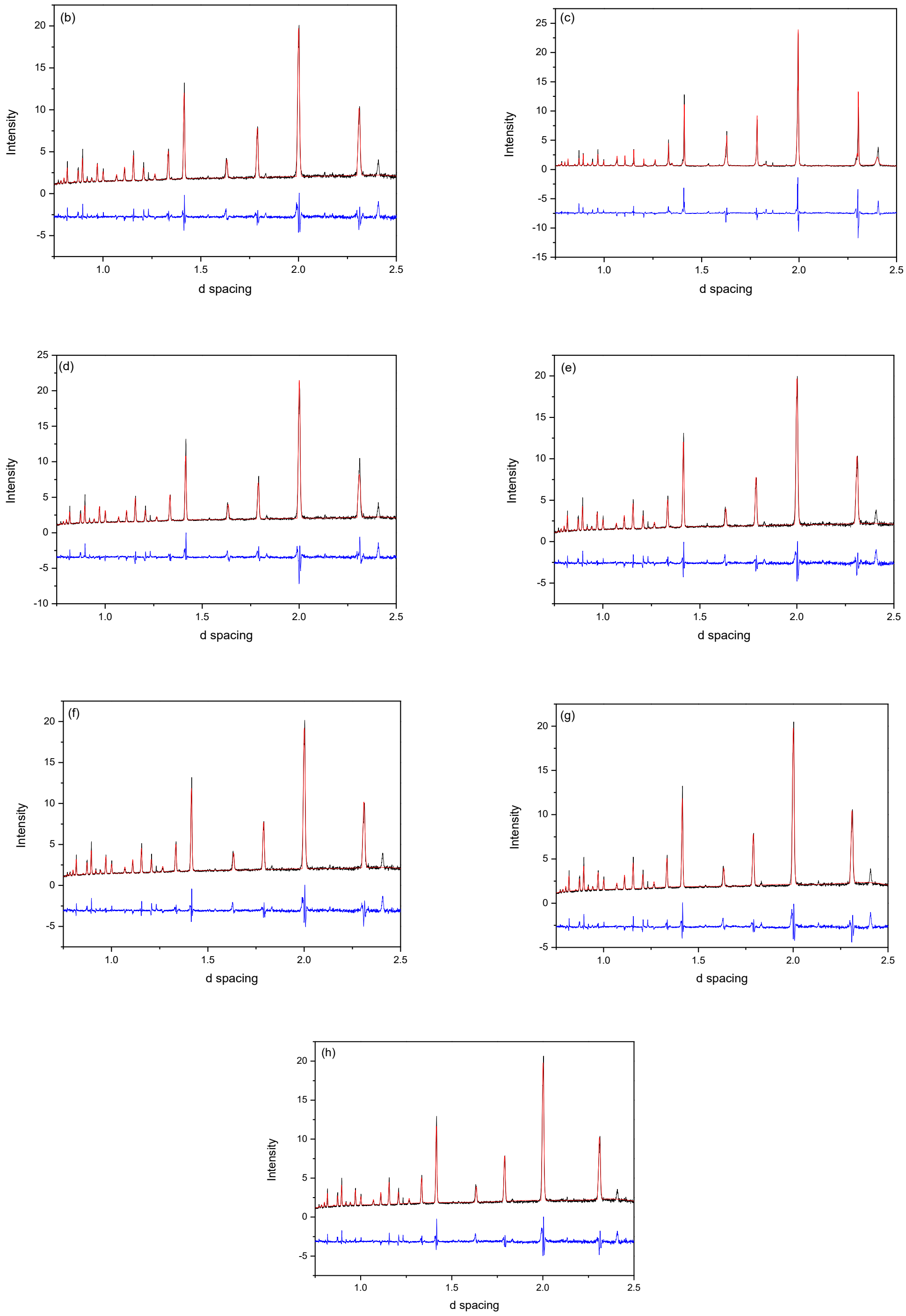

Figure 6.16: *Rietveld refinement profiles between 0.75Å and 2.5Å for neutron diffraction data collected for of* $Bi_{0.50}K_{0.50}Fe_{0.50}Nb_{0.50}O_{3}$*, showing reasonable fits for both peak shape and intensity. The black line represents experimental data, the red line the fitted model, and the subsequent blue line the difference between the data and the fit. This refinement uses the P4mm symmetry, and was recorded on the HRPD instrument at (a) 9K (b) 15K (c) 20K (d) 25K (e) 30K (f) 50K (g) 100K (h) 150K*

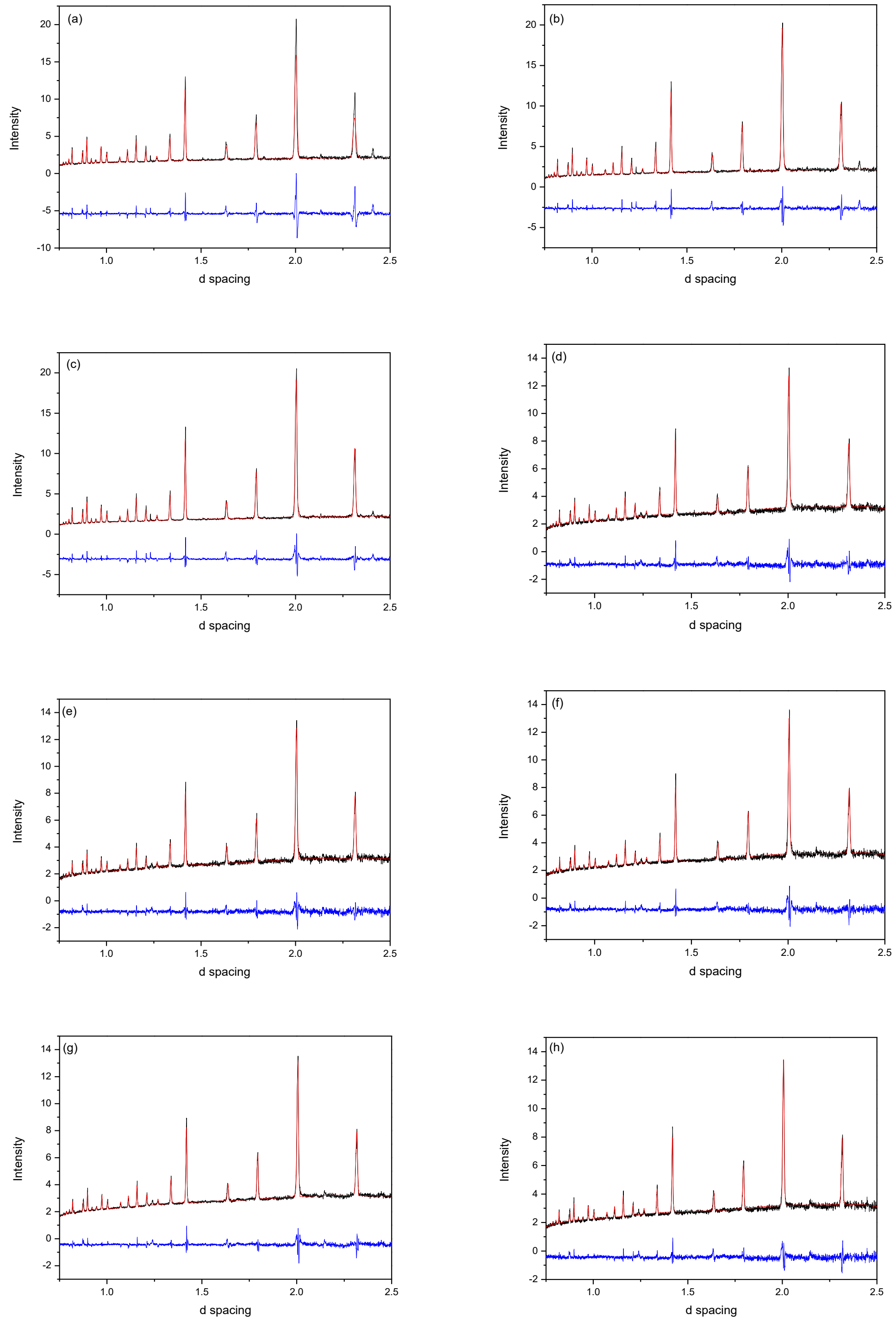

Figure 6.17: *Rietveld refinement profiles between 0.75Å and 2.5Å for neutron diffraction data collected for of* $Bi_{0.50}K_{0.50}Fe_{0.50}Nb_{0.50}O_3$*, showing reasonable fits for both peak shape and intensity. The black line represents experimental data, the red line the fitted model, and the subsequent blue line the difference between the data and the fit. This refinement uses the P4mm symmetry, and was recorded on the HRPD instrument at (a) 200K (b) 250K (c) 300K (d) 323K (e) 373K (f) 423K (g) 448K (h) 473K*

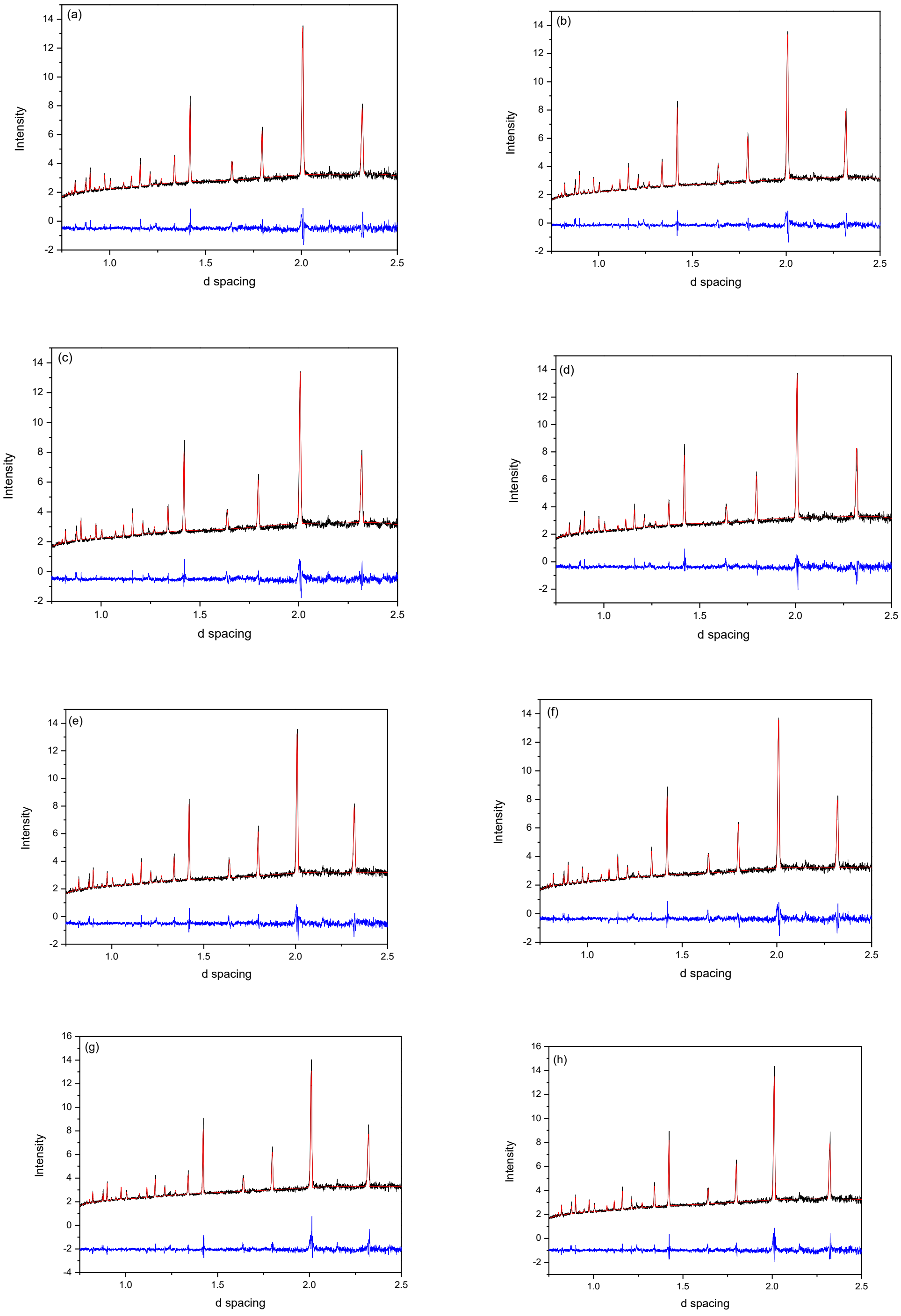

Figure 6.18: *Rietveld refinement profiles between 0.75Å and 2.5Å for neutron diffraction data collected for of* $Bi_{0.50}K_{0.50}Fe_{0.50}Nb_{0.50}O_3$, *showing reasonable fits for both peak shape and intensity. The black line represents experimental data, the red line the fitted model, and the subsequent blue line the difference between the data and the fit. This refinement uses the P4mm symmetry, and was recorded on the HRPD instrument at (a) 498K (b) 523K (c) 548K (d) 573K (e) 598K (f) 623K (g) 673K (h) 723K*

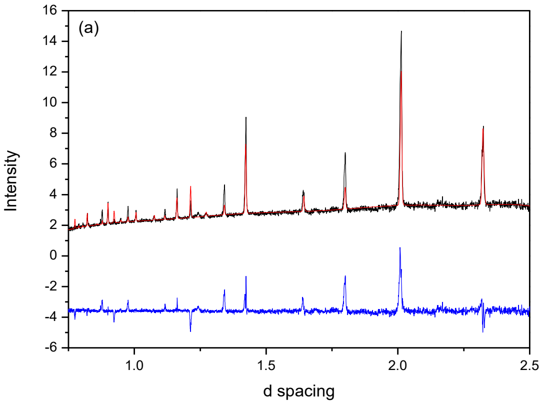

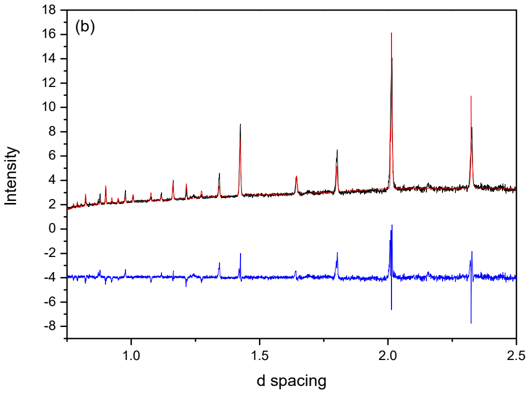

Figure 6.19: *Rietveld refinement profiles between 0.75Å and 2.5Å for neutron diffraction data collected for of* $Bi_{0.50}K_{0.50}Fe_{0.50}Nb_{0.50}O_{3}$, *showing reasonable fits for both peak shape and intensity. The black line represents experimental data, the red line the fitted model, and the subsequent blue line the difference between the data and the fit. This refinement uses the P4mm and Amm2 symmetries, and was recorded on the HRPD instrument at (a) 773K (b) 873K*

All compositions were loaded into 6 mm diameter cylindrical vanadium cans for data retrieval using room temperature synchrotron diffraction data, which was collected on the high resolution diffraction beamline (I11) at the Diamond Light Source, UK (l = 0.826943(5) Å and 2θ zeropoint = 0.001533(3)).

Table 6.7.1*: Table showing the lattice parameters and χ^2, wRp and Rp refinement parameters, along with the phase %, any secondary phases, M-O bond lengths and angles for the B site Fe^{3+} ion, cell volume and atomic positions and thermal information for synchrotron data $Bi_{1-x}K_xFe_{1-x}Nb_xO_3$ refined in the R3c symmetry. All of this data was extracted from the GSAS refinement suite.*

$Bi_{1-x}K_xFe_{1-x}Nb_xO_3$	x	0.1	0.2
Phase		R3c	R3c
Lattice parameters	a	5.600	5.883
	b	5.600	5.883
	c	13.840	13.761
Tetragonality (c/a)		2.471	2.339
M-O	1	2.079	2.071
	2	2.007	2.012
Cell Volume		376.02	375.89
Atom Positions	A (0,0,0)	0.000	0.000
		0.000	0.000
		0.000	0.000
	Uiso	0.016	0.016
	B (x,x,x)	0.000	0.000
		0.000	0.000
		0.224	0.224
	Uiso	0.128	0.128
	O (x,x,x)	0.445	0.445
		0.028	0.028
		0.956	0.956
	Uiso	0.123	0.123
Occupancy	K	0.923	0.824
	Bi	0.076	0.176
	Nb	0.862	0.862
	Fe	0.138	0.138
χ ^2		16.320	22.490
Fitted	wRp	0.215	0.159
	Rp	0.169	0.127
Background	wRp	0.245	0.242
	Rp	0.196	0.183
R(A cation)		1.379	1.408
R(Bcation)		0.645	0.644
Tolerance factor		0.961	0.971

***Table 6.7.2**: Table showing the lattice parameters and χ^2, wRp and Rp refinement parameters, along with the phase %, any secondary phases, M-O bond lengths and angles for the B site Fe^{3+} ion, cell volume and atomic positions and thermal information for synchrotron data $Bi_{1-x}K_xFe_{1-x}Nb_xO_3$ refined in the P4mm symmetry. All of this data was extracted from the GSAS refinement suite.*

$Bi_{1-x}K_xFe_{1-x}Nb_xO_3$	**x**	0.4	0.5	0.6	0.7
Phase		P4mm	P4mm	P4mm	P4mm
Lattice parameters	**a**	4.000	4.004	4.010	4.006
	b	4.000	4.004	4.010	4.006
	c	3.998	3.997	3.995	4.010
Tetragonality (c/a)		0.999	0.998	0.996	1.001
M-O	**1**	1.863	1.835	1.787	1.734
	2	2.135	2.262	2.266	2.276
	3	2.004	2.019	2.022	2.018
Cell Volume		63.98	64.08	64.24	64.350
Atom Positions	**A (0,0,0)**	0.000	0.000	0.000	0.000
		0.000	0.000	0.000	0.000
		0.000	0.000	0.000	0.000
	Uiso	0.122	0.069	0.058	0.043
	B (x,x,x)	0.500	0.550	0.500	0.500
		0.500	0.500	0.500	0.500
		0.482	0.450	0.461	0.440
	Uiso	0.013	0.015	0.008	0.006
	O (x,x,x)	0.500	0.500	0.500	0.500
		0.500	0.500	0.500	0.500
		0.016	0.016	0.016	0.016
	Uiso	0.010	0.010	0.010	0.010
	O (x,x,x)	0.500	0.500	0.500	0.500
		0.000	0.000	0.000	0.000
		0.515	0.515	0.527	0.378
	Uiso	0.010	0.010	0.010	0.010
Occupancy	**K**	0.690	0.489	0.307	0.192
	Bi	0.310	0.501	0.693	0.808
	Nb	0.526	0.531	0.359	0.241
	Fe	0.474	0.469	0.639	0.759
χ ^2		8.560	10.640	12.390	10.430
Fitted	**Rp**	0.150	0.161	0.167	0.179
	wRp	0.119	0.124	0.135	0.142
Background	**Rp**	0.190	0.197	0.216	0.244
	wRp	0.158	0.161	0.179	0.195
R(A cation)	**Rp**	1.466	1.495	1.524	1.553
R(Bcation)		0.643	0.643	0.642	0.642
Tolerance factor		0.992	1.002	1.013	1.023

***Table 6.7.3**: Table showing the lattice parameters and χ^2, wRp and Rp refinement parameters, along with the phase %, any secondary phases, M-O bond lengths and angles for the B site Fe^{3+} ion, cell volume and atomic positions and thermal information for synchrotron data $Bi_{1-x}K_xFe_{1-x}Nb_xO_3$ refined in the Amm2 symmetry. All of this data was extracted from the GSAS refinement suite.*

$Bi_{1-x}K_xFe_{1-x}Nb_xO_3$	x	0.8
Phase		P4mm
Lattice parameters	a	4.009
	b	4.009
	c	4.001
Tetragonality (c/a)		0.998
M-O	1	1.736
	2	2.264
	3	2.021
Cell Volume		64.301
Atom Positions	A (0,0,0)	0.000
		0.000
		0.000
	Uiso	
	B (x,x,x)	0.500
		0.500
		0.450
	Uiso	
	O (x,x,x)	0.500
		0.500
		0.016
	Uiso	
	O (x,x,x)	0.500
		0.000
		0.515
	Uiso	
Occupancy	K	0.194
	Bi	0.806
	Nb	0.190
	Fe	0.810
χ ^2		16.980
Fitted	Rp	0.195
	wRp	0.156
Background	Rp	0.253
	wRp	0.204
R(A cation)	Rp	1.582
R(Bcation)		0.641
Tolerance factor		1.033

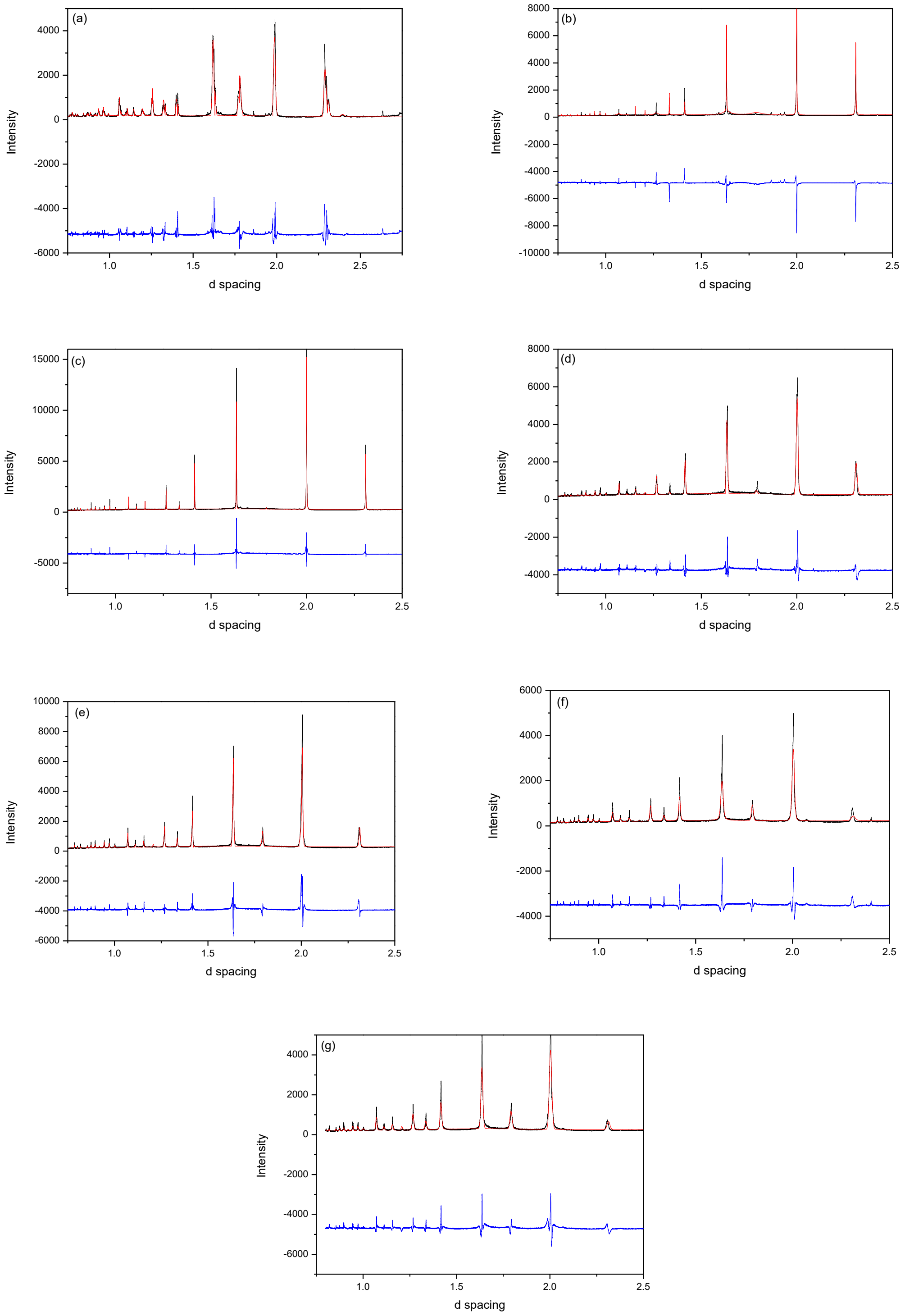

Figure 6.20: *Rietveld refinement profiles between 0.75Å and 2.5Å for synchrotron data collected for of* $Bi_{1-x}K_xFe_{1-x}Nb_xO_3$*, showing reasonable fits for both peak shape and intensity. The black line represents experimental data, the red line the fitted model, and the subsequent blue line the difference between the data and the fit. This refinement uses the P4mm symmetry, and was recorded on the Ill instrument at for values of x= (a) 0.10 (b) 0.20 (c) 0.40 (d) 0.50 (e) 0.60 (f) 0.70 (g) 0.80*

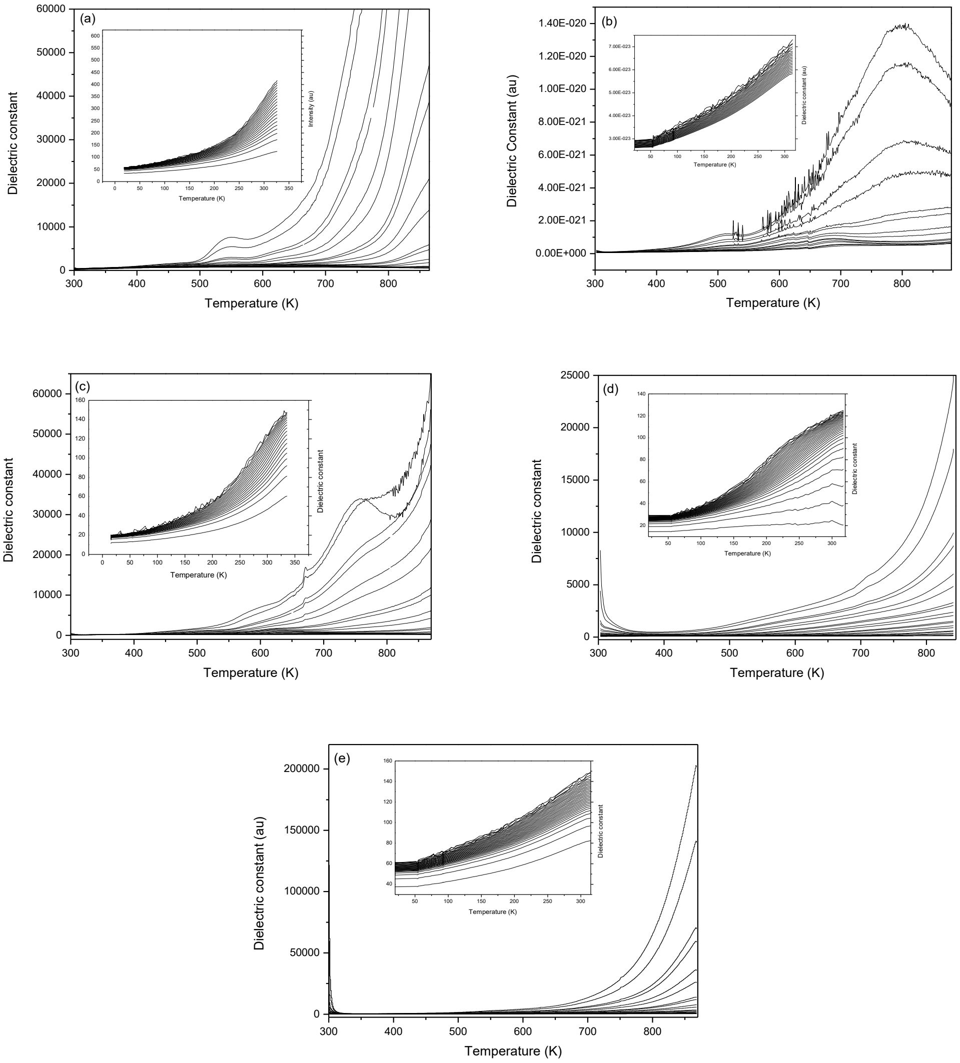

Figure 6.21: *Dielectric constant data collected for* $Bi_{1-x}K_xFe_{1-x}Nb_xO_3$ *using the frequencies at which the reading was taken between 100Hz and 10MHz. The data shows some high permittivity relaxor like electrode effect. Data is shown for compositions of x= (a) 0.10 (b) 0.20 (c) 0.40 (d) 0.50 (e) 0.80, other composition were not measured due to issues with pellet formation.*

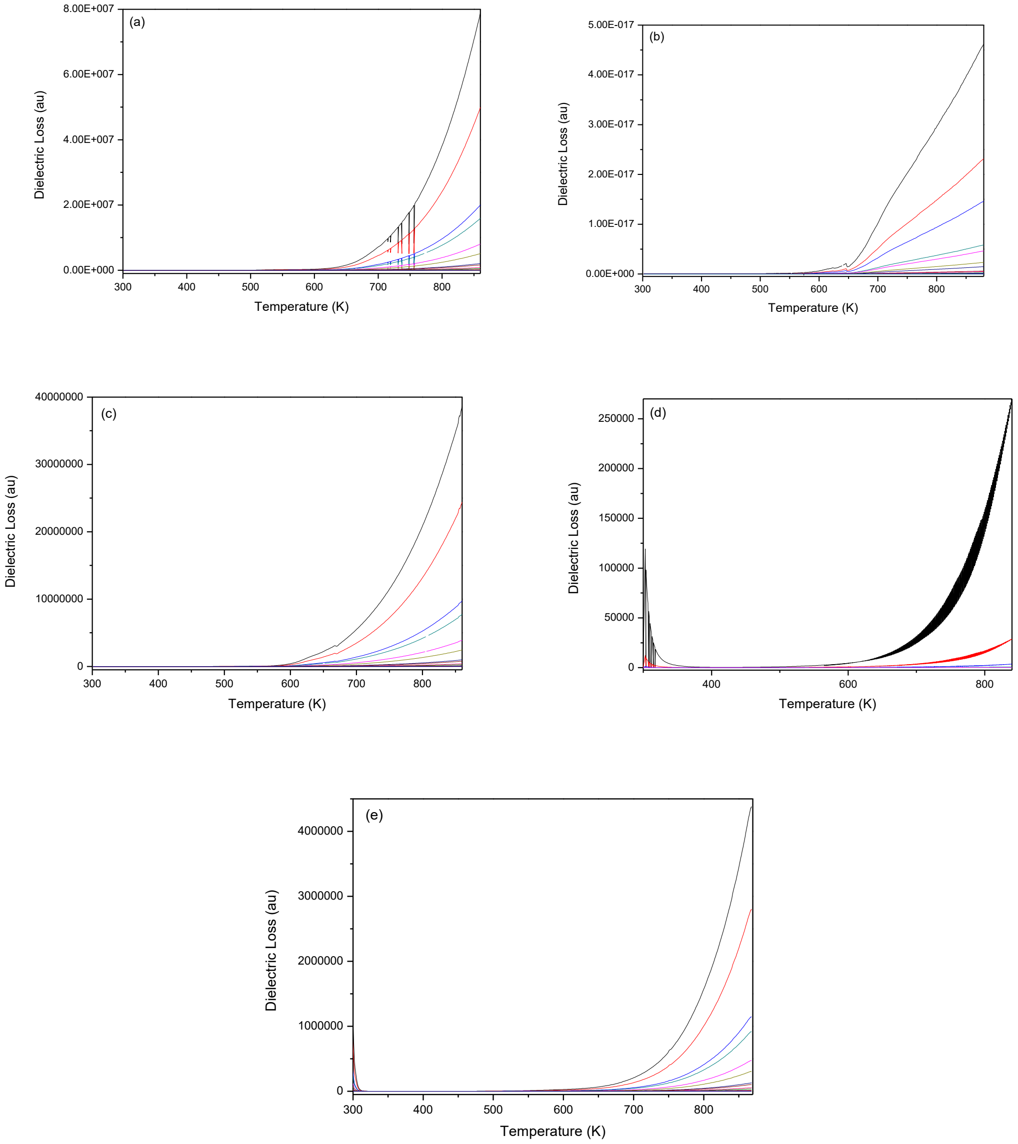

Figure 6.22: *Dielectric data showing the calculated dielectric loss collected for $Bi_{1-x}Dy_xFeO_3$ each colour represent the frequency at which the reading was taken between 100Hz and 10MHz. Data is shown for compositions of x= (a) 0.10 (b) 0.20 (c) 0.40 (d) 0.50 (e) 0.80, other composition were not measured due to issues with pellet formation.*

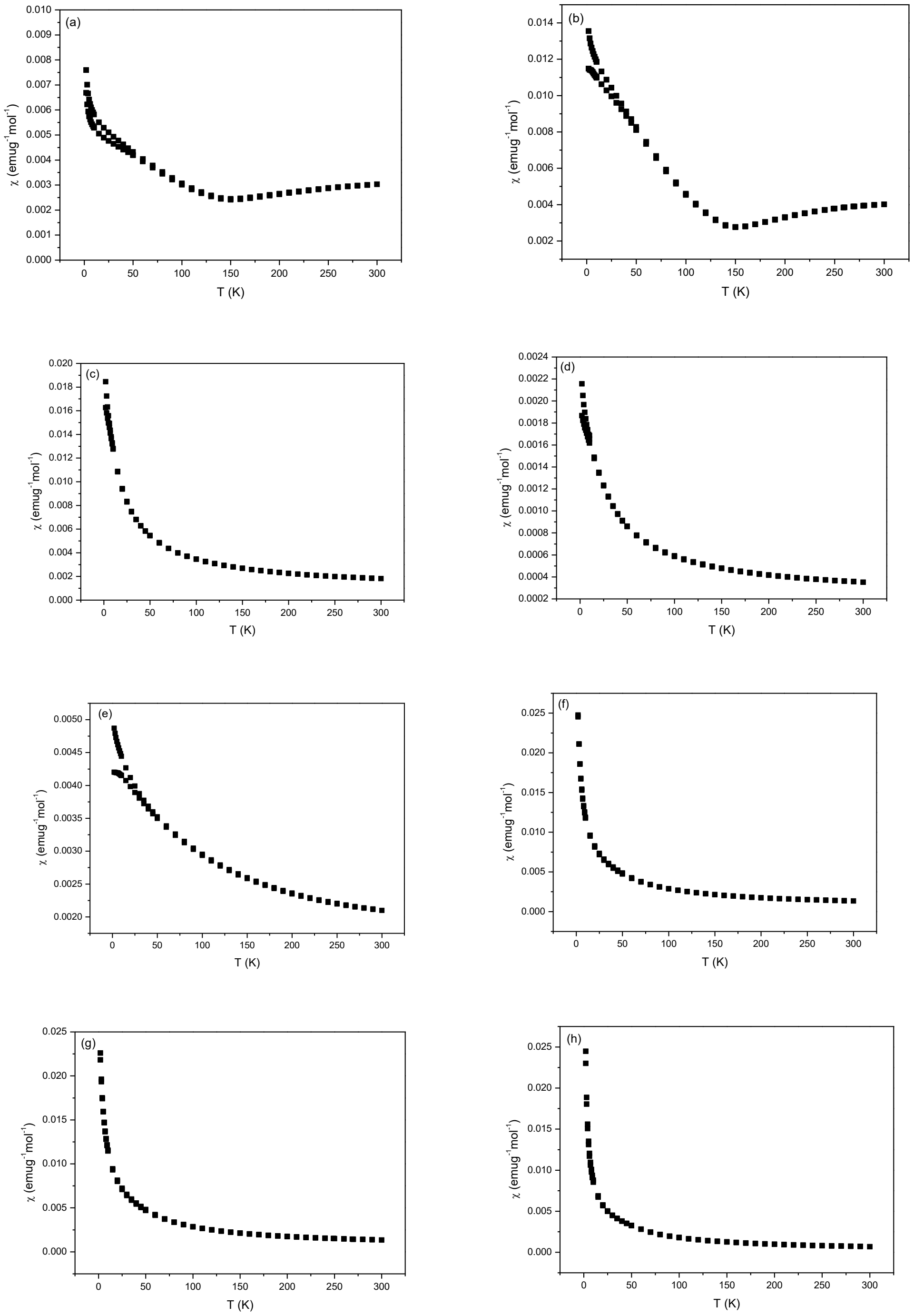

Figure 6.23: *SQUID data taken of* $Bi_{1-x}K_xFe_{1-x}Nb_xO_3$ *at the ISIS Neutron facility, showing ZFC/FC data for compositions of x= (a) 0.10 (b) 0.20 (c) 0.40 (d) 0.50 (e) 0.60 (f) 0.70 (g) 0.80 (h) 0.90*

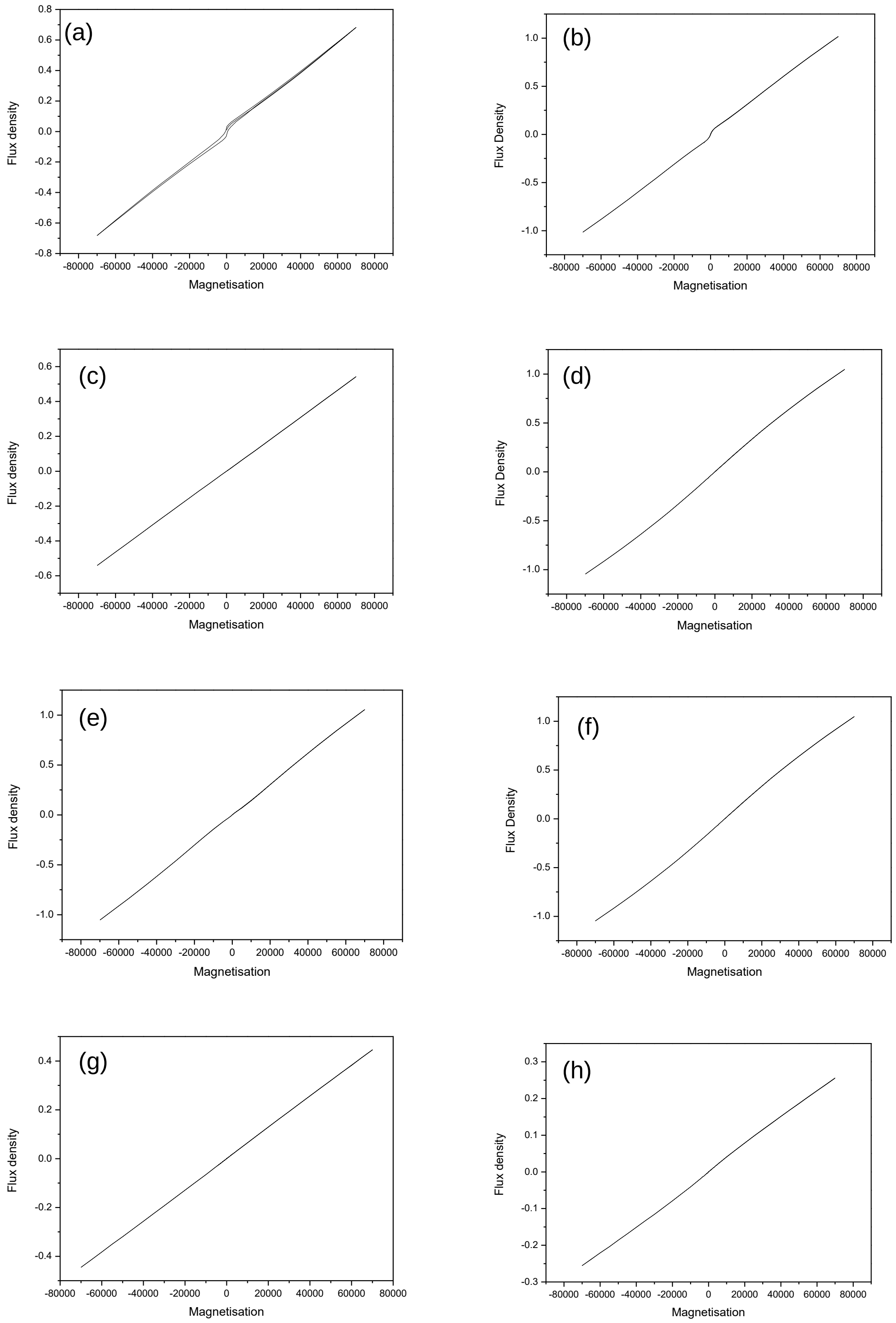

Figure 6.24: *Hysteresis loops recorded at the ISIS Neutron facility for* $Bi_{1-x}K_xFe_{1-x}Nb_xO_3$ *compositions of x= (a) 0.10 (b) 0.20 (c) 0.40 (d) 0.50 (e) 0.60 (f) 0.70 (g) 0.80 (h) 0.90*

Raman spectra were collected on a Horiba Yvon Jobin LabRAM instrument. Room temperature mapping was performed using a 633 nm laser over an area of approximately 50μm × 50μm. These measurements were performed using ten integrations with a two second acquisition time with ×50 objective and 600 lines per mm grating over a Raman shift range of between 80 cm-1 and 1280 cm-1. Single point high resolution Raman spectroscopy was performed with a 633 nm wavelength laser at 77 K using a Linkam Examina THMS 600 cold stage. Measurements were performed using ten integrations with a one second acquisition time with a ×50 objective and 1800 lines per mm grating.

Figures 6.24 gives the Raman spectra collected for the $Bi_{1-x}K_xFe_{1-x}Nb_xO_3$ materials in the composition range $0.0 \leq x \leq 1.0$. Raman spectra were collected by Dr D C Arnold at the University of Kent.

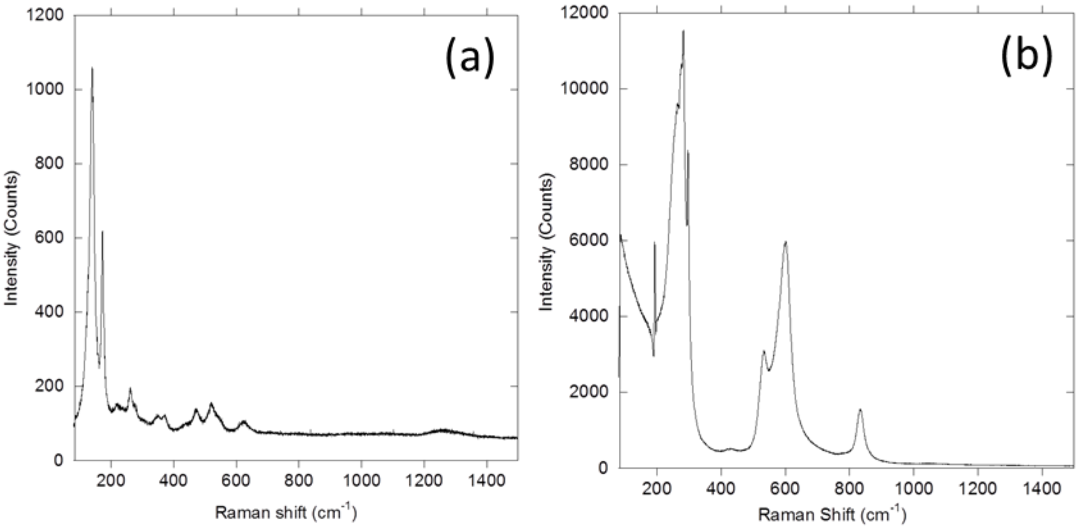

Figure 6.25.1: *Raman spectra collected at room temperature for (a)* $BiFeO_3$ *(b)* $KNbO_3$

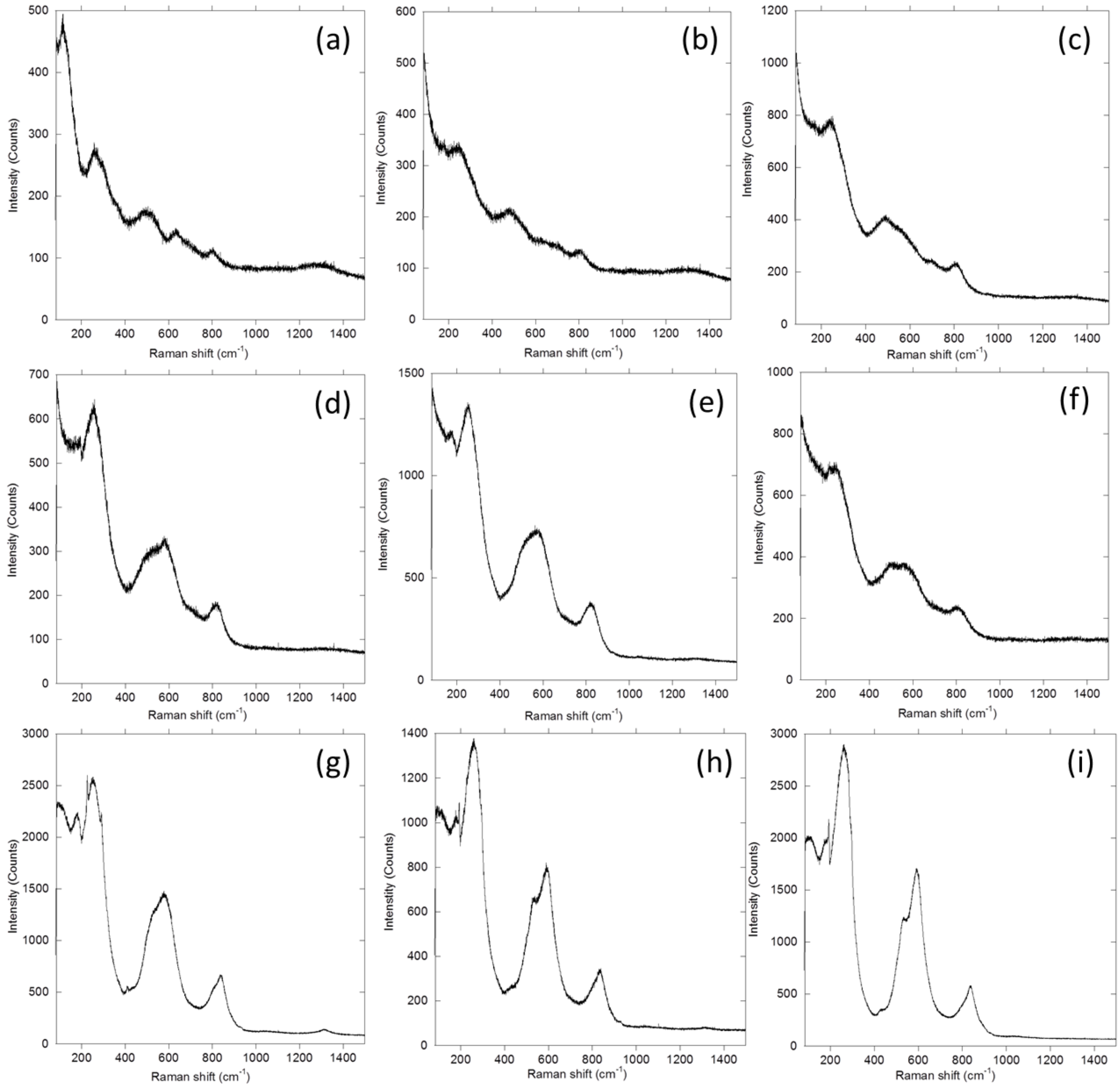

Figure 6.25.2: *Raman spectra collected at room temperature for (a) $Bi_{0.90}K_{0.10}Fe_{0.90}Nb_{0.10}O_3$ (b) $Bi_{0.80}K_{0.20}Fe_{0.80}Nb_{0.20}O_3$, (c) $Bi_{0.70}K_{0.30}Fe_{0.70}Nb_{0.30}O_3$, (d) $Bi_{0.60}K_{0.40}Fe_{0.60}Nb_{0.40}O_3$, (e) $Bi_{0.50}K_{0.50}Fe_{0.50}Nb_{0.50}O_3$, (f) $Bi_{0.40}K_{0.60}Fe_{0.40}Nb_{0.60}O_3$, (g) $Bi_{0.30}K_{0.70}Fe_{0.30}Nb_{0.70}O_3$, (h) $Bi_{0.20}K_{0.80}Fe_{0.20}Nb_{0.80}O_3$ and (i) $Bi_{0.10}K_{0.90}Fe_{0.10}Nb_{0.90}O_3$.*

40,262 words